ADAPTIVE DROPLET-BASED MEMBRANOUS SOFT MATERIALS

by

MICHELLE M. MAKHOUL-MANSOUR

(Under the Direction of Eric Freeman)

ABSTRACT

Embedding synthetic materials with the ability to morph on-demand opens a new solution space for many engineering fields: from chemical computing platforms and drug carriers to passive sensors and soft robotic actuators. In such applications, more traditional components can be too large, heavy, non-biocompatible, or power intensive. Fortunately, nature offers a fascinating set of examples where function follows form. For instance, widely considered to lack traditional muscular and nervous systems, plants can exert autonomous movements in response to external stimuli. Alternatively, animal tissues are known to competently use a small number of choreographed localized cellular intercalations to influence their overall shape. More recently, synthetic bottom-up biology has been used in adjunction to precision technologies, like digital microfluidics, to recombine functional modules towards multifunctional synthetic tissues. The focus of this work is embedding structural and chemical adaptability into membranous droplet-based soft materials. This dissertation builds on previous work from the Droplet Interface Bilayer (DIB) technique which assembles structures of lipid membranes at the interface of aqueous microdroplets dispersed in an oil phase. This work studies the structural and chemical adaptation of DIB-based materials to external optical, electrical, mechanical, and even magnetic conditions carried through naturally inspired strategies of transmembrane communications and cellular intercalations.

The first part of this work investigates the incorporation of magnetic fluids (ferrofluids) into DIB-based materials and its influences on the material properties, performance, and communication. Tissue-inspired morphing is then accomplished by applying magnetic fields in both experimental and modeling strategies, which generates intercalation events inspired from natural reconfiguration mechanisms observed in embryonic morphogenesis and gastrulation. The second part of this work examines novel strategies for enabling chemical-based adaptation through molecular communication in DIB-tissues akin to natural intracellular communication pathways. Molecular communication can be achieved by controlling the membranes' permeability using photopolymerizable lipids. This directional permeability can be used in conjunction to the magnetically enabled adaptation to generate soft tissues whose chemical composition and functionality relate back to their shape yielding optimized response mechanisms that bridge the gap between biological systems and soft matter frameworks.

INDEX WORDS: Stimuli responsive materials, stabilized adhesive emulsions, droplet microfluidics, ferrofluids, self-assembly, electromagnetic manipulation, tissue adaptability, cellular-inspired tissue reconfiguration, model lipid membranes, photopolymerizable lipids.

ADAPTIVE DROPLET-BASED MEMBRANOUS SOFT MATERIALS

by

MCHELLE M. MAKHOUL-MANSOUR

B.E., Lebanese American University, Lebanon, 2015

A Dissertation Submitted to The Graduate Faculty of The University of Georgia in Partial Fulfilment of The Requirements of The Degree

DOCTOR OF PHILOSOPHY

ATHENS, GEORGIA

2021

©2021

MICHELLE M. MAKHOUL-MANSOUR

All Rights Reserved

ADAPTIVE DROPLET-BASED MEMBRANOUS SOFT MATERIALS

by

MICHELLE M. MAKHOUL-MANSOUR

Major Professor: Eric Freeman

Committee: Donald Leo

Leidong Mao

Andy Sarles

Electronic Version Approved:

Ron Walcott

Vice Provost for Graduate Education and Dean of the Graduate School

The University of Georgia

December 2021

DEDICATION

To Mama, Baba, Elie and Charbel, this work is dedicated to you.

Your endless love, advice, sacrifices, and prayers got me through this.

I love you.

"Just as the constant increase of entropy is the basic law of the universe, so it is the basic law of life to be ever more highly structured and to struggle against entropy."- Vaclav

Havel

ACKOWLEDGEMENTS

Without the support of many people the completion of this dissertation would never have occurred. I wish to express my sincere appreciation and thanks to the following people:

Dr. Eric Freeman, my major professor, who gave me continuous support, guidance, encouragement, and suggestions. His patience with me was wonderful.

Dr. Donald Leo, Dr. Leidong Mao and Dr. Andy Sarles, whose support, excellent suggestions and assistance has helped me to achieve my goals.

And last, but never least, to Nicholas Filla who was always there for me when I needed him. Thank you for your help, support, and love. I am very so lucky to have you in my life.

TABLE OF CONTENT

	Page
ACKNOWLEDGEMENTS	v
LIST OF TABLES	X
LIST OF FIGURES	xiii
CHAPTER	
1. INTODUCTION	1
Objectives	13
Document Overview	15
References	21
2. LITERATURE REVIEW: DROPLET-BASED MEMBRANOUS	SOFT
MATERIALS	28
Abstract	29
Introduction	29
Mechanics Of Droplet Interface Bilayers	38
Formation of Droplet Interface Bilayers	47
Functionalized Droplet Interface Bilayer Materials	56
Conclusion And Future Prospects	66
References	68

3.	FERROFLUID-BASED DROPLET INTERFACE BILAYER NETWORKS
	82
	Abstract83
	Introduction83
	Materials87
	Methods91
	Results and Discussion99
	Conclusions
	References
4.	RECONFIGURING DROPLET INTERFACE BILAYER NETWORKS
	THROUGH SACRIFICIAL MEMBRANES
	Abstract113
	Introduction113
	Materials and Methods117
	Experimental Methodology118
	Discussion of Experimental Comparisons
	Model Extension
	Conclusions
	References
5.	IMBUING MEMBRANOUS MATERIALS WITH MAGNETICALLY
	DRIVEN RECONFIGURATION EVENTS
	Abstract140
	Introduction140

	Results and Discussion
	Conclusion
	Methodology
	References
6.	PHOTOPOLYMERIZED MICRODOMAINS IN BOTH LIPID LEAFLETS
	ESTABLISH DIFFUSIVE TRANSPORT PATHWAYS ACROSS
	BIOMIMETIC MEMBRANES
	Abstract
	Introduction
	Materials and Methods
	Results and Discussion
	Conclusion
	References
7.	ENABLING MEMBRANOUS SOFT MATERIALS WITH THE ABILITY
	TO MORPH THROUGH LIPID RAFTS
	Abstract
	Introduction
	Materials
	Methods
	Results
	Discussion
	Conclusion
	Pafaranaas 222

8. CONCLUSIONS AND SUMMARY236
Summary- Overview of this Document
Contributions239
Final Remarks241
APPENDICES
A. SUPPLEMENTARY INFORMATION: IMBUING MEMBRANOUS
MATERIALS WITH MAGNETICALLY DRIVEN RECONFIGURATION
EVENTS242
B. SUPPLEMENTARY INFORMATION: PHOTOPOLYMERIZED
MICRODOMAINS IN BOTH LIPID LEAFLETS ESTABLISH DIFFUSIVE
TRANSPORT PATHWAYS ACROSS BIOMIMETIC MEMBRANES253
C. SKIN-INSPIRED SOFT MATERIAL WITH DIRECTIONAL
MECHANOSENSATION277

LIST OF TABLES

Page
Table 3.1 : Measurements Obtained for DIBs with and without ferrofluids at 22°C101
Table 4.1: Surface Evolver Model Inputs 122
Table 4.2: Circuit Model Inputs 123
Table 7.1: Results for monolayer tension with varying lipid mixtures at three selected
temperatures. The mixture of DPhPC, sphingomyelin, and cholesterol is known to generate
lipid rafts at room temperature which dissipate with elevated temperature. Notably, these
compositions (highlighted in pink) are the only mixtures which exhibit trends in the
monolayer temperature. The final case (2:1:2) provides an opposing trend compared to the
2:1:1 and 1:1:1 mixtures (tension increases with temperature rather than decreases)
Table 7.2: Droplets with a DPhPC:bSM:Chol molar composition of 1:1:1 were injected at
46 °C and given enough time for monolayer formation. The oil temperature was then
reduced to 22 °C and then the droplets were brought together to usher membrane formation.
The properties of these membranes were consequently recorded, and the average (n=3) and
standard deviation reported
Table 7.3: Droplets with a DPhPC:bSM:Chol molar composition of 1:1:1 were injected
at 22 °C and given enough time for monolayer formation. The droplets were brought

together to usher membrane formation. The oil temperature was then raised to 34 then 46
°C before cycling back to 22 °C and consequently 46 °C. The droplets were not separated
at any given stage and the membrane remained formed. The properties of these membranes
were recorded at each stage, and the average (n=3) and standard deviation reported.

Table 7.5: Droplets with a DPhPC:bSM:Chol molar composition of 1:0:0 were injected at 22 °C and given enough time for monolayer formation. The droplets were brought together to usher membrane formation. The oil temperature was then raised to 34 then 46 °C before cycling back to 22 °C and consequently 46 °C. The droplets were not separated at any given stage and the membrane remained formed. The properties of these membranes were recorded at each stage, and the average (n=3) and standard deviation reported.

Table 7.6: Droplets with a DPhPC:bSM:Chol molar composition of 1:1:1 and 1:0:0 (asymmetric membrane) were injected at 22 °C and given enough time for monolayer formation. The droplets were brought together to usher membrane formation. The oil temperature was then raised to 34 then 46 °C before cycling back to 22 °C and consequently 46 °C. The droplets were not separated at any given stage and the membrane remained

formed. The properties of these membranes were re	corded at each stage, and the average
(n=3) and standard deviation reported	230

LIST OF FIGURES

Page

Figure 1.1: At a fundamental level, living organisms are generally composed of one or
more cells (cellular units). These units are then organized into tissues then by extension
organs. Cells have been classified as prokaryotes and eukaryotes with the main difference
between the two being the presence of a nucleus (prokaryotic cells lack a nucleus, while
eukaryotic cells have a nucleus and hence prokaryotic cells are simpler in composition).
Examples of prokaryotes are bacteria and archaea. Examples of eukaryotes are fungi,
plants, and animals. Both cell categories have a basic common feature: a plasma
membrane, also referred to as cellular membrane. This membrane delimits the cell, blocks
external pathogens, contains receptors and channels that allow specific molecules, that
mediate cellular and extracellular activities to pass between organelles and between the cell
and the outside environment; and separates vital but incompatible metabolic processes
conducted within different cellular units
Figure 1.2: The existence of a cellular membrane has been speculated since the invention
of the early microscope and the plant cell wall being clearly detected. Following this, the
lipid nature of the cell membrane was suggested, and several models were proposed to
describe its structure from the "lipoid theory of narcosis" (Overton 1880) to the more recent
fluid mosaic model (Singer and Nicholson 1972)

Figure 1.3: Phospholipids are a key component of cellular membranes. (a) Amphiphilic
phospholipid molecules are lipids with a hydrophilic head containing a phosphate group,
and two hydrophobic tails derived from fatty acids, joined by a together by a glycerol
molecule. Some of the phospholipid tails are saturated and some are unsaturated. The more
unsaturated they are, the more fluid the membrane. (b) Due to their amphiphilic nature,
phospholipids can form alternative configurations such as micelles, reverse micelles,
planar bilayers and liposomes
Figure 1.4: The Droplet Interface Bilayer (DIB) technique assembles soft biomimetic lipid
membranes at the interface of lipid-coated aqueous microdroplets dispersed in an oil phase.
Upon formation, the area of the interfacial lipid membrane is governed through a balance
of monolayer and bilayer tensions reflected through an external angle of contact and
gradually expands until the tensions at the annulus are balanced as given by Young's
equation11
Figure 1.5: Droplet interface bilayers (DIBs) allow for the formation of webs of lipid
membranes between aqueous droplets that approximate living tissues. The membranes
may be functionalized to adapt their structure to various external stimuli, producing
transmembrane exchanges and adaptations in the adhered droplet structure12
Figure 1.6: The incorporation of a magnetic fluid or ferrofluid within the droplet phases
for the creation of magnetically responsive DIB arrays is investigated first. Once
compatibility is established, potential applications of the ferrofluid-enabled DIBs are
showcased by remotely modifying membrane qualities through magnetic fields14

Figure 1.7: Multiple lipid encased water droplets may be linked together in oil to form large networks of droplet interface bilayers thus creating a new class of stimuli-responsive materials for applications in sensing, actuation, drug delivery, and tissue engineering. One particular problem of interest is understanding the impact of the coalescence of two neighboring droplets on the overall structural integrity of the network. Droplet networks with tailored architectures are synthesized with the aid of magnetic motor droplets containing a biocompatible ferrofluid. The equilibrium configuration of the droplet networks is compared to computational prediction which defines the overall stability by summing the interfacial energies. Once the networks are completed, failure in selected membranes is induced. As the targeted droplets coalesce together, the equilibrium structure of the network is altered, and the remaining droplets may shift to new configurations dictated by their minimized mechanical energies.16 Figure 1.8: Inspired by the hierarchy and compartmentalization of natural tissues, we synthetize a droplet-based material containing webs of lipid membranes. Such materials are traditionally static and do not interact with external conditions, posing future challenges in their practical applications. Adaptability is explored here by infusing the platform with ferrofluids, rendering the material sensitive to external magnetic force fields. Adaptation via structural changes is further optimized by implementing strategies observed in natural tissues during the morphogenesis and gastrulation phases of embryonic development. We show that when exposed to magnetic forces, DIB-tissues adapt by changing their internal structure and establishing new internal communication pathways, an approach inspired by

Figure 1.9: Using the Droplet Interface Bilayer (DIB) platform, a complex network of stabilized emulsive droplets interconnected through interfacial lipid bilayers can be constructed. Such structures are responsive to different types of external triggers and exhibit pre-meditated and precise output signals. The nature of the response can be controlled through tailored bilayer/droplet composition. Different transmembrane peptide and protein channels can be incorporated within the aqueous phase of the DIB platform to achieve patterned conductive pathways linking multiple compartments together. Herein, we explore the capability of patterning conductive pathways one-droplet thick in resolution by infusing the aqueous phase with photopolymerizable lipids. Red droplets contain DPhPC phospholipids, green droplets contain DPhPC and αHl, lilac droplets contain DPhPC and Gramicidin monomers while different shades of blue droplets are the droplets containing a mixture of DPhPC and 23:2 DiynePC photopolymerizable lipids. The arrow shows a conductive pathway formed between droplets containing photopolymerizable lipids. The darkest droplets have the highest concentration of a target species. Transport can be therefore carried through droplets infused with photopolymerizable lipids.20 Figure 2.1: (a) It has been proposed that basic biochemical components can be used to construct synthetic cellular systems. One example of this are empty cells or liposomes, which are bordered with semi-permeable lipid bilayers and mediate exchange through transmembrane channels. Each liposome can be a standalone functional unit. (b) In contrast droplet pairs are connected with an interfacial lipid bilayer in the DIB technique to produce a single functional unit. Unlike liposomal systems, the properties of lipid membranes are in this case dictated by the bordering droplet pair and hence any rearrangement in the placement of these droplets will result in changes in the properties and composition of

Figure 2.2: The droplet interface bilayer (DIB) technique. A single lipid bilayer is formed at the interface of two lipid-coated aqueous microdroplets brought into contact. Schematic and experimental images of the formation of a DIB viewed (a) from the top/bottom and (b) from the side. (c) Schematic representation of the experimental setup used for DIB formation/characterization. Aqueous droplets are deposited on agarose-coated silver/silver chloride electrodes and submerged in oil. Side view and top view cameras connected to a microscope are used to acquire images of the formed bilayer. (b) and (c) are adapted from ref (18) Copyright Royal Society of Chemistry 2019. Lipids can be dispersed in the (d) water phase (lipid-in), (e) oil phase (lipid-out) or (f) both phases. The area of the DIB is governed through a balance of monolayer and bilayer tensions reflected through an external angle of contact. (g) Multiple droplets can be connected to form a 2D or even 3D membranous structure. Upon the formation of a single membrane, the spherical droplets deform into spherical caps, delimited by the dimensions of the interfacial bilayer. On a larger scale, similarly to tightly packed emulsive systems, DIB networks can exhibit regular hexagonal close-packing lattices distribution when optimal oil phases and lipid mixtures are used. Various integral transmembrane channels can be embedded in droplets and used to establish communication pathways within the material. Scale bar 250 µm.

Figure 2.3: Summary of DIB mechanics and dependencies. (a) Schematic representation of the effect of packing density on the adaptability and the stability of DIB tissue. As adhesion between droplets is increased, the contact angle, membrane area, and adhesion energy are increased, leading to denser networks. (b) Properties of DIBs were assessed using custom fabricated hydrogel microelectrodes, investigating the effect of the oil used on the specific capacitance of lipid membranes and their rate of formation. (c) The time for the membrane to reach 2/3 of its normalized size (defined here as the rise time) can be plotted against the Laplace number (mirroring the effect of inertia, surface forces, and viscous forces). Parts b and c are adapted (data adapted) with permission from ref (51). Copyright 2018 American Chemical Society. (d) Cholesterol molecules insert themselves between phospholipid molecules resulting in more rigid membranes which is reflected through an increase in both the monolayer and bilayer tension. Data adapted with permission from ref (22). Copyright 2019 Royal Society Interface. (e) Further investigation into the effect of the oil phase showed that the interfacial energy for a pair of adhered droplets as a function of the normalized distance between their centers (offset by the equilibrium distance) is also varying for different oils. Membranes that are more favorable to form show a greater range of deformation prior to separation. Adapted with permission from ref (24). Copyright 2018 AIP Biomicrofluidics. (f) Intended to provide an explanation for the spontaneous liquidlike tissue behavior, the DAH models tissues as emulsive systems: cells behave similarly to microdroplets whose varying degrees of surface adhesion (illustrated by using different colors blue and pink) cause them to spontaneously reorganize and minimize their interfacial free energy (β , cortical tension at free cell surface; and β *, residual tension in a cell at contact).

Figure 2.4: Various methods for the assembly of smaller DIB networks in a repeatable fashion. (a) Experimental images of DIBs formed using microfluidic channels. Each hydrodynamic trap can hold several lipid bilayers formed between two aqueous droplets. Reprinted with permission from ref (25). Copyright 2016 Lab on a Chip RSC. (b) Lipid-coated water droplets can be deposited into oil-infused hydrophobic surfaces and brought into contact forming 2D DIB structures. Reprinted with permission from ref (65). Copyright 2014 PNAS. (c) Laser-induced heating may be used to drive aqueous droplets into close proximity to each other resulting in the formation of lipid bilayers. Reprinted with permission from ref (66). Copyright 2010 American Chemical Society. (d) Magnetic fields may be used to assemble DIB networks by selectively infusing droplets with ferrofluids. The scale bar is 800 μm. Reprinted with permission from ref (24). Copyright 2018 AIP Biomicrofluidics.

Figure 2.5: High-membrane-density printing of encapsulated DIB tissues. (a) A glass micropipette is connected to a pressure clamp for pneumatic droplet deposition. A 3-axis manipulator is used to manipulate the micropipette to specific predefined coordinates. Adapted with permission from ref (28). Copyright 2018 Scientific Reports, Nature. (b) Side and (c) top view experimental images of a printed 3D DIB network. Parts b and c are adapted with permission from ref (73). Copyright 2017 International Society for Optics and Photonics SPIE. (d) Using the previously developed pneumatic droplet printing system, the process is repeated to generate webs of aqueous droplets. The printing process

is achieved on a heating plate using the experimental setup shown in part f ensuring that the encapsulating organogel is molten. (e) Once the final structure is produced, the heat is removed allowing the organogel to solidify. The organogel preserves the structural integrity of the material and can be removed from the substrate. Parts e and f are reprinted with permission from ref (28). Copyright 2018 Scientific Reports, Nature.50 Figure 2.6: Various methods for functionalizing DIB materials presented as changes in membrane conductivity. (A) (a) Alamethicin peptides exhibit a characteristic nonlinear conductivity. Adapted with permission from ref (91). Copyright 2019 ASME. (b) Photopolymerizable lipids can be cross-linked using UVC light forming transmembrane defects. Adapted with permission from ref (18). Copyright 2019 Royal Society of Chemistry. (c) V23T MscL can be activated in single DIBs by droplet compression. (B) (a) α HL can be used to establish exchange within a DIB tissue. Adapted with permission from ref (28). Copyright 2018 Scientific Reports, Nature. (b) MscL activity has been observed in networks of droplet interface bilayers (MTSET in the middle droplet). Adapted with permission from ref (96). Copyright 2020 Nature. (c) In large DIB networks, Alamethicin still requires transmembrane voltages of 70 mV. Adapted with permission from ref (28). Copyright 2018 Scientific Reports, Nature. (d) DIB networks can be rendered sensitive to green light through bacteriorhodopsin (BR). Adapted with permission from ref (30). Copyright 2007 American Chemical Society. (e) Droplets containing compatible polymerizable lipid profiles produce conductive pathways. Reprinted with permission from ref (18). Copyright 2019 Royal Society of Chemistry.55

Figure 2.7: Structural adaptation in natural cellular tissues inspires future development of DIB-based tissues. (A) Living tissues possess the ability to rearrange and reconfigure their cells relative to one another as well as to alter the area/shape of individual cells. Various cellular processes drive adaptation such as (a) shape/area change, (b) cell fusion, (c) rosette formation, and (d) cell extrusion. (B) These processes are being explored within the DIB platform. (a) Droplet fusion has been triggered through the application of a high transmembrane voltage, enabling rapid mixing of droplet contents. Reprinted with permission from ref (24). Copyright 2018 AIP Biomicrofluidics. The incorporation of biocompatible ferrofluids within the platform has allowed for a contact-free manipulation of stable DIB networks for the establishment of new communicative pathways shown in part b or the control of the membrane and droplet shape/area. Part b is reprinted with permission from ref (71). Copyright 2017 ASME. Part c is reprinted with permission from ref (15). Copyright 2018 American Chemical Society. Alternatively, electrical currents can be also employed to influence the droplets' and membranes' size through wetting/dewetting. Adapted with permission from ref (22). Copyright 2019 Royal Society Interface. (C) Future work on adaptive DIB structures will emphasize coupling changes in membrane permeability with changes in relative droplet positioning, producing networks of droplets that swap between communication modes enabled by external forces.60 Figure 3.1: The Droplet Interface Bilayer (DIB) technique. (a) When two nanoliter lipidcoated aqueous droplets are brought together a lipid bilayer membrane is spontaneously formed at the intersection (Bar represents 200 µm). This bilayer can be electrically modeled as a capacitor in parallel with a high amplitude resistor. (b) The interfacial tension of the

formed	bilayer	1S	balanced	with	the	two	opposing	monolay	/er	tensions	at	the	ınterfa	c1a
area														. 86

Figure 3.2: (a) The size distribution of maghemite nanoparticles within the ferrofluid showed a mean particle size of 10.250 nm with a standard deviation of 2.958 nm. (b) A transmission electron microscopy (TEM) image of the nanoparticles. Scale bar represents 20 nm. (c) Magnetization curve for the ferrofluid: given a known bulk magnetization of maghemite (370 kA/m) and a saturation magnetization (from curve) of 1.71 kA/m, the concentration of magnetic particles within the ferrofluid was estimated to be at 0.46% by volume. The ferrofluid exhibits no hysteresis and is superparamagnetic. The linear magnetic susceptibility shown as the red dashed line prior to saturation is 0.0413.88 Figure 3.3: Sketch of the PDMS substrate used for magnetowetting measurements. The vertical channel is approximately 1.1 mm in diameter.90 Figure 3.4: (a) Schematic representation of the pendant drop experiments for the measurement of interfacial surface tension. The diffused light of a halogen lamp passes through a Quartz cuvette filled with 3 mL of the lipid-oil mixtures in which a water or ferrofluid droplet is dispensed from a clean steel needle. Images are acquired through a CCD camera equipped with a zoom lens. (b) Acquired images of the droplets were analyzed using the open-source OpenDrop software. The interfacial tension was obtained through a curve-fitting process of the drop edge coordinates. (c) A typical measurement of the monolayer tension for a ferrofluid droplet in a lipid-in-oil mixture (DPhPC dissolved in a 1:1 (v: v) solution of Hexadecane and Silicone oils in a concentration of 0.5 mg/ml) shows that the interfacial tension decreases rapidly upon droplet formation in the lipid-oil.

The steady-state tension value obtained from these measurements was used to calculate the

Figure 3.6: Alpha-hemolysin insertion activity is measured as stepwise increases in the current measured with a constant applied voltage of +50 mV. Subplot (a) shows a typical scenario for a DIB formed between two water droplets. (b) shows the observed alpha-hemolysin behavior for a membrane formed between two ferrofluid droplets. Mixed droplet behavior is presented in (c) and (d) where, a water and a ferrofluid droplet were combined. In all cases, α HL was added at a concentration of 1.25 μ g/ml to the reference droplet. The obtained current traces were recorded in voltage clamp mode at a sampling frequency of 5 kHz and filtered and filtered at 1 kHz (using the embedded low-pass Bessel

Figure 4.2: Cross-sectional schematic of microdroplets with adhered interfaces. Green interfaces indicate lipid membranes with available pores for transport. While "bare" membranes provide an impermeable barrier to most species, restructuring the network by

coalescing the rightmost two droplets allows for pore insertion in the remaining membrane.
This enables passive diffusion between the remaining adjacent droplets post-coalescence.
116
110
Figure 4.3: The ferrofluid droplets were modeled as dodecagonal prisms elements in
Surface Evolver. The resulting droplet morphologies after minimization of the interfacial
energies match experimental observations
Figure 4.4: The electrical model for a single membrane consists of a capacitor and resistor
in parallel. This stencil may be combined into larger networks to produce linear systems of
differential equations describing the voltage drop across each membrane with prescribed
boundary conditions
Figure 4.5: Comparison between model predictions and experimental results for failure
across the central line of a hexagonally packed structure. a.1. Initial configuration -
electrode locations are marked. a.2. The application of the voltage spike resulted in the
coalescence of the three central droplets. b.1. The predicted Surface Evolver configuration
of the initial set of droplets b.2. The predicted configuration after rupturing the membranes.
c. Likely path of failure predicted by the electrical model. d. Comparison of experimentally
measured current and current predicted by the model with the inputs from Table 4.1. Scale
bars are 800 μm
Figure 4.6: Comparison between model predictions and experimental results for failure
across the outer ring of a hexagonally packed structure, demonstrating two possible
coalescence pathways. a.1. Initial configuration – electrode locations are marked. a.2-3.
Configurations after coalescence. b.1. The predicted Surface Evolver configuration of the

initial set of droplets b.2-3. The predicted configuration after rupturing the membranes. c.
Likely paths of failure predicted by the electrical model. Comparison of experimentally
measured current and current predicted by the model with the inputs from Table 4.1. Scale
bars are 800 μm
Figure 4.7 : Two additional comparison cases. a.1-2 Initial configuration – electrode
locations are marked. a.3-4 Configuration post coalescence. b.1-2. The predicted
configurations after rupturing the membranes. c.1-2 Likely paths of failure predicted by
the electrical model. Scale bars are 800 µm128
Figure 4.8 : The droplets in a single DIB may be approximated as two spherical caps with
a shared interface. It is possible to directly write functions for h and R as functions of and
Vol by assuming this geometry and constant droplet volumes. Setting the contact angle
to 90° produces a coalesced droplet pair as shown in b
Figure 4.9 : A single droplet (400 μm radius) within a DIB chain is constrained from
equilibrium in Surface Evolver on both sides by the specified displacement. As the droplet
is perturbed from a spherical cap, the total interfacial energy is increased. If tension is
applied, this leads to the eventual separation of the adhesive membranes at the horizontal
interfaces. Images across the top are taken from Surface Evolver
Figure 4.10: In larger networks, droplet coalescence exerts forces on neighboring droplets
but may be constrained by surrounding droplets. While rupturing a single droplet pair is
intuitive, larger networks behave as balanced structures and seek the minimum interfacial
energy for the entire network

Figure 4.11 : Two example cases showing the evolution of a network post formation. Red
symbols mark membranes that are selectively ruptured and green symbols indicate
locations where new membranes may form after network coalescence. These examples
demonstrate the ability to fold the network into new configurations through tailored
destruction of interfacial membranes
Figure 5.1: Schematic representation of the five main foundational rules that living
systems follow to survive and flourish. According to Ganti's chemoton model these criteria
include compartmentalization, growth and division (metabolism), information processing,
energy transduction (self-maintenance), and adaptability
Figure 5.2: Schematic representation of tension driven adhesion in (a) cellular tissues and
(b) DIB assemblies. According to the DAH (differential adhesion hypothesis), tissues can
be modeled as emulsive systems. The simultaneous presence of multiple degrees of surface
tension causes cells to reorganize spontaneously to minimize their interfacial free energy
in similar way to droplets in emulsions. In natural living tissues and liposomal aggregates,
interfaces are comprised of two adjacent lipid membranes in contrast to DIB-systems
where interfaces are formed between adhered lipid monolayers (resulting in a lipid bilayer).
144

Figure 5.3: Schematic representation of the main experimental setup: the pneumatic microdroplet injection system and the computer-controlled electromagnets' system. (a) Four solenoids with magnetic cores (EFI alloy) are placed as shown and used to magnetically control the position of ferrofluid droplets injected into the oil medium. The power input of the solenoids is computer controlled with a user interface connected to an

external microcontroller (ARDUINO), a relay system and a power supply. (b) Microdroplets are deposited into the oil dish using a computer-controlled pneumatic system. Microinjectors are pressurized using a pressure-clamp system connected to an external microcontroller (ARDUINO) and custom-guided through a user-interface. (c) Various compositions of DIB structures can be constructed by depositing magnetic (EMG 507- black color) and non-magnetic (aqueous buffer- blue color) microdroplets into an oil medium. Droplets are then brought into contact using a user-driven micropipette; interfacial bilayers are formed giving rise to a stable 2D membranous structure. Scale bars represent 600 µm each.

Figure 5.4: (a) Schematic representations (top view) of the manipulation of single membrane bordered by a ferrofluid droplet when applying different magnetic fields. An aqueous droplet is attached to an anchor (finely pulled glass tube with an agarose bead deposited at the tip). A ferrofluid droplet is then deposited in the same oil medium and a bilayer formed at the interface of these two droplets. The ferrofluid droplet typically relocates and centers its axis in a parallel direction to the activated electromagnet. Once the vector between the droplet centers is parallel with the field, the ferrofluid droplet starts elongating in the direction of the magnetic until it eventually separates. Before pulling away in the direction of the magnetic field, the ferrofluid droplet can rotate freely around the water droplet (without breaking the membrane) and align itself with the direction of the magnetic field. This produces a magnetic energy within the ferrofluid droplet that is reduced as the droplet approaches the magnet as shown by the normalized plot (offset by the minimum energy) and predicted by the model. The equilibrium distance between the droplet centers is increased while the overlapping membrane dimensions is reduced

(Hexadecane/AR20 2/1 volume mixture). (b) Necessary gradient of the magnetic field predicted for droplet separation as a function of the droplet radius and energy of adhesion for EMG509 and EMG507. Additional information on these ferrofluids is provided in the Supplementary Information. Solvents that produce more stable bilayers resulting in higher energy of adhesions require more force to separate. Smaller droplets are more difficult to manipulate since the magnetic energy scales with volume and the interfacial energy scales with area. For lower concentration ferrofluids (EMG509), this results in complete saturation prior to separation (shaded here in black). (c) Schematic representations and experimental images of membrane manipulation using electromagnets. A ferrofluid droplet (EMG507) is adhered to an anchored aqueous droplet and an electromagnet to the right is activated. The external oil phase (volume ratio of hexadecane and silicone oil) is varied and the variation in droplet adhesion is hence explored. Scale bar represents 500 μm. (d) Incrementing the magnetic field continues to reduce the membrane dimensions as predicted using the energetics model and confirmed experimentally. The current supplied to the electromagnet is varied and the interfacial dimensions and hence area recorded

Figure 5.5: The T1 event is a form of cellular intercalation event and is also known as local neighbor exchange (displayed in (a)): it is an active mechanism internally activated by cells. It is mediated through stress dissipation in tissues and may result in the formation of non-equilibrium tetrads. Colors are intended to aid in tracking relative cell location. (b) Here, we propose integrating intercalation mechanisms in DIB structures to further their adaptive nature. Intercalation mediated through membrane separation/reformation can be triggered using external force fields that can be tuned to affect on select microdroplets. (c)

Figure 5.6: Summary of the reproduced intercalation mechanisms in DIBs. Each case includes a sketch showing the mechanism in natural cellular tissues and a parallel schematic highlighting removed/formed DIB membranes, anchoring hydrogels, and location of the ferrofluid droplets as well as experimental images. Colors are intended to aid in tracking relative cell location. The folding/invagination (a) action uses ferrofluid droplets (b) to pinch droplets together about a hydrogel anchor. A first case uses two EMG 507 droplets while a second case shows a folding mechanism enabled by using two types of ferrofluids with different concentrations of magnetic particles. The extrusion mechanism (c) extracts the ferrofluid droplet from the center of a hexagonal packed structure to form new interfaces. This has been accomplished in (d) where a single a double extraction are

performed as shown by the experimental images' series (using EMG 507). DIB structures were formed with aqueous droplets (blue and white colors), EMG 507 (black color) and Figure 5.7: (a) Schematic representation and experimental results of the functionalized T1 neighbor exchange mechanism DIB network (formed with aqueous droplets (blue color), αHl infused aqueous buffer (2 µg/ml- white color) and EMG 507 (black color) droplets). Scale bars represent 600 µm each. (b) Current traces obtained for a constant +100 mV DC applied across the DIB networks shown respectively in (a) for the variation in αHL insertion activity upon the magnetic induction of a T1 rearrangement mechanism. Changes in the current reflect changes in the overall conductance of the tissue through insertion of the PFTs into individual bilayers. All measurements were recorded in voltage clamp mode at a sampling frequency of 10 kHz and filtered at 1 kHz (using the embedded low-pass Bessel filter -80 dB/decade). Post-acquisition, data was filtered at 500 Hz using a fourthorder Butterworth low-pass filter in MATLAB. Scale bars represent 600 µm each.160 **Figure 5.8**: (a) Plots of the ferrofluid magnetization M_{ferro} (EMG 507 and EMG 509 waterbased series) with an external field H_{ext} for the two selected ferrofluids including saturation effects. The dashed lines are the linear magnetization response provided by c_{ferro} , and the dotted lines are the saturation limits. (b) Plots of the interfacial energy (Eg) for a pair of adhered droplets as a function of the normalized distance between their centers offset by the equilibrium distance. (c) Quantified electromagnet response to supplied current. ...164 Figure 6.1: Schematic representation of the droplet interface bilayer (DIB) technique. After being introduced into an oil medium, aqueous droplets acquire a lipid coating referred to as lipid monolayer. As droplets are brought together, oil at their interface is gradually

Figure 6.3: Schematic representations: (a) Cross-linking of 23:2 DiynePC phospholipids after the application of UV-C light for 5 minutes. (b) (c) Cross-linking of 23:2 DiynePC lipids within a lipid bilayer when it was introduced from (b) one side and (c) two sides of the bilayer. As DiynePC polymerized, the lipid chains tightly packed together resulting in the formation of structural pores within the lipid bilayer whenever polymerizable lipids were present on both sides as shown in (c). Pores in this case are a result of polymerizable lipids tightly packing together forming discontinuities in the molecular distribution at the monolayer and bilayer levels. Owing to the positioning of the diacetylene groups within each lipid molecule and to the ordered alignment polymerization condition, no cross-leaflet

polymerization is anticipated. Polymerization is constricted to occur between molecules
present on the same leaflet
Figure 6.4: Summary of the oil/aqueous phases used in this work
Figure 6.5: Current traces obtained for a constant applied voltage of +100 mV before and
after application of UV-C light for 5 minutes. The red droplets contain DPhPC dissolved
at 2.5 mg/mL and blue droplets contain 1:4 mixture of 23:2 DiynePC:DPhPC dissolved at
2.5 mg/mL. The solvent is 2:1 hexadecane:silicone oil AR20 0.5 mg/mL DPhPC oil-lipid
mixture. In (a) the DIB is formed between two aqueous droplets only containing DPhPC.
No pore formation is noted after the application of UV-C, and the membrane remains
highly resistive. In (b) the DIB is formed between two aqueous droplets containing
polymerizable and non-polymerizable phospholipids. No pore formation is noted after the
application of UV-C. Similar traces were observed when the ratio of polymerizable to non-
polymerizable lipids were 1:2 and 1:8 by mass respectively and when hexadecane alone
was used as an external phase as well. All measurements were recorded in voltage clamp
mode at a sampling frequency of 10 kHz and filtered at 1 kHz (using the embedded low-
pass Bessel filter -80 dB/decade). Post-acquisition, data was filtered at 500 Hz using a
fourth-order Butterworth low-pass filter in MATLAB
Figure 6.6 : Current traces obtained for a constant applied voltage of +100 mV before and
after application of UV-C light for 5 minutes. The DIBs are formed between two aqueous
droplets containing polymerizable and non-polymerizable phospholipids (23:2 DiynePC
and DPhPC) dissolved at a concentration of 2.5 mg/ml in a 2:1 hexadecane:silicone oil AR
20 0.5 mg/mL DPhPC oil-lipid mixture. The ratio of polymerizable to non-polymerizable
lipids by mass was (a) 1:8, (b) 1:4, and (c) 1:2. Polymerizable lipids were introduced form

both sides of the bilayer. Similar trends can be observed when Hexadecane off is used as
an external phase. (d) Shows a schematic representation of the formed bilayer pre and post
UV-C curing. All measurements were recorded in voltage clamp mode at a sampling
frequency of 10 kHz and filtered at 1 kHz (using the embedded low-pass Bessel filter -80
dB/decade). Post-acquisition, data was filtered at 500 Hz using a fourth-order Butterworth
low-pass filter in MATLAB
Figure 6.7 : Measurement of the properties of lipid bilayers in hexadecane as well as 2:1
hexadecane:silicone oil AR20 DPhPC oil-lipid mixture for increasing concentrations of
polymerizable lipids dissolved in the aqueous phase (2.5 mg/ml total) pre and post UVC
exposure for 5 minutes. (a) shows the monolayer tension (mN/m), (b) shows the bilayer
tension (mN/m) ,(c) shows the bilayer's specific capacitance ($\mu F/cm^2$) while (d) shows the
bilayer's specific conductance (x10 ⁻² μS/cm2).
Figure 6.8: Current-voltage plots demonstrating pores formed post UV-C curing for
different concentrations of polymerizable phospholipids (2.5 mg/ml in total in the aqueous
phase) within the 2:1 hexadecane:silicone oil AR20 containing 0.5 mg/mL DPhPC lipid-
oil mixture. A 4 mV/s voltage-sweep for these bilayers was performed and current
responses recorded. All measurements were recorded in voltage clamp mode at a sampling
frequency of 10 kHz and filtered at 1 kHz (using the embedded low-pass Bessel filter -80
dB/decade). Post-acquisition, data was filtered at 500 Hz using a fourth-order Butterworth
low-pass filter in MATLAB
Figure 6.9: Current traces obtained for a constant applied voltage (+100 mV) and
illustrating the properties of αHL and DiynePC. In both cases the red droplets contain only

2.5 mg/ml of DPhPC. Droplets are dispersed in a 2:1 hexadecane:silicone DPhPC lipid oil

mixture to facilitate bilayer formation. A +200 mV DC potential is applied between the electrodes, resulting in approximately +100 mV per membrane. (1) The green droplets contain 1.25 μg/mL of dissolved αHl. Both droplet configurations shown in (1.a) and (1.b) result in the formation of a conductive pathway across the entire network since αHl is not required to insert from both sides of the membrane for pore formation. (2) Current traces obtained post application of a UV-C light for 5 minutes, illustrating the behavior of polymerized 23:2 DiynePC mixtures. The blue droplets contain a 1:4 mass ratio 23:2 DiynePC:DPhPC mixture dissolved at a total concentration of 2.5 mg/ml. In (2.a), the OFF configuration was switched by having a red droplet placed between two blue input droplets, stopping exchange across both membranes. In (2.b), the micro switch was turned to the ON configuration by moving the blue input droplets connected to the acquisition system so that all droplets containing polymerizable lipids were aligned in contrast with the case shown in (1.a) and (1.b). (1.c), (1.d), (2.c) and (2.d) show the images acquired for (1.a), (1.b), (2.a) and (2.b) respectively. All measurements were recorded in voltage clamp mode at a sampling frequency of 10 kHz and filtered at 1 kHz (using the embedded low-pass Bessel filter -80 dB/decade). Post-acquisition, data was filtered at 500 Hz using a fourth-order Butterworth low-pass filter in MATLAB. Scale bars represent 400 µm.197 **Figure 6.10**: Release of calcein from donor droplet (right droplet corresponding to the reference side of the bilayer) to the acceptor droplet (left droplet). The plot shows the percentage of calcein fluorescence vs time in the acceptor droplet (I_{acceptor}) vs the donor (I_{donor}) droplet for the four experimental cases. (a), (b), (c) and (d) show the respective fluorescence images for the DIBs. Bright areas indicate the presence of calcein while dark areas do not contain calcein. In all experimental cases, a -100 mV was being applied and

Figure 7.2: DIBs tested here were composed of DPhPC, bSM and Cholesterol at different molar compositions: (1) 1:0:0, (2) 2:1:1, (3) 2:0:1, (4) 1:1:1, (5) 1:0:1, and (6) 2:1:2. (2), (4) and (6) and lie in the L0+Ld phase coexistence region. While (1), (3) and (5) lie in the Ld phase. L0: liquid ordered, Ld: liquid disordered and S: solid/gel phase. The purple

CHAPTER 1

INTRODUCTION: DROPLET INTERFACE BILAYER

Shaped by millions of years of evolution, life as we know it is amazingly diverse, complex, and dynamic. What enables the formation, functioning and proliferation of living organisms remains at the very core of the quest to uncover the origins of life. Numerous efforts have led to the realization that all forms of life are governed by the same set of rules ensuring their existence, adaptation, flourishment, procreation, and subsistence. A comprehensive approach describes living systems as being a self-sustained chemical reaction capable of experiencing Darwinian evolution [1, 2] whenever subjected to adequate stimuli. More intensive conjectures hypothesize Ganti's chemoton as our last universal common ancestor or the original ancestor of all organisms [3, 4]. This abstract model (the oldest known computational model of a protocell dating back to 1952) suggests that any system satisfying the five main hallmarks of life is considered alive and by extension can be subjected to natural selection/evolution as well as encompassing selfsustaining cellular information guiding us to its ancestry and origins. Hence a living system is a progeny separate from the external continuous environment and is capable of both reproducing and functioning according to a preset program [4]. In other terms, living systems all share the following foundational principles: compartmentalization, growth and

division (metabolism), information processing, energy transduction (self-maintenance), and adaptability [3-5].

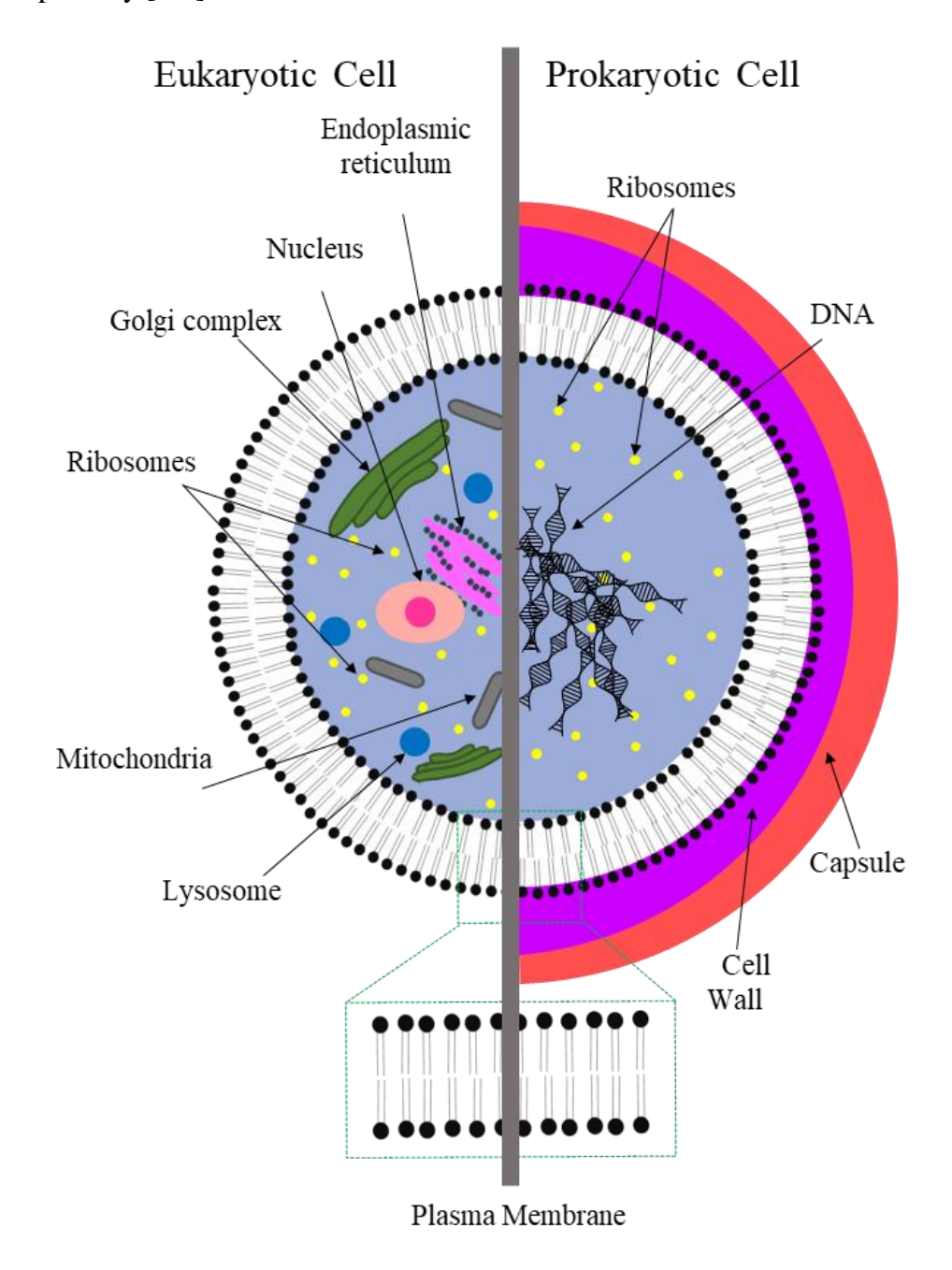


Figure 1.1- At a fundamental level, living organisms are generally composed of one or more cells (cellular units). These units are then organized into tissues then by extension organs. Cells have been classified as prokaryotes and eukaryotes with the main difference

between the two being the presence of a nucleus (prokaryotic cells lack a nucleus, while eukaryotic cells have a nucleus and hence prokaryotic cells are simpler in composition). Examples of prokaryotes are bacteria and archaea. Examples of eukaryotes are fungi, plants, and animals. Both cell categories have a basic common feature: a plasma membrane, also referred to as cellular membrane. This membrane delimits the cell, blocks external pathogens, contains receptors and channels that allow specific molecules, that mediate cellular and extracellular activities to pass between organelles and between the cell and the outside environment; and separates vital but incompatible metabolic processes conducted within different cellular units.

From an evolutionary perspective, compartmentalization is thought to have evolved in order to reduce the free diffusive loss and separate beneficial molecular components of life from parasites [6] hence preserving the self-sustaining information. It is believed to have emerged during the prebiotic life times and have led to the development of cellular life precursors (protocells) [7]. Often achieved in biological living systems through semi-permeable plasma cellular membranes [6] (Figure 1.1), compartmentalization allows for the formation of independent or even interconnected chemical/biological gradients within living systems while separating competing ones and regulating the exchange rates between complementary ones. Individual cells and their underlying tissues interact with each other and with their external environment through governed molecular/signal exchange mediated by plasma membranes in response to multiple types of external signals (mechanical, chemical, electrical, magnetic...).

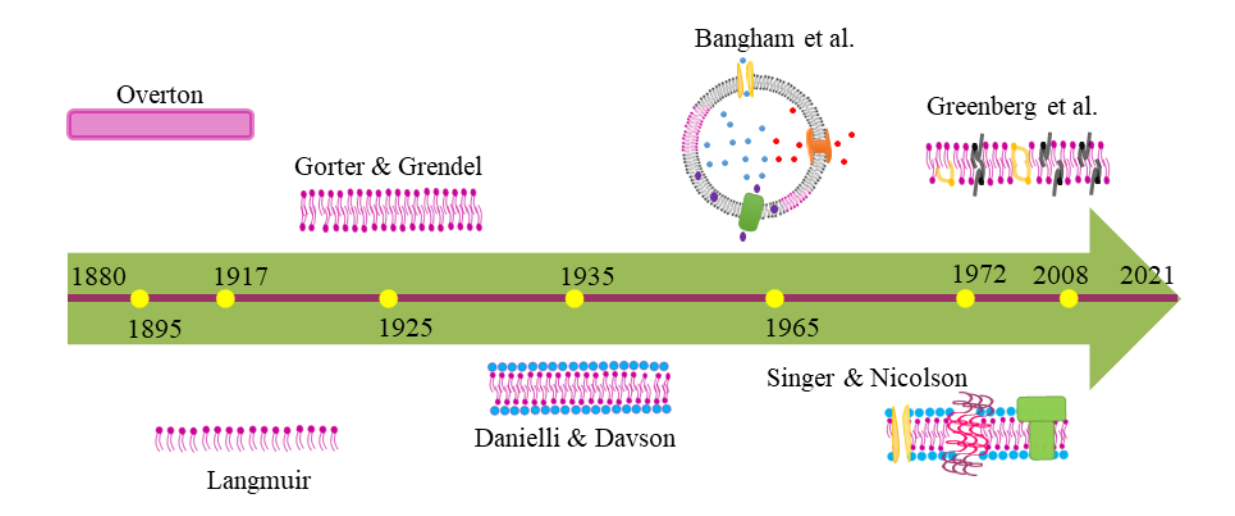


Figure 1.2- The existence of a cellular membrane has been speculated since the invention of the early microscope and the plant cell wall being clearly detected. Following this, the lipid nature of the cell membrane was suggested, and several models were proposed to describe its structure from the "lipoid theory of narcosis" (Overton 1880) to the more recent fluid mosaic model (Singer and Nicholson 1972).

The existence of a thin cellular membrane that separates the protoplasm from its environment was first suggested in the early 17th century with the invention of the early microscopes and the detection of such barrier in plant cells [8]. The theory of cellular membrane was then further developed by de Vries (1885), Pfeffer (1897) and Overton (1895-1899) [8] (Figure 1.2) who demonstrated that plant cells respond osmotically to variations in external solutions [9] thus suggesting the presence of a lipid barrier. Early notions about the membrane structure were indirectly derived from studies of membrane function and its chemical composition was inferred from its permeability properties.

A series of experiments in 1925 based on previous work conducted by Langmuir (1917) indicated that this membrane consisted of two molecular layers of lipids, in other

terms the plasma membrane is a lipid bilayer [10] (Figure 1.2 and Figure 1.3-b). Lipids being amphiphilic, possess a hydrophilic end and a hydrophobic one. The hydrophilic end contains a negatively charged phosphate group and is referred to as a headgroup, and the hydrophobic end usually consists of two long fatty acid tails and is referred to as the tailgroup [11] (Figure 1.3). In phospholipids for instance these groups are joined by a glycerol molecule [11] (Figure 1.3). Hence, in aqueous solutions, phospholipids are driven by hydrophobic interactions causing an aggregation in the tails to minimize interactions with the water molecules and resulting in the formation of various structures such as micelles, liposomes, and lipid bilayers (Figure 1.3-b).

During the next few decades scientific tools confirmed this theory by Gorter and Grendel [12], but controversy remained regarding the role of proteins in the cell membrane as it proved more challenging to characterize the properties of membrane proteins than those of membrane lipids. In 1935 Davson and Danielli hypothesized that the plasma membrane's structure is analogous to a sandwich based on earlier images recorded using electron micrographs where the proteins act as the bread and the lipids as the filling [13] (Figure 1.2). In 1972, Singer and Nicolson made a clear distinction between peripheral membrane proteins and integral ones and proposed a new model to better capture the plasma membrane function and structure: the fluid membrane mosaic model (F-MMM) [14] (Figure 1.2). According to this model, proteins make the mosaic that is inserted (either halfway or all the way through) and can freely float into the fluid, which is the lipid bilayer. And although not all plasma membrane structure (such as lipid rafts in the words of the Nicolson [15]- more details will be discussed in Chapter 7) or dynamics can be adequately explained through this model [15], the fluid membrane mosaic model has successfully

managed to capture and integrate previous diverse experiments on membrane physics and chemistry and is still widely accepted and used today [15] (with some additions through the years such as the lipid whisker model in 2008- Figure 1.2).

Albeit not being directly mentioned in the Chemoton model, another essential component for life stems from the need for compartmentalization and modularity: different modules cannot constitute a functional single organism if they do not act in unison in terms of response to external environment and resource management. Hence, establishing communication between different cells comes hand-in-hand with compartmentalization and modularity in living organisms. Naturally established through transmembrane peptide and protein channels [16-18], cellular communication moderates exchanges between different cellular compartments.

Living entities are far from equilibrium systems hence the need for active adaptability for endurance; it is the key for constructing artificial cellular-inspired systems and a major component of Ganti's model. Adaptability can occur either at the species level (evolutionary adaptability: a large number of individuals from the same species infer survival changes to their constitution and successfully transmit this change to offspring's [19]) or at the individual short-term level (best showcased through the capability of a single organism to respond to external stimuli).

A high-risk high-reward emerging area of research, synthetic biology describes efforts in multiple fields of science (including organic chemistry, materials science, mechanical engineering, biological engineering and biology to name a few) working in parallel. A sub-area of synthetic biology is protocell creation [20] defined through its goal to create minimal cellular systems and cellular-inspired materials. In its top-down

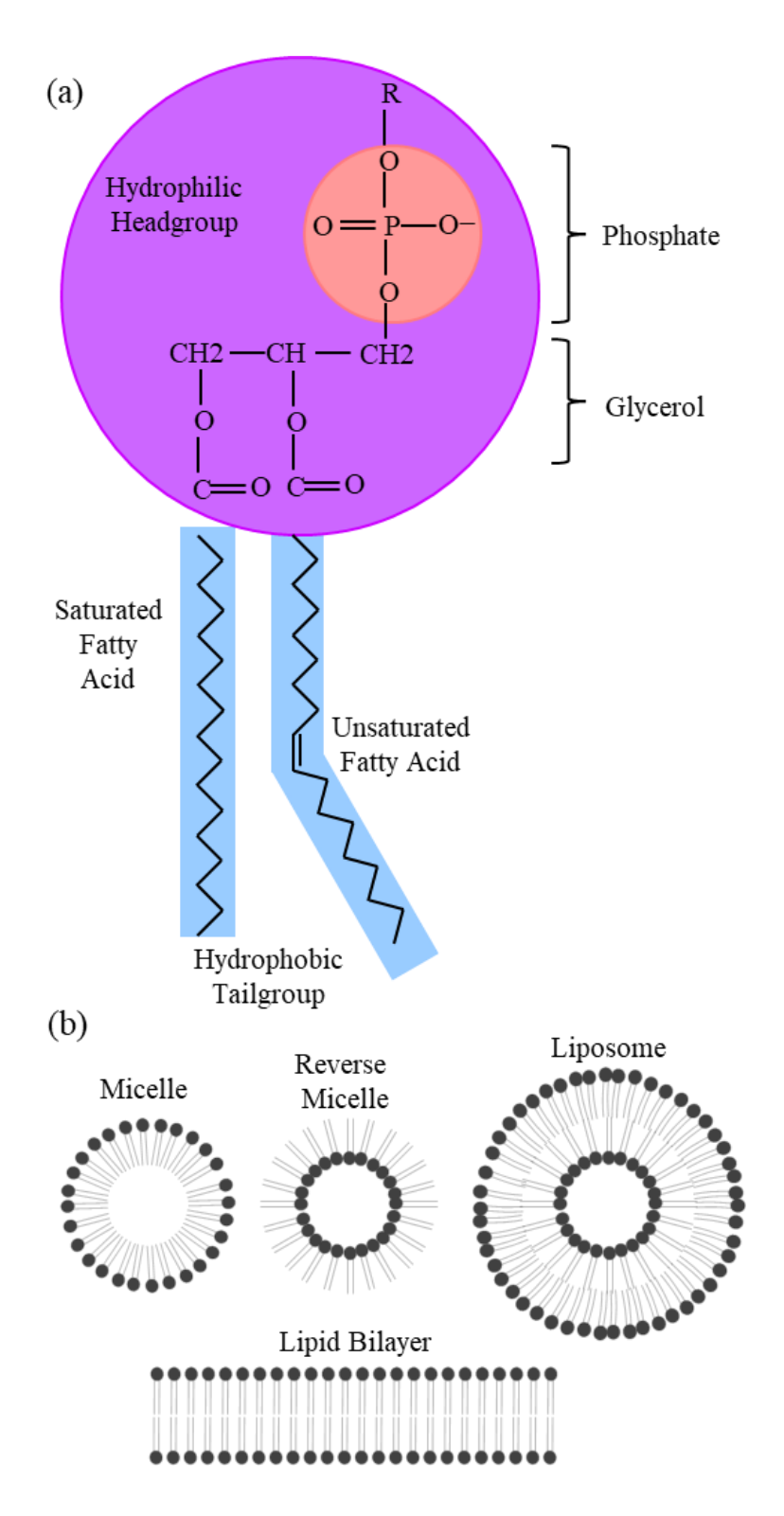


Figure 1.3- Phospholipids are a key component of cellular membranes. (a) Amphiphilic phospholipid molecules are lipids with a hydrophilic head containing a phosphate group, and two hydrophobic tails derived from fatty acids, joined by a together by a glycerol

molecule. Some of the phospholipid tails are saturated and some are unsaturated. The more unsaturated they are, the more fluid the membrane. (b) Due to their amphiphilic nature, phospholipids can form alternative configurations such as micelles, reverse micelles, planar bilayers and liposomes.

approach, it aims at adapting existing cellular life to create minimal cells and cellular-mimicking devices optimized to perform a specific function [3] starting from living cells and moving forwards by eliminating sub-cellular components until the desired functionality and stability are achieved. Meanwhile, bottom-up synthetic biology concerns itself with building cellular inspired structures distinct from natural cells starting from basic chemical components [21]. With many futuristic applications ranging from "chemical robots"[1] capable of responding to external environmental stimuli, to medical diagnosis, medical targeted drug delivery and diagnosis [6], molecular computing and most prominently multi-responsive tissue-like materials, bottom-up synthetic biology helps shaping the future of science and engineering.

While fully replicating cellular tissues *in vitro* is not a foreseeably attainable goal, synthetic biology can still seek inspiration from particular cellular collective or individual behaviors, self-assembly mechanics and even the hierarchy in structures. Modeling the behavior of certain tissues has been the subject of many speculations and theories. Widely postulated as an attempt to explain the spontaneous liquid-like tissue segregation, the Differential Adhesion Hypothesis (DAH) models the mechanics and thermodynamics governing certain tissues (epithelial [22, 23], embryonic [24-26] and even cancerous [27]) as being approximated to those of an emulsive system of two immiscible liquids. Intrinsic

surface tension forces would hence guide motility (a form of adaptation) of cells and cellular tissues [24, 28]. Stabilized adhesive emulsions are consequently a reliable tool of synthetic biology in replicating desired aspects of living tissues [29] employing principles of molecular self-assembly and interfacial chemistry.

A particular and relatively new instance of stabilized adhesive emulsions [30], the Droplet Interface Bilayer (DIB) technique assembles soft biomimetic lipid membranes at the interface of lipid-coated aqueous microdroplets dispersed in an oil phase [31, 32] and constitutes a suitable compromise between emulsion techniques and modeling biomimetic membranes in tightly controlled experimental setups. Water microdroplets are introduced into an oil medium; lipids can be either dispersed in the oil phase (the lipid-out technique [33]), in the water phase (the lipid-in technique [34, 35]), or in some instances in both phases for added stability [36]. After being given enough time for lipid self-organization at the water-oil interface [37], lipid-coated water droplets can be brought together. The interfacial lipid bilayer spontaneously forms at their interface as hydrophobic phospholipid tails (Figure 1.3-a) self-assemble [38] in a zipping motion expelling the trapped oil (Figure 1.4). By repeating this process multiple times using a multitude of microdroplets, 2D (Figure 1.4) [33, 36, 39-41] and even 3D [42-44] tissue-like structures can be formed with minimal raw materials.—In addition to the convenient scalability, this technique offers an ease of implementation, the option of assembling, separating and reassembling multiple lipid bilayers (without jeopardizing the integrity of the rest of the structure), as well as the ability to create asymmetric membranes [35, 36, 45] formed by multiple different types of lipids. During the past couple of decades, single DIBs have proven to be a powerful tool when studying lipid membranes' composition [46]/raft formation, lipid flip-flop mechanism [47], membrane permeability [45], membrane proteins' interaction and underlying molecular transport [48-51]. Albeit these interesting applications on a single bilayer level, tissues formed by scaling the DIB technique venture into more varied territories including soft chemical robots [1], medical diagnosis [6], energy storage and conversion [32, 52, 53], light-sensing [36, 54, 55], and the creation of a new class of biocompatible engineered tissues [44, 56-58]. A more in-depth literature review of this platform is provided in the following chapter (Chapter 2).

DIB-based Tissues and the Hallmarks of Living Systems: Inherent Criteria

Whether through their very own construction platform or through additional functionalization, DIB-based membranous materials inherently check many of the Chemoton criteria essential for life creation and sustainability. In fact, owing to their emulsive nature, DIB tissues are highly compartmentalized: individual aqueous compartments are separated by semi-permeable lipid bilayers yet can communicate ondemand through protein channels or light-induced membrane pore-defects (more on this topic in the following chapters). These structures have shown promising behaviors in terms of energy transduction and information processing (two additional criteria).

However, when traditionally constructed, DIB-based tissues do not exhibit the capability of modifying their internal structure in response to adequate external simulation and many efforts are currently being dedicated to enable these structures with an adaptability feature. In fact, non-adaptive DIB-systems have been used when studying single membrane mechanical/electrical behavior, model certain aspects of natural tissue behavior under stresses, explore jamming of emulsions, and investigate the mechanics of microdroplets. And while these studies are interesting on their own, DIB-based tissues have

the potential of being engineered into smart-materials with a clear biocompatibility advantage. By definition, smart materials are dynamic and adaptive hence the interest in further developing these structures.

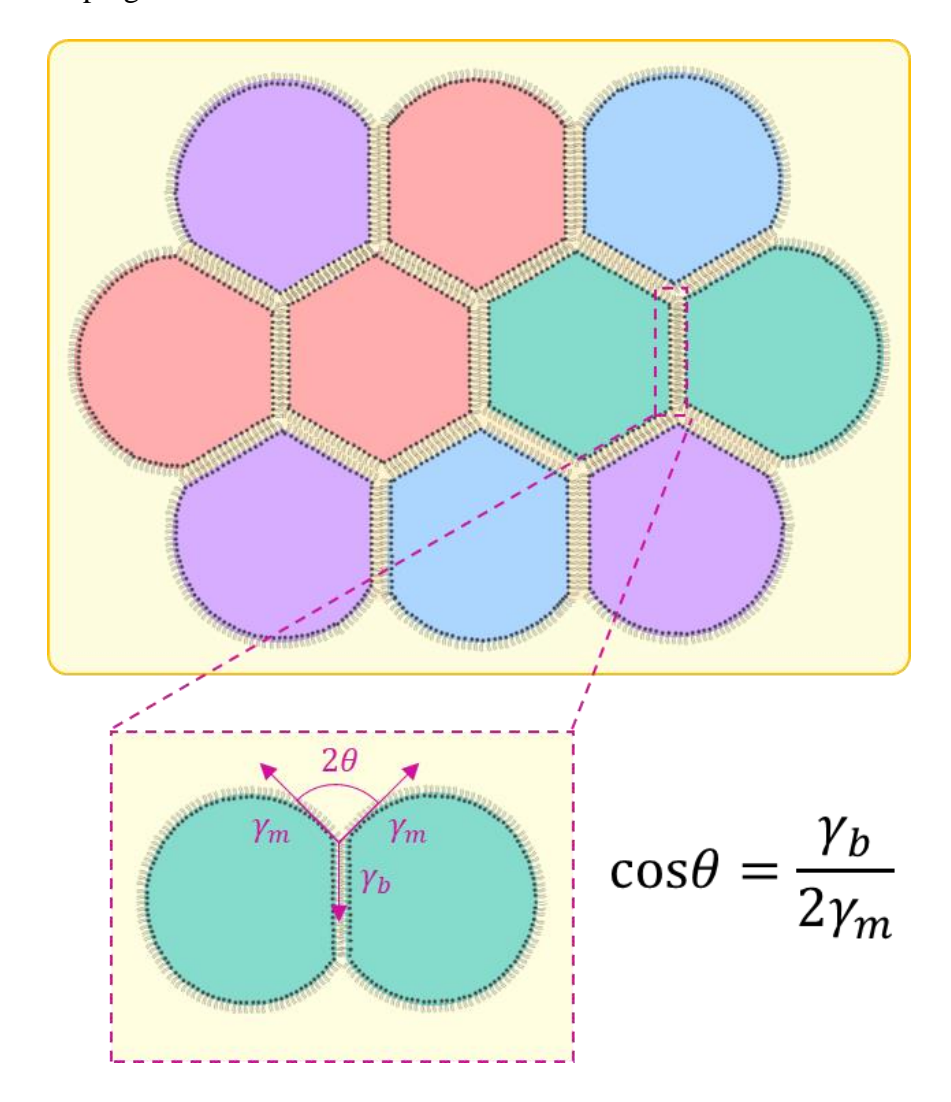


Figure 1.4- The Droplet Interface Bilayer (DIB) technique assembles soft biomimetic lipid membranes at the interface of lipid-coated aqueous microdroplets dispersed in an oil phase. Upon formation, the area of the interfacial lipid membrane is governed through a balance of monolayer and bilayer tensions reflected through an external angle of contact and gradually expands until the tensions at the annulus are balanced as given by Young's equation.

DIB-based Tissues and the Hallmarks of Living Systems: the Need for Adaptive Smart Materials

Tackling the hallmarks of the chemoton model would therefore considerably advance the capacities of DIB-based tissues by enabling them with naturally developed, approved and optimized strategies for survival and self- maintenance. In addition to the widespread adaptation of these membranous materials, DIB-based tissues still face multiple challenges that ought to be addressed prior to moving to more advanced phases of implementation and interactive applications including the difficulty in their high throughput manufacturing, some associated limitations in their complexity, and issues with instability. Formulating solutions to these obstacles requires an extensive knowledge of the unique mechanics of the emulsive material.

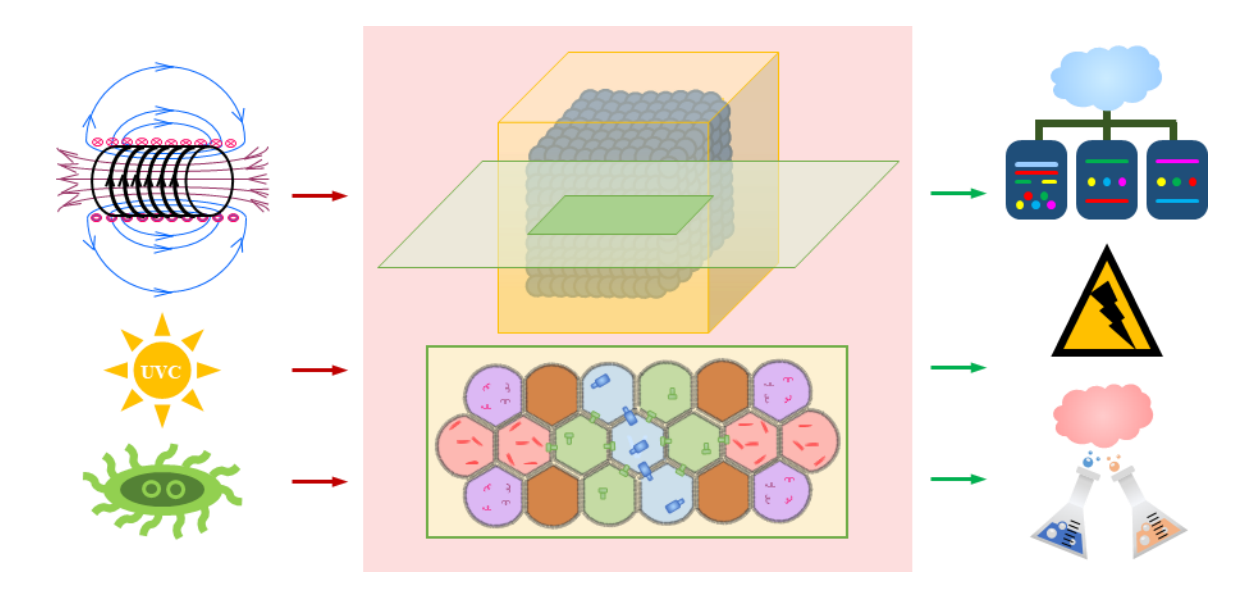


Figure 1.5- Droplet interface bilayers (DIBs) allow for the formation of webs of lipid membranes between aqueous droplets that approximate living tissues. The membranes may be functionalized to adapt their structure to various external stimuli, producing transmembrane exchanges and adaptations in the adhered droplet structure.

1.1. Objectives

This dissertation documents the further development and improvement of a new class of synthetic membranous materials using the DIB platform. Our main goal is to enable both structural and chemical adaptation of DIB-based tissues using naturally-inspired strategies. New means of imbuing this material with a stimuli-responsive behavior are explored through the incorporation of biomolecules, peptide/protein channels, polymeric lipids, and magnetic fluids. Such strategy further exploits the potentials of DIB-based materials through added mechanical, electrical, magnetic, chemical, and optical behavior. It is possible to incorporate a portion of the biological tissue functionality into DIB-based materials, and this incorporation enhances their synthetic long-term synaptic plasticity. Notable scientific contributions of these efforts are listed below.

- i. Testing the operating mechanism and activity of different transmembrane biomolecules/polymerizable molecules in droplet interface bilayers and their response to specific applied stimuli in order to optimize intra-tissue communication schemes. Photopolymerizable lipids (in particular 23:2 DiynePC polymerizable at 254 nm), have demonstrated their ability to establish directional communication pathways in DIB tissues that can only occur between compartments of compatible lipid composition (a concept previously theorized but not tested in planar membranes or DIBs). This development would hence enable DIB-based tissues with the ability to adapt to UVC light by altering their internal chemical composition, a strategy observed in cellular tissues.
- ii. Fabricating DIB-based tissues at the micrometer length scales with increased functionality by developing non-invasive methods for stimulating the membrane-based material and analyzing their impact on its functionality. Ferrofluids are successfully

introduced into the platform giving it magnetic capabilities and an ease of fabrication. Biocompatible in house fabricated and commercially available ferrofluids have shown their compatibility with the platform as well as their ability to infer non-invasive magnetically triggered structural adaptation and an ease in the construction of DIB systems. Upon acquisition of this objective, DIB-based systems can be sensitized to respond to magnetic force fields, a strategy that will be used in the subsequent objectives to infer structural adaptation.

iii. Developing methods (experimental or computational) for assessing the internal material reaction to different stimulation types and predicting its theoretical behavior. Experimental methods involving ferrofluid and a built magnetic trigger station have been developed. Magnetic compartments have been shown to alter the equilibrium structure of DIB-based materials by inferring transitional states where droplets will shift into new equilibrium configurations. The use of ferrofluids have also simplified the study of post-failure equilibrium configurations in 2D DIB networks where experimental results were compared and verified computational predictions.

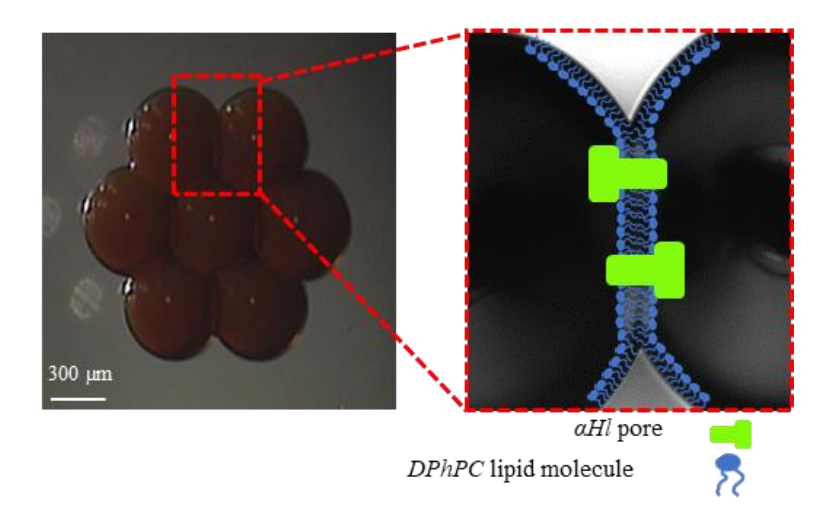


Figure 1.6- The incorporation of a magnetic fluid or ferrofluid within the droplet phases for the creation of magnetically responsive DIB arrays is investigated first. Once compatibility is established, potential applications of the ferrofluid-enabled DIBs are showcased by remotely modifying membrane qualities through magnetic fields.

iv. Exploring natural tissue structural adaptive behavior and interfacial chemistry properties (interfacial tension and its analogy to cortical tension) to engineer DIB-systems with optimal structural morphing adaptation features. In other terms, inspiration is drawn from intercalation events observed in natural cellular tissues to enhance and optimize dynamic reconfiguration phenomena implemented in DIB networks. Owing to both their emulsive and membranous natures, DIBs are the perfect candidate for tissue-inspired structural adaptation mediated through emulsive jamming. The influence of lipid composition through lipid rafts and its effect of interfacial tensions is then utilized in light of the DAH theory (differential adhesion hypothesis) in efforts to thermally induce these events.

1.2. Document Overview

This chapter introduced the motivation behind enabling adaptation in synthetic tissue-like materials and touched on some background information concerning cellular systems, lipid membranes and the droplet interface bilayer (DIB) technique. The motivation, approach, and road map to achieving dynamic structural adaptation in DIB-tissues are presented in the Introduction as well. The research efforts presented herein are primarily experimental with intersections of modeling/computational sections.

Meanwhile, in Chapter 2, an extensive literature review on the recent advances in the construction, manipulation and functionalization of DIB structures (Figure 1.5) as well as the platform itself, is presented with special focus on contributions from the Biomembranes Engineering Lab at UGA (and by extension research conducted by the author and presented in this document).

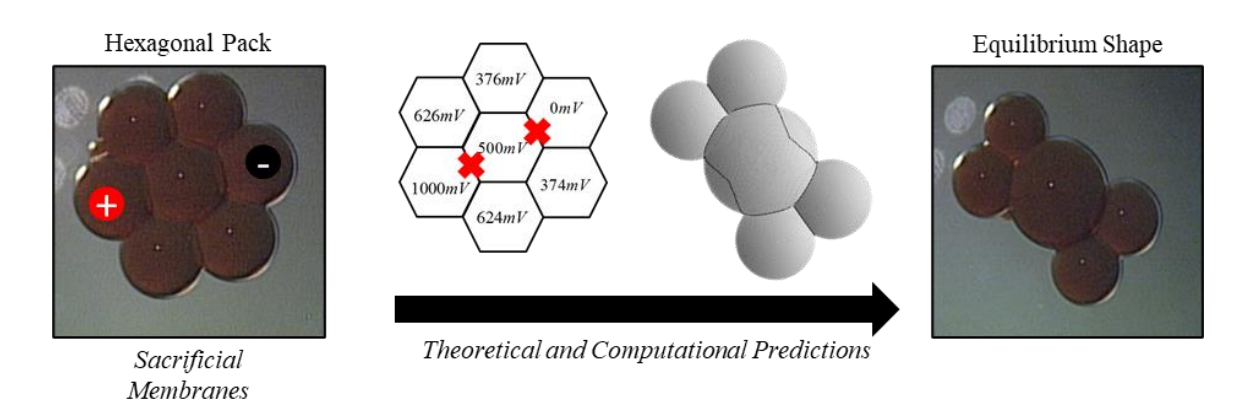


Figure 1.7- Multiple lipid encased water droplets may be linked together in oil to form large networks of droplet interface bilayers thus creating a new class of stimuli-responsive materials for applications in sensing, actuation, drug delivery, and tissue engineering. One particular problem of interest is understanding the impact of the coalescence of two neighboring droplets on the overall structural integrity of the network. Droplet networks with tailored architectures are synthesized with the aid of magnetic motor droplets containing a biocompatible ferrofluid. The equilibrium configuration of the droplet networks is compared to computational prediction which defines the overall stability by summing the interfacial energies. Once the networks are completed, failure in selected membranes is induced. As the targeted droplets coalesce together, the equilibrium structure of the network is altered, and the remaining droplets may shift to new configurations dictated by their minimized mechanical energies.

Chapter 3 explores the introduction of biocompatible ferrofluids into the DIB platform (Figure 1.6). The compatibility of ferrofluids in terms of interfacial membrane properties and the ability to sustain transmembrane peptide/protein channel is established and then utilized to infer magnetic sensing capabilities on DIB-networks. Their introduction into the platform has also allowed for an easier and contact-free assembly of DIB systems.

Chapter 4 builds on results obtained in Chapter 3 and utilizes ferrofluid based DIB networks to study the effect of localized membrane failure on their structure. Failure is induced in select membrane via electrical shocks (Figure 1.7). Remaining droplets rearrange into new configurations, redirecting the droplet-droplet exchange pathways. Experimental outcomes are consequently compared to predictions provided by a coupled mechanical-electrical model, then advanced configurations are proposed.

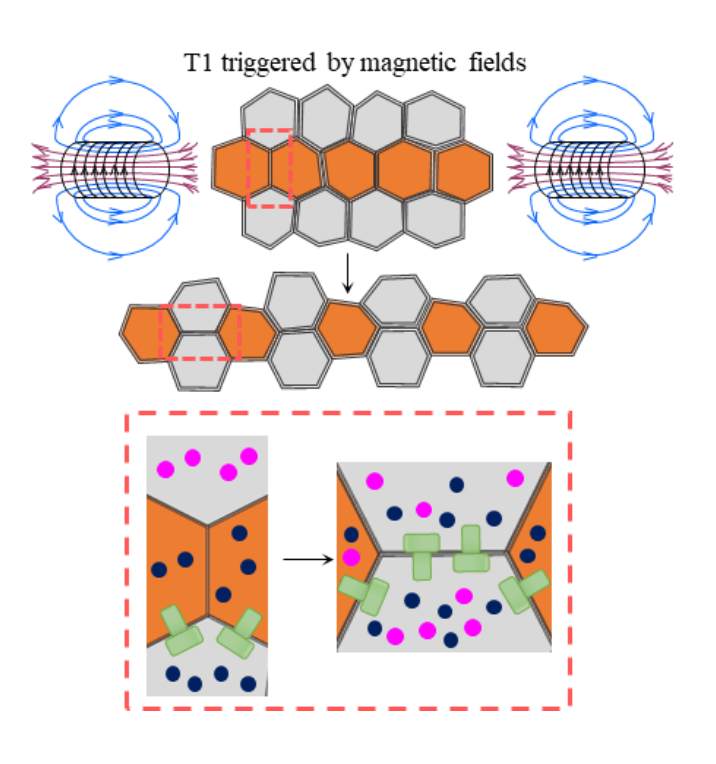


Figure 1.8- Inspired by the hierarchy and compartmentalization of natural tissues, we synthetize a droplet-based material containing webs of lipid membranes. Such materials are traditionally static and do not interact with external conditions, posing future challenges in their practical applications. Adaptability is explored here by infusing the platform with ferrofluids, rendering the material sensitive to external magnetic force fields. Adaptation via structural changes is further optimized by implementing strategies observed in natural tissues during the morphogenesis and gastrulation phases of embryonic development. We show that when exposed to magnetic forces, DIB-tissues adapt by changing their internal structure and establishing new internal communication pathways, an approach inspired by nature.

Chapter 5 culminates the efforts of ferrofluid introduction into DIB-based tissues. Inspired by nature where function follows form [59], adaptive architectures within the DIB-platform are explored and enabled with a sensitivity to magnetic force fields. DIB membranes are linked to the properties of both adhered droplets-unlike natural tissues inspiring their structure-hence, rearranging the droplets within a larger structure alters the internal patterns of communication. Activating external magnetic force fields in heterogenous DIB structures containing ferrofluid and non-ferrofluid droplets, generates transition rearrangement events in the membranes bordering magnetic compartments (Figure 1.8). This approach further enables the development of smart biocompatible DIB-materials where internal structure dictates functionality.

Chapter 6 focuses on establishing directional and remotely activated communicative pathways within DIB-systems that can be used in conjunction to intercalation-based adaptation to create structures where shape dictates function.

Traditionally these pathways are generated by using dissolving pore-forming toxins (PFTs) in the aqueous phase. However, transport then is enabled in all membranes bordering the droplets containing the dissolved PFT leading to diffusive losses. Photopolymerizable phospholipids (23:2 DiynePC) when incorporated within the aqueous phase of the DIB platform (Figure 1.9), have shown the ability to establish conductive pathways in the lipid membranes post-exposure to UV-C light. Notably these pathways are only formed in the membrane if both adhered droplets have compatible lipid profiles. Consequently, the incorporation of photo-polymerizable phospholipids within the aqueous phase of DIB networks can improve the resolution of the patterned conductive pathways and reduce diffusive loss.

Chapter 7 discusses ongoing research inspired by the DAH (differential adhesion hypothesis) where intercalation events are carried through differences in "tissue surface tension". The effect of lipid rafts (formed through heat exposure followed by cooling) and its effect on interfacial tension, energy of adhesion and angle of contact is then investigated. The possibility of inducing intercalation events through changes in membrane size post heat exposure and cooling (in a similar way to electrowetting) is also considered.

A final chapter then closes this document with a summary of the scientific contributions and possible future directions.

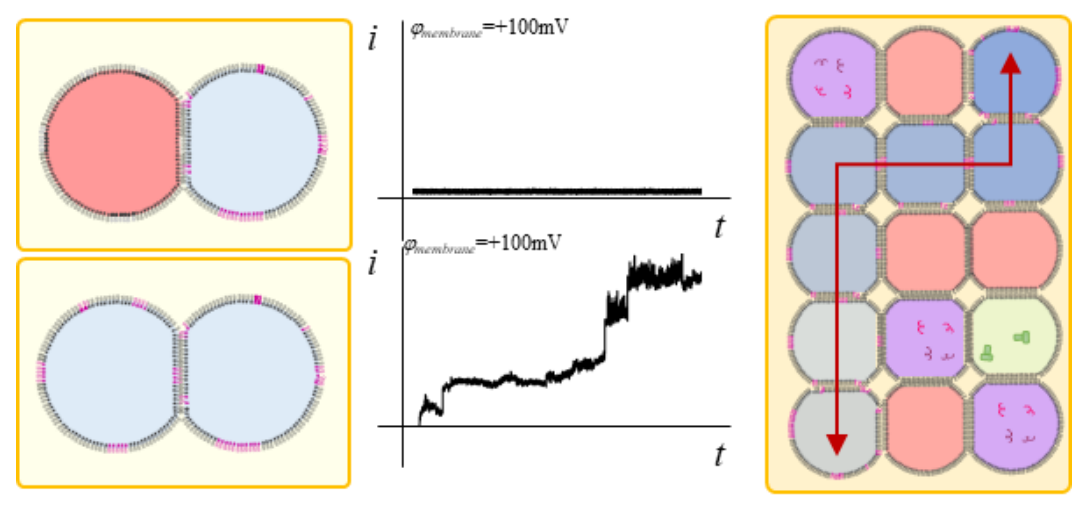


Figure 1.9- Using the Droplet Interface Bilayer (DIB) platform, a complex network of stabilized emulsive droplets interconnected through interfacial lipid bilayers can be constructed. Such structures are responsive to different types of external triggers and exhibit pre-meditated and precise output signals. The nature of the response can be controlled through tailored bilayer/droplet composition. Different transmembrane peptide and protein channels can be incorporated within the aqueous phase of the DIB platform to achieve patterned conductive pathways linking multiple compartments together. Herein, we explore the capability of patterning conductive pathways one-droplet thick in resolution by infusing the aqueous phase with photopolymerizable lipids. Red droplets contain DPhPC phospholipids, green droplets contain DPhPC and \(\alpha H \), lilac droplets contain DPhPC and Gramicidin monomers while different shades of blue droplets are the droplets containing a mixture of DPhPC and 23:2 DiynePC photopolymerizable lipids. The arrow shows a conductive pathway formed between droplets containing photopolymerizable lipids. The darkest droplets have the highest concentration of a target species. Transport can be therefore carried through droplets infused with photopolymerizable lipids.

1.3. References

- 1. Urban, P.L., Compartmentalised chemistry: from studies on the origin of life to engineered biochemical systems. New Journal of Chemistry, 2014. **38**(11): p. 5135-5141.
- 2. Joyce, G., D. Deamer, and G. Fleischaker, *Origins of life: the central concepts*.

 Deamer, DW, 1994.
- 3. Vanuytsel, S., J. Carniello, and M.I. Wallace, *Artificial Signal Transduction across Membranes*. ChemBioChem, 2019. **20**(20): p. 2569-2580.
- 4. Gánti, T., *The principles of life*. 2003: Oxford University Press.
- 5. Yewdall, N.A., A.F. Mason, and J.C. Van Hest, *The hallmarks of living systems:* towards creating artificial cells. Interface focus, 2018. **8**(5): p. 20180023.
- 6. Aufinger, L. and F.C. Simmel, *Establishing communication between artificial cells*. Chemistry—A European Journal, 2019. **25**(55): p. 12659-12670.
- 7. Monnard, P.-A. and P. Walde, *Current ideas about prebiological compartmentalization*. Life, 2015. **5**(2): p. 1239-1263.
- 8. Branton, D. and D.W. Deamer, *Membrane Structure*, in *Membrane Structure*. 1972, Springer. p. 1-70.
- 9. Smith, H.W., The plasma membrane, with notes on the history of botany. Circulation, 1962. **26**(5): p. 987-1012.
- 10. Edidin, M., *Lipids on the frontier: a century of cell-membrane bilayers.* Nat Rev Mol Cell Biol, 2003. **4**(5): p. 414-8.
- 11. Colin, L.A. and Y. Jaillais, *Phospholipids across scales: lipid patterns and plant development.* Current Opinion on Plant Biolgy, 2020. **53**: p. 1-9.

- 12. Gorter, E. and F. Grendel, *On Bimolecular Layers of Lipoids on the Chromocytes of the Blood.* J Exp Med, 1925. **41**(4): p. 439-43.
- 13. Danielli, J.F. and H. Davson, *A contribution to the theory of permeability of thin films*. Journal of Cellular and Comparative Physiology, 1935. **5**(4): p. 495-508.
- 14. Singer, S.J. and G.L. Nicolson, *The fluid mosaic model of the structure of cell membranes*. Science, 1972. **175**(4023): p. 720-31.
- 15. Nicolson, G.L., *The Fluid-Mosaic Model of Membrane Structure: still relevant to understanding the structure, function and dynamics of biological membranes after more than 40 years.* Biochim Biophys Acta, 2014. **1838**(6): p. 1451-66.
- 16. Loewenstein, W.R., *Junctional intercellular communication: the cell-to-cell membrane channel.* Physiological Reviews, 1981. **61**(4): p. 829-913.
- 17. Casey, P.J., *Protein lipidation in cell signaling*. Science, 1995. **268**(5208): p. 221-225.
- 18. Ahmed, K.A. and J. Xiang, *Mechanisms of cellular communication through intercellular protein transfer*. Journal of cellular and molecular medicine, 2011.

 15(7): p. 1458-1473.
- 19. Weinkamer, R. and P. Fratzl, *Mechanical adaptation of biological materials—The examples of bone and wood*. Materials Science and Engineering: C, 2011. **31**(6): p. 1164-1173.
- 20. A. O'Malley, M., et al., *Knowledge-making distinctions in synthetic biology*. BioEssays, 2008. **30**(1): p. 57-65.
- Szostak, J.W., D.P. Bartel, and P.L. Luisi, *Synthesizing life*. Nature, 2001.
 409(6818): p. 387-390.

- 22. Weliky, M. and G. Oster, *The mechanical basis of cell rearrangement. I. Epithelial morphogenesis during Fundulus epiboly.* Development, 1990. **109**(2): p. 373-386.
- 23. Guillot, C. and T. Lecuit, *Mechanics of epithelial tissue homeostasis and morphogenesis*. Science, 2013. **340**(6137): p. 1185-1189.
- 24. PHILLIPS, H.M., Liquid-tissue mechanics in amphibian gastrulation: germ-layer assembly in Rana pipiens. American Zoologist, 1978. **18**(1): p. 81-93.
- 25. Phillips, H. and M. Steinberg, *Embryonic tissues as elasticoviscous liquids. I. Rapid and slow shape changes in centrifuged cell aggregates.* Journal of cell science, 1978. **30**(1): p. 1-20.
- 26. Shawky, J.H. and L.A. Davidson, *Tissue mechanics and adhesion during embryo development*. Developmental biology, 2015. **401**(1): p. 152-164.
- 27. Mierke, C.T., *Initiation of a neoplasm or tumor*. 2015, IOP Publishing: Bristol, UK.
- 28. David, R., et al., *Tissue cohesion and the mechanics of cell rearrangement*.

 Development, 2014. **141**(19): p. 3672-3682.
- 29. Pontani, L.-L., et al., *Biomimetic emulsions reveal the effect of mechanical forces on cell–cell adhesion*. Proceedings of the National Academy of Sciences, 2012. **109**(25): p. 9839-9844.
- 30. Bibette, J., F.L. Calderon, and P. Poulin, *Emulsions: basic principles*. Reports on Progress in Physics, 1999. **62**(6): p. 969.
- 31. Funakoshi, K., H. Suzuki, and S. Takeuchi, *Lipid bilayer formation by contacting monolayers in a microfluidic device for membrane protein analysis*. Analytical chemistry, 2006. **78**(24): p. 8169-8174.

- 32. Bayley, H., et al., *Droplet interface bilayers*. Molecular BioSystems, 2008. **4**(12): p. 1191-208.
- 33. Makhoul-Mansour, M., et al., Ferrofluid-Based Droplet Interface Bilayer Networks. Langmuir, 2017. **33**(45): p. 13000-13007.
- 34. Hwang, W.L., et al., Electrical Behavior of Droplet Interface Bilayer Networks: Experimental Analysis and Modeling. Journal of the American Chemical Society, 2007. **129**(38): p. 11854-11864.
- 35. Hwang, W.L., et al., *Asymmetric droplet interface bilayers*. Journal of the American Chemical Society, 2008. **130**(18): p. 5878-5879.
- 36. Makhoul-Mansour, M.M., et al., *Photopolymerized microdomains in both lipid leaflets establish diffusive transport pathways across biomimetic membranes*. Soft Matter, 2019. **15**(43): p. 8718-8727.
- 37. Venkatesan, G.A., et al., Adsorption Kinetics Dictate Monolayer Self-Assembly for Both Lipid-In and Lipid-Out Approaches to Droplet Interface Bilayer Formation.

 ACS-Langmuir, 2015. **31**(47): p. 12883-12893.
- 38. Sitte, P., Role of lipid self-assembly in subcellular morphogenesis, in Cytomorphogenesis in plants. 1981, Springer. p. 401-421.
- 39. Challita, E.J., M.M. Makhoul-Mansour, and E.C. Freeman, *Reconfiguring droplet* interface bilayer networks through sacrificial membranes. Biomicrofluidics, 2018. **12**(3): p. 034112.
- 40. Nguyen, M.-A., et al., *Hydrodynamic trapping for rapid assembly and in situ* electrical characterization of droplet interface bilayer arrays. Lab on a Chip, 2016. **16**(18): p. 3576-3588.

- 41. Czekalska, M.A., et al., A droplet microfluidic system for sequential generation of lipid bilayers and transmembrane electrical recordings. Lab Chip, 2015. **15**(2): p. 541-8.
- 42. Wauer, T., et al., Construction and manipulation of functional three-dimensional droplet networks. ACS Nano, 2014. **8**(1): p. 771-9.
- 43. Ma, S., et al., *Gel Microrods for 3D Tissue Printing*. Advanced Biosystems, 2017. **1**(8): p. e1700075.
- 44. Challita, E.J., et al., *Encapsulating Networks of Droplet Interface Bilayers in a Thermoreversible Organogel.* Scientific reports, 2018. **8**(1): p. 6494-6505.
- Milianta, P.J., et al., Water permeability across symmetric and asymmetric droplet interface bilayers: interaction of cholesterol sulfate with DPhPC. Langmuir, 2015.
 31(44): p. 12187-12196.
- 46. El-Beyrouthy, J., et al., A new approach for investigating the response of lipid membranes to electrocompression by coupling droplet mechanics and membrane biophysics. Journal of the Royal Society Interface, 2019. **16**(161): p. 20190652.
- 47. Taylor, G., et al., Electrophysiological interrogation of asymmetric droplet interface bilayers reveals surface-bound alamethicin induces lipid flip-flop.

 Biochimica et Biophysica Acta (BBA)-Biomembranes, 2019. **1861**(1): p. 335-343.
- 48. Findlay, H.E., N.J. Harris, and P.J. Booth, *In vitro synthesis of a Major Facilitator Transporter for specific active transport across Droplet Interface Bilayers*.

 Scientific reports, 2016. **6**: p. 39349.

- 49. Huang, J., et al., *Direct quantitation of peptide-mediated protein transport across a droplet-interface bilayer*. Journal of the American Chemical Society, 2011. **133**(40): p. 15818-15821.
- 50. Najem, J.S., et al., Activation of bacterial channel MscL in mechanically stimulated droplet interface bilayers. Scientific Reports, 2015. **5**(13726).
- 51. Sarles, S.A. and D.J. Leo, *Tailored Current--Voltage Relationships of Droplet-Interface Bilayers Using Biomolecules and External Feedback Control.* Journal of Intelligent Material Systems and Structures, 2009. **20**(10): p. 1233-1247.
- 52. Holden, M.A., D. Needham, and H. Bayley, *Functional bionetworks from nanoliter* water droplets. Journal of the American Chemical Society, 2007. **129**(27): p. 8650-8655.
- 53. Maglia, G., et al., *Droplet networks with incorporated protein diodes show collective properties*. Nature Nanotechnology, 2009. **4**: p. 437-440.
- 54. Punnamaraju, S., H. You, and A. Steckl, *Triggered release of molecules across droplet interface bilayer lipid membranes using photopolymerizable lipids*. Langmuir, 2012. **28**(20): p. 7657-7664.
- 55. Booth, M.J., et al., *Light-activated communication in synthetic tissues*. Sci Adv, 2016. **2**(4): p. e1600056.
- 56. Booth, M.J., et al., *Droplet Networks, from Lipid Bilayers to Synthetic Tissues*, in *Encyclopedia of Biophysics*, G. Roberts and A. Watts, Editors. 2019, Springer Berlin Heidelberg: Berlin, Heidelberg. p. 1-13.
- 57. Villar, G., A.D. Graham, and H. Bayley, *A tissue-like printed material*. Science, 2013. **340**(6128): p. 48-52.

- 58. Sarles, S.A. and D.J. Leo, *Physical encapsulation of droplet interface bilayers for durable, portable biomolecular networks.* Lab on a Chip, 2010. **10**(6): p. 710-7.
- 59. Watson, P., Function follows form: generation of intracellular signals by cell deformation. The FASEB journal, 1991. **5**(7): p. 2013-2019.

CHAPTER 2

LITERATURE REVIEW: DROPLET-BASED MEMBRANOUS SOFT MATERIALS¹

¹ M. M. Makhoul-Mansour, E. C. Freeman, Langmuir 2021, 37, 3231. Reprinted with permission of the publisher.

2.1. Abstract

Inspired by the structure and functionality of natural cellular tissues, DIB (droplet interface bilayer)-based materials strategically combine model membrane assembly techniques and droplet microfluidics using the bottom-up approach to synthetic biology. These structures have shown promising results in applications ranging from biological computing to chemical microrobots. This review briefly explores recent advances in the areas of construction, manipulation and functionalization of DIB networks, discusses their unique mechanics, and focuses on the contributions of our lab in the advancement of this platform. We also reflect on some of the limitations facing DIB-based materials and how they might be addressed, motivating promising applications enabled through their refinement.

2.2. Introduction

Biologically inspired engineering is an interdisciplinary effort (including organic chemistry, materials science, mechanical engineering, biological engineering, and biology to name a few contributing fields) with the goal of mimicking naturally evolved systems to produce new technologies. One approach in bioinspired engineering involves the bottom-up approach to synthetic biology, which replicates biological functionality in simplified structures by assembling the system from individual components. With many potential applications including chemical robots [1-4], artificial tissues capable of responding to external environmental stimuli [5], targeted drug delivery and diagnosis [6], and molecular computing [7], bottom-up synthetic biology offers many new opportunities in material design.

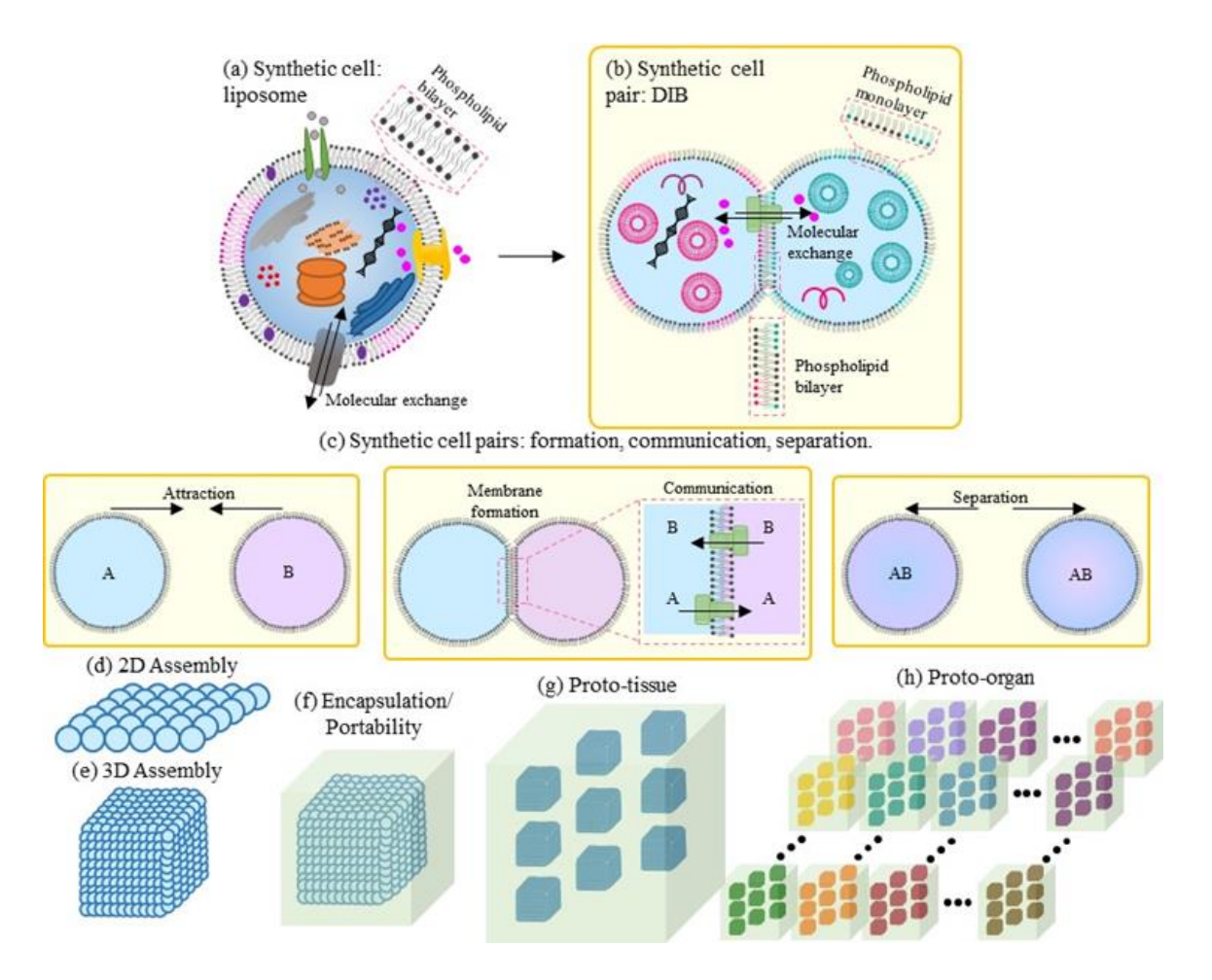


Figure 2.1 - (a) It has been proposed that basic biochemical components can be used to construct synthetic cellular systems. One example of this are empty cells or liposomes, which are bordered with semi-permeable lipid bilayers and mediate exchange through transmembrane channels. Each liposome can be a standalone functional unit. (b) In contrast droplet pairs are connected with an interfacial lipid bilayer in the DIB technique to produce a single functional unit. Unlike liposomal systems, the properties of lipid membranes are in this case dictated by the bordering droplet pair and hence any rearrangement in the placement of these droplets will result in changes in the properties and composition of interfacial bilayers. (c) These droplet pairs can be brought together to initiate droplet-droplet exchange. Afterwards, droplet pairs can be separated resulting in two compartments

with updated molecular composition. DIBs can be used to construct (d) 2D and (e) 3D membranous tissues in oil and water mediums. (f) Further efforts are focused on enhancing the portability of these materials by developing various encapsulation strategies. It has been suggested that the multicompartmentalization of DIB-structures within an organogel could approximate a proto-tissue as shown in (g), and a collection of connected proto-tissue units would ambitiously approximate a proto-organ as shown in (h).

A subset of bottom-up synthetic biology is protocell creation, defined by its goal of constructing minimal cellular systems and cell-inspired materials. While fully replicating cellular tissues in vitro is not a foreseeably attainable goal, synthetic biology can still seek inspiration from particular cellular behaviors [8], using self-assembly mechanics [9] to replicate desired cellular attributes (Figure 2.1-g and Figure 2.1-h). Ideally these biologically-inspired structures would retain several characteristics of living cells, including their modularity, compartmentalization, and communication [6], widely considered part of the foundation for basic living systems per Ganti's chemoton model [10]. One particular subfield of bioinspired engineering and cell-inspired materials involves the use of stabilized adhesive emulsions [11]. The droplet interface bilayer (DIB) technique assembles lipid membranes at the interfaces of lipid-coated aqueous microdroplets dispersed in an oil phase [12, 13]. The lipid membranes reproduced in this technique mimic an essential cellular structure that is highly impermeable to hydrophilic molecules and provides cellular boundaries and architectures [14], and the DIB technique produces an interconnected web of these membranes.

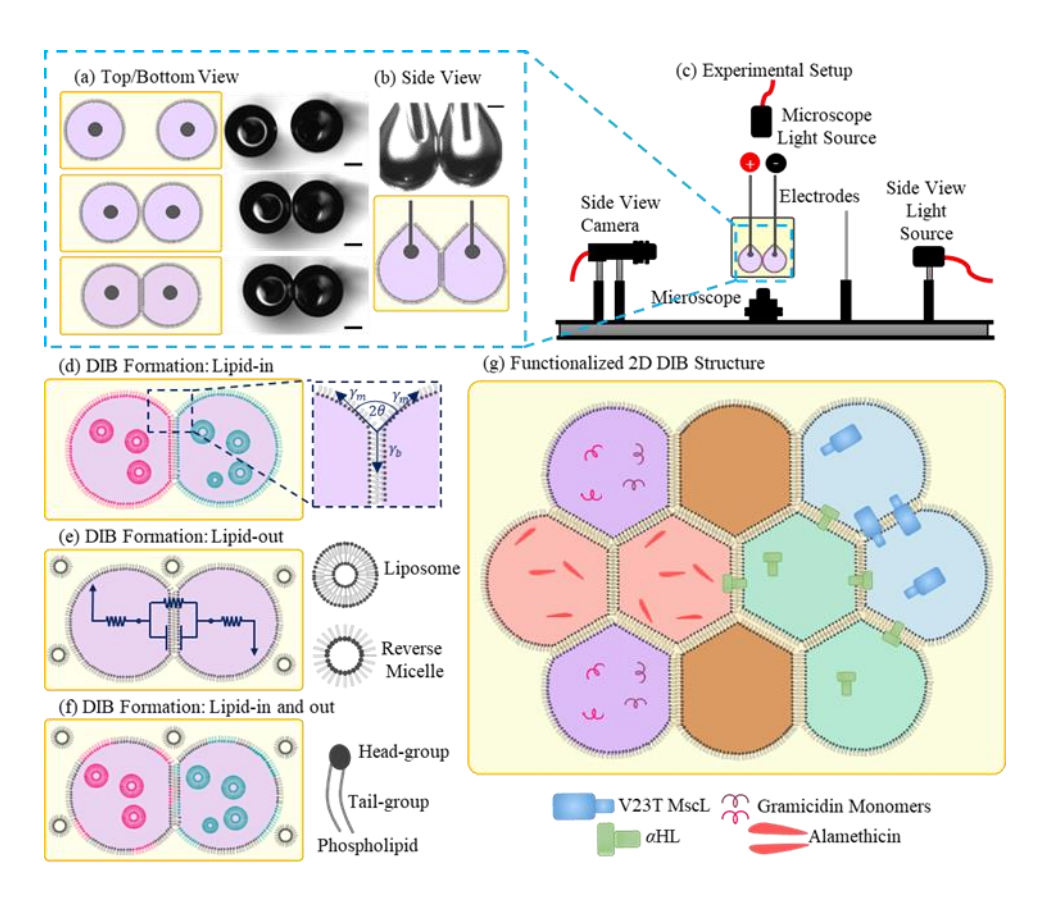


Figure 2.2 - The droplet interface bilayer (DIB) technique. A single lipid bilayer is formed at the interface of two lipid-coated aqueous microdroplets brought into contact. Schematic and experimental images of the formation of a DIB viewed (a) from the top/bottom and (b) from the side. (c) Schematic representation of the experimental setup used for DIB formation/characterization. Aqueous droplets are deposited on agarose-coated silver/silver chloride electrodes and submerged in oil. Side view and top view cameras connected to a microscope are used to acquire images of the formed bilayer. (b) and (c) are adapted from ref (18) Copyright Royal Society of Chemistry 2019. Lipids can be dispersed in the (d) water phase (lipid-in), (e) oil phase (lipid-out) or (f) both phases. The area of the DIB is governed through a balance of monolayer and bilayer tensions reflected through an external angle of contact. (g) Multiple droplets can be connected to form a 2D or even 3D membranous structure. Upon the formation of a single membrane, the spherical droplets

deform into spherical caps, delimited by the dimensions of the interfacial bilayer. On a larger scale, similarly to tightly packed emulsive systems, DIB networks can exhibit regular hexagonal close-packing lattices distribution when optimal oil phases and lipid mixtures are used. Various integral transmembrane channels can be embedded in droplets and used to establish communication pathways within the material. Scale bar 250 μ m.

Formed at the interface of two connected lipid-coated water droplets (as compared to traditional liposomes- Figure 2.1-a), DIB membranes possess properties that depend on the composition of their bordering compartments (Figure 2.1-b and Figure 2.1-c). Using varying sets of spatially arranged aqueous droplets with varying compositions, 2D and 3D droplet-based tissues (Figure 2.1-d and Figure 2.1-e) with different functionalities can be formed by altering the relative placement of the droplets within the tissue. In this article we discuss the basic mechanics of DIBs, followed by an overview of new platforms developed for constructing and functionalizing (Figure 2.1-c) larger synthetic droplet-based tissues as well as their inherent structural properties.

Aqueous microdroplets are introduced into an oil medium with lipids either dispersed in the oil phase (the lipid-out technique [15]: Figure 2.2-e), in the water phase (the lipid-in technique [16, 17]: Figure 2.2-d), or in some instances in both phases for enhanced stability [18] (Figure 2.2-f). The permeability, structure, and stability of the generated membranes may be modulated by varying each one of these compositions (most notably the lipid compositions [6, 19-22]). In some cases, amphiphilic block copolymers are used in place of lipids for additional stability [21]. After sufficient time for the assembly of lipid monolayers at the water-oil interface [23], lipid-coated water droplets can be brought into contact with neighboring droplets. The interfacial lipid bilayer spontaneously

forms at their points of contact as the hydrophobic phospholipid tails arranged at the droplet surfaces self-assemble in a zipping motion, expelling the oil initially separating the droplets. By repeating this connection process multiple times within a collection of microdroplets, 2D [15, 18, 24, 25] (Figure 2.2-g) and even 3D [26-28] (Figure 2.1-e and Figure 2.1-f) tissue-inspired structures may be formed. In addition to the convenient modularity and scalability of DIBs, the DIB technique enables sequential assembly of membranes through separation and reassembly of the lipid bilayers between the droplets without jeopardizing the integrity of the rest of the structure or causing the droplets to coalesce. The DIB platform also allows for the simple creation of asymmetric membranes [17, 18] (Figure 2.1 and Figure 2.2) by varying the lipid composition within adjacent droplets.

DIB-based materials can be functionalized using bioinspired methods for initiating exchange between the adhered compartments, temporarily adjusting the characteristics of the lipid barriers between the droplets. Often dispersed among the aqueous phases, transmembrane channels self-assemble within membranes bordering the droplet in which they reside, altering the permeability of the interfacial bilayers as shown in Figure 2.2-g. Many of these embedded channels respond to varying stimuli including electrical, chemical, and mechanical inputs [14, 29], allowing for controlled droplet-droplet exchange on demand. The collective behavior of these membranes working in parallel determines the emergent functionality of the tissue and enables their responses to varying external conditions. These droplet-based materials have been used for soft chemical robots [1, 2], energy storage and conversion [13, 30, 31], light-sensing [18, 32, 33], and the creation of a new class of engineered tissues [28, 34-36].

DIB-based membranous materials inherently satisfy many of the chemoton model criteria essential for sustainable life. DIB tissues are highly compartmentalized and modular yet can initiate droplet-droplet communication on-demand through modified membrane permeability. However, DIB-based tissues still face multiple challenges that need to be addressed, including difficulty in their manufacturing, associated limitations in their complexity, and issues with membrane instability. Since the functionality governed by droplet-droplet exchanges is dependent on the relative arrangement of the droplets within the material, novel droplet deposition schemes are often required for creating larger interconnected networks droplet by droplet [28, 35, 37, 38]. Additionally, the responses of the droplet-based tissues are limited by available membrane activation mechanisms – original DIB materials relied on embedded electrodes but recent effort have expanded to include more biologically-relevant schemes [18, 39] to enable their use outside of the laboratory, or suggested activation through mechanical forces [40-42]. Finally, the droplets are often prone to coalescence given their fluid-in-fluid construction and metastable nature of the adhered droplet pairs. Substantial efforts have focused on either reducing their coalescence through encapsulation [28, 43] or harnessing the phenomena for enabling droplet-droplet mixing [44, 45] and restructuring [24].

Formulating solutions to these obstacles requires familiarity with the mechanics of the droplet-based material. We begin by examining the influence of the solvent and surfactant selection on the macroscopic material properties, and how these selections govern membrane assembly and stability. Next, we discuss recent advances in the construction, manipulation, characterization and functionalization of these membrane-based soft materials with an emphasis on dynamic structures. Final notes will include the

current challenges facing the proposed material and how these challenges may be potentially addressed.

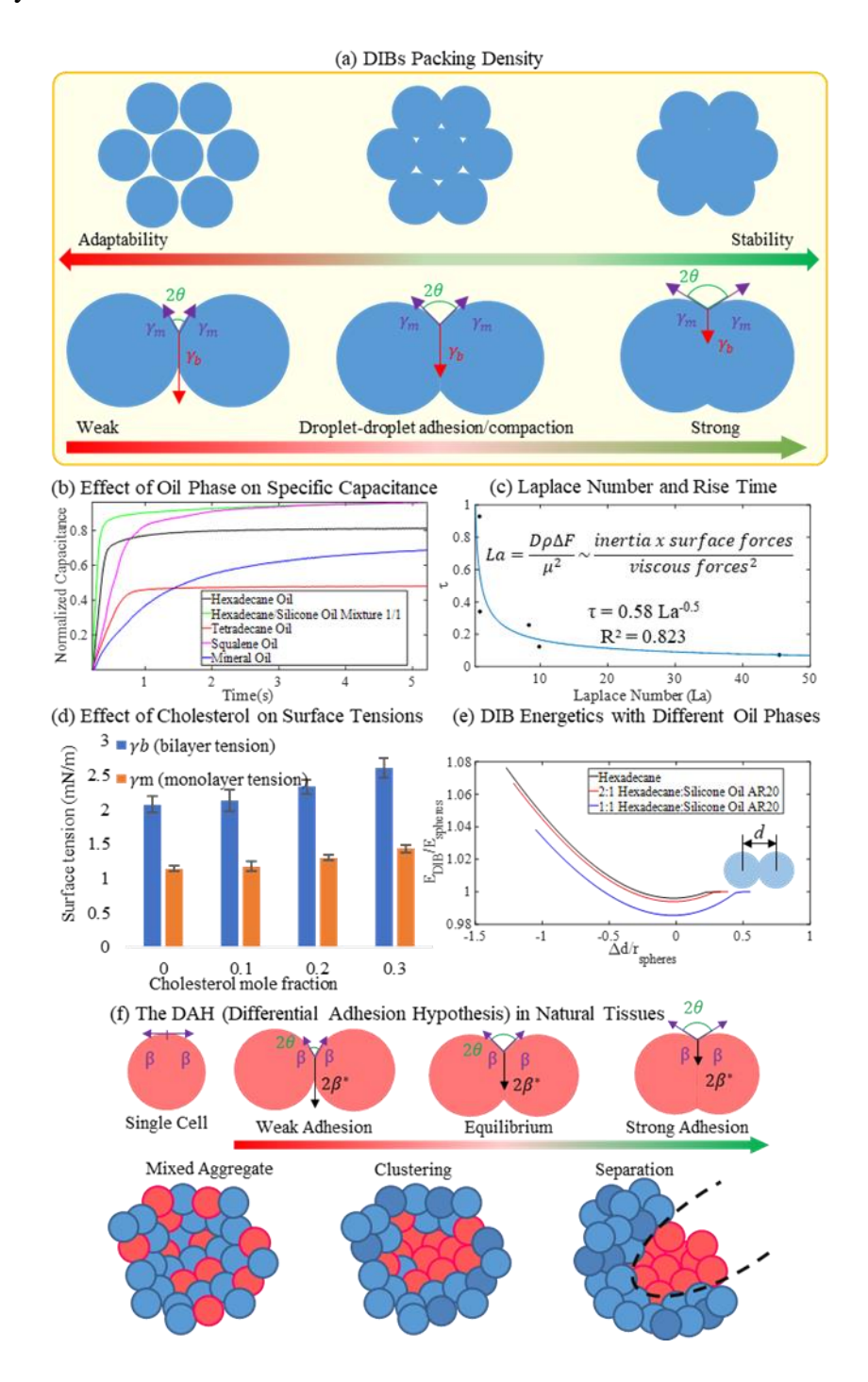


Figure 2.3- Summary of DIB mechanics and dependencies. (a) Schematic representation of the effect of packing density on the adaptability and the stability of DIB tissue. As

adhesion between droplets is increased, the contact angle, membrane area, and adhesion energy are increased, leading to denser networks. (b) Properties of DIBs were assessed using custom fabricated hydrogel microelectrodes, investigating the effect of the oil used on the specific capacitance of lipid membranes and their rate of formation. (c) The time for the membrane to reach 2/3 of its normalized size (defined here as the rise time) can be plotted against the Laplace number (mirroring the effect of inertia, surface forces, and viscous forces). Parts b and c are adapted (data adapted) with permission from ref (51). Copyright 2018 American Chemical Society. (d) Cholesterol molecules insert themselves between phospholipid molecules resulting in more rigid membranes which is reflected through an increase in both the monolayer and bilayer tension. Data adapted with permission from ref (22). Copyright 2019 Royal Society Interface. (e) Further investigation into the effect of the oil phase showed that the interfacial energy for a pair of adhered droplets as a function of the normalized distance between their centers (offset by the equilibrium distance) is also varying for different oils. Membranes that are more favorable to form show a greater range of deformation prior to separation. Adapted with permission from ref (24). Copyright 2018 AIP Biomicrofluidics. (f) Intended to provide an explanation for the spontaneous liquidlike tissue behavior, the DAH models tissues as emulsive systems: cells behave similarly to microdroplets whose varying degrees of surface adhesion (illustrated by using different colors blue and pink) cause them to spontaneously reorganize and minimize their interfacial free energy (β , cortical tension at free cell surface; and β^* , residual tension in a cell at contact).

2.3. Mechanics Of Droplet Interface Bilayers

DIBs provide a liquid-in-liquid platform for producing webs of lipid membranes. Their mode of formation results in a collection of unique mechanics, combining aspects of lipid membrane physics and droplet mechanics. We will begin with an overview of the relations between DIB composition and membrane quality, then we will move to how these relations lead to unique, emergent behaviors of DIB tissues.

Membrane Properties and Influences

The adhered structure of a DIB-based synthetic tissue is determined by the properties of its individual interfaces. The properties of each lipid membrane are primarily determined by the surfactant composition of the bordering microcompartments as well as the selected solvent that provides the external phase. The functionality of the membranous tissue as a whole is shaped by the properties of the individual membranes within the tissue (Figure 2.1 and Figure 2.2). Consequently, any change in the properties or relative arrangements of the droplets comprising the membranes will induce changes in the overall characteristics of the tissue. These changes may include either macroscopic changes in the arrangement of the droplets or local changes within the individual membranes themselves.

The emulsive nature of DIBs offers parallels to several discussions of the mechanics of living tissues. Emulsive phenomena observed in natural tissues are commonly explained through the DAH (differential adhesion hypothesis [46] Figure 2.3-f), which suggests that both living tissues and emulsive systems exhibit similar packing behavior based on the minimization of interfacial energy [47]. This aggregation driven packing with droplets is enabled through the ability of microdroplets to deform from their original spherical shape. On an elementary DIB level, upon the formation of an interfacial

bilayer, the droplets transition from a spherical shape to a spherical cap delimited by the dimensions of the membrane. The area of the membrane is governed through a balance of monolayer and bilayer tensions reflected through an external angle of contact (Figure 2.2-d) and gradually expands until the tensions at the annulus are balanced [20, 48, 49] as given by Young's equation:

$$\gamma_h = 2\gamma_m \cos\theta \tag{2.1}$$

where γ_m , γ_b , and θ are the monolayer, bilayer tension and the contact angle, respectively. Upon assembling multiple droplets into 2D and then 3D tissues, the droplet compartments adopt more complex polyhedral shapes governed by the number of neighboring droplets and their position relative to open and solid surfaces. Previous studies in oil-in-water [50] and water-in-oil [11, 48] stabilized microemulsions have shown that the external angle of contact between microdroplets is a crucial factor in the structural stability of compact systems. The importance of this angle of contact is mostly noted in emulsions and systems where the interfacial film thickness is significantly reduced; this decrease in thickness is generally accompanied with an increase in the volume fraction φ , or the volume of the aqueous phase divided by the volume of the oil phase in the synthetic tissue. As the film thickness further decreases, an angle approaching 35.26° yields a volume fraction approximating unity [50]. The same study by Princen et al. found that the type of packing assumed does not significantly matter when evaluating the film thickness and volume fraction and their dependence on certain parameters [50]. Similarly, in DIB structures, Alcinesio et al. have reported the equilibrium angle of contact to be the key factor governing the structural stability of 3D DIB tissues (defined as resistance of the adhesive droplets to coalescence) and a key geometrical constraint in the positioning of water microdroplets relatively to one another [37]. When θ approaches the theoretically derived angle from the geometry of the system, valued at 35.3°, the DIB networks exhibit regular hexagonal close-packing lattices distribution with minimal geometric defects with monodisperse droplets. The optimal droplet packing here was described to the closest possible packing that significantly reduces unoccupied space between microdroplets [47] (Figure 2.1-e and Figure 2.2-d). Tightly packed membranous tissues significantly reduce the possibility of droplets sliding between different tissue levels and allow for the precise patterning of materials with conductive pathways one-droplet thick [6, 18, 26, 33, 35, 39]. From Equation 2.1, the equilibrium θ depends on interfacial tensions (monolayer and bilayer), both of which are affected by the oil [20, 22, 48], and surfactant compositions [22]. Consequently, the structural stability of DIB tissues can be regulated by varying the contents of the polar and apolar phases.

Another way to describe the contact angle is through droplet-droplet adhesion. A strong droplet-droplet adhesion results in more tightly packed and hence more stable DIB structures (Figure 2.3-a). This adhesion can be quantified using adhesion energy, defined as the energy cost for formation of the interfacial bilayer starting from two distinct amphiphilic monolayers as a reference point (also referred to as membrane's free energy of adhesion ε or $-\Delta F$ [48]):

$$-\Delta F = 2\gamma_m - \gamma_b = 2\gamma_m (1 - \cos\theta)$$
 (2.2)

The energy of adhesion is directly associated with the interactions of the two surfactant monolayers [51], and provides a point of comparison for membranes with varying lipid/oil/aqueous compositions. The higher the amount of energy saved by the

formation of a bilayer, the more favorable and consequently more stable the produced membranes (Figure 2.3-e).

Figure 2.3-b shows the normalized capacitance of different membranes scanned using a hydrogel microelectrode and formed using different continuous phases (data produced by our group from Challita et al. was extracted and processed for the creation of this figure [52]). Since all membranes formed with this technique have a similar area dictated by the dimensions of the hydrogel microelectrode, such measurements isolate the effect of the oil phase on the membrane formation. The influence is quantified by observing the time it takes these bilayers to reach 2/3 of their equilibrium area referred to here as the initial rapid rise time (τ). By fitting the capacitance into a function similar to the one depicted by Freeman et al. [41], fast rise times for different membranes can be obtained and analyzed in light of calculated Laplace numbers (La). The Laplace number also known as the Suratman number (Su) can be found using the following equation:

$$La = \frac{D\rho\Delta F}{\mu^2} \sim \frac{inertia\ x\ surface\ forces}{viscous\ forces^2} \tag{2.3}$$

where μ is the dynamic viscosity of the oil, ρ is the relative density of the aqueous/oil phases, and D is the characteristic length scale (here defined as the droplet diameter D). Plotting the characteristic rise time for membrane formation in different oils vs. La, an empirical equation linking the two and reflecting the dynamics of the membrane formation (Figure 3-c) is found. Smaller Laplace numbers indicate a greater influence of the viscosity while larger ones show a behavior dominated by the inertia and surface forces. Smaller La have shown larger rise times (τ) indicating that these bilayers typically require more time to form. While this time difference might seem insignificant for single membrane applications, larger DIB tissues involving collections of microdroplets require rapid

adhesion as depositing the droplets faster that the membrane stabilization time may result in structural instabilities and ultimately failure. Consequently the 1:1 hexadecane:silicone oil AR20 mixture is frequently used for rapid assembly of DIB networks[26, 28].

This particular mixture of hexadecane and silicone oil AR20 with suspended zwitterionic phospholipids (DPhPC 1,2-diphytanoyl-sn-glycero-3-phosphocholine) provides increased membrane stability [20], rapid membrane assembly time [23] and a closer density balance between the oil and aqueous phases to reduce gravitational influences. This lower relative density allows sufficient time for monolayer formation before the droplet settles and limits gravitational forces when constructing 3D tissues [15, 24, 26, 35]. The enhanced stability can be attributed to a reduction in trapped oil within DIBs formed in silicone: hexadecane oil mixtures compared to membranes formed with hexadecane or decane or other alkane oils [20] (Figure 2.3-b, Figure 2.3-c and Figure 2.3e). Known for being a poor phospholipid solvent, the addition of silicone oil AR20 was first found to increase the stability of adhesive water-in-oil emulsions [48]. A 1/1 volume mixture of hexadecane and silicone oils produces interfacial phospholipid membranes displaying a θ of 30.06° [15].

The lipid mixtures also influence the interfacial membrane properties [22, 23, 53]. Mixtures of cholesterol and DPhPC have been shown to restrict the movement of DPhPC phospholipids within the monolayers, leading to a more rigid, well-packed membranes as demonstrated recently by our measurements of the membrane response to electrocompression [22]. Cholesterol molecules integrate themselves between the acyl chains of DPhPC molecules, increasing the monolayer tension (Figure 2.3-d). Yet, this effect varies with the chain length of the lipid that cholesterol is mixed with, and the effect

can be predicted by comparing the hydrophobic tail chain length of both surfactants. Reports have shown that bilayers formed between phospholipids with up to 16-carbon acyl chains are thickened by the introduction of cholesterol, in contrast to bilayers formed between lipids with 18-carbon chains upon the introduction of cholesterol [20, 22]. Alcinesio et al. have analyzed the effects of oil phase and lipid composition on the stability of DIB-tissues by introducing both silicone oil and POPC (1-palmitoyl-2-oleoyl-sn-glycero-3-phosphocholine) lipids into a undecane DPhPC solution used to form 2D and 3D DIB networks [37]. Their results show that θ can be related back to the selected volume fraction of silicone oil AR20 in a mixture of undecane and silicone oil as well as the selected lipid composition (the mole fraction of POPC in a mixture of DPhPC and POPC). *Electrical Properties and Modeling*

The lipid membrane provides a low permittivity hydrophobic core that is near impermeable to dissolved species within the droplets. Consequently, a DIB is often electrically approximated as a capacitor in parallel with a high amplitude resistor [13, 30] (Figure 2.2-e). When perfectly sealed, the membrane's resistance is often in the order of $G\Omega$ - $T\Omega$ [13] hence the ohmic current is often negligible, and the overall current can be approximated as capacitive. Furthermore, the DIB platform brings an aspect of modularity. The droplets are an unsupported liquid-in-liquid structure, and it is possible to connect multiple droplets together forming networks of interconnected lipid membranes. The electrical properties of networks of lipid membranes are typically modeled using a network stencil through nodal voltage analysis, producing a system of differential equations describing the voltage distribution across each of the connected membranes as modeled extensively by our group [16, 54]. These stencils have been combined with equations

describing the underlying exchange of charged species associated with the currents to describe gradual shifts in droplet contents [29], and linked to the behavior of osmotically-driven actuators [35]. Furthermore, lipid membranes can be functionalized with protein channels and pore forming toxins strategically dispersed within aqueous compartments yielding conductive communication pathways spanning the tissue (Figure 2.6). This produces variable resistances between the droplets, in addition to triggering active transport using chemical fuel such as ATP [55].

Mechanical Properties and Behavior

Another unique aspect of DIB-based materials is their response to mechanical perturbation. This may be attributed to the weak elasticity of microfluidic droplets and capillary forces [56-58]. The energetic cost of formation for DIB networks is obtained by multiplying the tension of each interface (monolayer/bilayer) by their respective areas and can be combined with gravitational influences and other contributions as demonstrated for modeling DIBs [24]. The shape of the adhered droplets at equilibrium represents the minimization of this value with given volume constraints on the droplets [58]. Perturbing the droplets leads to a distortion away from their desired minimal shape [56], providing a form of weak elasticity where the droplets continually seek their minimum energy configuration in response to changing environmental constraints or boundaries. This has been used to regulate the membrane area with great success, either pulling the droplets apart [22, 49, 59] or varying the dimensions of an aperture between the droplets [60]. Furthermore, is possible to shift adhered droplets between metastable positions through the careful application of mechanical forces and constraints [40].

The stiffness and stability of the adhered droplet configuration is linked to their interfacial tensions (Figure 2.2-a). If the membrane formation is energetically favorable, then the energy well representing the metastable state becomes deeper and requires greater forces for separation as demonstrated by our group (Figure 2.2-e) [40]. Consequently, if reconfiguration or separation of the droplets (defined as adaptation of the structure) is desired then a balance between ease of membrane formation and ease of separation must be achieved. The overall stiffness of the material is related to the monolayer tension, and the difficulty in separating the droplets is related to the energy of adhesion. Selecting the proper solvent and lipid combination is crucial when tailoring a network for a desired stiffness (Figure 2.2-a).

DIB based tissues are inherently different from their natural inspiration in the very description of the interfaces between their constituent modules. In natural living tissues, cell-cell interfaces are comprised of two adjacent cellular barriers. Consequently, separating two cells often does not significantly alter the activity of each individual unit comprising the pair. Meanwhile, in the case of DIB systems, the lipid barriers are comprised of the lipid-leaflets coating bordering compartments (Figure 2.1-a and Figure 2.1-c). Hence, the properties of DIB membranes reflect the compositions of the adhered droplet pair [17, 18, 32] and rearranging droplets within DIB-structures fundamentally changes the properties of the membranes within the tissue by breaking these pairs apart and reforming them between different droplets. The functionality of the overall material is hence linked to its own internal structure.

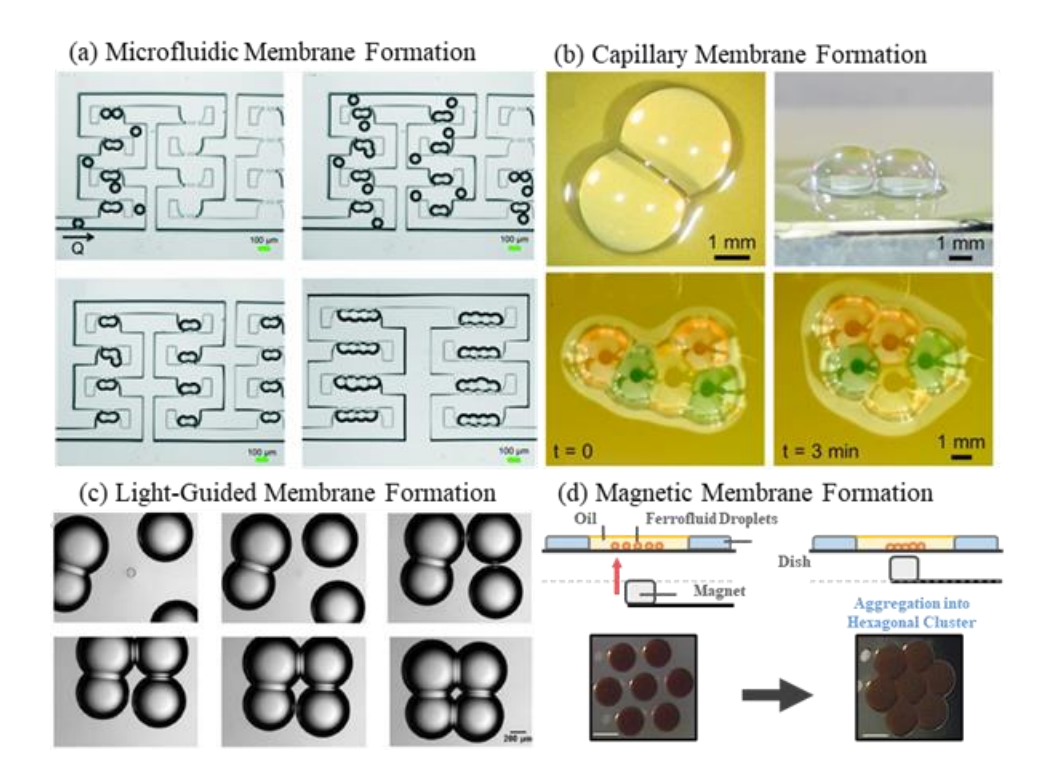


Figure 2.4- Various methods for the assembly of smaller DIB networks in a repeatable fashion. (a) Experimental images of DIBs formed using microfluidic channels. Each hydrodynamic trap can hold several lipid bilayers formed between two aqueous droplets. Reprinted with permission from ref (25). Copyright 2016 Lab on a Chip RSC. (b) Lipid-coated water droplets can be deposited into oil-infused hydrophobic surfaces and brought into contact forming 2D DIB structures. Reprinted with permission from ref (65). Copyright 2014 PNAS. (c) Laser-induced heating may be used to drive aqueous droplets into close proximity to each other resulting in the formation of lipid bilayers. Reprinted with permission from ref (66). Copyright 2010 American Chemical Society. (d) Magnetic fields may be used to assemble DIB networks by selectively infusing droplets with ferrofluids. The scale bar is 800 μm. Reprinted with permission from ref (24). Copyright 2018 AIP Biomicrofluidics.

2.4. Formation of Droplet Interface Bilayers

DIB materials are best described as a combination of stabilized adhesive emulsions and model membrane assembly techniques. As discussed previously, several DIB properties such as membrane thickness, dimensions, and droplet stiffness are largely determined by the selected solvents and lipids, allowing for flexibility in their manufacturing. It is possible to scale the DIB platform from a single membrane up to an entire membrane-based tissue by continuing to add adhered droplets in the desired pattern. Techniques for generating DIB tissues can be characterized according to the droplet manipulation mechanism, the size/complexity of the resulting material, and the speed of assembly. Here we provide an overview of these techniques based on the number of membranes present in the individual functional units, referred to as the membrane density. Low Membrane Density Methods

First, we discuss techniques for forming DIB networks with a smaller number of connected droplets, or low-membrane density methods. These methods are often compatible with parallel or rapid formation. The simplest structure formed through the DIB technique involves two aqueous droplets pipetted into an oil dish and manually driven into contact using either the tip of a micropipette (or the tip of a finely pulled glass rod) or guided by the electrodes [13]. The rate of formation of the lipid monolayers at the water-oil interface depends on the adsorption kinetics of phospholipids and by extension on the phase in which the amphiphiles are present [20, 23]. After a sufficient time for the acquisition of a lipid monolayer at the droplet surfaces, the droplets are brought into contact resulting in an initial thinning of the lipid-lipid interface. Lipid tail-groups spontaneously draw together in a zipping motion and exclude a significant quantity of the trapped oil

between the droplets triggering the formation of an interfacial lipid bilayer (Figure 2.2). The inclusion of microelectrodes allows for the application of an electrical potential to confirm the formation of the membrane as well for the assessment of the ionic current flowing through embedded transmembrane channels using electrophysiological techniques. Simple 2D and even 3D (pyramids containing 14 droplets) [26] membrane structures can be formed using this technique as well. 2D membrane structures can likewise be patterned within pre-designed microfluidic devices [36, 61] and channels [25] (Figure 2.4-a).

Microfluidic channels provide manipulation through hydrodynamics for high throughput generation of DIB structures in rapid succession [62-64], connecting several droplets together in microfluidic traps. These approaches are best applied towards screening applications wherein the smaller DIB clusters provide a model environment for studying an interaction in parallel [63, 65]. Superhydrophobic oil-coated surface have been used to connect colliding water droplets otherwise suspended in air into interfacial bilayers [66] with potential applications for screening compounds in the air (Figure 2.4-b).

Optical strategies for droplet manipulation have also been developed exploring light-induced capillary effects and displaying many advantages including contact-free minimally invasive droplet manipulation. One of these strategies used the thermocapillary effect and convective fluid motion to optically manipulated lipid-coated microdroplets into contact using lasers [67] (Figure 2.4-c). Optical-tweezers approaches have been adopted for the manipulation of DIB-structures [67] resulting in the formation and effective manipulation (and even droplet fusion) of 2D membranous structures. This strategy was also explored for sculpting and fusing biomimetic vesicle networks [68] where vesicles are

interconnected by axon-like tethers. The further use of transmembrane channels facilitated molecular transport and initiating protein expression across these structures post laser-induced vesicle fusion.

Standard droplet manipulation techniques are compatible with DIB formation as well. Using electrowetting on dielectric (EWOD), two or more aqueous microdroplets can be manipulated together into contact forming DIB-based structures [69, 70]. Highly conductive electrolyte solutions can be directed using relatively low currents with minimal joule heating resulting in droplets' motion and increased wettability [69, 71].

The ability to magnetically influence aqueous microdroplets was first explored by Wauer et al. by embedding select compartments with magnetic beads [26, 45]. Magnetic droplets were used to drag and position the remaining aqueous droplets to a submillimeter precision using a permanent magnet. Another alternative was developed by our group through the incorporation of biocompatible ferrofluids into the DIB platform [15, 24, 72, 73]. First we demonstrated that the ferrofluid was compatible with DIBs, exhibiting minimal changes in functionality and able to accommodate transmembrane channels [72]. Two types of magnetically infused DIB networks were formed: ferrofluid-based structures and mixed water-ferrofluid based structures. Homogeneous ferrofluid based DIB networks were formed by injecting magnetically infused droplets into a lipid-oil mixture and then gradually bringing a permanent magnet closer to the dish so that droplets adhered together and spontaneously formed bilayers [15, 24, 72, 73] (Figure 2.4-d). Mixed networks with both ferrofluid and water droplets were formed by manually injecting both magnetic and aqueous droplets into a lipid-oil medium and then using ferrofluid droplets manipulated

using permanent magnets to progressively recruit water drops into a connected structure [15, 24, 72, 73].

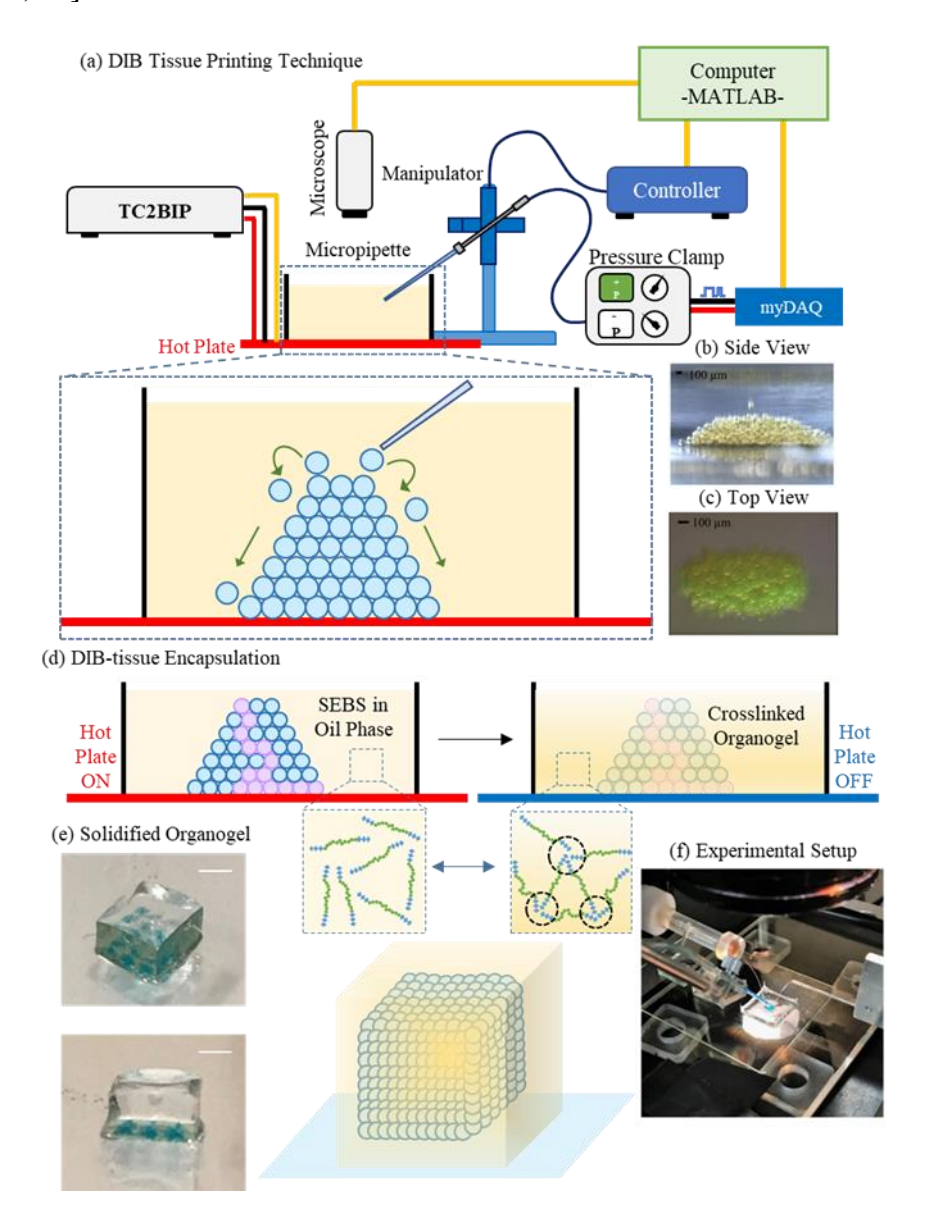


Figure 2.5- High-membrane-density printing of encapsulated DIB tissues. (a) A glass micropipette is connected to a pressure clamp for pneumatic droplet deposition. A 3-axis manipulator is used to manipulate the micropipette to specific predefined coordinates. Adapted with permission from ref (28). Copyright 2018 Scientific Reports, Nature. (b) Side and (c) top view experimental images of a printed 3D DIB network. Parts b and c are

adapted with permission from ref (73). Copyright 2017 International Society for Optics and Photonics SPIE. (d) Using the previously developed pneumatic droplet printing system, the process is repeated to generate webs of aqueous droplets. The printing process is achieved on a heating plate using the experimental setup shown in part f ensuring that the encapsulating organogel is molten. (e) Once the final structure is produced, the heat is removed allowing the organogel to solidify. The organogel preserves the structural integrity of the material and can be removed from the substrate. Parts e and f are reprinted with permission from ref (28). Copyright 2018 Scientific Reports, Nature.

High Membrane Density Methods

When forming larger functional networks of DIBs containing many interconnected droplets, several considerations are necessary since the precise relative arrangements of the droplets is essential. Larger structures approaching the tissue-scale often require a droplet-on-demand approach where the droplets are deposited sequentially with varying components. The concept of using 3D printer-based systems for the generation of DIB tissues enabled the production of compartmentalized tissues with preset functionalities determined by the droplet patterning. A key advantage of combining 3D printing with the DIB-platform is the ability to link hundreds/thousands of microcompartments of different chemical profiles with high spatial/temporal control to produce more complex membranous structures in relatively short time [28, 35, 74]. However, such approach is faced with the possible structural instabilities in the droplet-based tissues arising for example from droplet coalescence or sliding prior to membrane formation. Hence, the

properties of the oil phase and surfactant mixture as well as membrane formation time ought to be optimized for further development of the printing algorithm.

Villar et al. developed a 3D micro/nanodroplets printer comprising two printing nozzles connected to piezoelectric transducers [35]. Micro and nanodroplets can be injected in an oil bath and their respective x-y positions regulated through a computer-controlled micromanipulator. Droplet ejection and dimensions are a function of the pulse width and voltage supplied, with several droplet characteristics that provide a repeatable and reliable droplet ejection in the range $\sim 30-60~\mu m$ [35]. Since positioning of the printing nozzle in the z direction was unnecessary for droplet release, droplet deposition, incubation time (~ 1 s) and bilayer formation ($\sim 1-3$ s) could be achieved in under 5 s [35].

A second approach was later adopted by our lab by developing a pressure-based 3D droplet printer for the formation of DIB-based tissues [28, 74] (Figure 2.5-a, b, c and f). A glass capillary is mounted on a micromanipulator and connected to a microinjector, both synchronized and controlled via computer. A multi-capillary holder was design to allow for the use of multiple capillary tubes containing different lipid mixtures simultaneously. Microdroplets are first formed at the tip of the glass capillary by controlling the pressure provided for the capillary tubes connected to a pneumatic system (computer-controlled). Following formation, droplets are released by vertically removing the tip of the capillary tube from the oil medium into air in a snap off motion using capillary forces. The process is then repeated as needed to produce networks of aqueous droplets with varying inflated dimensions (on average a single droplet every few seconds). The snap off motion results in longer deposition time (in comparison to the previously described approach) as the printing nozzle is introduced and removed from the oil medium for each droplet. However,

this approach allows for variable dimensions of the printed droplets based on inflation time and pressure [28].

Microfluidic channels have also been adapted for the controlled and high-throughput generation of larger 2D and 3D DIB structures [75, 76]. Branched microfluidic devices generate DIB structures according to the contours of the canals while a linear channel is used to construct 2D and 3D networks. Although the above experiments focus on droplets of differing lipid composition, the methodologies could equally be extended to incorporate droplets with varying encapsulated components.

Encapsulation of Synthetic Tissues

Although these structures remained stable for several days when printed in oil, one of the key challenges facing further development of these materials is their sensitivity to external environments (inherent instabilities leading to membrane failure) contributing to their possible degradation outside of controlled laboratory conditions. One approach to ensuring stability involves using hydrogels within the aqueous phase to provide a solid droplet core [45, 77, 78]. Hydrogels are water-swollen networks of crosslinked hydrophilic polymers often used in cell culture applications as an artificial extracellular matrix. The hydrogels are ionically conductive and permit electrical measurements when hydrated with a buffer solution. Hydrogels can be used as building blocks for DIB materials with applications ranging from electrical circuits to mechanical devices [78].

Alternatively, DIBs may be fully encapsulated and shielded from the environment in a solid substrate, producing a liquid-in-solid configuration. The first approach for this employed a flexible substrate containing two enclosures for the droplets to further control membranes properties [79] introducing the regulated attachment method. Similar

approaches suggested encapsulating bilayer membrane structures in hydrogels [80-82] forming multiple interconnected membranous zones inspired by the concept of protoorgans.

Recent research by our group and others has focused on using thermoreversible organogels within the oil phase to provide a robust and flexible encapsulation strategy that may be reset with heat [28, 43] (Figure 2.5-d and Figure 2.5-e). This involves the dissolution of a thermoreversible triblock copolymer within the oil phase (SEBS, Poly(styrene-b-ethylene-co-butylene-b-styrene)). SEBS forms a polymeric matrix within the gel at room temperature but shifts to a fluid phase when the temperature is elevated to a higher-level dependent on the polymer concentration [28] (Figure 2.5-c). The result is a liquid-in-gel material that may be temporarily softened to enable droplet deposition and assembly, then cooled to provide a soft encapsulating matrix.

The oil phase of DIB-based systems poses challenges to their use in physiological environments and in applications such as biosensors and compartmentalized drug delivery systems. Multisomes have been explored as an alternative encapsulation technique. Aqueous interconnected lipid-coated microdroplets can be embedded in an oil-in-water droplet [83, 84], producing a multiphase emulsion. The functionalization of multisomes was studied through their response to pH and temperature, establishing transmembrane channel activity and communication to the external water phase [84]. Further steps in fully functionalizing multisomes towards medicinal applications established their use as compartments for "genomes" in an in-situ protein synthesis in defined regions [85]. The ability to establish communication with the exterior water phase makes multisomes a promising encapsulation strategy for drug-delivery and molecular scanning applications

and paves the way for future works where higher-order cellular characteristics can be integrated into the synthetic tissues.

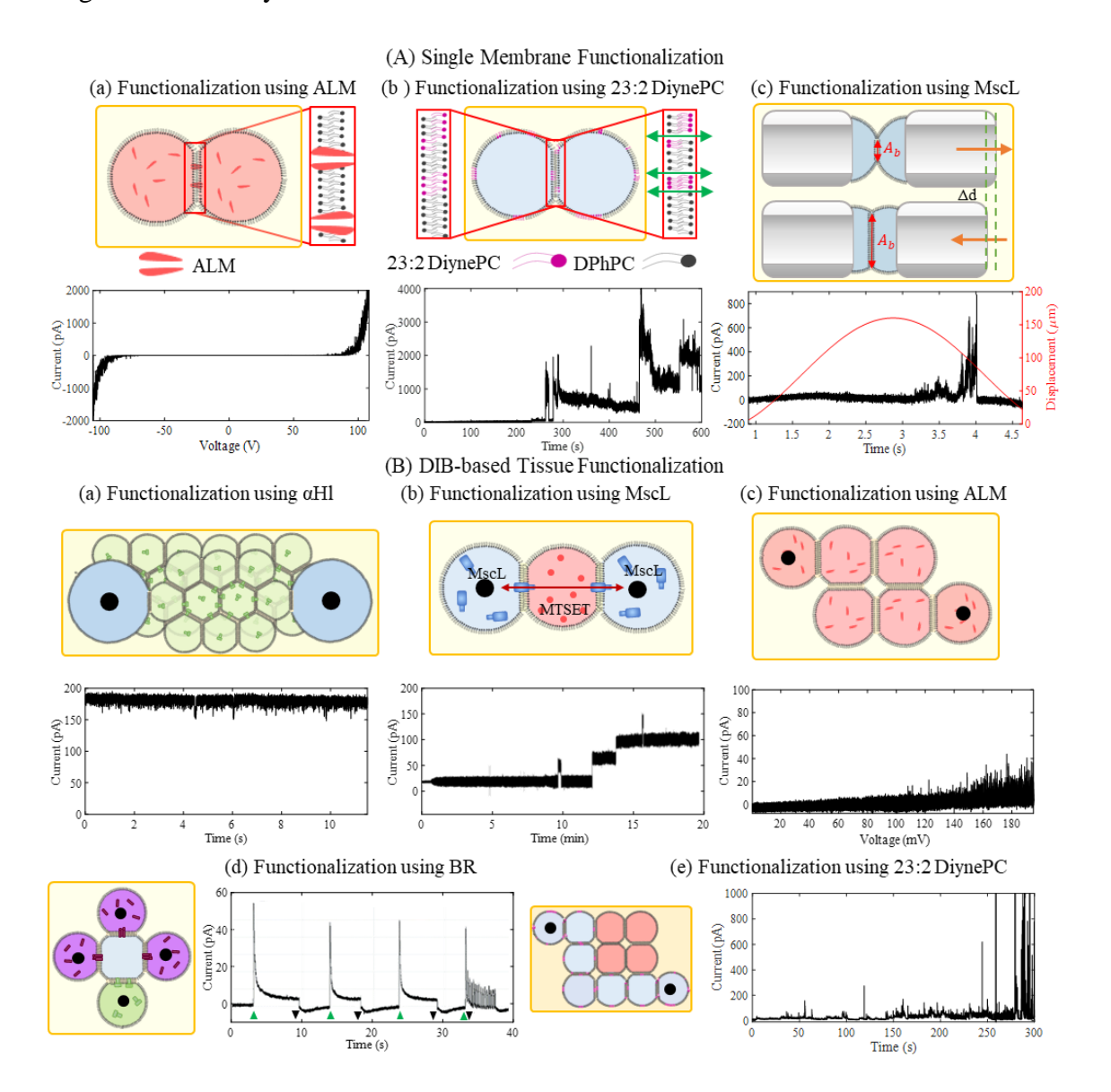


Figure 2.6- Various methods for functionalizing DIB materials presented as changes in membrane conductivity. (A) (a) Alamethicin peptides exhibit a characteristic nonlinear conductivity. Adapted with permission from ref (91). Copyright 2019 ASME. (b) Photopolymerizable lipids can be cross-linked using UVC light forming transmembrane defects. Adapted with permission from ref (18). Copyright 2019 Royal Society of Chemistry. (c) V23T MscL can be activated in single DIBs by droplet compression. (B)

(a) αHL can be used to establish exchange within a DIB tissue. Adapted with permission from ref (28). Copyright 2018 Scientific Reports, Nature. (b) MscL activity has been observed in networks of droplet interface bilayers (MTSET in the middle droplet). Adapted with permission from ref (96). Copyright 2020 Nature. (c) In large DIB networks, Alamethicin still requires transmembrane voltages of 70 mV. Adapted with permission from ref (28). Copyright 2018 Scientific Reports, Nature. (d) DIB networks can be rendered sensitive to green light through bacteriorhodopsin (BR). Adapted with permission from ref (30). Copyright 2007 American Chemical Society. (e) Droplets containing compatible polymerizable lipid profiles produce conductive pathways. Reprinted with permission from ref (18). Copyright 2019 Royal Society of Chemistry.

2.5. Functionalized Droplet Interface Bilayer Materials

Efforts have been directed at enabling DIB-tissues with the ability to sense and react to external triggers. These membranous tissues can be designed to either change their internal chemical composition or their overall droplet architecture (more ambitiously a combination of both) to adapt to external environments. DIB-based materials traditionally have been designed to respond to external stimuli by changing their internal chemical compositions, accomplished via internal diffusion pathways that allow for molecular flow akin to chemical computing [6, 39]. More recent attempts have explored adaptive architectures within DIB tissues, a strategy also inspired by nature where function follows form [86-88]. In the following sections, we will discuss these various methods for enabling DIB functionality.

Changing Internal Chemical Composition

Communication between the droplets is what enables changes in the chemical composition within the tissue and determines the functionality of the network, whether it be signal rectification [31], osmotic actuation [35], detection and sensing [84, 89], or mechanosensing [41, 90, 91]. Communication defined here as molecular transit between compartments is an important condition for modular multi-cellular design of engineered materials, stemming directly from the chemoton requirements of life [10]. In DIB systems, communication is achieved by governing the permeability of the interfacial bilayers in response to external stimuli, functionalizing the tissues and individual membranes. Here, targeted permeability can be achieved either using integral transmembrane channels, lipid packing allowing for the diffusion of different species across the lipid membranes, or some combination of the two.

Inspired by nature, model lipid membranes can be functionalized with integral protein channels and pore forming toxins strategically dispersed within the aqueous compartments and producing communication pathways spanning DIB tissues (Figure 2.6 and Figure 2.2-g). Most intrinsic protein/peptide channels whether single-pass, multi-pass or multi-subunit include residues with hydrophobic side chains that interact with fatty acyl groups of the membrane phospholipids and α helices or multiple β strands spanning the membrane [92]. Standard approaches to characterizing DIB-based materials have involved the use of electrophysiological equipment, which allows the user to prescribe voltages within the droplets which may then be used to detect and measure the activity of transmembrane channels or activate electrically sensitive ones. Typically, the presence of an ohmic current is an indicator of a transmembrane porous activity. Extensively reported

in the literature [13, 15-18, 26-28, 30, 31, 34, 35, 39, 74], alpha-hemolysin (αHL) has been the main channel of choice when establishing communication in membranous DIB networks (Figure 2.6-B-a). One-droplet thick pathways can be created by dispersing αHL in aqueous droplets and used to transport molecules across the structure. This allows for printed conductive pathways within the otherwise high-impedance material. 7R-αHL, a modified form of the pore, provides a diode-like behavior where steady-state conductivity is only enhanced for positive voltages. This was used to successfully demonstrate emergent properties in a 4 droplet cluster through signal rectification [31]. Similarly, DIBs can be functionalized with water-soluble peptides such as Alamethicin [18, 19, 25, 36, 93] producing a voltage-dependent pore activity. Alamethicin is particularly noteworthy as it provides a voltage-dependent conductivity similar to 7R-αHL; however, it requires an input voltage above a threshold for activation as shown in Figure 2.6-A-a and Figure 2.6-B-c. Gramicidin channels across DIBs [18, 71, 94] are formed from the dimerization of monomers from each monolayer leaflet, these pores exhibit a selectivity for small monovalent cations [95, 96] and provide a way of establishing directional communication only between compartments containing the antimicrobial dimer.

More complex membrane proteins can also be used functionalize DIB structures. These are reconstituted into proteoliposomes and added within the aqueous droplet dispersion. The activity of potassium channels (KcsA [71]) and different mechanosensitive channels (Piezo-1[97], MscS [97]and MscL [98-103]) (Figure 2.6-A-c and Figure 2.6-B-b) has been investigated in lipid membranes. Cyclically producing changes in the membrane tensions [100, 104] at lower frequencies [100-103] (through mechanical

distortions to the droplets bordering the membrane) have been successfully used as a strategy to activate V23T-MscL (Figure 2.6-A-c).

In many cases these embedded electrodes are impractical, either due to difficulties in manufacturing, challenges in portability, or difficulty in simultaneously interrogating multiple membranes. A collection of alternative means of establishing internal communication relying on more biologically relevant activation mechanisms has been developed. Active transport applications may be defined as cases which facilitate "uphill" transport against the energetic gradient in these soft materials and establish out-of-equilibrium conditions rather than relying on preset gradients [6, 105]. The most common approach employed in DIB-based materials involves the transduction of light energy into chemical energy through light-sensitive bacteriorhodopsin [30, 89, 106] (Figure 2.6-2-d). This has been used for the creation of artificial eyes and light sensors by patterning the droplets in an appropriate fashion.

Alternatively, the lipid composition of the membrane itself may be tailored to enhance permeability. This is the approach typically taken for liposomal drug delivery, and there are a variety of options to ensure transport across a lipid membrane [107]. Inner-tissue communication can be achieved by utilizing lipid self-assembly (raft formation) and polymerization principles to alter membrane permeability without channels or poreforming toxins. This alternative route for membrane permeabilization occurs through two mechanisms: graded or all-or-none [108, 109]. The all-or-none mechanism typically results from a complete bilayer failure as in the case of membrane fusion during vesicle trafficking or cellular apoptosis [108]. Meanwhile, a graded mechanism permeabilization process typically results either from pore formation/insertion in bilayers [109] or transient

alterations associated with lipid rearrangement and phase boundary defects [107]. The methods selected in DIBs focus more on graded release rather than all-or-none to limit droplet coalescence. Similar methods would be appropriate in polymer-based DIBs, taking advantage of the wealth of research available on stimuli-responsive liposomal/polymersomal drug delivery [110]. Multi-component lipids bilayer mixtures

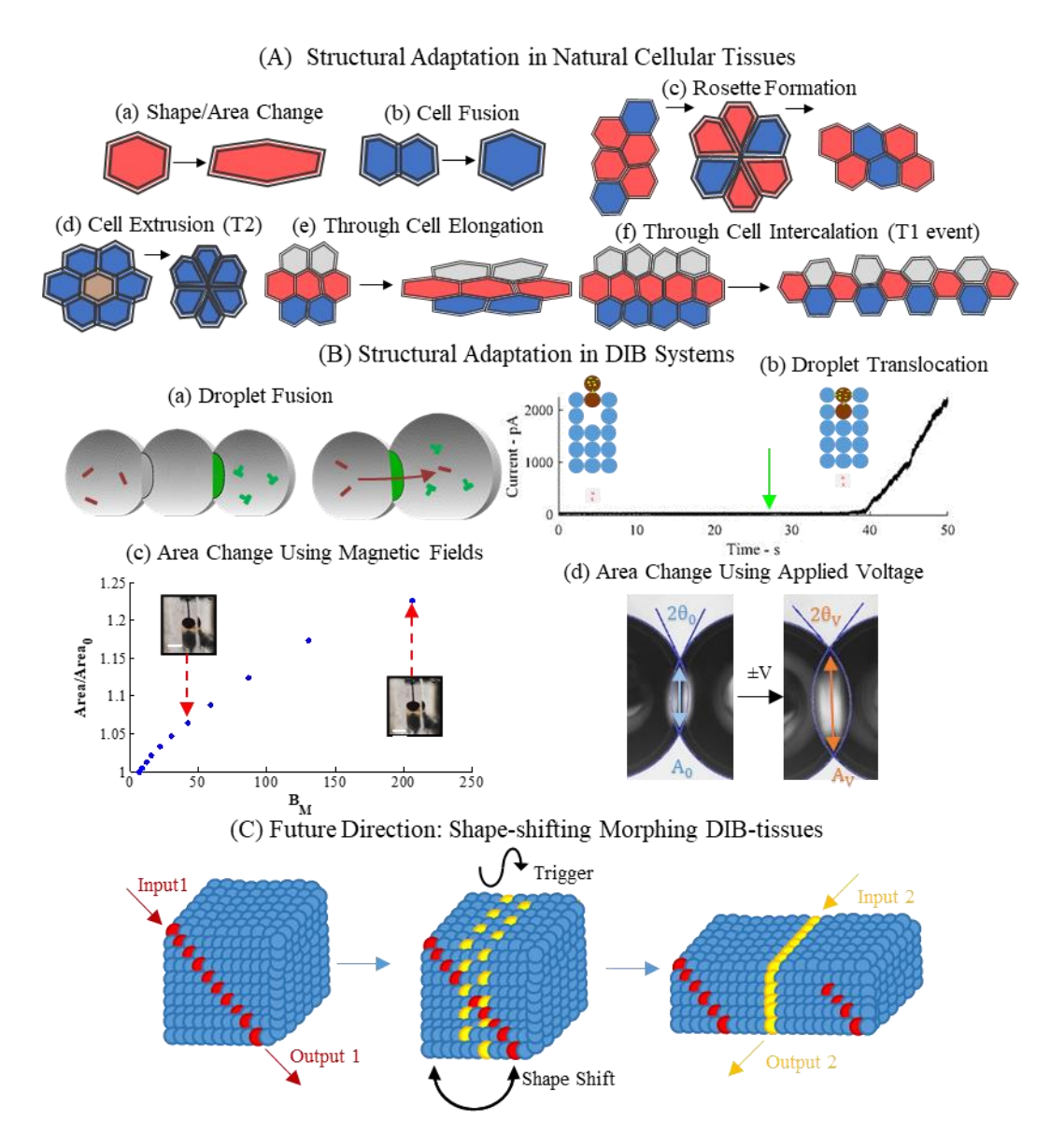


Figure 2.7- Structural adaptation in natural cellular tissues inspires future development of DIB-based tissues. (A) Living tissues possess the ability to rearrange and reconfigure their

cells relative to one another as well as to alter the area/shape of individual cells. Various cellular processes drive adaptation such as (a) shape/area change, (b) cell fusion, (c) rosette formation, and (d) cell extrusion. (B) These processes are being explored within the DIB platform. (a) Droplet fusion has been triggered through the application of a high transmembrane voltage, enabling rapid mixing of droplet contents. Reprinted with permission from ref (24). Copyright 2018 AIP Biomicrofluidics. The incorporation of biocompatible ferrofluids within the platform has allowed for a contact-free manipulation of stable DIB networks for the establishment of new communicative pathways shown in part b or the control of the membrane and droplet shape/area. Part b is reprinted with permission from ref (71). Copyright 2017 ASME. Part c is reprinted with permission from ref (15). Copyright 2018 American Chemical Society. Alternatively, electrical currents can be also employed to influence the droplets' and membranes' size through wetting/dewetting. Adapted with permission from ref (22). Copyright 2019 Royal Society Interface. (C) Future work on adaptive DIB structures will emphasize coupling changes in membrane permeability with changes in relative droplet positioning, producing networks of droplets that swap between communication modes enabled by external forces.

show a potential for triggered disruption of lipid packing leading to a graded permeability mechanism that operates in a similar way to pore forming proteins (PFPs) or toxins (PFTs). The incorporation of photopolymerizable lipids in the DIB platform is relatively recent [32] despite their presence in liposome-based drug-delivery applications [107, 111, 112] for decades [111, 113]. Our approach to this idea demonstrated that cross-membrane transmission with these light-sensitive lipids is shown to occur only in bilayers that

incorporate polymerizable lipids within both leaflets, necessitating compatible lipid profiles combined with exposure to appropriate wavelength UV-light [18] (Figure 2.6-A-b and Figure 2.6-B-e). This produces exchange within the tissue dependent on the properties of the adhered droplet pairs [18, 93].

A rapidly developing area is the integration of living cells and artificial cells by encapsulating cellular machinery or whole living cells within the droplets. The use of cell-free machinery for the production of α HL enables the initiation of communication between droplets through biological mechanisms and gene circuitry [39]. Encapsulating living cells within the membranous architecture and observing their collective response was just recently demonstrated as well [38]. The integration of living and artificial cellular systems is an emerging field [6, 114] that provides exciting new alternatives for these membrane-based materials.

Shape Shifting

DIB tissues are often employed as static structures and the structural layout of these tissues is confined to the initial selected pattern. Thus, each printed tissue provides a singular formulation and functionality. While such membranous tissues offer opportunities for the study of tissue mechanics and fundamental scientific processes in biological interfaces and self-assembly, their static nature poses limitation when exploring potential applications where adaptability is required. More robust functionalities such as chemical microrobots for example would require more dynamic structures where the material functionality may be altered as needed.

Inspired by natural instances such as the capability for bone tissues response to chronic and occasional mechanical stresses for example [86-88] through changes in the cell

shape (Figure 2.7-A-a), DIB-materials can be functionalized to respond to external stimuli through structural adaptations either at the single droplet level or at the entire tissue level. Again, a unique property of DIB materials relative to living tissues is that the membranes determining droplet-droplet exchanges are formed between droplet pairs. Therefore, the properties of the membranes are in part determined by the qualities of the individual droplets, including the membrane structure [18, 65] and gradients across the membrane generated by droplet compositions [35, 115]. Consequently, changes in the overall shape of the droplets/entire structure will also affect transport properties within the synthetic tissue. This is particularly relevant for cases where transport is only enabled with either matching or asymmetric lipid compositions [18, 53].

Transmembrane voltages provided through external electrodes may be used to drive electrowetting (Figure 2.7-B-d), altering the membrane areas through electrical signals and providing a form of single-interface shape change. As noted previously, the relative dimensions of the monolayer and bilayers are a function of their minimized interfacial energies, with membrane dimensions dependent on the energy of adhesion. If transmembrane voltages are supplied, this produces an apparent reduction in the bilayer tensions through electrowetting [20-22, 116] which in turn produces a temporary increase in the membrane area between the droplets. Recent research has proposed using the inherent asymmetry in wetting/dewetting rates [41, 117] in DIBs to produce a form of neuromorphic materials as well, utilizing the DIB membranes as memcapacitors [118]. Membrane-based memory is obtained by applying a variable transmembrane potential and observing the transient wetting behaviors of the droplets. These phenomena allow for the

membrane dimensions to gradually adapt to repeated pulses of voltages, approximating short-term synaptic activity.

Another instance mostly unique to DIBs is the ability to trigger the material structural response by mechanically perturbing certain constitutive droplets, exploiting the fact that DIB tissues are deformable given the innate weak elasticity of the adhered droplets [56, 57]. Distorting the droplets produces transient changes in the membrane tensions [100, 104] as well as changes in the membrane dimensions [40, 60]; consequently, mechanical force may be used to either modulate membrane activities or produce changes in the structure of the adhered droplets. Traditionally, such functionalization at the individual membranes level typically involves direct contact with the droplets comprising the DIB, either electrodes attached to micromanipulators [49, 59, 79] or deformable flexible substrates [79] or even magnetic fields [15] (Figure 2.7-B-c). These approaches offer dynamic control over the DIB membrane dimensions. Our recent research highlights the ability of interfacial bilayers to generate capacitive currents (akin to a Kelvin probe) when subjected to periodic deformations [41, 42, 91, 119, 120]. Periodic droplet distortion in a high-frequency regime generates flexoelectric currents through membrane distortion [41, 42]. This flexoelectricity has been used as a basis for enabling DIB structures with sensing abilities particularly vibration detection and detection of nearby air flow using single membrane DIBs [90, 91, 120] as well as larger membrane networks [41, 119].

While direct manipulation of two adhered droplets to generate a desired response within the membrane is readily achievable using manual micromanipulators, direct mechanical contact with each droplet is impractical in high membrane-density cases. To rectify this, microfluidic methods for droplet manipulation may be used as an alternative.

Many of these techniques have been applied towards the creation of droplet structures as discussed previously; here we discuss their use in promoting changes in the membranous structure.

One proposed contact free microfluidic method for accomplishing changes/deformations in the shape of the material without moving individual cells is through osmotic flux. Naturally, tissues have the ability to deviate from their initial shape through swelling/deswelling without having to shift/move individual cells. Preset concentration gradients drive water exchange between the droplets, causing swelling and shrinking phenomena. This was used to great effect when printing self-folding droplet patterns [35], converting preset ionic concentration gradients between the droplets into changes in shape.

However, living tissues also exhibit the ability to rearrange the relative positions of their individual cells to adapt to external environments. Reproducing these events within DIBs is being explored by our group, taking cues from reconfiguration observed in living tissues. These events most notably occur during early stages of embryonic development (including cell shape change in Figure 2.7-A-a, cell fusion in Figure 2.7-B-b, rosette formation in Figure 2.7-A-c, tissue elongation through either elongation in Figure 2.7-A-e or intercalation in Figure 2.7-A-f, and non-apoptotic extrusion [46] in Figure 2.7-A-d).

Cell fusion (Figure 2.7-A-b) has been emulated in DIBs previously through targeted droplet fusion (Figure 2.7-B-a), allowing for the mixing of their contents and adjustment of the membranous structure [24, 45]. Reconfiguration without requiring coalescence was recently investigated by our laboratory, applying forces on the adhered droplets to shift then between metastable states and change their connected neighbors and organization [40,

72, 73]. Hybrid membranous tissues containing both aqueous and ferrofluid (magnetic sensitive) droplets were generated and adhered together. Strategically applying external magnetic force fields yielded rearrangement events in the membranes neighboring magnetic micro-droplets marked by the separation of interfacial bilayers followed by the formation of new ones (a simple preliminary example of this was demonstrated in Figure 2.7-B-b through magnetically induced droplet translocation). Magnetic compartments shift and reach new equilibrium situations, adjusting the underlying internal structure of the overall tissue (Figure 2.7-B-b). This may be used to adjust the composition of the membranes within the DIB, altering the exchange of information [18, 53]. DIB tissues with the ability to adapt to external environment (an essential component of Ganti's postulated chemoton and of the hallmarks of life) can be used and built on in the further development of smart tissues where internal structure dictates functionality. The function of such tissues can be directly controlled by triggering changes in their structures.

2.6. Conclusion And Future Prospects

Droplet-based materials offer a robust model platform for recreating simple cellular phenomena associated with exchange across their membranous barriers. In this review, we have explored recent advances in the construction, manipulation, and functionalization of these materials and how the selected components shape the overall properties and stability of the resulting tissue. Next, we summarized how these materials may be used and improved, highlighting how their unique physics allow for new applications that combine synthetic and living systems and exploit their unique emulsive elasticity for adaptability.

There are still many challenges facing these materials. They are delicate and relatively simplistic when compared to living cellular systems. Ongoing research attempts

to address each of these shortcomings, including new encapsulation techniques for prolonging durability, new surfactants that provide more stable membranes, and incorporation of living and artificial elements within the same DIB tissue. Each of these fields has rapidly expanded in recent years, prompted by a more thorough understanding of the underlying emulsive mechanics responsible for DIB characteristics.

While admirable research has been performed shifting these droplet-based materials towards more biomimetic designs, we must still recognize that the best path forward should interweave the natural and synthetic aspects, opting to take advantage of the non-biological roots of the platform to augment cellular functionalities. Based on the summarized material presented here, we propose that future directions in the development of optimized DIB-tissues should implement both functionalization strategies for the material, combining shape changes with changes in membrane permeability. Ideally, DIB-materials should be designed to adapt their droplet structure in response to supplied external forces, leading to evolutions in droplet composition through diffusion across newly formed pathways. In these applications, the form of DIB-based materials would dictate their function and the emulsive foundation of DIBs provide a metastable, dynamic form. Linking membrane permeability to relative droplet positioning and reliably generating reconfiguration events within the tissue will provide new functionalities for the material concept (Figure 2.7-C).

Our research group has been investigating strategies that enable DIB materials with the ability to respond to external force fields, self-support in an organogel matrix and establish communication between neighboring droplet compartments is governed by matching droplet compositions. It is believed that this platform could have additional applications in compartmentalized chemistry, membrane particle interactions studies, chemical microrobots specializing in biocompatible precise actuation and high-throughput membrane screening once these envisioned advances are completed.

2.7. References

- 1. Urban, P.L., Compartmentalized chemistry: from studies on the origin of life to engineered biochemical systems. New Journal of Chemistry, 2014. 38(11): p. 5135-5141.
- 2. Jones, G., et al., Autonomous droplet architectures. Artificial life, 2015. 21(2): p. 195-204.
- 3. Fu, F., et al., Bioinspired living structural color hydrogels. Science Robotics, 2018. 3(16): p. eaar8580.
- 4. Yu, Y., et al., Microfluidic Generation of Microsprings with Ionic Liquid Encapsulation for Flexible Electronics. Research 2019: p. 6906275.
- 5. Zhang, Z.H., et al., Bioinspired conductive cellulose liquid-crystal hydrogels as multifunctional electrical skins. Proceedings of the National Academy of Sciences of the United States of America, 2020. 117(31): p. 18310-18316.
- 6. Aufinger, L. and F.C. Simmel, Establishing Communication Between Artificial Cells. Chemistry-a European Journal, 2019. 25(55): p. 12659-12670.
- 7. Stojanovic, M.N., D. Stefanovic, and S. Rudchenko, Exercises in molecular computing. Accounts of Chemical Research, 2014. 47(6): p. 1845-52.
- 8. Gopfrich, K., I. Platzman, and J.P. Spatz, Mastering Complexity: Towards Bottom-up Construction of Multifunctional Eukaryotic Synthetic Cells. Trends in Biotechnology, 2018. 36(9): p. 938-951.

- 9. Collier, J.H., et al., Multi-component extracellular matrices based on peptide self-assembly. Chemical Society Reviews, 2010. 39(9): p. 3413-24.
- 10. Gánti, T., Introduction, in Chemoton theory: theoretical foundations of fluid machineries, P.G. Mezey, Editor. 2003, Kluwer Academic/Plenum Publishers. p. 1-8.
- 11. Bibette, J., F.L. Calderon, and P. Poulin, Emulsions: basic principles. Reports on Progress in Physics, 1999. 62(6): p. 969.
- 12. Funakoshi, K., H. Suzuki, and S. Takeuchi, Lipid bilayer formation by contacting monolayers in a microfluidic device for membrane protein analysis. Analytical chemistry, 2006. 78(24): p. 8169-8174.
- 13. Bayley, H., et al., Droplet interface bilayers. Molecular BioSystems, 2008. 4(12): p. 1191-208.
- 14. Stephen, A.S. and J.L. Donald, Membrane-based biomolecular smart materials. Smart Materials and Structures, 2011. 20(9): p. 094018.
- 15. Makhoul-Mansour, M., et al., Ferrofluid-Based Droplet Interface Bilayer Networks. Langmuir, 2017. 33(45): p. 13000-13007.
- 16. Hwang, W.L., et al., Electrical Behavior of Droplet Interface Bilayer Networks: Experimental Analysis and Modeling. Journal of the American Chemical Society, 2007. 129(38): p. 11854-11864.
- 17. Hwang, W.L., et al., Asymmetric droplet interface bilayers. Journal of the American Chemical Society, 2008. 130(18): p. 5878-5879.
- 18. Makhoul-Mansour, M.M., et al., Photopolymerized microdomains in both lipid leaflets establish diffusive transport pathways across biomimetic membranes. Soft Matter, 2019. 15(43): p. 8718-8727.

- 19. Taylor, G.J. and S.A. Sarles, Heating-enabled formation of droplet interface bilayers using Escherichia coli total lipid extract. Langmuir, 2015. 31(1): p. 325-37.
- 20. Taylor, G.J., et al., Direct in situ measurement of specific capacitance, monolayer tension, and bilayer tension in a droplet interface bilayer. Soft Matter, 2015. 11(38): p. 7592-605.
- 21. Tamaddoni, N., et al., Reversible, voltage-activated formation of biomimetic membranes between triblock copolymer-coated aqueous droplets in good solvents. Soft Matter, 2016. 12(23): p. 5096-109.
- 22. El-Beyrouthy, J., et al., A new approach for investigating the response of lipid membranes to electrocompression by coupling droplet mechanics and membrane biophysics. Journal of the Royal Society Interface, 2019. 16(161): p. 20190652.
- 23. Venkatesan, G.A., et al., Adsorption Kinetics Dictate Monolayer Self-Assembly for Both Lipid-In and Lipid-Out Approaches to Droplet Interface Bilayer Formation. ACS-Langmuir, 2015. 31(47): p. 12883-12893.
- 24. Challita, E.J., M.M. Makhoul-Mansour, and E.C. Freeman, Reconfiguring droplet interface bilayer networks through sacrificial membranes. Biomicrofluidics, 2018. 12(3): p. 034112.
- 25. Nguyen, M.-A., et al., Hydrodynamic trapping for rapid assembly and in situ electrical characterization of droplet interface bilayer arrays. Lab on a Chip, 2016. 16(18): p. 3576-3588.
- 26. Wauer, T., et al., Construction and manipulation of functional three-dimensional droplet networks. ACS Nano, 2014. 8(1): p. 771-9.

- 27. Ma, S., et al., Gel Microrods for 3D Tissue Printing. Advanced Biosystems, 2017. 1(8): p. e1700075.
- 28. Challita, E.J., et al., Encapsulating Networks of Droplet Interface Bilayers in a Thermoreversible Organogel. Scientific reports, 2018. 8(1): p. 6494-6505.
- 29. Freeman, E.C., et al., Multiscale modeling of droplet interface bilayer membrane networks. Biomicrofluidics, 2015. 9(6): p. 064101.
- 30. Holden, M.A., D. Needham, and H. Bayley, Functional bionetworks from nanoliter water droplets. Journal of the American Chemical Society, 2007. 129(27): p. 8650-8655.
- 31. Maglia, G., et al., Droplet networks with incorporated protein diodes show collective properties. Nature Nanotechnology, 2009. 4: p. 437-440.
- 32. Punnamaraju, S., H. You, and A. Steckl, Triggered release of molecules across droplet interface bilayer lipid membranes using photopolymerizable lipids. Langmuir, 2012. 28(20): p. 7657-7664.
- 33. Booth, M.J., et al., Light-activated communication in synthetic tissues. Sci Adv, 2016. 2(4): p. e1600056.
- 34. Booth, M.J., et al., Droplet Networks, from Lipid Bilayers to Synthetic Tissues, in Encyclopedia of Biophysics, G. Roberts and A. Watts, Editors. 2019, Springer Berlin Heidelberg: Berlin, Heidelberg. p. 1-13.
- 35. Villar, G., A.D. Graham, and H. Bayley, A tissue-like printed material. Science, 2013. 340(6128): p. 48-52.
- 36. Sarles, S.A. and D.J. Leo, Physical encapsulation of droplet interface bilayers for durable, portable biomolecular networks. Lab on a Chip, 2010. 10(6): p. 710-7.

- 37. Alcinesio, A., et al., Controlled packing and single-droplet resolution of 3D-printed functional synthetic tissues. Nature Communications, 2020. 11(1): p. 2105.
- 38. Zhou, L., et al., Lipid-Bilayer-Supported 3D Printing of Human Cerebral Cortex Cells Reveals Developmental Interactions. Advanced Materials, 2020: p. 2002183.
- 39. Dupin, A. and F.C. Simmel, Signalling and differentiation in emulsion-based multi-compartmentalized in vitro gene circuits. Nature chemistry, 2019. 11(1): p. 32-39.
- 40. Makhoul-Mansour, M.M., et al., Adaptive Compartmentalized Synthetic Tissues with Magnetically- Driven Intercalation Events 2021: Unpublished Work.
- 41. Freeman, E.C., et al., The mechanoelectrical response of droplet interface bilayer membranes. Soft Matter 2016. 12: p. 3021-3031.
- 42. Kancharala, A., E. Freeman, and M. Philen, A comprehensive flexoelectric model for droplet interface bilayers acting as sensors and energy harvesters. Smart Materials and Structures, 2016. 25(10): p. 104007.
- 43. Venkatesan, G.A. and S.A. Sarles, Droplet immobilization within a polymeric organogel improves lipid bilayer durability and portability. Lab on a Chip, 2016. 16(11): p. 2116-2125.
- 44. Kong, L., et al., Chemical polyglycosylation and nanolitre detection enables single-molecule recapitulation of bacterial sugar export. Nature Chemistry, 2016. 8(5): p. 461-9.
- 45. Downs, F.G., et al., Multi-responsive hydrogel structures from patterned droplet networks. Nature Chemistry, 2020. 12(4): p. 363-371.
- 46. Mierke, C.T., Initiation of a neoplasm or tumor, in Physics of Cancer. 2015, IOP Publishing: Bristol, UK. p. 1-54.

- 47. Fan, J., et al., Creation of Faceted Polyhedral Microgels from Compressed Emulsions. Small, 2017. 13(31): p. 1701256.
- 48. Thiam, A.R., N. Bremond, and J. Bibette, From stability to permeability of adhesive emulsion bilayers. Langmuir, 2012. 28(15): p. 6291-8.
- 49. Gross, L.C., et al., Determining membrane capacitance by dynamic control of droplet interface bilayer area. Langmuir, 2011. 27(23): p. 14335-42.
- 50. Princen, H., M. Aronson, and J. Moser, Highly concentrated emulsions. II. Real systems. The effect of film thickness and contact angle on the volume fraction in creamed emulsions. Journal of Colloid and Interface Science, 1980. 75(1): p. 246-270.
- 51. Bergeron, V., J. Martin, and L. Vovelle, Interaction of droplets with a surface: impact and adhesion. Agro Food Industry Hi-Tech, 1999. 10(5): p. 21-23.
- 52. Challita, E.J. and E.C. Freeman, Hydrogel Microelectrodes for the Rapid, Reliable, and Repeatable Characterization of Lipid Membranes. Langmuir, 2018. 34(50): p. 15166-15173.
- 53. Strutt, R., et al., Activating mechanosensitive channels embedded in droplet interface bilayers using membrane asymmetry. Chemical Science, 2021.
- 54. Creasy, M.A., et al., Deterministic model of biomolecular networks with stimuliresponsive properties. Journal of Intelligent Material Systems and Structures, 2014: p. 1045389X14536004.
- 55. Sundaresan, V.B. and D.J. Leo, Modeling and characterization of a chemomechanical actuator using protein transporter. Sensors and Actuators B: Chemical, 2008. 131(2): p. 384-393.

- 56. Lacasse, M.D., G.S. Grest, and D. Levine, Deformation of small compressed droplets. Phys Rev E Stat Phys Plasmas Fluids Relat Interdiscip Topics, 1996. 54(5): p. 5436-5446.
- 57. Morse, D.C. and T.A. Witten, Droplet Elasticity in Weakly Compressed Emulsions. Europhysics Letters, 1993. 22(7): p. 549-555.
- 58. Berthier, J. and K.A. Brakke, The physics of microdroplets. 2012: John Wiley & Sons.
- 59. Syeda, R., et al., Screening blockers against a potassium channel with a droplet interface bilayer array. Journal of the American Chemical Society, 2008. 130(46): p. 15543-8.
- 60. Sarles, S.A. and D.J. Leo, Regulated attachment method for reconstituting lipid bilayers of prescribed size within flexible substrates. Anal Chem, 2010. 82(3): p. 959-66.
- 61. Sarles, S.A., et al., Bilayer formation between lipid-encased hydrogels contained in solid substrates. ACS applied materials & interfaces, 2010. 2(12): p. 3654-3663.
- 62. Carreras, P., et al., A microfluidic platform for size-dependent generation of droplet interface bilayer networks on rails. Biomicrofluidics, 2015. 9(6): p. 064121.
- 63. Czekalska, M.A., et al., Passive and parallel microfluidic formation of droplet interface bilayers (DIBs) for measurement of leakage of small molecules through artificial phospholipid membranes. Sensors and Actuators B-Chemical, 2019. 286: p. 258-265.
- 64. King, P.H., et al., Interdroplet bilayer arrays in millifluidic droplet traps from 3D-printed moulds. Lab on a chip, 2014. 14(4): p. 722-729.

- 65. Taylor, G., et al., Electrophysiological interrogation of asymmetric droplet interface bilayers reveals surface-bound alamethicin induces lipid flip-flop. Biochimia Biophysica Acta- Biomembranes, 2019. 1861(1): p. 335-343.
- 66. Boreyko, J.B., et al., Air-stable droplet interface bilayers on oil-infused surfaces. Proc Natl Acad Sci U S A, 2014. 111(21): p. 7588-93.
- 67. Dixit, S.S., et al., Light-driven formation and rupture of droplet bilayers. Langmuir, 2010. 26(9): p. 6193-6200.
- 68. Bolognesi, G., et al., Sculpting and fusing biomimetic vesicle networks using optical tweezers. Nature Communications, 2018. 9(1): p. 1882.
- 69. Poulos, J.L., et al., Electrowetting on dielectric-based microfluidics for integrated lipid bilayer formation and measurement. Applied Physics Letters, 2009. 95(1): p. 013706.
- 70. Punnamaraju, S. and A.J. Steckl, Voltage control of droplet interface bilayer lipid membrane dimensions. Langmuir, 2011. 27(2): p. 618-26.
- 71. Aghdaei, S., et al., Formation of artificial lipid bilayers using droplet dielectrophoresis. Lab on a Chip, 2008. 8(10): p. 1617-1620.
- 72. Makhoul-Mansour, M., E.J. Challita, and E.C. Freeman. Ferrofluid Droplet Based Micro-Magnetic Sensors and Actuators. in ASME 2017 Conference on Smart Materials, Adaptive Structures and Intelligent Systems. 2017. American Society of Mechanical Engineers.
- 73. Makhoul-Mansour, M., E.J. Challita, and E.C. Freeman, Chain Failure Events in Microfluidics Membrane Networks, in ASME 2016 Conference on Smart Materials, Adaptive Structures and Intelligent Systems SMASIS 2016. 2016 American Society of Mechanical Engineers Digital Collection: Stowe, Vermont, USA. p. 1-9.

- 74. Challita, E.J., et al. A 3D printing method for droplet-based biomolecular materials. in Nanosensors, Biosensors, Info-Tech Sensors and 3D Systems 2017. 2017. International Society for Optics and Photonics.
- 75. Stanley, C.E., et al., A microfluidic approach for high-throughput droplet interface bilayer (DIB) formation. Chemical Communications, 2010. 46(10): p. 1620-2.
- 76. Elani, Y., et al., Novel technologies for the formation of 2-D and 3-D droplet interface bilayer networks. Lab on a Chip, 2012. 12(18): p. 3514-20.
- 77. Sarles, S.A., J.W. Madden, and D.J. Leo, Hair cell inspired mechanotransduction with a gel-supported, artificial lipid membrane. Soft Matter, 2011. 7: p. 4644-4653.
- 78. Sapra, K.T. and H. Bayley, Lipid-coated hydrogel shapes as components of electrical circuits and mechanical devices. Scientific Reports, 2012. 2: p. 848.
- 79. Sarles, S.A. and D.J. Leo, Regulated attachment method for reconstituting lipid bilayers of prescribed size within flexible substrates. Analytical chemistry, 2010. 82(3): p. 959-966.
- 80. Bayoumi, M., et al., Multi-compartment encapsulation of communicating droplets and droplet networks in hydrogel as a model for artificial cells. Sci Rep, 2017. 7: p. 45167.
- 81. Baxani Kamal, D., Hydrogel encapsulated droplet interface bilayer networks as a chassis for artificial cells and a platform for membrane studies, in Cardiff School of Pharmacy and Pharmaceutical Science. 2017, Cardiff University.
- 82. Li, J., et al., Formation of Polarized, Functional Artificial Cells from Compartmentalized Droplet Networks and Nanomaterials, Using One-Step, Dual-Material 3D-Printed Microfluidics. Advanced Science, 2020. 7(1): p. 1901719.

- 83. Elani, Y., et al., Microfluidic generation of encapsulated droplet interface bilayer networks (multisomes) and their use as cell-like reactors. Chemical Communications, 2016. 52(35): p. 5961-4.
- 84. Villar, G., A.J. Heron, and H. Bayley, Formation of droplet networks that function in aqueous environments. Nature nanotechnology, 2011. 6(12): p. 803.
- 85. Elani, Y., R.V. Law, and O. Ces, Protein synthesis in artificial cells: using compartmentalisation for spatial organisation in vesicle bioreactors. Physical Chemistry Chemical Physics, 2015. 17(24): p. 15534-7.
- 86. Watson, P., Function follows form: generation of intracellular signals by cell deformation. The FASEB journal, 1991. 5(7): p. 2013-2019.
- 87. Lanyon, L.E., Functional Strain in Bone Tissue as an Objective, and Controlling Stimulus for Adaptive Bone Remodeling. Journal of Biomechanics, 1987. 20(11-12): p. 1083-1089.
- 88. Maree, A.F.M., V.A. Grieneisen, and L. Edelstein-Keshet, How Cells Integrate Complex Stimuli: The Effect of Feedback from Phosphoinositides and Cell Shape on Cell Polarization and Motility. PLOS Computational Biology, 2012. 8(3): p. e1002402.
- 89. Schild, V.R., et al., Light-Patterned Current Generation in a Droplet Bilayer Array. Scientific Reports, 2017. 7.
- 90. Sarlo, R., J.S. Najem, and D.J. Leo, Flow field sensing with bio-inspired artificial hair cell arrays. Sensors and Actuators B-Chemical, 2016. 236: p. 805-814.
- 91. Tamaddoni, N., E.C. Freeman, and S.A. Sarles, Sensitivity and directionality of lipid bilayer mechanotransduction studied using a revised, highly durable membrane-based hair cell sensor. Smart Materials and Structures, 2015. 24(6): p. 065014.

- 92. Lodish, H., et al., Protein Structure and Function, in Molecular Cell Biology. 2008,W.H. Freeman and Company: New York, USA. p. 65-110.
- 93. Makhoul-Mansour, M.M. and E.C. Freeman, Photo-Triggered Soft Materials With Differentiated Diffusive Pathways, in ASME 2019 Conference on Smart Materials, Adaptive Structures and Intelligent Systems. 2019, American Society of Mechanical Engineers Digital Collection: Louisville, Kentucky, USA. p. 1-9.
- 94. Koner, S., et al., Memristive plasticity in artificial electrical synapses via geometrically reconfigurable, gramicidin-doped biomembranes. Nanoscale, 2019. 11(40): p. 18640-18652.
- 95. Andersen, O., Ion movement through gramicidin A channels. Single-channel measurements at very high potentials. Biophysical journal, 1983. 41(2): p. 119-133.
- 96. O'Connell, A.M., R.E. Koeppe, and O.S. Andersen, Kinetics of gramicidin channel formation in lipid bilayers: transmembrane monomer association. Science, 1990. 250(4985): p. 1256-1259.
- 97. Syeda, R., et al., Piezo1 channels are inherently mechanosensitive. Cell reports, 2016. 17(7): p. 1739-1746.
- 98. Haylock, S., et al., Membrane protein mediated bilayer communication in networks of droplet interface bilayers. Communications Chemistry, 2020. 3(1): p. 1-8.
- 99. Makhoul Mansour, M.M., et al., A skin-inspired soft material with directional mechanosensation. Bioinspiration & Biomimetics, 2021.
- 100. Najem, J.S., et al., Activation of bacterial channel MscL in mechanically stimulated droplet interface bilayers. Sci Rep, 2015. 5: p. 13726.

- 101. Najem, J.S., et al., Mechanics of Droplet Interface Bilayer "Unzipping" Defines the Bandwidth for the Mechanotransduction Response of Reconstituted MscL. Advanced Materials Interfaces, 2016.
- 102. Rosholm, K.R., et al., Activation of the mechanosensitive ion channel MscL by mechanical stimulation of supported Droplet-Hydrogel bilayers. Sci Rep, 2017. 7: p. 45180.
- 103. Jorjadze, I., et al., Attractive emulsion droplets probe the phase diagram of jammed granular matter. Proceedings of the National Academy of Sciences, 2011. 108(11): p. 4286-4291.
- 104. Yasmann, A. and S. Sukharev, Properties of diphytanoyl phospholipids at the airwater interface. Langmuir, 2014.
- 105. Findlay, H.E., N.J. Harris, and P.J. Booth, In vitro synthesis of a Major Facilitator Transporter for specific active transport across Droplet Interface Bilayers. Scientific Reports, 2016. 6: p. 39349.
- 106. Booth, M., et al., Functional aqueous droplet networks. Molecular BioSystems, 2017.
- 107. Yavlovich, A., et al., Design of liposomes containing photopolymerizable phospholipids for triggered release of contents. Journal of thermal analysis and calorimetry, 2009. 98(1): p. 97-104.
- 108. Apellániz, B., et al., All-or-none versus graded: single-vesicle analysis reveals lipid composition effects on membrane permeabilization. Biophysical journal, 2010. 99(11): p. 3619-3628.

- 109. Sine, J., et al., Photo activation of HPPH encapsulated in "Pocket" liposomes triggers multiple drug release and tumor cell killing in mouse breast cancer xenografts. International journal of nanomedicine, 2015. 10: p. 125.
- 110. Meng, F., Z. Zhong, and J. Feijen, Stimuli-responsive polymersomes for programmed drug delivery. Biomacromolecules, 2009. 10(2): p. 197-209.
- 111. Freeman, F.J., J.A. Hayard, and D. Chapman, Liposomes formed from polymerizable diacetylenic phospholipids and their potential as drug delivery systems. Biochemical Society Transactions, 1987. 15.
- 112. Yavlovich, A., et al., Light-sensitive lipid-based nanoparticles for drug delivery: design principles and future considerations for biological applications. Molecular membrane biology, 2010. 27(7): p. 364-381.
- 113. Georger, J.H., et al., Helical and tubular microstructures formed by polymerizable phosphatidylcholines. Journal of the American Chemical Society, 1987. 109(20): p. 6169-6175.
- 114. Elani, Y., Interfacing Living and Synthetic Cells as an Emerging Frontier in Synthetic Biology. Angewandte Chemie-International Edition, 2020.
- 115. Xu, J., F.J. Sigworth, and D.A. LaVan, Synthetic protocells to mimic and test cell function. Adv Mater, 2010. 22(1): p. 120-7.
- 116. Rofeh, J. and L. Theogarajan, Instantaneous tension measurements in droplet interface bilayers using an inexpensive, integrated pendant drop camera. Soft Matter, 2020.
- 117. Li, Y.-J., et al., Non-linearity and dynamics of low-voltage electrowetting and dewetting. Physical Chemistry Chemical Physics, 2019. 21(33): p. 18290-18299.

- 118. Najem, J.S., et al., Dynamical nonlinear memory capacitance in biomimetic membranes. Nature communications, 2019. 10(1): p. 1-11.
- 119. Tamaddoni, N. and S.A. Sarles, Toward cell-inspired materials that feel: measurements and modeling of mechanotransduction in droplet-based, multi-membrane arrays. Bioinspiration & biomimetics, 2016. 11(3): p. 036008.
- 120. Sarles, S.A., J.D.W. Madden, and D.J. Leo, Hair cell inspired mechanotransduction with a gel-supported, artificial lipid membrane. Soft Matter, 2011. 7(10): p. 4644-4653.

CHAPTER 3

FERROFLUID-BASED DROPLET INTERFACE BILAYER NETWORKS²

 $^{^2}$ M. Makhoul-Mansour, W. Zhao, N. Gay, C. O'Connor, J. S. Najem, L. Mao, E. C. Freeman, ${\it Langmuir}$ **2017**, 33, 13000.

Reprinted with permission of the publisher.

3.1. Abstract

Droplet interface bilayer (DIB) networks allow for the construction of stimuliresponsive, membrane-based materials. Traditionally used for studying cellular transport phenomena, the DIB technique has proven its practicality when creating structured droplet networks. These structures consist of aqueous compartments capable of exchanging their contents across membranous barriers in a regulated fashion via embedded biomolecules, thus approximating the activity of natural cellular systems. However, lipid bilayer networks are often static and incapable of any reconfiguration in their architecture. In this study, we investigate the incorporation of a magnetic fluid or ferrofluid within the droplet phases for the creation of magnetically responsive DIB arrays. The impact of adding ferrofluid to the aqueous phases of the DIB networks is assessed by examining the bilayers' interfacial tensions, thickness, and channel activity. Once compatibility is established, potential applications of the ferrofluid-enabled DIBs are showcased by remotely modifying membrane qualities through magnetic fields. Ferrofluids do not significantly alter the bilayers' properties or functionality and can therefore be safely embedded within the DIB platform, allowing for remote manipulation of the interfacial bilayer properties.

3.2. Introduction

The droplet interface bilayer (DIB) technique has been used for studying membrane transport [1-5] and electrical interrogation of biological membranes [2, 6-11]. This platform involves the assembly of model cellular membranes between nanoliter aqueous droplets in an oil environment with lipids dissolved in either phase [2, 12, 13]. As the droplets are introduced into the oil reservoir, lipid molecules self-assemble in ordered monolayers on the surface of the aqueous droplets [14, 15]. When two lipid-coated droplets

are brought into contact, a bilayer lipid membrane forms at their interface as shown in Figure 3.1. While a single DIB may be useful for characterizing the properties of the lipid bilayer and the activity of embedded biomolecules, a prominent advantage of the DIB technique lies in its scalability: multiple droplets may be linked together forming a web of interconnected membranes [6, 16-20], deriving inspiration from the emergent properties of cellular organisms. Current advanced applications of the DIB platform trend towards the tissue-scale, creating vast interconnected droplet structures [17, 21, 22]. These applications have explored the possibility of using bilayer networks with embedded transporters for purposes such as the fabrication of a micro-sized half-wave rectifiers [6] or for the evaluation of the collective behavior of lipid bilayers upon the introduction of a pore-inducing peptide [20].

These membrane networks are mechanically responsive. Their adhered interfaces are governed by the balance of surface tensions at the point of contact [23] (as shown in Figure 3.1.b). The corresponding membrane properties may then be modified by applying mechanical forces or constraints to the droplets [8], forcing them to adapt a new equilibrium configuration [24, 25]. Nevertheless, direct manipulation requires a mechanical path to the droplets of interest – it is not feasible to manipulate droplets at the center of a cluster through traditional methods without jeopardizing the structural integrity of the whole. Thus, a contact-free methodology for manipulating selected droplets within the structures is necessary.

Remote actuation of droplets may be achieved through many different techniques: electrowetting [26], wetting gradient [27], thermal gradient [28], vibrations [29], dielectrophoresis [26, 30, 31], and magnetophoresis [32, 33]. Out of these options,

electrowetting and dielectrophoresis have been successfully combined with the DIB technique [30, 31]. However, as the volume fraction of the droplets increases these techniques become less appealing as all aqueous droplets will respond in a similar fashion to the external field. To counter this, the droplets must be selectively imbued with sensitivity to the manipulation mechanisms.

Magnetophoresis provides an optimal combination of flexibility and selectivity, may be achieved with simple magnets, and does not require specialized electrodes or substrates. Most organic materials exhibit negligible variations in magnetic susceptibility [34, 35], and consequently only droplets imbued with a magnetic susceptibility within a DIB network will perceptibly respond to an externally supplied magnetic field. Earlier works have demonstrated the potential uses of magnetic manipulation within the DIB technique by incorporating magnetic beads within the droplets [16] and using permanent magnets to guide the construction of 3D droplet networks. Unfortunately, these beads behave as a solid contained within the droplets, posing limitations to the incorporation of these magnetically imbued droplets within microfluidic chips or larger DIB structures. Such limitations may be circumvented through the use of magnetic fluids or ferrofluids. Ferrofluids consist of stable colloidal suspensions of magnetic nanoparticles (such as maghemite Fe₂O₃ or magnetite Fe₃O₄) coated with a suitable surfactant and dispersed within a carrier fluid. The size of the nanoparticles used in ferrofluids is small enough to cause these materials to behave as macroscopically continuous liquids. When applying an external magnetic field, the dispersed nanoparticles within the carrier fluid align themselves with the field producing a magnetic response. Once the external field is

removed Brownian motion rapidly scatters the nanoparticle orientation, eliminating any permanent magnetization and rendering the fluid superparamagnetic.

Contact-free manipulation and assembly of the droplet networks can be achieved by incorporating ferrofluids within the DIB platform. However, there is a risk of competition between the nanoparticles, stabilizing surfactants, and lipids at the oil-water interfaces. In this work, the qualities of DIBs are assessed to ensure that the lipid membrane functionality is retained as ferrofluids are introduced. This is achieved by measuring lipid bilayer's specific capacitance, tension, thickness, and energy of adhesion, then comparing the values for DIBs that have been formed with and without the use of ferrofluids. Next, the response of these membranes to the presence of a pore-forming toxin such as alphahemolysin is assessed. Finally, magnetic control of membrane dimensions is showcased as a proof-of-concept for remote manipulation of the DIB structures.

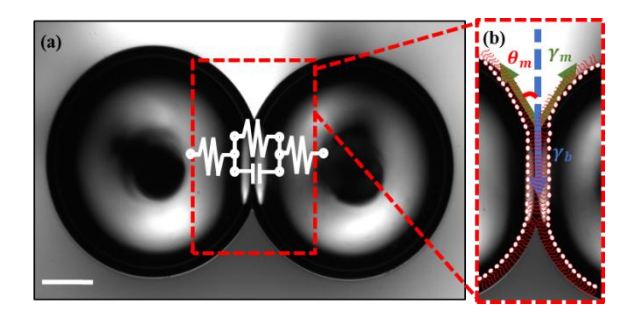


Figure 3.1- The Droplet Interface Bilayer (DIB) technique. (a) When two nanoliter lipid-coated aqueous droplets are brought together a lipid bilayer membrane is spontaneously formed at the intersection (Bar represents 200 µm). This bilayer can be electrically modeled as a capacitor in parallel with a high amplitude resistor. (b) The interfacial tension of the formed bilayer is balanced with the two opposing monolayer tensions at the interfacial area.

3.3. Materials

Lipid-in-Oil Solutions

The lipid-out method for DIB formation is used in this work, where lipids are dissolved in the oil phase. Zwitterionic lipids (1,2-diphytanoyl-sn-glycero-3-phosphocholine (DPhPC), Avanti Polar Lipids, Alabaster, AL) were suspended in a 1:1 (volume: volume) mixture of Hexadecane and Silicone Oil AR20 (both Sigma-Aldrich, St. Louis, MO) at a concentration of 0.5 mg/ml unless stated otherwise. All lipid solutions were sonicated for 80 minutes (Avanti Sonicator, Avanti Polar Lipids, Alabaster, AL) and afterwards stored at 2 °C.

Ferrofluid Solutions

Synthesis and Characterization of Ferrofluids

Ammonium hydroxide solution (28%), iron (II) chloride tetrahydrate (99%), iron (III) chloride hexahydrate (97%), nitric acid (70%), iron (III) nitrate nonahydrate (98%), and sodium hydroxide (98%) (all purchased from Sigma-Aldrich, St. Louis, MO) were used as received from the vendor. Maghemite nanoparticles were produced using a chemical co-precipitation method [36]. Typically, 50 mL of ammonium hydroxide solution was added into a mixture of 100 mL of 0.4 M iron (II) chloride tetrahydrate and 0.8 M iron (III) chloride hexahydrate, then stirred at room temperature for 30 minutes. The suspension was centrifuged at 2000×g for 3 minutes, and the obtained precipitate was dispersed in 200 mL of 2 M nitric acid and 0.35 M iron (III) nitrate nonahydrate and kept at 90 °C for 1 hour. During this time, the color of the mixture changed from black (Fe₃O₄) to reddish brown (Fe₂O₃). The maghemite nanoparticle suspension was further centrifuged at 3000×g for 3 minutes and finally dispersed in 120 mL of deionized (DI) water, resulting in a stable

dispersion with a pH of 1.5-2. 40 mL of Atlox 4913 (Croda, Edison, NJ), a graft copolymer solution, was added to the dispersion before raising pH to 7.0. The dispersion was then stirred for 1 hour, and the resulting ferrofluid was dialyzed (using a dialysis membrane purchased from Spectrum Labs, Rancho Dominguez, CA) against DI water (refreshed every 24 hours) for one week. Excess water was vaporized afterwards at 72 °C. Morphology and size of nanoparticles were characterized via transmission electron microscopy (TEM; FEI, Eindhoven, the Netherlands). Using a vibrating sample magnetometer (VSM; MicroSense, Lowell, MA) with a 2.15 T electromagnet, magnetic properties of the ferrofluid were measured (at room temperature). The magnetic moment of ferrofluid was measured over a range of applied fields from -20 to +20 kOe (all measurements were conducted in step field mode with a step size of 250 Oe/s).

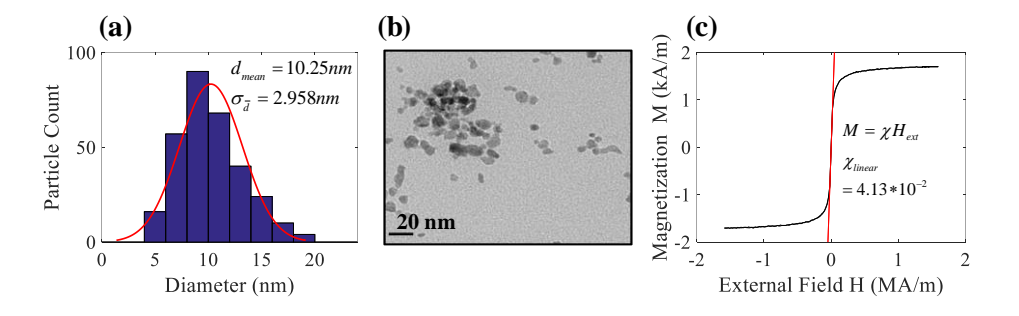


Figure 3.2- (a) The size distribution of maghemite nanoparticles within the ferrofluid showed a mean particle size of 10.250 nm with a standard deviation of 2.958 nm. (b) A transmission electron microscopy (TEM) image of the nanoparticles. Scale bar represents 20 nm. (c) Magnetization curve for the ferrofluid: given a known bulk magnetization of maghemite (370 kA/m) and a saturation magnetization (from curve) of 1.71 kA/m, the concentration of magnetic particles within the ferrofluid was estimated to be at 0.46% by volume. The ferrofluid exhibits no hysteresis and is superparamagnetic. The linear magnetic susceptibility shown as the red dashed line prior to saturation is 0.0413.

Ferrofluid Solutions for DIBs

The ferrofluid solutions used in this work are stable aqueous suspensions of magnetite (γ -Fe₂O₃) as described previously at a nanoparticle concentration of 0.46% by volume. 250 mM Potassium Chloride (KCl, Sigma-Aldrich, St. Louis, MO) and 10 mM 3-(N-morpholino) propanesulfonic acid (MOPS, Sigma-Aldrich, St. Louis, MO) salts were added to the ferrofluid solution. Solutions were systematically sonicated prior to each use. In the experiments involving alpha-hemolysin pores, the same ferrofluid solution mentioned here was used with the addition of 1M KCl and 10 mM of Trihydrochloride (Tris-HCl, Molecular Biology Grade- Promega Corporation, Madison, WI) instead. A concentration of 1.25 μ g/ml of wild-type Alpha-Hemolysin (α HL) from Staphylococcus aureus (Sigma Aldrich, St. Louis, MO) was then added to the solution before being stored at a temperature of 2 °C.

Aqueous Buffer Solutions for DIBs

An aqueous buffer solution was prepared by adding 250 mM KCl and 10 mM MOPS resulting in a pH of 6.98. This solution was used in all experiments except for the ones involving αHL where a 10 mM Tris-HCl, 1 M KCl buffer solution (pH 7.0, as measured) was used.

PDMS Dishes

Polydimethlysiloxane (PDMS) mixtures were created from SYLGARD 184 Silicone Elastomer Base (Dow Corning Corporation, Midland, MI) with a 13:3 v: v ratio of base to curing agent. The solution was degassed in a vacuum oven for 15 minutes and then poured into molds and cured at 80 °C for 90 minutes.

Magnetowetting Substrate

PDMS mixtures were poured into long cylindrical tubes 5 mm in diameter with a flat plane carved one side for visibility. A 1.1 mm O.D. glass capillary (World Precision Instruments, Sarasota, FL) was inserted lengthwise into the center of the tube to form a well, and the PDMS was cured in a vacuum oven (VWR, Radnor, PA). The cured PDMS cylinder containing the well was broken into smaller sections, and the glass capillary was removed to create the central channel. A perpendicular channel was punched into the PDMS tube, orthogonally intersecting the central channel. The perpendicular channel and base of the central channel was filled with uncured polyethylene glycol dimethacrylate hydrogel (PEG-DMA, Polysciences Inc, Bucks County, PA) containing Irgacure (Sigma Aldrich, St. Louis, MO) as a photoinitiator. A silver-silver/chloride (Ag/AgCl) electrode (0.125 mm in diameter, GoodFellow, Coroapolis, PA) was threaded into the liquid hydrogel, and the gel was solidified by exposure to a high intensity UV LED (Thorlabs, Newton, NJ) for 3 minutes. The whole substrate was then adhered to a glass coverslip for stability. The final substrate (Figure 3.3) provides a compact encapsulated platform for investigating magnetowetting.

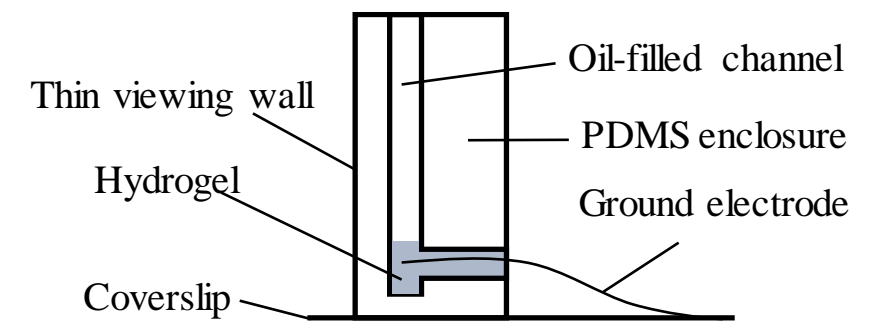


Figure 3.3- Sketch of the PDMS substrate used for magnetowetting measurements. The vertical channel is approximately 1.1 mm in diameter.

3.4. Methods

Creation of Magnetic Droplet Interface Bilayer Networks

Glass capillary tubes (KWIK-Fil Borosilicate Glass Capillaries, World Precision Instruments, Inc.-Sarasota, FL, reported dimensions:100mm in length 1.0 mm in outer diameter and 0.58 mm in inner diameter) were pulled to fine points using a programmable pipette puller (P-1000, Sutter Instruments, Novato, CA) with pretested settings for the pulling force, the chamber temperature and the holding time. The final inner diameter of the needle apertures was measured to be around 30 µm. These needles were then filled with either the aqueous buffer or ferrofluid solution using 34G microfils (World Precision Instruments, Sarasota, FL) and were attached to microinjectors (Sutter Instruments, Novato, CA) mounted on manual micromanipulators (Siskiyou, Grants Pass, OR). The PDMS well substrate was placed on the stage of a zoom microscope (Nikon SMZ1000, Tokyo, Japan) and filled with the lipid-oil solution. Droplets were systematically injected in the oil reservoir using a pressure-operated injector (FemtoJet 4i, Eppendorf) with specified injecting pressures and holding times to produce droplets with the desired diameters for each solution. After sufficient time for monolayer formation, a permanent magnet (neodymium (NdFeB) magnet, K&J Magnetics, Inc.) was gradually brought closer to the dish containing the droplets. For cases containing only ferrofluid droplets, the magnet pulled the ferrofluid droplets into contact at a single location and the DIB networks were readily formed. Upon the removal of the magnet, the droplets remained adhered in a structured membrane network. For the case where DIB networks are formed using a combination of both ferrofluid and water droplets, a permanent magnet mounted on a 3axis manipulator (Siskiyou, Grants Pass, OR) was used to the move the ferrofluid droplets through the medium to gradually recruit the water droplets into a larger structure.

Measurement of Interfacial Tensions

Surface tensions of lipid monolayers formed at the oil-water and oil-ferrofluid interfaces were evaluated using the pendant drop method [13, 37]. In this technique, the interfacial tension (IFT) of a fluid-fluid interface is determined from a digitized series of images acquired for a suspended pendant drop of one of the liquid phases (here water or ferrofluid) formed at the tip of a needle and submerged in the second phase (here the lipidoil mixture). These images are then used to evaluate the IFT with an accuracy of ± 0.1 mN/m [38-41] through a Python-based curve-fitting process of the drop edge coordinates [37, 42]. A simple experimental system was used for the pendant-drop tensiometry as shown in Figure 3.4.a. The diffused light of a Quartz Tungsten-halogen lamp (QTH10/M - Quartz Tungsten-Halogen Lamp, M4 Tap, Thorlabs, Newton, NJ) passes through a Quartz cuvette (10mm cuvette cell spectrometer open top, Science Outlet, Tsuenwan, Hong Kong) filled with 3 mL of the lipid-oil mixtures in which a water or ferrofluid droplet is dispensed from a clean 30 G steel needle (Harvard Apparatus, Holliston, MA). Images are captured using a CCD camera (high sensitivity DCC1240C, Thorlabs, Newton, NJ) to which zoom lenses (6.5X zoom lenses with a 0.7 - 4.5X magnification range, Thorlabs, Newton, NJ) were attached through a mount adapter (MVLCMC - C-mount adapter for zoom lens extension tubes, Thorlabs, Newton, NJ). In order to prevent any wetting that might occur at the tip of the needle, clean wipes (Kimwipe, Kimberly-Clark Professional, Roswell, GA) were used to remove any water or ferrofluid residual before droplets were formed.

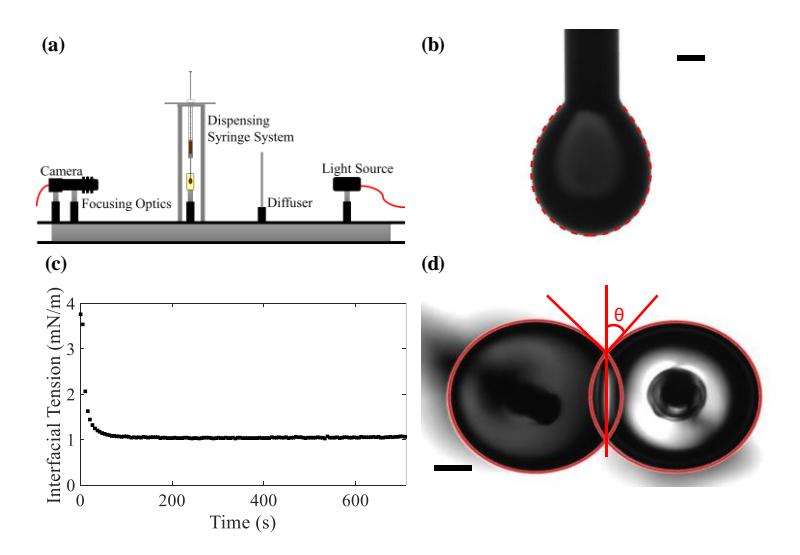


Figure 3.4- (a) Schematic representation of the pendant drop experiments for the measurement of interfacial surface tension. The diffused light of a halogen lamp passes through a Quartz cuvette filled with 3 mL of the lipid-oil mixtures in which a water or ferrofluid droplet is dispensed from a clean steel needle. Images are acquired through a CCD camera equipped with a zoom lens. (b) Acquired images of the droplets were analyzed using the open-source OpenDrop software. The interfacial tension was obtained through a curve-fitting process of the drop edge coordinates. (c) A typical measurement of the monolayer tension for a ferrofluid droplet in a lipid-in-oil mixture (DPhPC dissolved in a 1:1 (v: v) solution of Hexadecane and Silicone oils in a concentration of 0.5 mg/ml) shows that the interfacial tension decreases rapidly upon droplet formation in the lipid-oil. The steady-state tension value obtained from these measurements was used to calculate the bilayer tension using Equation (3.1). (d) The membrane's area, length, and external contact angle were found for each analyzed bilayer using a MATLAB code for image analysis. Droplets were fitted to circles and geometric relations were used to derive the interfacial area and angle of contact.

Measurements of DIB Specific Capacitance, Adhesion Energy and Thickness

As shown in Figure 3.1.a, a DIB can be electrically approximated as a capacitor in parallel with a high amplitude resistance [2, 5]. Since the membrane resistance is often in the order of $G\Omega$ [2, 43], the resistive current is often ignored or compensated for, and the overall current of a bilayer simplified to its capacitive component. This capacitance may then be estimated by measuring the current necessary for charging the membrane to a prescribed voltage. Normalizing this capacitance with respect to area allows for a quick diagnostic of bilayer thickness, configuration, and integrity [9-11].

The area of the membrane is governed by the balance of IFTs at the monolayer-bilayer annulus as depicted in Figure 1.b. Upon formation, the membrane expands until the tensions at the annulus are balanced [9, 44, 45]. The equilibrium relationship between the bilayer tension γ_b and the two opposing monolayer tensions γ_m deviating from the normal plane by an angle of contact θ is given by:

$$\gamma_h = 2\gamma_m cos\theta \tag{3.1}$$

The contact angle depends on the balance of the interfacial tensions and will remain constant in the absence of any external constraints [7, 8, 46], and is directly related to the minimization of interfacial energies for the two droplets [35]. The bilayer tension can therefore be found for a given combination of measured monolayer tensions and contact angles for a membrane at equilibrium. These two tensions will allow for the evaluation of the bilayer's adhesion energy also referred to as membrane's free energy of adhesion ΔF [45]:

$$\Delta F = 2\gamma_m - \gamma_b = 2\gamma_m (1 - \cos\theta) \tag{3.2}$$

The energy of adhesion is directly linked to the interactions of the two surfactant monolayers [47, 48] – consequently it is a reliable point of comparison for membranes with similar oil/lipid compositions. As the monolayers draw together from infinity to the equilibrium membrane distance, the energy is reduced by the integrated disjoining pressure Π summing the combined steric, electrostatic, and Van der Waals forces interactions between the lipid tails. This is equivalent to the energy of adhesion as defined above and characterizes the favorability of the adhered film [14, 15, 49].

$$\gamma_b = 2\gamma_m - \int_{\infty}^{h_e} \pi dh \tag{3.3}$$

$$\Delta F = \int_{\infty}^{h_e} \pi dh \tag{3.4}$$

The equilibrium thickness of the membrane may be characterized by its specific capacitance C_m . Knowing that C_m varies with the amount of solvent remaining in the bilayer's hydrophobic region [9, 44, 50, 51], results obtained for different types of DIBs suggest the amount of residual oil remaining within the bilayer. It has also been established that C_m is related to the thickness of the bilayer's hydrophobic region D_C as well as its dielectric permittivity ε_r [50, 52]:

$$C_m = \frac{\varepsilon_r \varepsilon_0}{D_C} \tag{3.5}$$

with ε_0 representing the permittivity of vacuum. For the following calculations, we assumed the value of ε_r to be equal to that of long-hydrocarbon chain molecules (2.2[9, 53]). It should be noted that DC is not necessarily the equilibrium film thickness h_e . Both

 D_C and C_m values allow for quantification of any induced effect (or the lack thereof) when the magnetic nanoparticles are incorporated into the DIB technique.

Droplets (~300 µm radius) were deposited on agarose (2% by weight EZ Pack Agarose LE, Molecular Biology Grade, Benchmark Scientific, Sayresville, NJ) coated silver/silver chloride electrodes (125 µm in diameter, GoodFellow, Coroapolis, PA). Each electrode was mounted on a three-axis manual micromanipulator (Siskiyou, Grants Pass, OR) for control over the droplet positions and electrode manipulation. All electrical measurements (membrane capacitance as well as channel recordings) were recorded in voltage clamp mode (Whole Cell $\beta=1$) using the Axopatch 200B patch clamp amplifier and the Digidata 1550 data acquisition system (Molecular Devices, Sunnyvale, CA) at a sampling frequency of 5 kHz and filtered at 1 kHz (using the embedded low-pass Bessel filter -80 dB/decade). The nominal capacitance of the bilayers was evaluated using a 40 Hz, 10 mV AC triangular wave (33120A function generator, Hewlett Packard, Palo Alto, CA). Background capacitance (also referred to as stray capacitance), arising from any residual capacitance in the different acquisition system components was accounted for before making any measurement by using the patch clamp amplifier's built-in whole-cell capacitance compensation. The value of the bilayer's capacitance was obtained using a MATLAB code from the recorded square wave current response and the corresponding applied voltage. For each analyzed case, an image of the DIB was taken through the inverted microscope using a CCD camera (DFC365 FX, Leica, Wetzlar, Germany) once the bilayer was given enough time to form and stabilize. These images were exported and analyzed using a MATLAB code that fits the droplets into circles and uses geometric

equalities to derive the bilayer area and angle of contact as illustrated in Figure 3.4.d using a calibrated pixel-micron value from the microscope software.

The bilayer formed between the droplets was characterized by the visible intersecting chord on the inverted microscope, assuming that the membrane exhibits minimal ellipticity due to gravitational effects. The nominal specific capacitance Cm was evaluated for each different case using the values obtained from the bilayer's capacitance and area measurements. Droplets with a radius of 300 µm and an assumed surface tension of approximately 1 mN/m [44] provide a Bond number on the order of 0.01 as shown in Equation 3.6, minimizing gravitational effects for this particular oil-water combination where the density difference is 110 kg/m3. Here is the difference in density between the two phases, is the gravitational constant, is the radius of the droplet, and is the monolayer surface tension.

$$B_O = \frac{\Delta \rho g R^2}{\gamma_m} \tag{3.6}$$

Alpha-Hemolysin Functionality

Alpha-hemolysin (αHL) obtained from Staphylococcus aureus bacteria is a mushroom-shaped, homo-oligomeric, transmembrane, pore-forming toxin [54, 55] that acts as a natural lysis inducing agent. With a well-known structure and transmembrane electrical activity [1, 54-57], alpha-hemolysin pore-bilayer unique configuration was used here as a tool to assess the functionality of the ferrofluid-based DIBs. The insertion activity of the pore-forming toxin (PFT) was examined in four different cases: a control case with

two water droplets, a case with two ferrofluid droplets, and mixed water-ferrofluid DIBs with alternating droplet locations. In all cases, αHL was added at a concentration of 1.25 $\mu g/ml$ to the reference side of the bilayer. The obtained current traces (for a DC applied voltage of 50 mV) were recorded in voltage clamp mode (Whole Cell β =1) at a sampling frequency of 5 kHz and filtered at 1 kHz (using the embedded low-pass Bessel filter -80 dB/decade). Post-acquisition, a 500 Hz fourth order Butterworth low-pass filter was used in MATLAB when plotting obtained data.

Magnetowetting

The magnetowetting substrate channel described previously was filled with the oillipid solution, forming a lipid monolayer on the hydrogel surface at the bottom of the channel. A 1.1-mm diameter ferrofluid droplet was deposited at the channel entrance using the same protocol from the formation of magnetic DIB networks and allowed to gradually descend through the channel due to gravitational forces, accumulating a lipid coating as it descended from the surrounding oil. Upon contacting the hydrogel at the bottom of the channel, a droplet-hydrogel bilayer (DHB) formed spontaneously between the gel and the ferrofluid droplet. An Ag/AgCl electrode (125 μm in diameter- GoodFellow, Coroapolis, PA) was then inserted into the ferrofluid droplet from above using a 3-axis manual micromanipulator (Siskiyou, Grants Pass, OR), providing electrical characterization of the DHB through the ground electrode placed in the hydrogel support. These electrodes were connected to a Multiclamp 700B patch clamp amplifier and the Digidata 1550 data acquisition system (Molecular Devices, Sunnyvale, CA) and the capacitance of the membrane was measured using the same protocol from the previous measurements of bilayer capacitance, calculating the area of the membrane through the value through the

obtained specific capacitance values for ferrofluid-buffer combinations. A permanent magnet was placed on a translating stage (PT1/M single axis translation stage with standard micrometer, Thorlabs, Newton, NJ) underneath the slide and gradually moved closer to the substrate in 1 mm increments using the micrometer, increasing the strength of the exerted magnetic field and causing the interfacial membrane between the ferrofluid droplet and the hydrogel support to expand. Visualization of the droplet in the channel was achieved through an inspection microscope with a CCD camera (Motic, Hong Kong).

3.5. Results and Discussion

Creation of Ferrofluid-Enabled Droplet Interface Bilayer Networks

Ferrofluid droplets were easily assembled into larger DIB structures through the introduction of an external magnetic field as described previously. The droplets were dispersed within the oil and a permanent magnet was used to bring the droplets into contact. The magnet was removed after membrane formation, and the structure remained in place even in the absence of a magnetic field. These structures are stable and allowed for the combination of water and ferrofluid droplets in DIB clusters as shown in Figure 3.5.

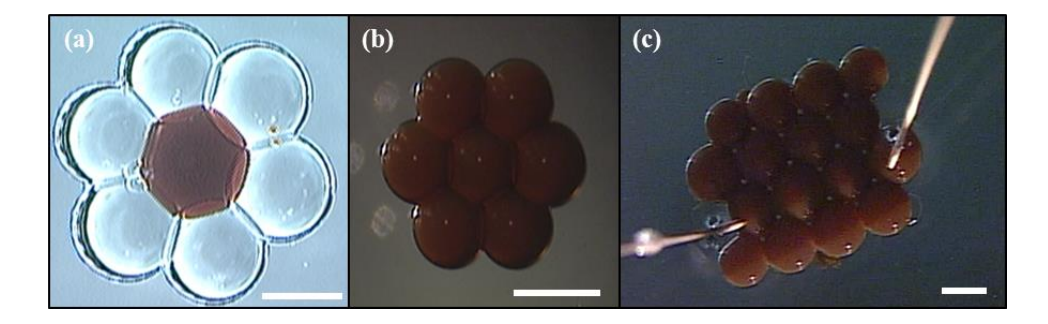


Figure 3.5- Use of ferrofluid nanoliter droplets for the fast and easy construction of 2D DIB structures. In subplot (a), a single ferrofluid droplet previously introduced to a lipid-oil reservoir was controlled with an external magnet to gradually recruit additional droplets

into a hexagonal-shaped DIB cluster. The end result was a stable DIB network that included both aqueous and ferrofluid droplets. Meanwhile, in the cases where exclusively ferrofluid droplets were used as shown in (b) and (c), a quick and automatic self-assembly of the networks was induced through a permanent magnet: as the magnet was brought closer to the lipid-oil dish, the lipid-coated ferrofluid droplets were pulled into contact with each other and the lipid bilayers formed spontaneously. Once the magnetic source was removed, the networks preserved their structural integrity and the droplets remained in contact. Scale bars represent 750 μ m.

Measurement and Comparisons of Ferrofluid DIB Specific Capacitance, Tension,
Adhesion Energy and Thickness

Table 3.1 shows the average values and standard deviations for the obtained equilibrium monolayer and bilayer tensions (resting bilayer tension obtained when no additional external mechanical force is being applied to the droplets), external contact angle, specific capacitance, and thickness and energy of adhesion of bilayers formed for DIBs with and without ferrofluids. The results show that the obtained values for each of the bilayers' properties are similar, indicating that the incorporation of ferrofluids within the aqueous phase does not influence the properties of the formed lipid bilayers. While it is possible that the surrounding monolayer is a mixture of both the phospholipids and excess ATLOX surfactant, any excess ATLOX is wicked away from the bilayer membrane during formation as shown by Jeong et al. [58]. Consequently, the underlying structure of the bilayer appears unchanged. This may be further validated by observing the behavior of pores and channels within the membrane

Table 3.1- Measurements Obtained for DIBs with and without ferrofluids at 22°C.

Туре	C _m (µF/cm ²)	γ _m (mN/m)	γ _b (mN/m)	$2\theta_m(deg)$	D _c (Å)	ΔF (mN/m)
Water (n=13)	0.553	1.113	1.958	60.219	33.786	0.267
	(±0.094)	(±0.174)	(±0.300)	(±5.783)	(±7.577)	(±0.064)
Ferrofluid (n=11)	0.583	1.119	1.936	59.365	32.002	0.291
	(± 0.030)	(±0.151)	(±0.241)	(±1.311)	(±1.802)	(±0.038)

Alpha-Hemolysin Functionality in Ferrofluid DIBs

To determine whether αHl is still functional in ferrofluid DIBs, we examined the formation of conductive pores in various combinations of water and ferrofluid droplets. A total of 96 αHL insertion events (22 from the cases shown in Figure 3.6.a, 27 from 3.6.b, 22 from 3.6.c, and 25 from 3.6.d) were examined. The corresponding single pore conductance ranged between 0.379 and 1.258 nS (with a total average of 0.866 nS and a standard deviation of 0.202 nS). In all cases, the measured single pore conductances fell within previously reported ranges for α HI [57, 59] demonstrating that functional peptide pores can still be embedded with ferrofluid DIBs. The variance in pore conductance is largely due to the structural difference of αHl. The alpha-hemolysin pore is formed by selforganizing heptameric monomers however, the existence of several stable hexamer oligomeric structures that can be inserted into the lipid bilayer is highly probable and well supported by previous studies [57, 59]. As depicted in Figure 3.6.b, 3.6.c and 3.6.d, potential blocking events occur when the ferrofluid droplets are used. However, despite the occurrence of these blocking events, the PFT is still functional within these bilayers, and thus can be used in larger DIB structures involving magnetically-responsive droplets.

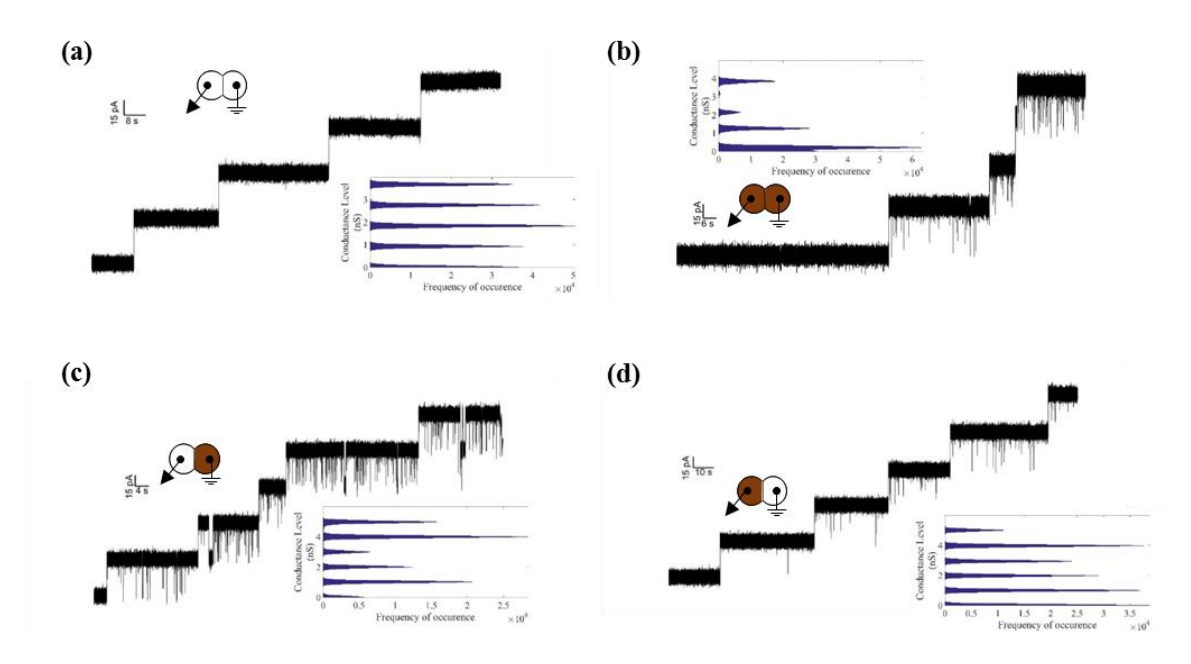


Figure 3.6- Alpha-hemolysin insertion activity is measured as stepwise increases in the current measured with a constant applied voltage of +50 mV. Subplot (a) shows a typical scenario for a DIB formed between two water droplets. (b) shows the observed alpha-hemolysin behavior for a membrane formed between two ferrofluid droplets. Mixed droplet behavior is presented in (c) and (d) where, a water and a ferrofluid droplet were combined. In all cases, αHL was added at a concentration of 1.25 μg/ml to the reference droplet. The obtained current traces were recorded in voltage clamp mode at a sampling frequency of 5 kHz and filtered and filtered at 1 kHz (using the embedded low-pass Bessel filter -80 dB/decade). Post-acquisition, data was filtered at 500 Hz using a fourth order Butterworth low-pass filter in MATLAB. Possible blocking events occur whenever ferrofluid is being incorporated. However, all observed channel insertion events showed conductivities that fall within the acceptable reported range.

Ferrofluids for the Formation of DHBs and Magnetowetting

The successful incorporation of ferrofluids within the DIB platform allows for manipulation of select droplets through a magnetic field. Similar to the regulated attachment method [60], this allows for indirect control over the membrane dimensions as shown in Figure 3.7, plotting the change in membrane area against a magnetic Bond number. This quantifies the impact of the magnetic body force relative to the interfacial tension force [61, 62] (Equation 3.7). In this case, the tension of the droplet-oil interface is very low (Table 3.1), and this dimensionless number quickly increases upon exposure to a permanent magnet.

$$B_M = \frac{\mu_0 \Delta \chi H_{ext}^2 Vol^{1/3}}{2\gamma_m} \tag{3.7}$$

Here μ_0 is the permeability constant ($4\pi \times 10^{-7}$), $\Delta\chi$ is the difference in magnetic susceptibilities between the ferrofluid and oil (Figure 3.2), $H_{\rm ext}$ is the intensity of the applied magnetic field, Vol is the droplet volume (~ 500 nL), and γ_m is the surface tension of the ferrofluid droplet taken from Table 3.1 (1.19 mN/m). The ferrofluid droplet is flattened upon exposure to a magnetic field, increasing its interfacial area as depicted in Figure 3.7. As the magnet is brought gradually closer to the channel substrate, the droplet shifts from a half-sphere to a more flattened, cylindrical shape within the channel. The offset in the plot in the magnetic Bond number is due to the resolution of the experiment – perceptible changes in membrane area did not occur when the magnet was moved further away. This behavior was reversible; once the magnet was removed the membrane shrank back to its original dimensions. No perceptible changes in membrane area were observed

for control cases with water droplets instead of ferrofluid droplets when the magnet was brought closer to the membrane.

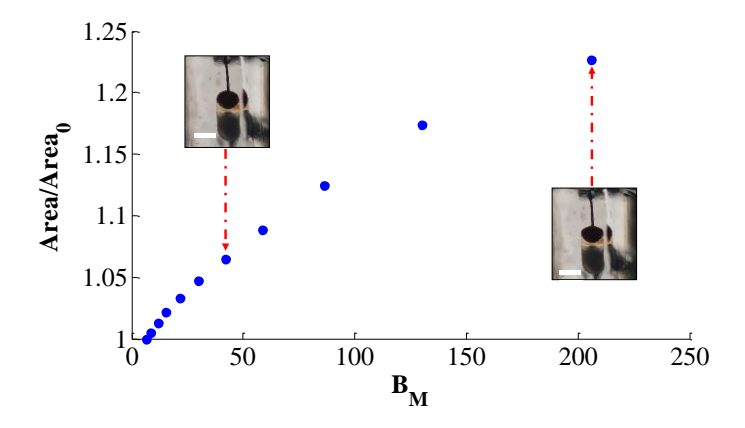


Figure 3.7- Magnetowetting or the control over the membrane area through a magnetic field was demonstrated by compressing a ferrofluid droplet into a hydrogel support. The proximity of the magnet was increased in a stepwise fashion of 1 mm per increment, and the membrane grew in response. When the permanent magnet was removed, the membrane resumed its original equilibrium dimensions. The ratio of the evolving membrane area with respect to its original area increases with an increasing magnetic Bond number as shown. The scale bars on the insets represent 1 mm.

3.6. Conclusions

The incorporation of ferrofluids within the aqueous phases of the droplet interface bilayer technique for the repetitive assembly of functional and stable bilayer networks was investigated. Our analysis has shown that the functionality of the membranes was not significantly altered by the presence of the magnetic fluid. Bilayers formed between magnetically responsive droplets exhibit properties (specific capacitance, contact angle, monolayer tension, bilayer tension, and energy of adhesion) that fall within the range of

their non-magnetic counterparts. Droplet-droplet transport can still be established through alpha-hemolysin pores further increasing the potential uses of ferrofluids within DIB-based materials. Ferrofluids allow for contact-free manipulation of membrane properties such as dynamic tuning of membrane properties through externally supplied magnetic fields while retaining the classic functionalities of DIB networks. Building more complex 3D bilayer networks with incorporated ferrofluid droplets is a promising step towards the creation of a magnetically responsive and reconfigurable droplet networks.

3.7. References

- 1. Hwang, W.L., et al., Electrical Behavior of Droplet Interface Bilayer Networks: Experimental Analysis and Modeling. Journal of the American Chemical Society, 2007. 129(38): p. 11854-11864.
- 2. Bayley, H., et al., Droplet interface bilayers. Molecular BioSystems, 2008. 4(12): p. 1191-208.
- 3. Hwang, D.K., D. Dendukuri, and P.S. Doyle, Microfluidic-based synthesis of non-spherical magnetic hydrogel microparticles. Lab on a Chip, 2008. 8(10): p. 1640-1647.
- 4. Funakoshi, K., H. Suzuki, and S. Takeuchi, Lipid bilayer formation by contacting monolayers in a microfluidic device for membrane protein analysis. Analytical chemistry, 2006. 78(24): p. 8169-8174.
- 5. Holden, M.A., D. Needham, and H. Bayley, Functional bionetworks from nanoliter water droplets. Journal of the American Chemical Society, 2007. 129(27): p. 8650-8655.
- 6. Maglia, G., et al., Droplet networks with incorporated protein diodes show collective properties. Nature Nanotechnology, 2009. 4: p. 437-440.

- 7. Najem, J.S., et al., Activation of bacterial channel MscL in mechanically stimulated droplet interface bilayers. Scientific Reports, 2015. 5(13726).
- 8. Freeman, E.C., et al., The mechanoelectrical response of droplet interface bilayer membranes. Soft Matter 2016. 12: p. 3021-3031.
- 9. Gross, L.C., et al., Determining membrane capacitance by dynamic control of droplet interface bilayer area. Langmuir, 2011. 27(23): p. 14335-42.
- 10. Gross, L.C., O.K. Castell, and M.I. Wallace, Dynamic and reversible control of 2D membrane protein concentration in a droplet interface bilayer. Nano Lett, 2011. 11(8): p. 3324-8.
- 11. Leptihn, S., et al., Constructing droplet interface bilayers from the contact of aqueous droplets in oil. Nat Protoc, 2013. 8(6): p. 1048-57.
- 12. Hwang, W.L., et al., Asymmetric droplet interface bilayers. Journal of the American Chemical Society, 2008. 130(18): p. 5878-5879.
- 13. Venkatesan, G.A., et al., Adsorption Kinetics Dictate Monolayer Self-Assembly for Both Lipid-In and Lipid-Out Approaches to Droplet Interface Bilayer Formation. ACS-Langmuir, 2015. 31(47): p. 12883-12893.
- 14. Bibette, J., F.L. Calderon, and P. Poulin, Emulsions: basic principles. Reports on Progress in Physics, 1999. 62(6): p. 969.
- 15. Leal-Calderon, F., V. Schmitt, and J. Bibette, Emulsion science: basic principles.2007: Springer Science & Business Media.
- 16. Wauer, T., et al., Construction and manipulation of functional three-dimensional droplet networks. ACS Nano, 2014. 8(1): p. 771-9.

- 17. Booth, M.J., et al., Light-activated communication in synthetic tissues. Sci Adv, 2016. 2(4): p. e1600056.
- 18. Sarles, S.A. and D.J. Leo, Physical encapsulation of droplet interface bilayers for durable, portable biomolecular networks. Lab on a Chip, 2010. 10(6): p. 710-7.
- 19. Sarles, S.A. and D.J. Leo, Membrane-based biomolecular smart materials. Smart Materials and Structures, 2011. 20(9): p. 094018.
- 20. Nguyen, M.A., et al., Hydrodynamic trapping for rapid assembly and in situ electrical characterization of droplet interface bilayer arrays. Lab Chip, 2016. 16(18): p. 3576-88.
- 21. Villar, G., A.D. Graham, and H. Bayley, A tissue-like printed material. Science, 2013. 340(6128): p. 48-52.
- 22. Bayoumi, M., et al., Multi-compartment encapsulation of communicating droplets and droplet networks in hydrogel as a model for artificial cells. Sci Rep, 2017. 7: p. 45167.
- 23. Dixit, S.S., et al., Droplet Shape Analysis and Permeability Studies in Droplet Lipid Bilayers. ACS-Langmuir, 2012. 28(19): p. 7442-7451.
- 24. Lacasse, M.-D., et al., Model for the elasticity of compressed emulsions. Physical review letters, 1996. 76(18): p. 3448.
- 25. Mason, T. and J. Bibette, Shear rupturing of droplets in complex fluids. Langmuir, 1997. 13(17): p. 4600-4613.
- 26. Pollack, M.G., R.B. Fair, and A.D. Shenderov, Electrowetting-based actuation of liquid droplets for microfluidic applications. Applied Physics Letters, 2000. 77(11): p. 1725-1726.

- 27. Yamada, R. and H. Tada, Manipulation of Droplets by Dynamically Controlled Wetting Gradients. Langmuir, 2005. 21(10): p. 4254-4256.
- 28. Jiao, Z., et al., Thermocapillary actuation of droplet in a planar microchannel. Microfluidics and Nanofluidics, 2007. 5(2): p. 205-214.
- 29. Hao, P., et al., Driving liquid droplets on microstructured gradient surface by mechanical vibration. Chemical Engineering Science, 2011. 66(10): p. 2118-2123.
- 30. Aghdaei, S., et al., Formation of artificial lipid bilayers using droplet dielectrophoresis. Lab on a Chip, 2008. 8(10): p. 1617-1620.
- 31. Poulos, J.L., et al., Electrowetting on dielectric-based microfluidics for integrated lipid bilayer formation and measurement. Applied Physics Letters, 2009. 95(1): p. 013706.
- 32. Egatz-Gómez, A., et al., Discrete magnetic microfluidics. Applied Physics Letters, 2006. 89(3): p. 034106.
- 33. Pipper, J., et al., Catching bird flu in a droplet. Nat Med, 2007. 13(10): p. 1259-63.
- 34. Berthier, J., Micro-drops and digital microfluidics. 2012: William Andrew.
- 35. Berthier, J. and K.A. Brakke, The physics of microdroplets. 2012: John Wiley & Sons.
- 36. Zhao, W.J., et al., Label-Free and Continuous-Flow Ferrohydrodynamic Separation of HeLa Cells and Blood Cells in Biocompatible Ferrofluids. Advanced Functional Materials, 2016. 26(22): p. 3990-3998.
- 37. Berry, J.D., et al., Measurement of surface and interfacial tension using pendant drop tensiometry. Journal of Colloid and Interface Science, 2015. 454: p. 226-237.
- 38. Miller, R., et al., Measuring dynamic surface and interfacial tensions. Advanced Materials, 1992. 4(5): p. 370-374.

- 39. Girault, H., D. Schiffrin, and B. Smith, Drop image processing for surface and interfacial tension measurements. Journal of Electroanalytical Chemistry and Interfacial Electrochemistry, 1982. 137(2): p. 207-217.
- 40. Cheng, P., et al., Automation of axisymmetric drop shape analysis for measurements of interfacial tensions and contact angles. Colloids and Surfaces, 1990. 43(2): p. 151-167.
- 41. Hansen, F. and G. Rødsrud, Surface tension by pendant drop: I. A fast standard instrument using computer image analysis. Journal of colloid and interface science, 1991. 141(1): p. 1-9.
- 42. Lin, S.-Y., et al., An examination on the accuracy of interfacial tension measurement from pendant drop profiles. Langmuir, 1995. 11(10): p. 4159-4166.
- 43. Danelon, C., et al., Cell membranes suspended across nanoaperture arrays. Langmuir, 2006. 22(1): p. 22-25.
- 44. Taylor, G.J., et al., Direct in situ measurement of specific capacitance, monolayer tension, and bilayer tension in a droplet interface bilayer. Soft Matter, 2015. 11(38): p. 7592-605.
- 45. Thiam, A.R., N. Bremond, and J. Bibette, From stability to permeability of adhesive emulsion bilayers. Langmuir, 2012. 28(15): p. 6291-8.
- 46. S.Najem, J., et al., Mechanosensitive Channels Activity in a Droplet Interface Bilayer System, in MRS. 2014 p. 171-176.
- 47. Bergeron, V., Forces and structure in thin liquid soap films. Journal of Physics: Condensed Matter, 1999. 11(19): p. R215.

- 48. Bergeron, V., J. Martin, and L. Vovelle, Interaction of droplets with a surface: impact and adhesion. Agro Food Industry Hi-Tech, 1999. 10(5): p. 21-23.
- 49. Bibette, J., et al., Stability Criteria for Emulsions. Physical Review Letters 1992. 69(16): p. 2440-2443.
- 50. White, S.H., A Study of Lipid Bilayer Membrane Stability Using Precise Measurements of Specific Capacitance. Biophysical Journal, 1970. 10(12): p. 1127-1148.
- 51. Requena, J. and D.A. Haydon, The lippmann equation and the characterization of black lipid films. Journal of Colloid and Interface Science, 1975. 51(2): p. 315-327.
- 52. Wobschall, D., Voltage dependence of bilayer membrane capacitance. Journal of Colloid and Interface Science, 1972. 40(3): p. 417-423.
- 53. Valincius, G., et al., Soluble amyloid β -oligomers affect dielectric membrane properties by bilayer insertion and domain formation: implications for cell toxicity. Biophysical journal, 2008. 95(10): p. 4845-4861.
- 54. Song, L., et al., Structure of Staphylococcal alpha -Hemolysin, a Heptameric Transmembrane Pore. Science, 1996. 274(5294): p. 1859-1865.
- 55. Gouaux, J.E., et al., Subunit stoichiometry of staphylococcal alpha-hemolysin in crystals and on membranes: a heptameric transmembrane pore. Proceedings of the National Academy of Sciences, 1994. 91(26): p. 12828-12831.
- 56. Holden, M.A. and H. Bayley, Direct introduction of single protein channels and pores into lipid bilayers. Journal of the American Chemical Society, 2005. 127(18): p. 6502-6503.
- 57. Tsuji, Y., et al., Droplet split-and-contact method for high-throughput transmembrane electrical recording. Analytical chemistry, 2013. 85(22): p. 10913-10919.

- 58. Jeong, D.W., et al., Enhanced stability of freestanding lipid bilayer and its stability criteria. Sci Rep, 2016. 6: p. 38158.
- 59. Belmonte, G., et al., Pore formation by Staphylococcus aureus alpha-toxin in lipid bilayers. European Biophysics Journal, 1987. 14(6): p. 349-358.
- 60. Sarles, S.A. and D.J. Leo, Regulated attachment method for reconstituting lipid bilayers of prescribed size within flexible substrates. Analytical chemistry, 2010. 82(3): p. 959-966.
- 61. Zhu, G.-P., et al., Nonlinear deformation of a ferrofluid droplet in a uniform magnetic field. Langmuir, 2011. 27(24): p. 14834-14841.
- 62. Nguyen, N.-T., Deformation of ferrofluid marbles in the presence of a permanent magnet. Langmuir, 2013. 29(45): p. 13982-13989.

CHAPTER 4

RECONFIGURING DROPLET INTERFACE BILAYER NETWORKS THROUGH $SACRIFICIAL\ MEMBRANES^3$

³ M. M. Makhoul-Mansour, E. J. Challita, E. C. Freeman, Biomicrofluidics 2018, 12, 034112. Reprinted with permission of the publisher. MMM and EJC are equal contributors.

4.1. Abstract

The droplet interface bilayer (DIB) platform allows for the fabrication of stimuliresponsive emulsions, using phospholipids as an organic surfactant in water-in-oil mixtures. In this approach lipid-coated droplets are adhered together in arranged networks, forming lipid bilayer membranes, and establishing selective transport pathways between neighboring aqueous subcompartments. The resulting material is a biologically-inspired emulsion that exhibits emergent properties wherein different droplets accomplish different functions, similar to multicellular organisms. These networks have been successfully applied towards biomolecular sensing and energy harvesting applications. However, unlike their source of inspiration, these droplet structures are often static. This limitation not only renders the networks unable to adapt or modify their structure and function after formation but also limits their long-term use as passive ionic exchange between neighboring droplet pairs may initiate immediately after the membranes are established. This work addresses this shortcoming by rupturing selected sacrificial membranes within the collections of droplets to rearrange the remaining droplets into new configurations, redirecting the droplet-droplet exchange pathways. This is accomplished through electrical shocks applied between selected droplets. Experimental outcomes are compared to predictions provided by a coupled mechanical-electrical model for the droplet networks, then advanced configurations are proposed using this model.

4.2. Introduction

The droplet interface bilayer (DIB) technique has rapidly gained popularity as a platform for studying membrane transport mechanics and for developing biologically-inspired smart materials and microdevices [1-4]. Highly tailorable and robust, this

technique allows for the construction of lipid bilayers between aqueous droplets in an oil reservoir with dissolved lipids, providing a self-assembled collection of lipid bilayer membranes at the intersections of lipid-coated droplets [5]. The droplets gradually acquire a lipid coating once they are immersed in a lipid-oil medium, where the phospholipid molecules form monolayers at the water-oil interfaces. When two lipid-coated aqueous droplets are brought into contact, the oil in the surrounding medium is gradually expelled, and the ordered lipid monolayers adhere together into a lipid bilayer membrane [6, 7]. This bilayer provides a suitable scaffold for the reconstitution of stimuli-responsive biomolecules, thus allowing for applications such as biosensing [8] and osmotic actuation [9] through the controlled exchange of fluid and ions between the droplets.

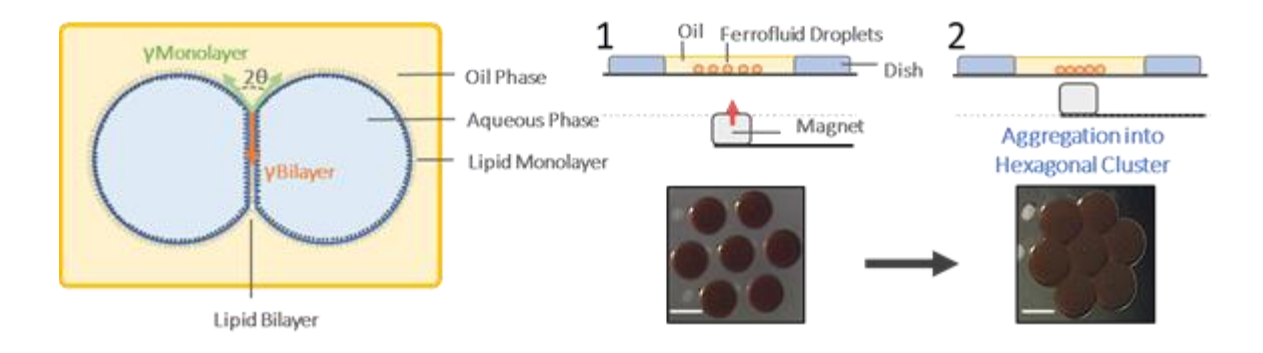


Figure 4.1- A lipid membrane can be formed at the interface of two nanoliter lipid-coated aqueous droplets in an oil reservoir by bringing these droplets into contact. The membrane may be approximated as a capacitor in parallel with a high-impedance resistor whose dimensions are dictated by the balance of surface tensions at the surrounding annulus. At equilibrium, the bilayer tension is balanced by two equal monolayer tensions deviating from the bilayer centerline with an angle θ as shown. When multiple droplets are brought together, more complex DIB structures can be formed. This is accomplished through

ferrofluids in this work, bringing the droplets together using a permanent magnet. Scale bar is $800 \ \mu m$.

Without transporters, these lipid-based membranes are nearly impermeable to ions. A widely accepted electrical representation for these membranes is the Hodgkin-Huxley model [10], where a single DIB is represented as a capacitor in parallel with a variable resistor representing the selective transport [11]. Consequently, any electrical potential applied across a web of DIBs will be divided across multiple membranes governed by the relative dimensions and locations of the bilayer interfaces. These membranes are also dynamic [12] and their equilibrium dimensions are dictated by the balance of monolayer and bilayer tensions at the point of contact as shown in Figure 4.1 [13]. This enables a response to mechanical constraints which has been demonstrated in the literature, both for the regulation of the adhered membrane area [14] as well as the development of biological mechanosensors [12, 15-17].

While a single bilayer is suitable for biophysical studies of membrane properties and transport [17-20], a unique strength of the DIB technique lies in its scalability. By connecting multiple droplets [3, 4, 11, 21], larger DIB networks may be formed. These networks exhibit emergent properties [22], where the observed response of the network is controlled by the gradual collective exchange of contents between neighboring droplets within the network. As an example, it is possible to set some initial gradient within the DIB network that powers the network functionality for applications such as osmotic actuation [3, 13] and the creation of biologically-inspired batteries [23]. A downside to this methodology is that once the network is formed, diffusion will initiate between the

neighboring droplets and the stored energy will begin to gradually dissipate. This introduces complications when developing droplet-based materials for long-term use, since the majority of DIB applications use static architectures that do not change over the material lifespan. Living cellular organisms circumvent this in part by constantly reshaping and adapting their membrane architecture, which has yet to be incorporated into a DIB platform.

A proposed solution for these static DIB network architectures is the use of selective droplet coalescence, where target membranes are ruptured to trigger network reconfiguration. The structure of the adhered network as a whole obeys classical emulsion mechanics and will seek new equilibrium configurations once a membrane is removed from consideration. This leads to a rearrangement of the droplets and may be used to form or separate existing membranes or complete pathways for transport as shown in Figure 4.2. Selective membrane collapse has already been used to facilitate mixing between two droplets [18] for similar applications but has not been applied towards larger droplet networks.

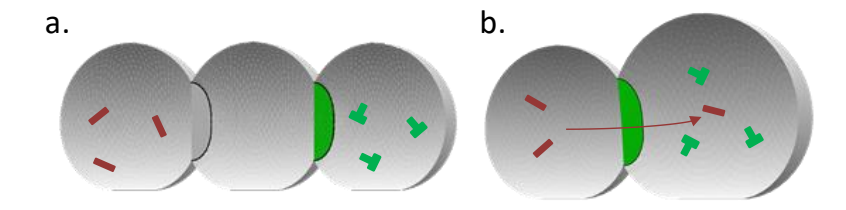


Figure 4.2- Cross-sectional schematic of microdroplets with adhered interfaces. Green interfaces indicate lipid membranes with available pores for transport. While "bare" membranes provide an impermeable barrier to most species, restructuring the network by coalescing the rightmost two droplets allows for pore insertion in the remaining membrane. This enables passive diffusion between the remaining adjacent droplets post-coalescence.

To study the mechanics of DIB network reconfiguration through coalescence, clusters of droplets will be created and allowed to adhere into connected DIB networks. The interfacial membranes within these structures will then be selectively ruptured through an electrical pulse, causing a redistribution of the fluid volume and adjustment of the remaining droplets. A model is proposed based on the minimization of the interfacial energy to capture these reconfiguration events and will be validated against experimental results. The goal of the work is identifying methods for droplet network reconfiguration to enable on-demand release of stored internal gradient.

4.3. Materials and Methods

Ferrofluids

A ferrofluid solution was used to easily manipulate the droplets into networks [24]. Ferrofluids solutions are stable colloidal suspensions of magnetic nanoparticles coated with a surfactant to prevent aggregation within a carrier fluid [25]. Ferrofluid droplet motion may be guided through externally applied magnetic fields. The ferrofluid solutions used in this work consisted of a stable aqueous suspensions of magnetite (γ-Fe₂O₃) [24] with a nanoparticle concentration of 0.46% by volume. 250 mM Potassium Chloride (KCl, Sigma-Aldrich, St. Louis, MO) and 10 mM 3-(N-morpholino) propanesulfonic acid (MOPS, Sigma-Aldrich, St. Louis, MO) salts were added. Solutions were systematically filtered (Sterile Syringe Filter 0.2μm PES, VWR) and sonicated prior to each use for a minimum of 20 minutes to ensure homogeneity. Previous research has established that these ferrofluids are compatible with DIB networks and minimally influence the membrane properties [25].

Lipid Solutions

The lipid-out technique was used in this work, dissolving the lipids in the oil phase [26]. Zwitterionic lipids (1,2-diphytanoyl-sn-glycero-3-phosphocholine (DPhPC), Avanti Polar Lipids, Alabaster, AL) were dissolved in a 1:1(volume: volume) mixture of silicone oil AR20 and hexadecane oil (Sigma-Aldrich, St. Louis, MO) at a concentration of 0.5 mg/ml throughout all of the experiments. Hexadecane was used as a solvent in order to minimize the amount of oil retained in the bilayer upon membrane formation [27], while silicone oil AR20 was mixed with it to enhance the stability of the bilayer, reduce gravitational effects [3], and reduce the monolayer formation time as shown in the literature [28]. All lipid-oil solutions are sonicated (Avanti Sonicator, Avanti Polar Lipids, Alabaster, AL) upon fabrication and before each experiment. Solutions were stored at 2-8 °C when not in use.

4.4. Experimental Methodology

DIB Network Formation

The tip of a pulled pipette (KWIK-Fil Borosilicate Glass Capillaries, World Precision Instruments, Inc) filled with the previously described ferrofluid solution was introduced into a Sylgard 184 (Dow Corning Corporation, Midland, MI) Silicone Elastomer Base (PDMS) (13:3 v:v ratio of base to curing agent) dish comprised of a 15 mm diameter circular hole at the center of a 30 mm square surface. Ferrofluid droplets of equal diameter (800 µm) were systematically injected into the solution using a pressure-based injector (FemtoJet 4i, Eppendorf, Hauppauge, NY). After allowing time for lipid monolayer formation at their oil-water interfaces, droplets were collected by a permanent magnet. The droplets were gradually drawn together and bilayers spontaneously formed at their interfaces as they came into contact creating a simple tightly-packed hexagonal-

shaped DIB network as shown in Figure 4.1. After membrane formation, the magnet was removed, and the droplets retained their connected framework. This approach allowed for the rapid creation of DIB networks.

The electrical properties of the network were measured using agarose-coated (2% by weight EZ Pack Agarose LE, Molecular Biology Grade, Benchmark Scientific, Sayresville, NJ) silver/silver-chloride (Ag/AgCl) electrodes (125 µm in diameter, GoodFellow, Coroapolis, PA) mounted on three-axis manual micromanipulators (Siskiyou, Grants Pass, OR). Upon network formation and magnet removal, the electrodes were introduced into the desired droplets. Failure in these networks was induced by applying a 1V electrical impulse to the desired failure locations in the networks causing an instantaneous rupture of select membranes through electroporation [29]. Post-failure images were acquired both when electrodes were still in the oil reservoir as well as post taking them out.

Modeling Methodology

The goal of this work is to explore the dynamic reconfiguration of DIB networks when specific droplet pairs coalesce due to the electrical pulse. The coalescence of two previously distinct droplet volumes generates a shift in the network configuration and may be used to study the change in network behaviors. A two-component model is necessary to capture the electrical properties of the DIB network as well as the configuration post-coalescence.

The mechanical properties of emulsive systems are often described as the summation of the interfacial energies, or the product of the total surface areas multiplied by the corresponding surface tension [30, 31]. A classical DIB system is mainly defined by

two surface tensions $\gamma_{monolayer}$ and $\gamma_{bilayer}$, where $\gamma_{monolayer}$ refers to the monolayer surface tension and $\gamma_{bilayer}$ refers to the bilayer surface tension as shown in Figure 4.1. The total energy in a DIB network may be approximated as the sum of the interfacial tensions and their areas $A_{monolayer}$ and $A_{bilayer}$:

$$E = \gamma_{monolayer} A_{monolayer} + \gamma_{bilayer} A_{bilayer}$$
(4.1)

The equilibrium configuration may be found as the minimization of the total energy with the volume of the fluid as a constraint. This leads to the formation of the lipid bilayer membranes if the energy of adhesion is positive [27, 32, 33], defined in DIBs as:

$$\Delta F = A_{membrane} (2\gamma_{monolayer} - \gamma_{bilayer}) \tag{4.2}$$

This equation describes the change in interfacial energy when replacing two lipid monolayers with a single lipid bilayer. According to parametric studies on DIB configurations this value is optimized in cases with a 50/50 hexadecane/silicone oil AR20 mixture [27].

The ratio of the equilibrium bilayer area with respect to those of the monolayers is governed by the contact angle between the droplets (θ_m) [13] (Figure 4.1) resulting from the balance of tensions at the annulus of contact. As the DIB is formed, the monolayers exert a tension on the interfacial membrane, causing it to grow and expand. This continues until the tension in the bilayer reaches its equilibrium value dictated by the monolayer tensions as shown in Equation (4.3):

$$2\gamma_{monolayer}\cos(\theta_m) = \gamma_{bilayer} \tag{4.3}$$

Surface Evolver Model

Based on the observed properties of the emulsive membrane network, the network's equilibrium structure may be approximated by minimizing the interfacial energies with constant volume constraints [31]. However, the equations generated for adhered droplets

generally do not allow for an analytical solution, so numerical approximations are necessary.

To this end the open-source computational software Surface Evolver [34] was used to predict the equilibrium shapes of the droplet clusters. An initial approximation of the droplet surfaces is provided, and the software seeks to find the lowest interfacial energy configuration available with the given constraints. DIBs were approximated in this software by defining their adhered interfaces, relative density, fluid volumes, and interfacial tensions. While Surface Evolver provides a suitable platform for studying coalescence events in networks of DIBs it can only predict the equilibrium state of the system i.e. it cannot capture the momentum of the droplets or the mechanics of membrane creation/destruction. Therefore, the results obtained may be used to guide the development of these membrane clusters with some limitations.

Surface Evolver Model Initialization

In DIB networks the droplets often adapt a hexagonally packed geometry. Experimental results obtained for seven ferrofluid droplets demonstrated this as shown Figure 4.1. Dodecagonal prisms are the most efficient at capturing the final configuration of hexagonal packing and thus were used to present the initial conformation of the droplets. The monolayer and bilayer surface tensions and the specific gravity considered in the model are shown in Table 4.1, and an example of a converged solution is shown in Figure 4.3. Monolayer and bilayer surface tensions were determined by comparing the experimental results and model predictions and are well within the expected ranges for this DIB configuration [25, 27].

Droplet coalescence was simulated by setting the collapsed interface's tension to zero, effectively removing the interface from energy minimization considerations (Equation 4.1). This allows the interface to deform and expand freely as needed with no cost. The volumes of the coalesced droplet pair are combined, and the zero-tension interface allows the coalesced droplets to form one larger droplet. The surrounding droplets are consequently pulled into a new equilibrium, allowing for network reconfiguration.

Table 4.1- Surface Evolver Model Inputs.

Variable	Value	Source
Fluid phase density	$1007~kg/m^3$	Measured
Oil phase density	890 kg/m^3	Measured
Monolayer surface tension	1.12 mN/m	Calibrated [24, 27]
Bilayer surface tension	1.825 mN/m	Calibrated [24, 27]

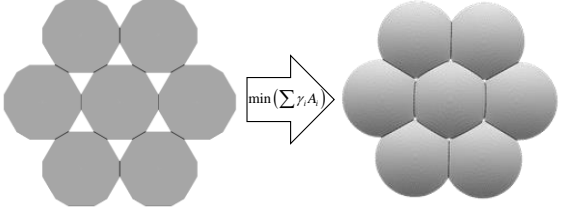


Figure 4.3- The ferrofluid droplets were modeled as dodecagonal prisms elements in Surface Evolver. The resulting droplet morphologies after minimization of the interfacial energies match experimental observations.

Electrical Circuit Models for DIB networks

The failure mechanism selected for this study is coalescence through electroporation or exceeding the voltage threshold necessary for membrane failure. Recall that single DIB membranes without embedded channels may be approximated as a capacitor in parallel with a high amplitude resistor [35-38]. The balance of the resistances in the aqueous phases and across the membrane allows for a simplified model at low

frequencies of operation where the resistance of the aqueous phases is ignored [38] as shown in Figure 4.4. The membrane capacitance and conductance both scale with the area of the membrane, and values for the specific capacitance and conductance are obtained from the literature as shown in Table 4.2.

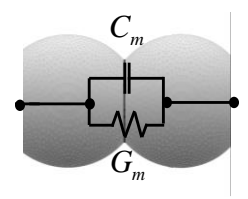


Figure 4.4- The electrical model for a single membrane consists of a capacitor and resistor in parallel. This stencil may be combined into larger networks to produce linear systems of differential equations describing the voltage drop across each membrane with prescribed boundary conditions.

Table 4.2- Circuit Model Inputs.

Variable	Value	Source
Bilayer specific capacitance	$0.583 \ \mu F/cm^2$	[24]
Bilayer specific conductance	$0.14~\mu\text{S/cm}^2$	[39]

The bilayer dimensions are exported from the Surface Evolver predictions and the membrane dimensions are assumed constant up until failure with no electrowetting [38, 39], providing an electrical approximation of the DIB network using the per-area values in Table 4.2. The current through the membrane may be calculated using Equation 4.4, where G_m is the membrane conductance, C_m is the membrane capacitance, and dV/dt is the change in the transmembrane potential with respect to time. Kirchhoff's current law is employed for each droplet to write a balance of current thus creating a linear system of differential equations for the nodal voltages, one value for each of the droplets within the cluster

(Equation 4.4). This system of differential equations is solved using ode15s in MATLAB. The model results for the nodal voltages show how the voltage is divided across each individual membrane, predicting the likely path of failure under an electrostatic load.

$$[C] \left\{ \frac{dV}{dt} \right\} + [G]\{V\} = 0$$

$$\left\{ \frac{dV}{dt} \right\} = [C]^{-1} (-[G]\{V\})$$
(4.4)

Current is estimated by calculating the necessary current for charging the source droplet. Distribution of the voltage across the membrane network is influenced by the location of the electrodes, configuration of the membranes, and their relative interfacial areas. These may be tuned to accomplish selective destruction of the sacrificial membranes, altering the network shape.

Model Validation

With the coupled electrical-tension model established, it is possible to predict the most likely chain of failure in a droplet network with the application of a voltage and the network configuration post-failure. Seven different cases were examined to test the hypotheses and demonstrate network folding. Each case is built on the seven-droplet structure as seen in Figure 4.3, as this structure was easily achieved using the ferrofluid droplets.

The first case is shown in Figure 4.5, where the applied voltage impulse spanned across the central droplets. The coupled model predicted that the most likely path of failure occurred between the electrodes, matching the experimental observations. Once the central membranes were ruptured by the voltage impulse, the collection of droplets adapt a new configuration, matching the configuration predicted by the Surface Evolver.

To further compare the model predictions against experimental data, a triangle wave voltage is simulated in the model and the resulting square-wave current is compared against experimental data (Figure 4.5.d). The tensions are calibrated to provide a match with the experimental data, and the resulting values are shown Table 4.1. All of these values are appropriate and fall within the expected ranges for ferrofluid DIBs [25] in this particular solvent.

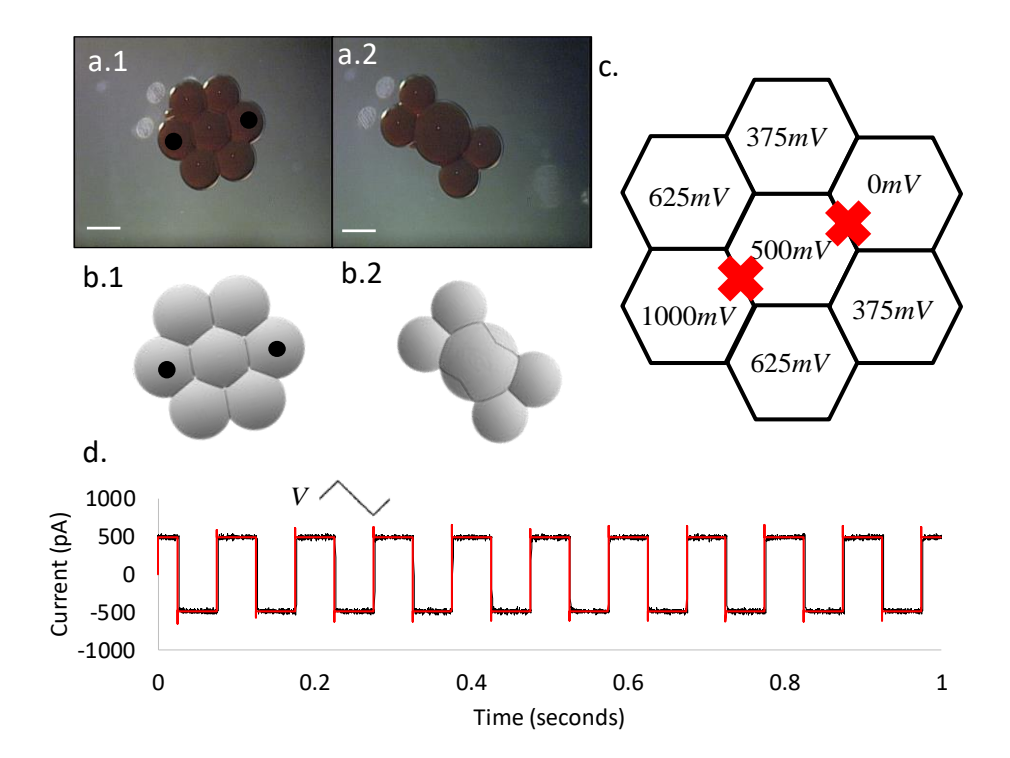


Figure 4.5- Comparison between model predictions and experimental results for failure across the central line of a hexagonally packed structure. a.1. Initial configuration – electrode locations are marked. a.2. The application of the voltage spike resulted in the coalescence of the three central droplets. b.1. The predicted Surface Evolver configuration of the initial set of droplets b.2. The predicted configuration after rupturing the membranes. c. Likely path of failure predicted by the electrical model. d. Comparison of experimentally

measured current and current predicted by the model with the inputs from Table 4.1. Scale bars are $800 \ \mu m$.

This process was repeated for a case where the path of failure was set to occur across the outer ring of the hexagonal-packed droplet structure (Figure 4.6). In this particular instance, the rupture pathway was stochastic, alternating between the central droplets and the outer droplets. This prediction was also shared by the model, showing that the voltage drops across the two membrane pathways were equivalent. The configuration post-coalescence matches as well. Interestingly, when failure occurred across the outer droplet ring, the adhesive forces between the droplets caused the outer droplet ring to contract and compress the central droplets. Since the density of the oil is similar to the density of the aqueous droplets and the selected oil mixture maximizes the energy of adhesion [27], the collapsed 2D structure is able to elevate the central droplet to accommodate the ring contraction (Figure 4.6.a.3). This may provide an opportunity for folding planar DIB structures into 3D structures when gravitational effects are minimized.

The current is compared again in a similar fashion to the procedure described for Figure 4.5. The same values (Table 4.1, Table 4.2) used for calibration (Figure 4.5) are employed as these studies were taken for the same ferrofluid and lipid solutions, and a match is produced between the experimental data and model predictions. This provides further assurance that the Surface Evolver model is appropriate for predicting the equilibrium configurations of DIB networks, and that the membranes formed in the experimental work are similar to membranes produced in the past.

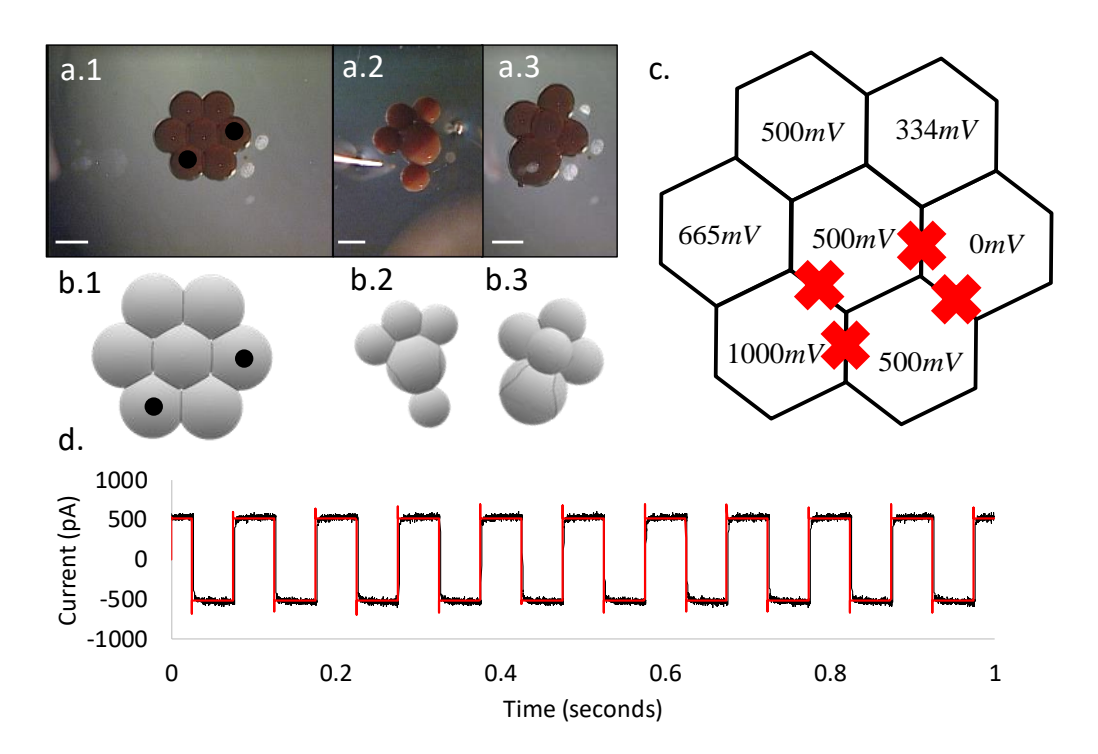


Figure 4.6- Comparison between model predictions and experimental results for failure across the outer ring of a hexagonally packed structure, demonstrating two possible coalescence pathways. a.1. Initial configuration – electrode locations are marked. a.2-3. Configurations after coalescence. b.1. The predicted Surface Evolver configuration of the initial set of droplets b.2-3. The predicted configuration after rupturing the membranes. c. Likely paths of failure predicted by the electrical model. Comparison of experimentally measured current and current predicted by the model with the inputs from Table 4.1. Scale bars are 800 μm.

Two additional cases are summarized in Figure 4.7. As before, the predicted morphologies post-coalescence and paths of coalescence match the experimental results, illustrating the effectiveness of the Surface Evolver approach for predicting DIB network configuration.

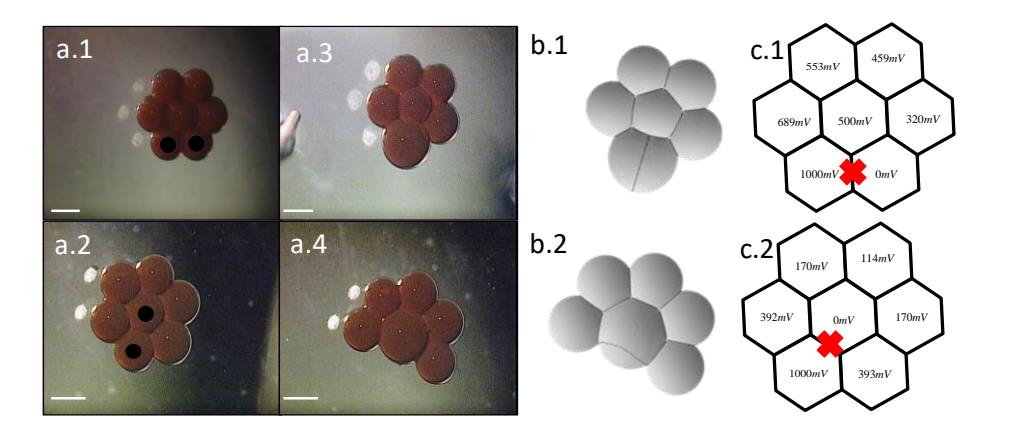


Figure 4.7- Two additional comparison cases. a.1-2 Initial configuration – electrode locations are marked. a.3-4 Configuration post coalescence. b.1-2. The predicted configurations after rupturing the membranes. c.1-2 Likely paths of failure predicted by the electrical model. Scale bars are $800 \, \mu m$.

4.5. Discussion of Experimental Comparisons

From the preliminary results, the failure of designated sacrificial membranes results in an intuitive contraction of collapsed droplets. This contraction effectively redistributes the remaining attached droplets and demonstrates the capability to fold a two-dimensional network into a three-dimensional structure as shown in Figure 4.6. It should be noted that this behavior is dependent on the DIB composition – if for example hexadecane alone was used as the oil phase, the energy of adhesion would be diminished, gravitational forces will increase, and the droplets would likely separate rather than fold together [27].

4.6. Model Extension

With the model validated against experimental data for both the mechanical (Surface Evolver via equilibrium configurations) and electrical (capacitor-resistor approximation via membrane failures and measured currents) components, the next step is

to investigate how these sacrificial membranes may be employed to allow for changes in larger DIB networks.

The mechanics of droplet coalescence are relatively simple for a two droplet pair as shown in Figure 4.8. As the membrane fails the two spherical caps collapse together, causing a contraction of the droplet heights and an expansion along the former adhered interface. The equations for this collapse may be written as a function of the contact angle as shown in Equation 4.5, with the necessary assumption that the droplets will behave as spherical caps with a constant volume per droplet Vol. If the droplets coalesce, the contact angle is effectively 90 degrees as predicted by the modified Young's equation (Equation 4.3) and the radius R increases while the cap height h is reduced, causing simultaneous contraction and expansion as shown in Figure 4.8.b.

$$R = \left(\frac{3Vol}{\pi(\cos\theta + 1)^{2}(2 - \cos\theta)}\right)^{\frac{1}{3}}$$

$$h = \left(\frac{3Vol}{\pi(\cos\theta + 1)^{2}(2 - \cos\theta)}\right)^{\frac{1}{3}}(1 + \cos\theta)$$
a.
$$b.$$

$$\theta_{m} : 90^{\circ}$$

$$h$$

$$\frac{1}{2R}$$

Figure 4.8- The droplets in a single DIB may be approximated as two spherical caps with a shared interface. It is possible to directly write functions for h and R as functions of and Vol by assuming this geometry and constant droplet volumes. Setting the contact angle to 90° produces a coalesced droplet pair as shown in b.

This coupled contraction-expansion mechanic adequately describes the observed behaviors in the collapsed networks. However, there are limitations to this – these droplets are effectively soft particles and are capable of adapting non-spherical configurations if necessary. The assumption of the spherical cap geometry, while useful, is not always valid.

This was demonstrated previously in several DIB studies [12, 17, 40], where two droplets were compressed together to regulate the size of the adhered interface. This is a modification from the previous discussion – rather than defining the membrane tension and assuming spherical cap geometry, external constraints are enforced on the droplets, forcing them to adapt non-spherical configurations. While equations for compressed droplets have been derived assuming non-wetting conditions [31], these do not match the DIB conditions and Surface Evolver is necessary for determining the surfaces.

Plotting the predicted total interfacial energy while compressing a droplet with two interfacial membranes shows a net increase in the total energy, even as the interfacial tensions remain unchanged (Figure 4.9). This represents a resistance to the deformation, demonstrating that while the droplet may be deformed away from a spherical case it will exert a restitution force in an attempt to regain the spherical shape. In addition, if tension is applied to the droplets there is a point where the membranes are separated entirely, and the droplet resumes a spherical shape without the adhesive membranes.

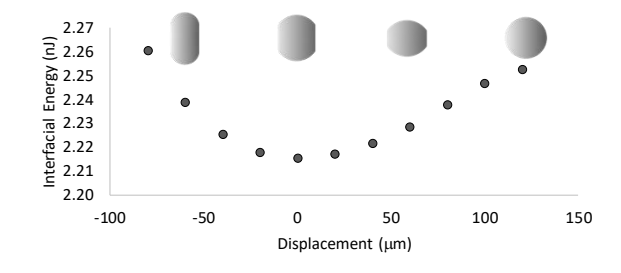


Figure 4.9- A single droplet (400 µm radius) within a DIB chain is constrained from equilibrium in Surface Evolver on both sides by the specified displacement. As the droplet

is perturbed from a spherical cap, the total interfacial energy is increased. If tension is applied, this leads to the eventual separation of the adhesive membranes at the horizontal interfaces. Images across the top are taken from Surface Evolver.

This illustrates a crucial component of the DIB restructuring phenomena. While each droplet connection may be loosely approximated as a spring, these springs are also capable of disconnecting once the droplets are sufficiently separated. Therefore, it is possible to tailor a coalescence event that causes contraction in the droplet network where certain adhesive interfaces or transport bridges are removed, dramatically reshaping the network behavior.

This elasticity of the droplets must be considered in the framework of larger networks as well where the entire network adapts a mutually agreeable configuration. Combining the observations from Figure 4.8 and Figure 4.9 predicts that coalescence will generate a combination of forces in the contracting and expanding directions as the coalesced droplet attempts to expand to a spherical configuration. In networks, the balance of adhesive forces between the droplets will restrict this motion. As shown in Figure 4.10, a small coalescence event in the center of a tightly packed DIB network results in an imperceptible change at the outer boundary – while the coalesced droplets do exert a force on their surrounding neighbors, they are not able to resume a spherical shape. The droplets that border the coalesced group are distorted from their ideal shapes, while the impact is diminished as we move further from the center.

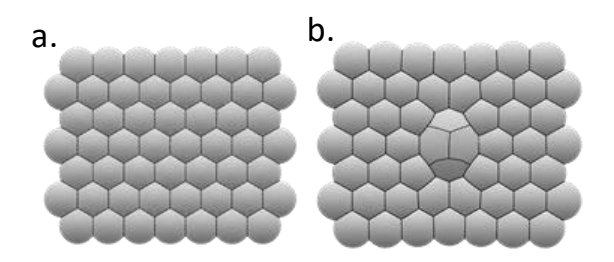


Figure 4.10- In larger networks, droplet coalescence exerts forces on neighboring droplets but may be constrained by surrounding droplets. While rupturing a single droplet pair is intuitive, larger networks behave as balanced structures and seek the minimum interfacial energy for the entire network.

Two additional example cases are presented below in Figure 4.11. Here the deformation of an interior collection of monodisperse droplets causes a contraction of the surrounding droplets. This forces the droplets to accommodate the new constraints and allows for both the separation of adhered droplets and in some cases allows for the formation of new membranes as previously separated droplets come into contact (Figure 4.11.b.2). These behaviors are capable of initiating the exchange between neighboring droplets on demand, providing a methodology for enabling the DIB network functionality post-formation. As DIB complexity continues to increase, this will allow for dynamic droplet networks that are capable of changing configuration on demand.

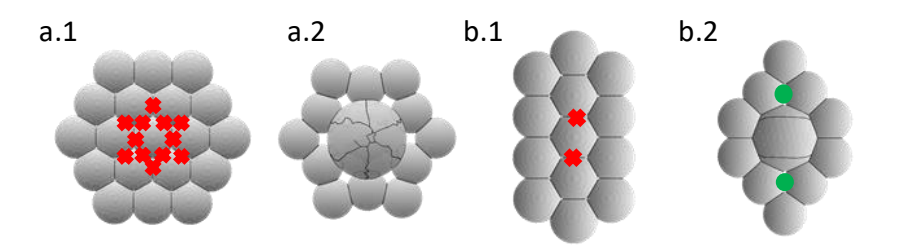


Figure 4.11- Two example cases showing the evolution of a network post formation. Red symbols mark membranes that are selectively ruptured and green symbols indicate

locations where new membranes may form after network coalescence. These examples demonstrate the ability to fold the network into new configurations through tailored destruction of interfacial membranes.

4.7. Conclusions

The droplet interface bilayer (DIB) technique is used to form complex networks of aqueous compartments joined by biological membranes. The configuration of such networks is dictated by the minimization of the interfacial energies present within the adhered droplet morphologies. As a result, any specific changes in the properties of these network or in the external mechanical constraints will cause the entire network to shift in search of a new equilibrium. This gives control over the membrane interfacial areas which may be tuned accordingly.

Here the reconfiguration of droplet networks was examined through a coupled mechanical/electrical framework. The results demonstrated that a DIB network is capable of dramatically changing its transport properties through controlled membrane collapse – changes in one region of the DIB cluster also influence the equilibrium configuration through the adhesive properties of the droplet interfaces. In this work failure was controlled through an applied voltage shock, but there are many other avenues available for selective collapse. Selective coalescence allows for the reconfiguration of droplet networks, which will allow for on-demand activation of DIB functionalities.

4.8. References

1. Bayley, H., et al., Droplet Interface Bilayers Royal Society of Chemistry 2008. 4(12): p. 1191-1208.

- 2. Peterman, M.C., et al., Ion Channels and Lipid Bilayer Membranes Under High Potentials Using Microfabricated Apertures. Biomedical Microdevices, 2002. 4(3): p. 231-236.
- 3. Villar, G., A.D. Graham, and H. Bayley, A tissue-like printed material. Science, 2013. 340(6128): p. 48-52.
- 4. Booth, M.J., et al., Light-activated communication in synthetic tissues. Sci Adv, 2016. 2(4): p. e1600056.
- 5. Nguyen, M.-A., et al., Hydrodynamic trapping for rapid assembly and in situ electrical characterization of droplet interface bilayer arrays. Royal Society of Chemistry-Lab on a Chip, 2016. 16: p. 3576-3588.
- 6. Bibette, J., et al., Stability Criteria for Emulsions. Physical Review Letters 1992. 69(16): p. 2440-2443.
- 7. de Gennes, P.-G., Some remarks on coalescence in emulsions or foams. Chemical Engineering Science, 2001. 56(19): p. 5449-5450.
- 8. Steller, L., M. Kreir, and R. Salzer, Natural and artificial ion channels for biosensing platforms. Analytical and bioanalytical chemistry, 2012: p. 1-22.
- 9. Sundaresan, V. and D. Leo, Modeling and characterization of a chemomechanical actuator using protein transporters. Sensors and Actuators B, 2008. 131: p. 383-393.
- 10. Hodgkin, A.L., A. Huxley, and B. Katz, Measurement of current-voltage relations in the membrane of the giant axon of Loligo. The Journal of Physiology, 1952. 116(4): p. 424-448.

- 11. Hwang, W.L., et al., Electrical Behavior of Droplet Interface Bilayer Networks: Experimental Analysis and Modeling. Journal of the American Chemical Society, 2007. 129(38): p. 11854-11864.
- 12. Freeman, E.C., et al., The mechanoelectrical response of droplet interface bilayer membranes. Soft Matter, 2016. 12(12): p. 3021-31.
- 13. Dixit, S.S., et al., Droplet shape analysis and permeability studies in droplet lipid bilayers. Langmuir, 2012. 28(19): p. 7442-51.
- 14. Sarles, S.A. and D.J. Leo, Regulated attachment method for reconstituting lipid bilayers of prescribed size within flexible substrates. Anal Chem, 2010. 82(3): p. 959-66.
- 15. Sarles, S.A., J.W. Madden, and D.J. Leo, Hair cell inspired mechanotransduction with a gel-supported, artificial lipid membrane. Soft Matter, 2011. 7: p. 4644-4653.
- 16. Tamaddoni, N., E.C. Freeman, and S.A. Sarles, Sensitivity and directionality of lipid bilayer mechanotransduction studied using a revised, highly durable membrane-based hair cell sensor. Smart Materials and Structures, 2015. 24(6): p. 065014.
- 17. Najem, J.S., et al., Activation of bacterial channel MscL in mechanically stimulated droplet interface bilayers. Sci Rep, 2015. 5: p. 13726.
- 18. Kong, L., et al., Chemical polyglycosylation and nanolitre detection enables single-molecule recapitulation of bacterial sugar export. Nat Chem, 2016. 8(5): p. 461-9.
- 19. Syeda, R., et al., Screening blockers against a potassium channel with a droplet interface bilayer array. J Am Chem Soc, 2008. 130(46): p. 15543-8.
- 20. Holden, M.A. and H. Bayley, Direct introduction of single protein channels and pores into lipid bilayers. Journal of the American Chemical Society, 2005. 127(18): p. 6502-6503.

- 21. Bayoumi, M., et al., Multi-compartment encapsulation of communicating droplets and droplet networks in hydrogel as a model for artificial cells. Scientific Reports, 2017. 7: p. 45167.
- 22. Maglia, G., et al., Droplet networks with incorporated protein diodes show collective properties. Nature Nanotechnology, 2009. 4(7): p. 437-440.
- 23. Xu, J., F.J. Sigworth, and D.A. LaVan, Synthetic protocells to mimic and test cell function. Adv Mater, 2010. 22(1): p. 120-7.
- 24. Makhoul-Mansour, M., et al., Ferrofluid-Based Droplet Interface Bilayer Networks. Langmuir, 2017. 33(45): p. 13000-13007.
- 25. Makhoul-Mansour, M., et al., Ferrofluid-Based Droplet Interface Bilayer Networks. Langmuir, 2017.
- 26. Hwang, W.L., et al., Asymmetric droplet interface bilayers. J Am Chem Soc, 2008. 130(18): p. 5878-9.
- 27. Taylor, G.J., et al., Direct in situ measurement of specific capacitance, monolayer tension, and bilayer tension in a droplet interface bilayer. Soft Matter, 2015. 11(38): p. 7592-605.
- 28. Wauer, T., et al., Construction and manipulation of functional three-dimensional droplet networks. ACS Nano, 2014. 8(1): p. 771-9.
- 29. Kotnik, T., et al., Cell membrane electroporation-Part 1: The phenomenon. IEEE Electrical Insulation Magazine, 2012. 28(5): p. 14-23.
- 30. Berthier, J. and K.A. Brakke, The physics of microdroplets. 2012: John Wiley & Sons.

- 31. Lacasse, M.D., G.S. Grest, and D. Levine, Deformation of small compressed droplets. Phys Rev E Stat Phys Plasmas Fluids Relat Interdiscip Topics, 1996. 54(5): p. 5436-5446.
- 32. Thiam, A.R., N. Bremond, and J.r.m. Bibette, From Stability to Permeability of Adhesive Emulsion Bilayers. Langmuir, 2012. 28(15): p. 6291-6298.
- 33. Leal-Calderon, F., V. Schmitt, and J. Bibette, Emulsion science: basic principles. 2007: Springer Science & Business Media.
- 34. Brakke, K.A., The Surface Evolver. Experimental Mathematics, 1992. 1(2): p. 141-165.
- 35. Creasy, M.A., et al., Deterministic model of biomolecular networks with stimuliresponsive properties. Journal of Intelligent Material Systems and Structures, 2014. 26(8): p. 921-930.
- 36. Freeman, E.C., et al., Multiscale modeling of droplet interface bilayer membrane networks. Biomicrofluidics, 2015. 9(6): p. 064101.
- 37. Hwang, W.L., et al., Electrical behavior of droplet interface bilayer networks: experimental analysis and modeling. J Am Chem Soc, 2007. 129(38): p. 11854-64.
- 38. Creasy, M.A., et al., Deterministic model of biomolecular networks with stimuliresponsive properties. Journal of Intelligent Material Systems and Structures, 2014: p. 1045389X14536004.
- 39. Venkatesan, G.A., et al., Adsorption kinetics dictate monolayer self-assembly for both lipid-in and lipid-out approaches to droplet interface bilayer formation. Langmuir, 2015. 31(47): p. 12883-12893.

40. Najem, J.S., et al., Mechanics of Droplet Interface Bilayer "Unzipping" Defines the Bandwidth for the Mechanotransduction Response of Reconstituted MscL. Advanced Materials Interfaces, 2016.

CHAPTER 5

IMBUING MEMBRANOUS MATERIALS WITH MAGNETICALLY-DRIVEN RECONFIGURATION EVENTS 4

 $^{^4}$ M. M. Makhoul-Mansour, J. B. El-Beyrouthy, L. Mao, E. C. Freeman, Submitted to Scientific Reports $27/09/2021.\,$

5.1. Abstract

Adaptive and bioinspired droplet-based materials are assembled using the droplet interface bilayer (DIB) platform, where lipid coated aqueous microdroplets are adhered together into interfacial bilayer membranes inspired by the boundaries of living cells. Recent efforts have been focusing on enabling DIB-systems with the ability to sense, actively respond and adapt to external environmental conditions. Inspired by nature where function follows form, adaptive architectures within the DIB-platform are explored and their sensitivity to magnetic force fields investigated to better achieve these desired functionalities. Unlike their natural inspiration, DIB membranes are linked to the properties of both adhered droplets; hence, rearranging the droplets within a larger structure alters the internal patterns of communication by separating and reforming the lipid membranes. In this work heterogeneous structures of magnetic and non-magnetic aqueous droplets are used. The oil solvent/magnetic particle concentration combinations are first optimized using a coupled experimental -computational approach; then the recommended material parameters are used in larger DIB structures. Activating external magnetic force fields generates transition rearrangement events in the membranes bordering magnetic compartments. In these incidents, microdroplets separate and reach new equilibrium positions, modifying the underlying membranous architecture and adjusting the material functionality. These findings further enable the development of smart biocompatible materials where internal structure dictates functionality.

5.2. Introduction

Defined by its goal of constructing minimal cellular systems and tissue-inspired biomaterials, protocell creation is a subdiscipline of bottom-up synthetic biology that has opened new research pathways from digitized chemical computing platforms that respond to the environment and drug carriers that unpack inside the body [1] to passive biocompatible sensors and novel soft robotic actuators where more traditional components such as solenoids and resistors may not be entirely compatible for use [2, 3]. In these applications materials inspired by cellular organisms attempt to embed some the capabilities of their living counterparts [4, 5] by approximating select characteristics of living cells. Ganti's chemoton [6], an abstract model for the fundamental unit of life, provides a set of criteria describing the mode of operation of living systems and thus can serve as a list of goals for materials inspired by living tissues [7] as illustrated in Figure 5.1. In this manuscript we will focus primarily on implementing structural adaptation in bioinspired membranous materials.

The droplet interface bilayer (DIB) technique, a particular subfield of cell inspired biomaterials involving stabilized adhesive emulsions [8, 9], assembles phospholipid membranes at the interfaces of surfactant-coated aqueous droplets dispersed in an oil environment [10, 11], enabling the creation of soft bioinspired structures [9, 12, 13]. Phospholipid surfactants may be dispersed in either phase or in both phases simultaneously [14-17]. These lipids then self-assemble at the droplet surfaces. Upon bringing the lipid-coated droplets into contact, a lipid bilayer forms spontaneously in a zipping mechanism expelling residual oil during the process and adhering the droplets together [10, 11, 18]. A particular formulation of stabilized adhesive emulsions [8, 10, 11, 19], the DIB platform may be used for the construction of membrane-based materials [15, 19-24]. Their liquid-in-liquid geometry allow for the repetitively assembly and separation of multiple lipid

bilayers, the produced networks are scalable and modular [12, 13, 19, 25-27], and the technique permits the simple creation of asymmetric membranes [14, 28].

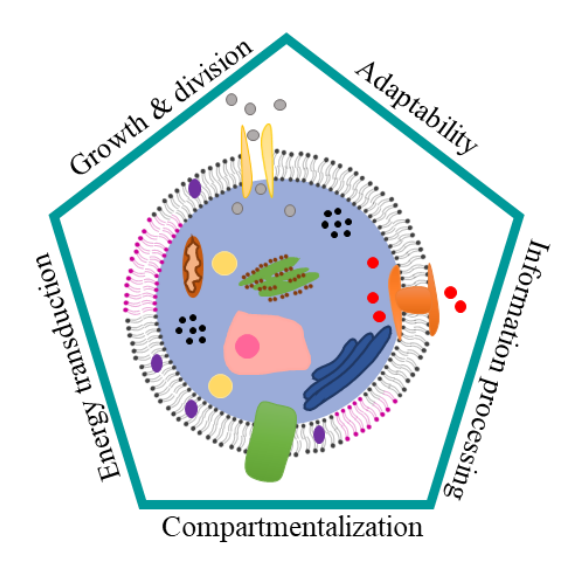


Figure 5.1- Schematic representation of the five main foundational rules that living systems follow to survive and flourish. According to Ganti's chemoton model these criteria include compartmentalization, growth and division (metabolism), information processing, energy transduction (self-maintenance), and adaptability.

DIB tissues formed using the previously described approach are often used as static structures. Owing to their structure (hydrophobic core), lipid membranes are selectively permeable hence the absence of communicative pathways between neighboring levels and compartments. Moreover, the structural layout of these tissues is very much confined to the structure selected during assembly and cannot shift or internally rearrange. And while such membranous tissues offer great opportunities for the study of simplified tissue mechanics and fundamental scientific processes in interfaces and self-assembly, a static membranous structure poses limitations when exploring applications where adaptability is required. Recent research efforts have concluded that DIB-based materials can be

functionalized to adapt to external triggers by either a) changing their internal chemical composition or b) shape-shifting [9]. The former (composition evolution) is traditionally accomplished via targeted permeabilization of interfacial membranes allowing for molecular flow akin to chemical computing [29, 30]. Interfacial membranes are functionalized either with stimuli-responsive molecules (enabling sensitivity to light [26, 31], voltage [32, 33], or mechanical inputs, [34-36]) or by impacting the behavior of lipid molecules to form diffusive pathways upon exposure to light [17, 37, 38]. Meanwhile, the latter (shape-shifting) is accomplished by inferring changes in the layout of aqueous compartments in response to suitable triggers. This work focuses on imbuing shape-shifting capabilities within DIB-structures that follow mechanisms inspired by natural tissues using magnetic forces.

Shape Shifting DIBs

In single DIB pairs, the dimensions of the adhered interfaces have historically been modified either using direct mechanical contact [34, 35, 39, 40] or voltage-controlled electrowetting effects [41-44]. However larger collections of droplets produce additional complexities for both of these approaches, especially when attempting to manipulate droplets within the center of an adhered structure.

Recent research has explored manipulating and tuning the structure of larger DIB networks. Morphing DIB-based structures, where the overall shape of the adhered droplets is adjusted through swelling and shrinking behaviors of the individual droplets, have been produced successfully in the past. These have been generated either using combinations of thermally-responsive hydrogels [20] and light-responsive nanoparticles [45] or osmotic swelling triggered by tailored composition gradients between adjacent droplets [19].

Furthermore, optics-based manipulation have been investigated using optical tweezers [46, 47] or magnetic particles [15, 45, 48, 49] for either controlling translational motion of the droplet networks or for the initial assembly of the interfaces. Each of these approaches for dynamic DIB materials primarily focuses on changes in the overall network shape. Here, we focus on morphing via adjusting the relative positioning of the droplets within the network. Reconfiguring the droplets leads to a permanent shift within the synthetic tissue between metastable states Combining such reconfigurable DIB network with embedded transporters will alter the pathways of exchange, especially when combined with transmembrane exchanges dependent on membrane asymmetry [17, 28, 37, 38, 50] as old membranes separate and new ones form (Figure 5.2.b).

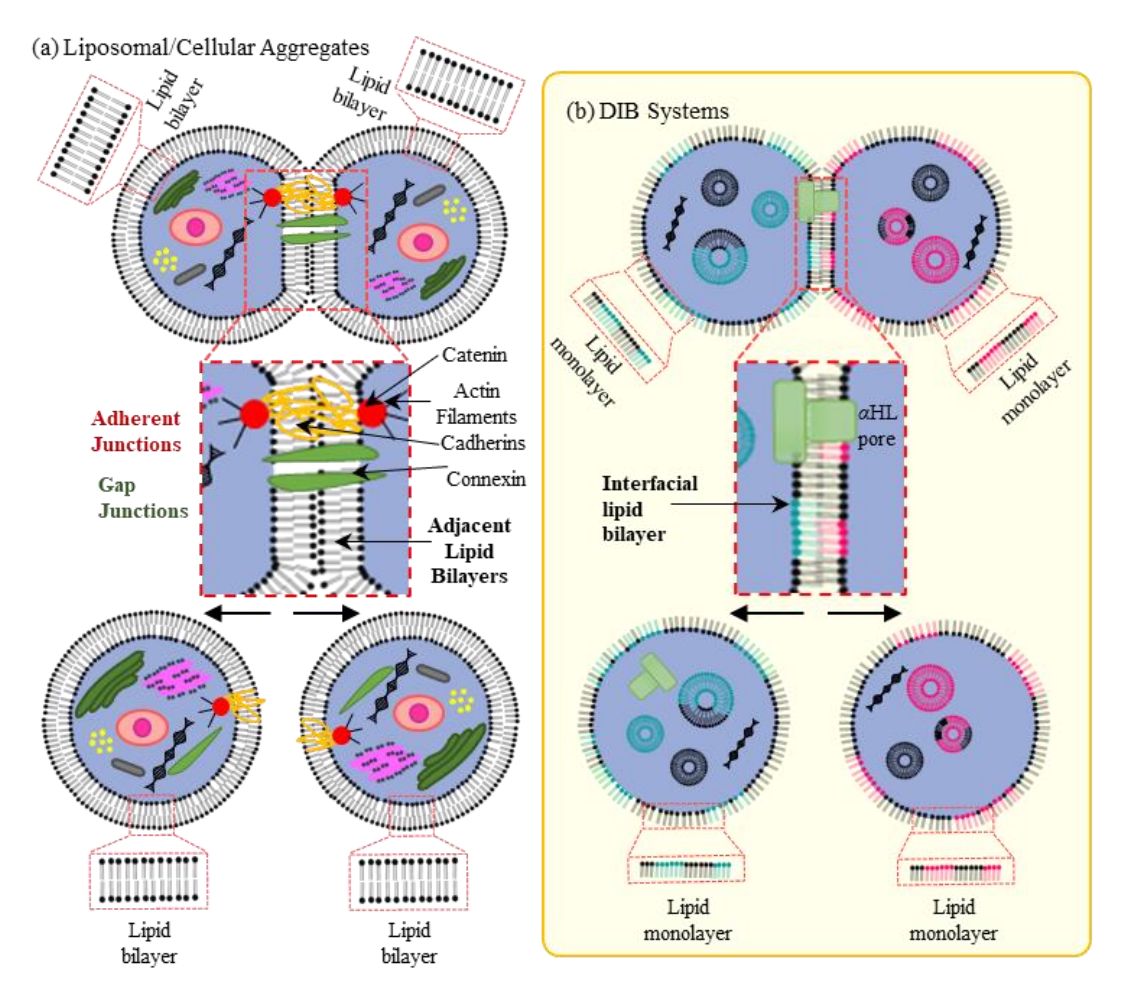


Figure 5.2- Schematic representation of tension driven adhesion in (a) cellular tissues and (b) DIB assemblies. According to the DAH (differential adhesion hypothesis), tissues can be modeled as emulsive systems. The simultaneous presence of multiple degrees of surface tension causes cells to reorganize spontaneously to minimize their interfacial free energy in similar way to droplets in emulsions. In natural living tissues and liposomal aggregates, interfaces are comprised of two adjacent lipid membranes in contrast to DIB-systems where interfaces are formed between adhered lipid monolayers (resulting in a lipid bilayer).

Natural Inspiration

Reconfigurable DIBs are inspired by cellular intercalation events observed during morphogenesis [51-54] including T1 event (intercalation also known as local neighbor exchange) [54, 55], invagination [56] and non-apoptotic extrusion [54]. Cellular tissues modify their orientation, shape, density and even overall structure through rearrangement events of the cells, granting a radically different cortical and intercellular stress profile [52, 53] best optimized for their circumstances. Structural changes in living tissues are partially accomplished by tuning the tension at individual cell-cell interfaces [51, 57-59] (Figure 5.2.a and Figure 5.5.a). In the droplet-based tissue, this tension is largely determined by the selected solvent and lipid compositions [16, 18, 42, 60], which are difficult to tune on a per-membrane basis. Standard methods for contact-free droplet manipulation in microfluidics relies on differences between the dispersed and continuous phases, such as differences in permittivity of the two phases for dielectrophoresis [61]. These methods are difficult to implement when the droplets are closely packed together, as each droplet will respond similarly and produce translation of the adhered droplets rather than reconfiguration. Consequently, an alternative method for generating forces that target only

selected droplets within the tissue is necessary. In this work we propose the use of magnetic fields coupled with distributed ferrofluid droplets to generate localized forces in the DIB structures, driving droplet decoupling and rearrangement (Figure 5.5.b). Aqueous ferrofluids may be safely encapsulated within single droplets within the DIB network, imbuing select droplets with magnetic susceptibility while their surrounding droplets remain unresponsive to magnetic fields [48], creating a magnetically heterogeneous DIB network. Previous work examined the compatibility of the DIB technique with ferrofluid droplets by assessing membrane properties with and without the presence of ferrofluid, noting minimal influence on the properties of the membranes [48]. Here we explore how these ferrofluid droplets may be used to provide biologically inspired shape-shifting droplet structures.

First, we examine magnetic manipulation of a single DIB interface through a combination of modelling and experimental work. Single droplet manipulation is examined and optimized for different magnetic particle concentration and oil composition. Next, we produce heterogeneous structures of magnetic and non-magnetic aqueous droplets within an oil medium centered between four electromagnets. Magnetic fields are then activated to selectively exercise forces within the magnetically heterogeneous collection of droplets. The magnetic ferrofluid subcompartments within the structure collectively respond to the magnetic field and adjust accordingly, rearranging the adhered network between different metastable configurations. Finally, we show how this may be used to enable communicative pathways within the tissue using magnetic fields.

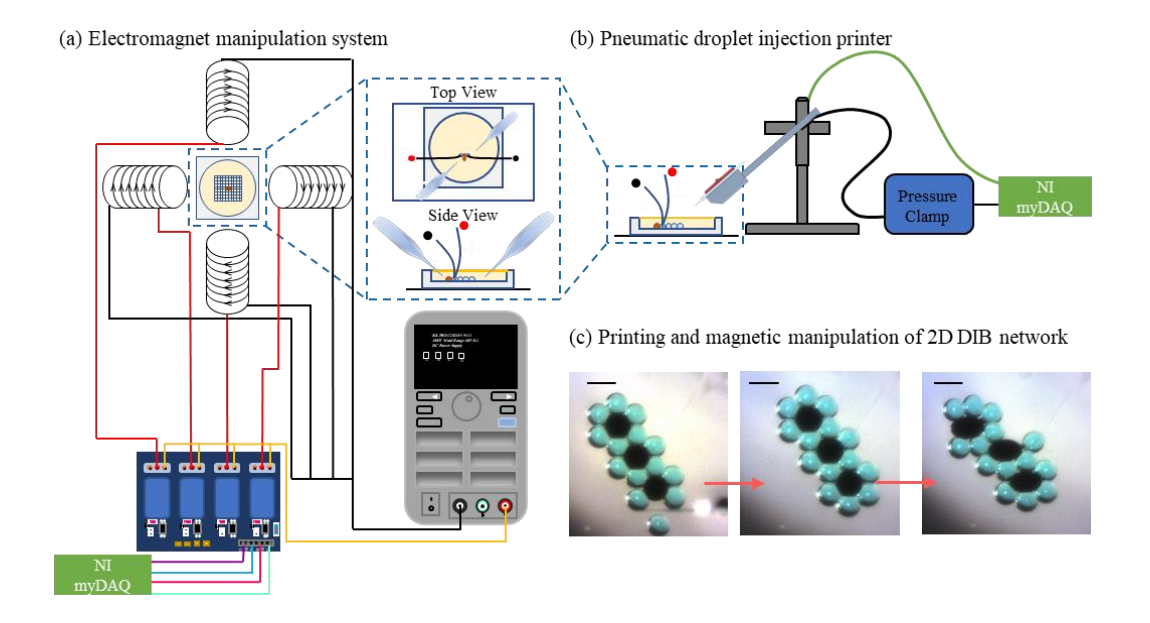


Figure 5.3- Schematic representation of the main experimental setup: the pneumatic microdroplet injection system and the computer-controlled electromagnets' system. (a) Four solenoids with magnetic cores (EFI alloy) are placed as shown and used to magnetically control the position of ferrofluid droplets injected into the oil medium. The power input of the solenoids is computer controlled with a user interface connected to an external microcontroller (ARDUINO), a relay system and a power supply. (b) Microdroplets are deposited into the oil dish using a computer-controlled pneumatic system. Microinjectors are pressurized using a pressure-clamp system connected to an external microcontroller (ARDUINO) and custom-guided through a user-interface. (c) Various compositions of DIB structures can be constructed by depositing magnetic (EMG 507- black color) and non-magnetic (aqueous buffer- blue color) microdroplets into an oil medium. Droplets are then brought into contact using a user-driven micropipette; interfacial bilayers are formed giving rise to a stable 2D membranous structure. Scale bars represent 600 µm each.

5.3. Results and Discussion

Manipulating Lipid Interfaces using a Magnetic Field

First, we investigate the mechanics involved in manipulating a single membranous interface using the apparatus described in Figure 5.3. For these experiments, a single ferrofluid droplet was adhered to an aqueous droplet anchored to a hydrogel-coated pipette and a magnetic field is supplied from the right as depicted in Figure 5.4.c. An energetics model was used to illustrate how the experimental parameters will influence the rearrangement of the droplets with a magnetic field, and predictions are compared to experimental results and then used to select the optimal ferrofluid/oil combination. This energetics model combines both the interfacial energy of the DIB with the magnetic energy produced by the magnetization of the ferrofluid droplet in response to electromagnetic activation (more details discussed in the Experimental Methodology section).

The interfacial energy (E γ) may be described by the monolayer and bilayer tensions (γ_m , γ_b) multiplied by their respective areas (A_m , A_b) as described in Equation 5.1 [59, 62]. The areas are approximated by assuming that the droplets will behave as adhered spherical caps with constant volumes. This assumption produces equations linking the distance between the droplet centers, their apparent radii, and the area of their adhered interface. Varying the distance between the droplet centers and solving numerically for the produced droplet geometry allows for a plot of the interfacial energy with respect to the distance between the droplets' centers measured from equilibrium as shown in Figure 5.4.a,c. All inputs for these results are provided in Tables S5.1-S5.3 (Appendix A).

$$E_{\nu} = \gamma_m A_m + \gamma_b A_b \tag{5.1}$$

The magnetic energy in the ferrofluid droplet (E_{mag}) is calculated as a function of the droplet volume (Vol_{ferro}), magnetic permeability of vacuum (μ_0), the external magnetic field evaluated at the center of the droplet (H_{ferro}), and the response of the droplet to the field (M_{ferro}) as described in Equation 5.2. This equation assumes that the ferrofluid droplet magnetization does not influence the external field and that the field within the droplet may be described by the value at the droplet center [63-65]. When an electromagnet is activated, the ferrofluid droplet becomes magnetized and produces a shift in this minimum energy as shown in Figure 5.4.a, altering the equilibrium distance between the droplets until droplets separate.

$$E_{mag} = -\frac{1}{2}\mu_0 Vol_{ferro} M_{ferro} H_{ext}$$
 (5.2)

The response of the droplet with a varying magnetic field is predicted using the approach described within the Modeling Methodology section. The new minimum energy for the combination of E_{mag} and E_{γ} is assumed to correspond to the distance between the droplet centers at equilibrium, reducing the total bilayer area between the droplets (A_b , Figure 5.4.a).

Using data provided by the vendor Ferrotech (further detailed in Table S5.2 in Appendix A), the necessary gradient of the magnetic field predicted for droplet separation as a function of the droplet radius and energy of adhesion for both EMG509 and EMG507 can be reproduced (Figure 5.4.b). From these plots we can infer two conclusions. First, smaller droplets are more difficult to manipulate using magnetic fields given that the magnetic energy scales with volume and the interfacial energy scales with area. Second, for lower concentration ferrofluids (EMG509), complete saturation is reached prior to separation (shaded in black in Figure 5.4.b lower panel). Previous works have shown that

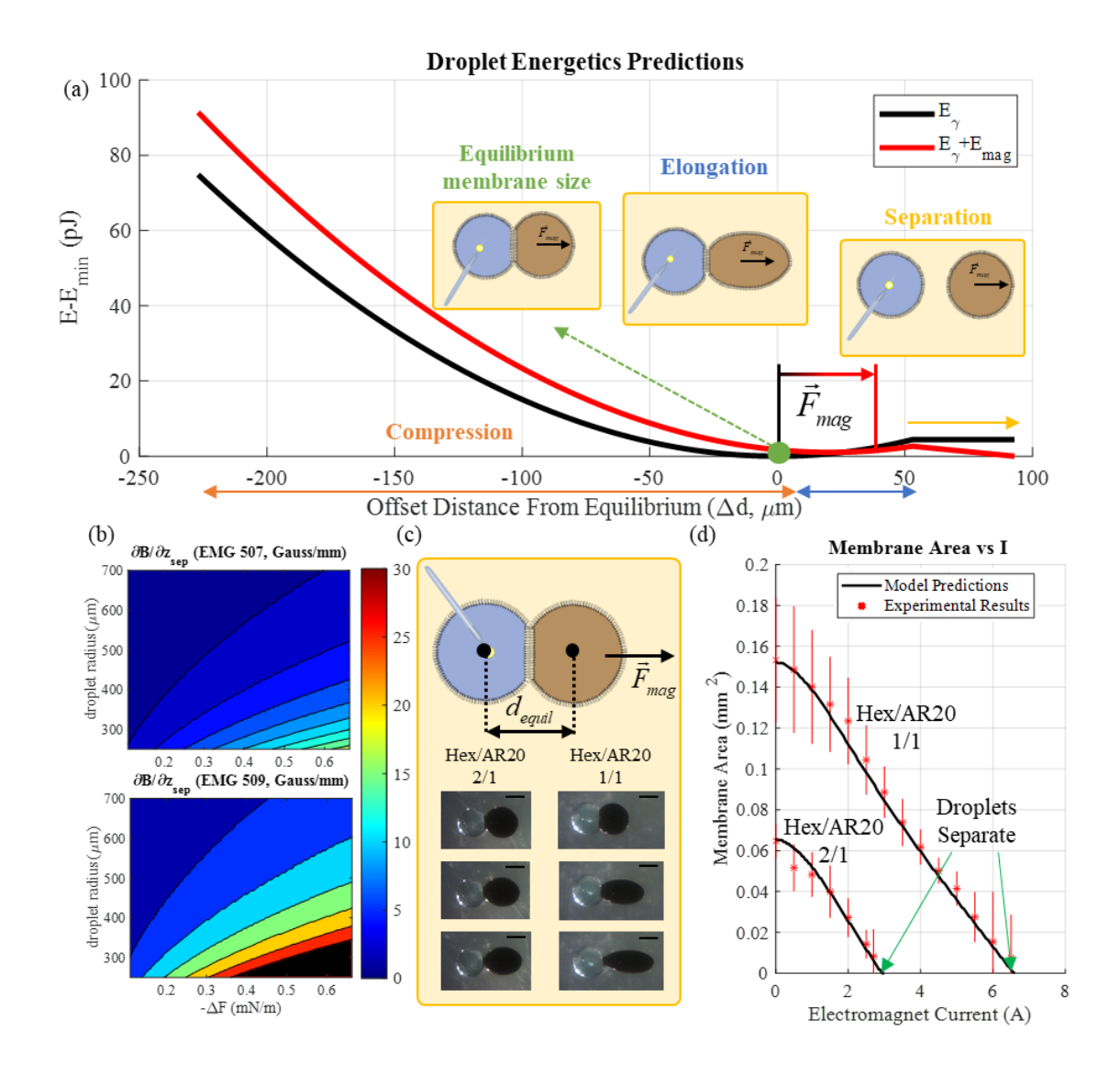


Figure 5.4- (a) Schematic representations (top view) of the manipulation of single membrane bordered by a ferrofluid droplet when applying different magnetic fields. An aqueous droplet is attached to an anchor (finely pulled glass tube with an agarose bead deposited at the tip). A ferrofluid droplet is then deposited in the same oil medium and a bilayer formed at the interface of these two droplets. The ferrofluid droplet typically relocates and centers its axis in a parallel direction to the activated electromagnet. Once the vector between the droplet centers is parallel with the field, the ferrofluid droplet starts elongating in the direction of the magnetic until it eventually separates. Before pulling

away in the direction of the magnetic field, the ferrofluid droplet can rotate freely around the water droplet (without breaking the membrane) and align itself with the direction of the magnetic field. This produces a magnetic energy within the ferrofluid droplet that is reduced as the droplet approaches the magnet as shown by the normalized plot (offset by the minimum energy) and predicted by the model. The equilibrium distance between the droplet centers is increased while the overlapping membrane dimensions is reduced (Hexadecane/AR20 2/1 volume mixture). (b) Necessary gradient of the magnetic field predicted for droplet separation as a function of the droplet radius and energy of adhesion for EMG509 and EMG507. Additional information on these ferrofluids is provided in the Supplementary Information. Solvents that produce more stable bilayers resulting in higher energy of adhesions require more force to separate. Smaller droplets are more difficult to manipulate since the magnetic energy scales with volume and the interfacial energy scales with area. For lower concentration ferrofluids (EMG509), this results in complete saturation prior to separation (shaded here in black). (c) Schematic representations and experimental images of membrane manipulation using electromagnets. A ferrofluid droplet (EMG507) is adhered to an anchored aqueous droplet and an electromagnet to the right is activated. The external oil phase (volume ratio of hexadecane and silicone oil) is varied and the variation in droplet adhesion is hence explored. Scale bar represents 500 μm. (d) Incrementing the magnetic field continues to reduce the membrane dimensions as predicted using the energetics model and confirmed experimentally. The current supplied to the electromagnet is varied and the interfacial dimensions and hence area recorded (averaged).

solvents that produce more stable bilayers result in higher energy of adhesions [17, 49] and hence would require more force to separate. The use of the 1:1 hexadecane: silicone oil AR20 solvent in DIBs has been traditionally preferred since it reduces gravitational influences on the droplets and allows for the formation of stable networks [15]. However, these membranes require more magnetic force to separate (Figure 5.8.b, more details in Modeling Methodology section). When compared to this mixture the 2:1 hexadecane:silicone oil AR20 combines both the advantages of reduced gravitational influences and overall network stability along with a reduced energetic penalty associated with droplet separation (Figure 5.8.b). Hence it seems that the use of EMG 507 in DIB networks constructed in a 2:1 hexadecane:silicone oil AR20 medium should allow for feasible droplet manipulation without jeopardizing the structural integrity of the system. This was further tested by experimentally examining the magnetic force that needs to be supplied to separate an EMG 507 droplet from a water droplet (with an interfacial membrane-Figure 5.4.c). Plotting the experimentally measured membrane area against the electromagnet current obtained from experiments for different oils and comparing the results against the predictions from the energetics model confirms the suggested mechanics for droplet separation (Figure 5.4.c-d). This further show how a higher energy of adhesion (resulting from an increased volume percent of silicone AR20 oil in the solvent phase) requires higher magnetic force (reflected through the current supplied to the electromagnets producing the field) for membrane separation. Examining the governing equations, several parameters of interest are provided. As mentioned previously, the field necessary to separate the droplets is governed by the energy of adhesion $(-\Delta F = 2\gamma_m - \gamma_b)$ of the selected lipids and solvent (Table S5.1) [16, 42], which governs the depth of the energy

well in Figure 5.4.a and Figure 5.8.b. The interfacial energy (E_{mag}) scales with the surface areas of the droplets (A_{m} , A_{b}). The magnetic energy (E_{mag}) scales with the ferrofluid properties (Table S5.2 and Figure 5.8.a) and ferrofluid volume (Vol_{ferro}). Consequently, the ratio of the magnetic energy and interfacial energy will increase with the droplet radius rferro. The droplet volume is readily adjusted by adjusting the printing parameters [27], while the energy of adhesion is largely a function of the selected continuous phase [16, 17]. These outcomes indicate using EMG 507 ferrofluid in DIB-systems that are constructed in a 2:1 hexadecane: silicone oil AR20 solvent is the most feasible combination for droplet manipulation. This combination is used for all following sections unless specified otherwise.

However, while the overall trends are similar, several discrepancies must be noted between the experimental cases and the model predictions. The model assumes the ferrofluid droplet remains spherical, while in reality the ferrofluid droplet elongates (Figure 5.4.c) in response to the magnetic field. Secondly, the increased density of the ferrofluid in comparison to the surrounding oil (Supplementary Tables SA.1-SA.2 Appendix A) causes the ferrofluid droplet to flatten. Third, the assumption that the magnetic field is uniform throughout the droplet may no longer be valid given the droplet dimensions. Fourth, the measurement of the monolayer tension of EMG 507 in oil was not feasible given that the ferrofluid exhibits a very low-tension interface with lipids and interacted with the dispensing syringe used for tension measurements. Values for the monolayer tension for ferrofluid droplets were consequently estimated to match the experimentally measured membrane areas without the magnetic field. The EMG 507 tension was estimated to be 0.88 mN.m⁻¹ in the 2:1 hexadecane: silicone oil AR20 and 0.84 mN.m⁻¹ in the 1:1

hexadecane: silicone oil AR20. These lower estimated monolayer tension values to correlate with the observed increased flattening of the ferrofluid droplets; however, this may also be a function of their increased density as well (Supplementary Table SA.2 Appendix A).

Still, this energetics model captures the mechanics associated with the magnetic manipulation of adhesive droplets and is provided for insights into how the magnetic reconfiguration may be tuned as the overall trends of the model and experimental results are in agreement. With the behaviors predicted by the energetics model comparing favorably to experimental results, the model may be extended to observe scaling phenomena involved with ferrofluid droplet separation and guide experimental design. In the next section, we explore how these simple mechanisms may be combined in larger collections of adhered droplet clusters to approximate reconfiguration events observed in living tissues covered previously.

Bioinspired Shape-Shifting within Droplet-Based Tissues

From the previous discussion, we observe that ferrofluid droplets are able to push, pull, and rotate around their adhered non-magnetic partners. The adhesive connections between the droplets provide a form of elasticity, and networks of these droplets may behave as collections of particles capable of separating and reconnecting as they change their relative positioning within the tissue. Consequently, a single ferrofluid droplet may be used to exert forces on adhesive bridges of interconnected droplets, driving separation of existing membranes and allowing the membranes to reform into new equilibriums within a network.

The amount of magnetic input necessary for reconfiguration increases with the number of adhered droplets and their overall orientation relative to the direction of the magnetic field. When the supplied magnetic force is smaller than the estimated value for droplet separation, reconfiguration cannot be achieved successfully: the weaker magnetic forces cannot successfully counteract the droplet-to-droplet adhesion. Meanwhile, providing much larger magnetic force input may result in membrane failure and droplet coalescence, initiated by the sudden excess force exerted by the ferrofluid droplets. After separation of the desired membranes, the magnetic field is removed, and the droplets are allowed to settle into a new equilibrium. It should be noted that the process for new membrane formation is dependent on the two monolayers successfully expelling the solvent from between the lipids and beginning the wetting process [66]. This typically required between 0-2 minutes for membrane formation in the experiments, but variation is still observed between cases.

Each reconfiguration event is accomplished using distributed ferrofluid droplets dispersed within the adhered network. Selected droplets are anchored using hydrogel-coated glass pipettes, enabling separation of droplets and subsequent reformation upon the removal of the magnetic field. The experiments are presented by a figure clearly showing both the original structure prior to magnetic perturbation and the produced structure after reconfiguration. In each of the cases, multiple samples were collected (n≥3) where the current supplied to the electromagnets as well as the time it took the mechanism to reach completion was recorded. The results displayed in this work were rotated to show the same activation direction for the sake of consistency; however, shape-shifting may be achieved in any direction.

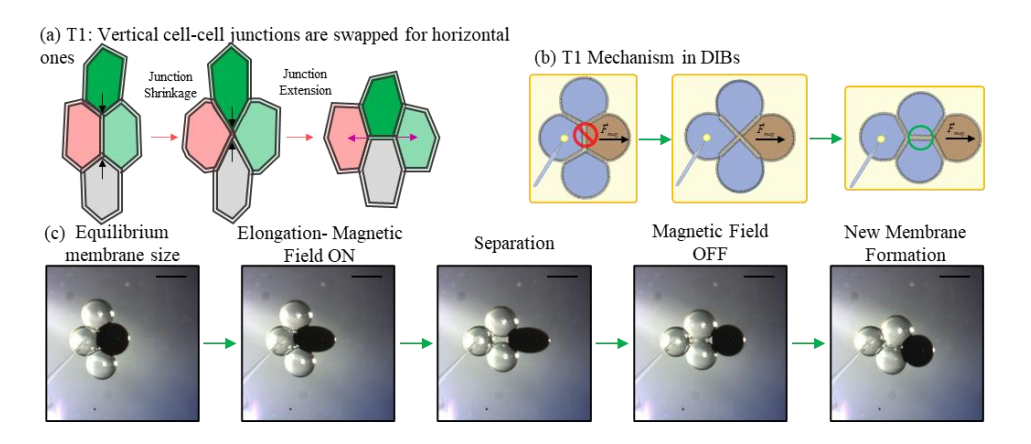


Figure 5.5- The T1 event is a form of cellular intercalation event and is also known as local neighbor exchange (displayed in (a)): it is an active mechanism internally activated by cells. It is mediated through stress dissipation in tissues and may result in the formation of non-equilibrium tetrads. Colors are intended to aid in tracking relative cell location. (b) Here, we propose integrating intercalation mechanisms in DIB structures to further their adaptive nature. Intercalation mediated through membrane separation/reformation can be triggered using external force fields that can be tuned to affect on select microdroplets. (c) Experimental images (top view) obtained when applying different magnetic fields triggering a T1 intercalation event in a set of four adhered microdroplets. Scale bar represents 600 µm. The ferrofluid droplet (EMG 507) is centered in a parallel direction to the activated electromagnet. Once the magnetic field is applied, the ferrofluid droplet starts elongating in the direction of the magnetic dragging the two adjacent aqueous droplets and gradually separating the vertical interfacial membrane. The magnetic energy within the ferrofluid droplet is reduced as the droplet approaches the magnet as shown by the energy plot (vs distance between centers of droplets). This mechanism continues until it eventually separates the vertical membrane junction and is followed by a relocation of the adjacent microdroplets. Once the vertical junction membrane is separated, the magnetic field is

turned OFF. After being given sufficient time (around 1 minute) a new horizontal membrane junction is formed akin to the T1 mechanism experienced by intercalating living cells.

The distribution of membranes in a simple four-droplet cluster may be rearranged through magnetically induced T1 events. In this configuration (Figure 5.5.b-c), a single ferrofluid droplet separates an existing vertical membrane and replaces this with a horizontal membrane. One aqueous droplet is fixed into place with a hydrogel anchor and the ferrofluid droplet is pulled away from this anchor using a magnetic field, separating the membrane between the ferrofluid and the anchor. As the ferrofluid droplet detaches, the neighboring droplets are pulled together after rotating along their neighboring surfaces and form a new horizontal membrane together. Such event required a supplied current for electromagnets ranging from 1.5 to 3.5 A for an estimate duration of 4-13 seconds (followed by an approximate duration of 60 seconds for the formation of new interfacial lipid membranes).

Folding is accomplished by attaching two ferrofluid droplets to the end of a droplet chain and anchoring the chain at the desired folding point. As shown in Figure 6.b, the ferrofluid droplets begin moving towards the activated electromagnet. The adhesive forces along the chain cause them to begin rotating the chain inwards towards the opposite side. Eventually the droplets rotate into contact and form a new membrane. This is the simplest reconfiguration mechanism as it does not require the separation of existing membranes and may be accomplished with minimal magnetic forces. The total movement required a magnetic energy per ferrofluid droplet ranging from 2.5 to 3.5 A supplied current per

electromagnet and took a norm of 16 seconds for separation with an additional average of 21 seconds for the new interfaces to form after the droplets were pulled into contact.

Extrusion is replicated by placing a ferrofluid droplet (EMG 507) at the center of packed hexagonal DIB structure as shown in Figure 5.6.c. When a magnetic field applied, the central ferrofluid droplet exerts local forces on the rest of the structure. As the magnetic droplet moves and deforms, bilayer junctions bordering it are separated. As the droplet moves out of the center of the cluster, attached droplets are repositioned and pulled into contact. Once the last bilayer is separated, the magnetic droplet is expelled from the DIB structure into the surrounding oil environment. Post- extrusion, the remaining non-magnetic droplets are pulled into contact with each other and form new membranes. The total movement required a 3.5-5.0 A supplied current for the electromagnet and needed an average of 17 seconds with an additional minute estimate for the new interfaces to form.

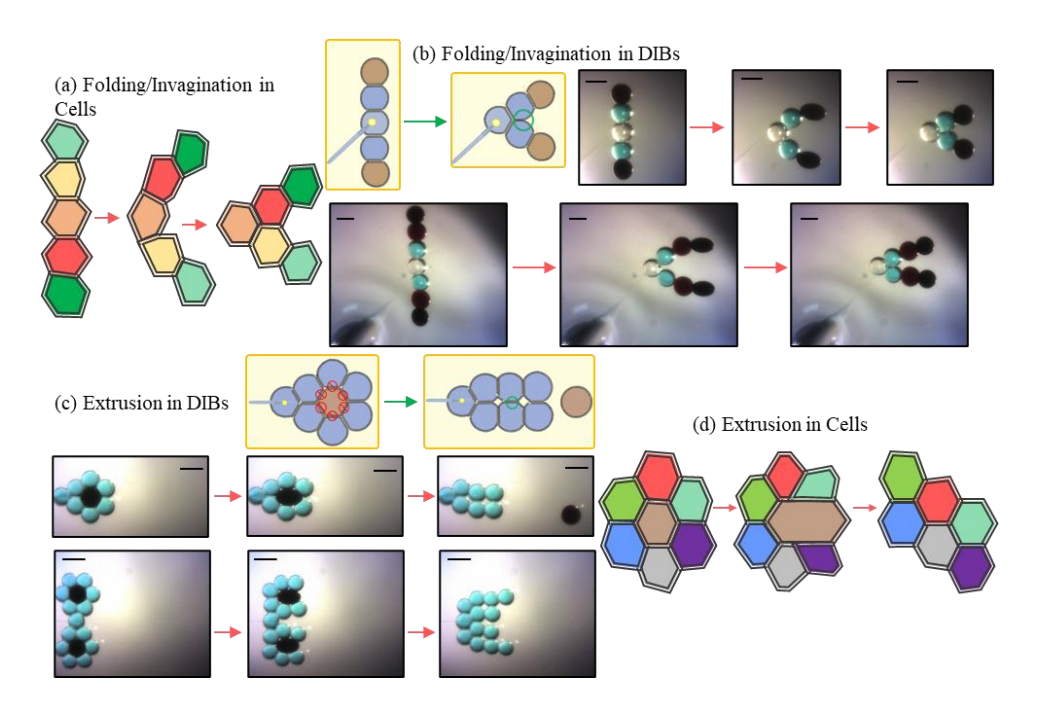


Figure 5.6- Summary of the reproduced intercalation mechanisms in DIBs. Each case includes a sketch showing the mechanism in natural cellular tissues and a parallel

schematic highlighting removed/formed DIB membranes, anchoring hydrogels, and location of the ferrofluid droplets as well as experimental images. Colors are intended to aid in tracking relative cell location. The folding/invagination (a) action uses ferrofluid droplets (b) to pinch droplets together about a hydrogel anchor. A first case uses two EMG 507 droplets while a second case shows a folding mechanism enabled by using two types of ferrofluids with different concentrations of magnetic particles. The extrusion mechanism (c) extracts the ferrofluid droplet from the center of a hexagonal packed structure to form new interfaces. This has been accomplished in (d) where a single a double extraction are performed as shown by the experimental images' series (using EMG 507). DIB structures were formed with aqueous droplets (blue and white colors), EMG 507 (black color) and EMG 509 (brown color) droplets. Scale bars represent 600 µm each.

Each of the described reconfiguration mechanisms may be combined in larger networks and executed simultaneously. Experimental demonstrations are provided in Figure 5.6.b-c. These may be accomplished using varying ferrofluid compositions (Supplementary Table SA.1 online), pre-set structures, and the same anchor scheme for providing fixed boundary conditions as before. Each of these figures presents the original structure, distorted structure during perturbation, and the new equilibrium structure produced after disabling the external magnetic field.

Application of Magnetically Enabled Reconfiguration of Bilayers Structure

As noted earlier, the rearrangement of the droplets within the DIBs also changes the nature of the membranes, as the properties of the membranes at the intersection of the droplets are determined by the droplet pair. Consequently, it is feasible to reconfigure the droplets to dramatically change their functionality as demonstrated here.

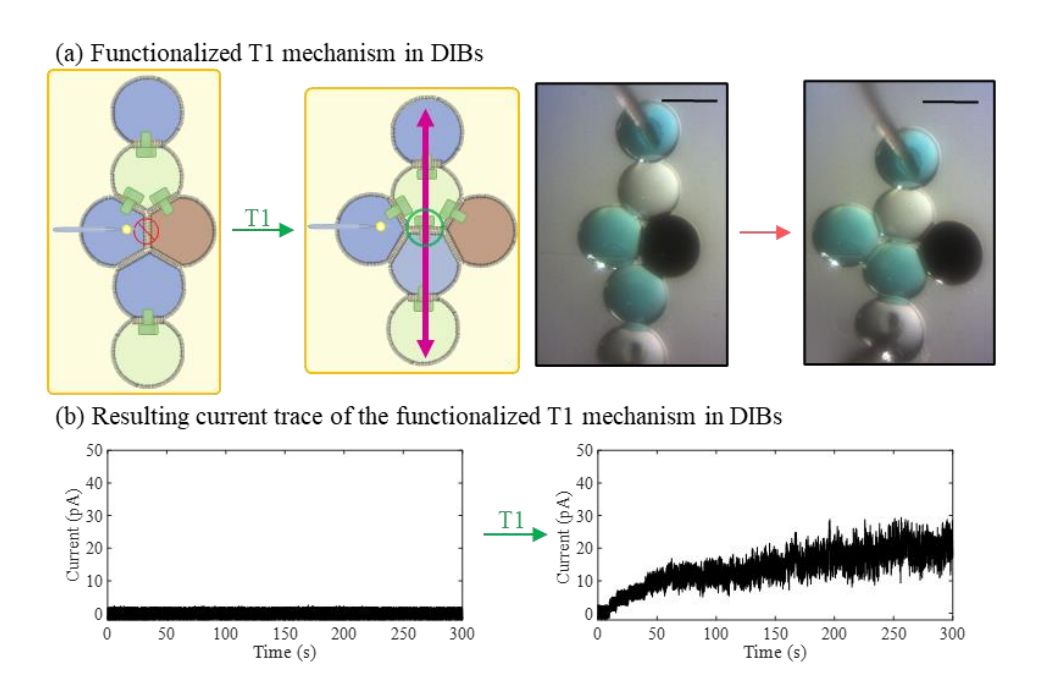


Figure 5.7- (a) Schematic representation and experimental results of the functionalized T1 neighbor exchange mechanism DIB network (formed with aqueous droplets (blue color), αHI infused aqueous buffer (2 μg/ml- white color) and EMG 507 (black color) droplets). Scale bars represent 600 μm each. (b) Current traces obtained for a constant +100 mV DC applied across the DIB networks shown respectively in (a) for the variation in αHL insertion activity upon the magnetic induction of a T1 rearrangement mechanism. Changes in the current reflect changes in the overall conductance of the tissue through insertion of the PFTs into individual bilayers. All measurements were recorded in voltage clamp mode at a sampling frequency of 10 kHz and filtered at 1 kHz (using the embedded low-pass Bessel filter -80 dB/decade). Post-acquisition, data was filtered at 500 Hz using a fourth-order Butterworth low-pass filter in MATLAB. Scale bars represent 600 μm each.

One of the simplest methods for enabling droplet-droplet exchange involves poreforming agents such as the pore forming toxin (PFT) alpha-hemolysin (α Hl). PFTs insert into lipid membranes without conformational states and create large non-gating channels [6], enhancing the diffusive exchange between the compartments [67]. As a proof of the capabilities of magnetically infused DIB structures in generating functional reversible structure rearrangement processes, we focused on enabling transport through selectively infusing αHl into droplet reconfiguration in a way that generates conductivity post magnetically triggered intercalation event. Figure 5.7 shows the effect of a magnetically guided T1 intercalation event on the measured conductivity of a DIB network. Upon the alignment of select microdroplets, αHl pores insert into bilayers allowing the passage of ions as showcased by the increase in measured current with 100 mV applied between the electrodes (Figure 5.7.b). Since the exchange across the membrane and the properties of the membranes themselves formed using this approach are largely dictated by the droplet compositions [33, 68-70], this new method for driving reconfiguration of the droplets may be used to establish new capabilities for the synthetic tissues.

5.4. Conclusion

In this work, we created droplet-based synthetic systems that swap between functional configurations using magnetic forces. First, the mechanics of droplet separation through magnetic forces was investigated using an energetics model and experimental data to estimate the magnetic field necessary for droplet separation as a function of droplet dimensions, ferrofluid properties, and selected solvents and lipids. The model predictions were compared against experimental results for validation and used to select an optimal combination of ferrofluid and oil phase. Next, the concept was then extended to the manipulation of ferrofluid droplets embedded within DIB clusters. The ferrofluid droplets are capable of exerting forces on their adhered neighbors, and can separate then recombine surrounding droplets, reshaping the membranous architecture. Several reconfiguration

events based on cellular intercalation events were demonstrated, and the findings were applied to larger networks as well. Finally, the technique was combined with selectively distributed pore forming toxins to produce a conductive pathway between two electrodes using a T1 rearrangement event.

The presented research emphasizes reconfiguration of the droplets comprising the material rather than overall shape changes, or shape-shifting. Altering the relative droplet locations within DIB tissues produces changes in the internal membranous architecture, and it is possible to adjust droplet-droplet exchange as a result. The results demonstrate a new approach for designing these bioinspired droplet networks with multiple functionalities that may be enabled and disabled as needed through magnetic fields and mechanical forces and can be built upon in future DIB-based material construction.

5.5. Methodology

Additional detailed experimental protocols and methodologies are provided in the Appendix A for replication.

Materials

Aqueous solutions were prepared with a standard buffer solution with (250 mM Potassium Chloride (KCl)) and (10 mM 3-(N-morpholino) propanesulfonic acid (MOPS)) added yielding a pH of 7.0. This solution was then used to produce solutions with and without dye for visualization, with and without lipids using standard techniques [17, 42], and with or without the pore-forming toxin alpha hemolysin for enabling diffusion between neighboring droplets. Aqueous ferrofluid solutions were acquired from Ferrotec, including EMG 507 and EMG 509. KCl and MOPS were added to match the osmolality of the buffer solution and produce a neutral pH while watching for settling and aggregation of the

nanoparticles. EMG 507 offers a stronger magnetic response in comparison to EMG 509, with the penalty of a substantially higher density and nanoparticle concentration. As a general rule the magnetic properties of the ferrofluid scale with the nanoparticle concentration by volume, providing a mechanism for enhancing the magnetic responsivity of the droplets. The selected oil phase consisted of various mixtures of hexadecane: silicone oil AR20 intended to produce a favorable balance of interfacial tensions [17, 49, 71]. Mixtures of 1:0, 1:1, and 2:1 were studied and the 2:1 mixture was found to both increase the bilayers' stability while facilitating the magnetic manipulation of droplets, and separation/reformation of membranes [16, 49], as determined through a combination of pendant drop tensiometry and visual measurements of bilayer tension. Lipids were added where specified. Aqueous lipid solutions underwent standard extrusion and sonication techniques prior to use.

Methods

An electromagnet-based manipulation system was assembled to remotely control magnetically susceptible droplets. A schematic representation of this setup is presented in Figure 5.3. Droplets of varying solutions are deposited on the working stage using a pneumatically-driven 3D-droplet printer described previously, modified to support multiple solutions [27]. After the droplets are deposited, they are manipulated using magnetic forces to produce the desired reconfiguration events. Four solenoids are mounted in the cardinal directions and selectively enabled through a LABVIEW interface. Designated anchor droplets are produced using glass rods coated in a hydrogel, providing fixed droplets for boundary conditions and enabling reconfiguration rather than translation of the network. Electrical measurements are conducted through standard electrophysiology

practices using two silver/silver-chloride wires connected to a patch-clamp apparatus. All measurements are conducted in a vibration isolation table within a Faraday cage, and images are recorded using a CCD camera attached to a zoom microscope.

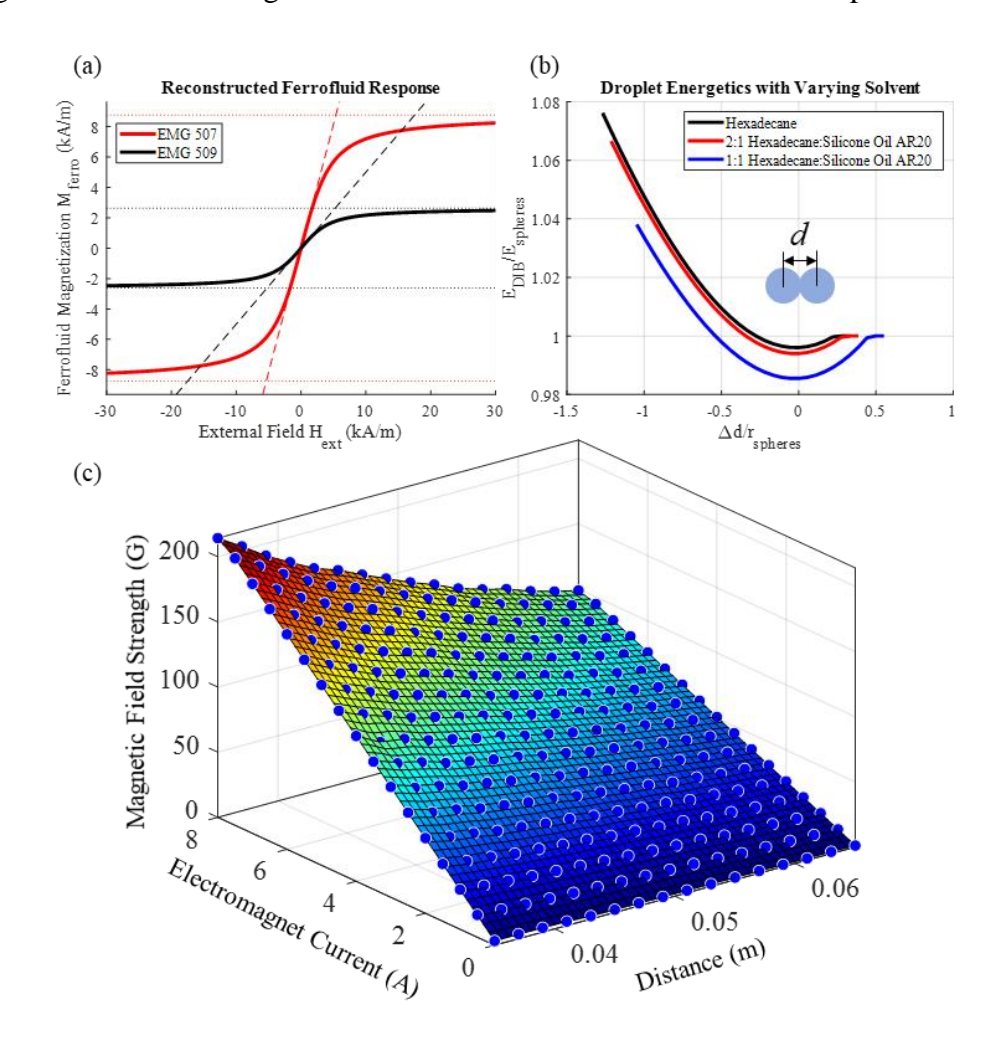


Figure 5.8- (a) Plots of the ferrofluid magnetization M_{ferro} (EMG 507 and EMG 509 water-based series) with an external field H_{ext} for the two selected ferrofluids including saturation effects. The dashed lines are the linear magnetization response provided by c_{ferro} , and the dotted lines are the saturation limits. (b) Plots of the interfacial energy ($E\gamma$) for a pair of adhered droplets as a function of the normalized distance between their centers offset by the equilibrium distance. (c) Quantified electromagnet response to supplied current.

Modeling Methodology

Overview of the Model

To approximate the response of DIBs to an externally supplied magnetic field, the summed contributions from interfacial energy $E\gamma$ and magnetic energy Emag are plotted, and the new equilibrium is found. The force on the droplets F may be approximated as the gradient of the two values as described in Equation 5.3.

$$\vec{F} \approx -\vec{\nabla}(E_{mag} + E_{\gamma}) \tag{5.3}$$

In this model we assume a 1-D axisymmetric behavior with droplet motion only considered in the z direction. The condition for equilibrium where F=0 may be written as a balance of the magnetic contributions and interfacial contributions in Equation 5.4:

$$\frac{\partial E_{mag}}{\delta z} = -\frac{\partial E_{\gamma}}{\delta z} \tag{5.4}$$

This corresponds to any local minimums in the energy with respect to z. The interfacial energy E_{γ} is a function of the monolayer and bilayer tensions (γ_m, γ_b) multiplied by their respective areas (A_m, A_b) .

$$E_{\gamma} = \gamma_m A_m + \gamma_b A_b \tag{5.5}$$

The summed interfacial energy for the DIB is calculated by assuming that the adhered droplets may be approximated as spherical caps. This is accomplished by defining the droplets as two entities with fixed volumes and a prescribed distance between their centers as shown in Figure S5.1. If the droplets radii R overlap, it is assumed that a bilayer is formed at their interface whose radius am may be calculated as a function of the droplet radius R and the height of the spherical cap h. However, the volume of the spherical cap must be added back into the original droplet volume and the apparent radius R must be recalculated which further influences am. The correct solution enforcing a fixed droplet volume is found through iteration.

Once values for R, h, and a_m are satisfactorily determined for the prescribed distance between the centers, the areas for the monolayer A_m and bilayer A_b may be calculated using Equation 5.6.

$$A_h = \pi a_m^2 \quad A_m = 4\pi R^2 - \pi (a_m^2 + h^2) \tag{5.6}$$

 $A_b = \pi a_m^2$ $A_m = 4\pi R^2 - \pi (a_m^2 + h^2)$ (5.6) Multiplying these values by their prescribed interfacial tensions produces the total droplet interfacial energy (Equation 5.5). Plotting this energy and altering the distance between the droplet centers then varying the selected solvent to vary the energy of adhesion produces Figure 5.8.b. This is similar to results predicted by Surface Evolver in a previous work [49].

Notably, the minimum energy matches the equilibrium contact angle prescribed by Young's law (Equation 5.7). This provides a description of the droplet-droplet interactions and the elasticity afforded by the adhesive emulsion that resists separation. The stronger the energy of adhesion, the greater the necessary magnetic field is necessary to separate the droplets.

$$2\nu_{m}\cos\theta_{m} = \nu_{h} \tag{5.7}$$

 $2\gamma_m cos\theta_m = \gamma_b \tag{5.7}$ Values for the interfacial tensions used in are provided in Supplementary Table SA.1 Appendix A. These values were obtained using pendant drop tensiometry for the monolayer tension γ_m combined with measured angle of contact through microscopy for the bilayer tension γ_b and Equation 5.7. For each case the aqueous phase was 250 mM KCl with 10 mM MOPS. Each measurement was repeated five times and standard deviations are provided.

The magnetic energy in the ferrofluid droplet Emag is a function of the droplet volume Volferro, magnetic permeability of vacuum μ₀, the external magnetic field evaluated at the center of the droplet H_{ferro} , and the response of the droplet to the field M_{ferro} as described in Equation 5.8.

$$E_{mag} = -\frac{1}{2}\mu_0 Vol_{ferro} M_{ferro} H_{ext}$$
 (5.8)

The external field H_{ext} is assumed to remain constant across the droplet interior. The droplet response is calculated as a function of this external field. The saturation M_{sat} and initial susceptibility χ_{ferro} variables are provided in Supplementary Table SA.2 Appendix A. The response of the ferrofluid may be approximated through a Langevin function $L(\alpha)$ [63, 72], accounting for saturation effects when all nanoparticles are aligned with the external magnetic field. As a result, the response M_{ferro} will be capped by the saturation magnetization M_{sat} of the ferrofluid shown in Equation 5.9.

$$M_{ferro} = M_{sat}L(\alpha) = M_{sat}\left(coth(\alpha) - \frac{1}{\alpha}\right)$$
 (5.9)

The Langevin function may be approximated through a Taylor series as described in Equation 5.10 [72]:

$$L(\alpha) \approx \frac{\alpha}{3} - \frac{x^3}{45} + \cdots \tag{5.10}$$

We use the linear approximation for $L(\alpha)$ to determine the coefficient α using the initial linear relationship between the ferrofluid magnetization M_{ferro} and external field H_{ext} as defined by the initial susceptibility χ ferro as described in Equation 5.11.

$$M_{ferro,linear} = \chi_{ferro} H_{ext} = M_{sat} \left(\frac{\alpha}{3}\right) \qquad \alpha \approx 3 \frac{\chi_{ferro} H_{ext}}{M_{sat}}$$
 (5.11)

Using the ferrofluid properties provided by the vendor in Supplementary Table SA.2 online it is possible to reconstruct the ferrofluid response to an external field for the two ferrofluids as shown in Figure 5.8.a. The predicted magnetization curves clearly fit with the provided saturation values (maximum bounds) and linear regions (fit of the slope about $H_{\text{ext}} = 0$).

These results assume that the droplets may be described as spherical caps. In reality upon the application of an increasing magnetic field/energy, the ferrofluid droplet stretches and elongates [73]. Furthermore, owing to gravitational effects (density of EMG 507 at 1120 kg.m⁻³ compared to the density of the lipid-oil mixture at 813 kg.m⁻³), ferrofluid droplets exhibit some flattening prior to the application of the magnetic field.

Calculating Magnetic Energy

The magnetic field produced within the electromagnet may be predicted by Equation 5.12 as a function of the maximum permeability of the soft iron core $\mu_{r,core}$, supplied current i_{mag} , turns per length N/L, and permeability [72]. Consequently, the magnetic field will scale approximately with the supplied current.

$$B_{\infty} \approx \mu_{r,core} \mu_0 \frac{N}{L} i_{mag} \tag{5.12}$$

The electromagnet configuration for examining droplet separation may be seen in Figure 5.3. The droplets were centered with the electromagnet (x=0, y=0) at a set distance from the surface of the electromagnet. The electromagnet dimensions and properties are provided in Supplementary Table SA.3 Appendix A.

The magnetic field B was measured experimentally using a DC Gaussmeter (GM1-ST, AlphaLab). This measurement was taken in 0.5 A increments from 0 to 8 A, the available range from the power supply. The probe location was varied in 2 mm increments using a manual micromanipulator (Siskiyou, Grants Pass, OR) and the measurements were repeated 3 times. Values were recorded at the center of the produced magnetic field (x,y=0, Figure 5.4). These values were then fit to a 3rd order polynomial surface (poly33) using MATLAB to interpolate the magnetic field for the droplet distance from the electromagnet and input currents as seen in Figure 5.8.c.

These equations do not account for deviations away from spherical droplet shapes, influence of droplet magnetization on the external field, or phenomena such as friction and solvent viscosity which will further influence the droplet dynamics [74]. However, they do capture the general mechanics and may be used to guide experimental design.

The response of the droplet with a varying magnetic field is predicted using the approach described previously. The new minimum energy for the combination of E_{mag} and E_{γ} is assumed to correspond to the distance between the droplet centers at equilibrium, reducing the total bilayer area between the droplets (A_b, Figure 5.4.c).

Plotting the visually measured membrane area vs. electromagnet current obtained from experiments and comparing the results against the predictions from the energetics model confirms the suggested mechanics for droplet separation (Figure 5.4.c-d). However, while the overall trends are similar, several discrepancies must be noted as mentioned in the Results section. However, the energetics model captures the mechanics associated with the magnetic manipulation of adhesive droplets and is provided for insights into how the magnetic intercalation events can be tuned.

5.6. References

- 1. Yavlovich, A., et al., Light-sensitive lipid-based nanoparticles for drug delivery: design principles and future considerations for biological applications. Molecular membrane biology, 2010. 27(7): p. 364-381.
- 2. Gopfrich, K., I. Platzman, and J.P. Spatz, Mastering Complexity: Towards Bottom-up Construction of Multifunctional Eukaryotic Synthetic Cells. Trends in Biotechnology, 2018. 36(9): p. 938-951.

- 3. Channon, K., E.H.C. Bromley, and D.N. Woolfson, Synthetic biology through biomolecular design and engineering. Current Opinion in Structural Biology, 2008. 18(4): p. 491-498.
- 4. Pontani, L.-L., et al., Biomimetic emulsions reveal the effect of mechanical forces on cell–cell adhesion. Proceedings of the National Academy of Sciences, 2012. 109(25): p. 9839-9844.
- 5. Stevens, M.M. and G. Mecklenburg, Bio-inspired materials for biosensing and tissue engineering. Polymer international, 2012. 61(5): p. 680-685.
- 6. Vanuytsel, S., J. Carniello, and M.I. Wallace, Artificial Signal Transduction across Membranes. ChemBioChem, 2019. 20(20): p. 2569-2580.
- 7. Gánti, T., The principles of life. 2003: Oxford University Press.
- 8. Bibette, J., F.L. Calderon, and P. Poulin, Emulsions: basic principles. Reports on Progress in Physics, 1999. 62(6): p. 969.
- 9. Makhoul-Mansour, M.M. and E.C. Freeman, Droplet-Based Membranous Soft Materials. Langmuir, 2021. 37(11): p. 3231-3247.
- 10. Funakoshi, K., H. Suzuki, and S. Takeuchi, Lipid bilayer formation by contacting monolayers in a microfluidic device for membrane protein analysis. Analytical chemistry, 2006. 78(24): p. 8169-8174.
- 11. Bayley, H., et al., Droplet interface bilayers. Molecular BioSystems, 2008. 4(12): p. 1191-208.
- 12. Booth, M.J., et al., Droplet Networks, from Lipid Bilayers to Synthetic Tissues, in Encyclopedia of Biophysics, G. Roberts and A. Watts, Editors. 2019, Springer Berlin Heidelberg: Berlin, Heidelberg. p. 1-13.

- 13. Booth, M., et al., Functional aqueous droplet networks. Molecular BioSystems, 2017.
- 14. Hwang, W.L., et al., Asymmetric droplet interface bilayers. Journal of the American Chemical Society, 2008. 130(18): p. 5878-5879.
- 15. Wauer, T., et al., Construction and manipulation of functional three-dimensional droplet networks. ACS Nano, 2014. 8(1): p. 771-9.
- 16. Taylor, G.J., et al., Direct in situ measurement of specific capacitance, monolayer tension, and bilayer tension in a droplet interface bilayer. Soft Matter, 2015. 11(38): p. 7592-605.
- 17. Makhoul-Mansour, M.M., et al., Photopolymerized microdomains in both lipid leaflets establish diffusive transport pathways across biomimetic membranes. Soft Matter, 2019. 15(43): p. 8718-8727.
- 18. Venkatesan, G.A., et al., Adsorption Kinetics Dictate Monolayer Self-Assembly for Both Lipid-In and Lipid-Out Approaches to Droplet Interface Bilayer Formation. ACS-Langmuir, 2015. 31(47): p. 12883-12893.
- 19. Villar, G., A.D. Graham, and H. Bayley, A tissue-like printed material. Science, 2013. 340(6128): p. 48-52.
- 20. Bayoumi, M., et al., Multi-compartment encapsulation of communicating droplets and droplet networks in hydrogel as a model for artificial cells. Sci Rep, 2017. 7: p. 45167.
- 21. Ma, S., et al., Gel Microrods for 3D Tissue Printing. Advanced Biosystems, 2017. 1(8): p. e1700075.
- 22. Sarles, S.A. and D.J. Leo, Physical encapsulation of droplet interface bilayers for durable, portable biomolecular networks. Lab on a Chip, 2010. 10(6): p. 710-7.

- 23. Elani, Y., et al., Engineering multi-compartment vesicle networks. Chemical Science, 2013. 4(8): p. 3332.
- 24. Stanley, C.E., et al., A microfluidic approach for high-throughput droplet interface bilayer (DIB) formation. Chemical Communications, 2010. 46(10): p. 1620-2.
- 25. Maglia, G., et al., Droplet networks with incorporated protein diodes show collective properties. Nature Nanotechnology, 2009. 4: p. 437-440.
- 26. Booth, M.J., et al., Light-activated communication in synthetic tissues. Sci Adv, 2016. 2(4): p. e1600056.
- 27. Challita, E.J., et al., Encapsulating Networks of Droplet Interface Bilayers in a Thermoreversible Organogel. Scientific reports, 2018. 8(1): p. 6494-6505.
- 28. Stephenson, E.B. and K.S. Elvira, Biomimetic artificial cells to model the effect of membrane asymmetry on chemoresistance. Chem Commun (Camb), 2021. 57(53): p. 6534-6537.
- 29. Aufinger, L. and F.C. Simmel, Establishing Communication Between Artificial Cells. Chemistry-a European Journal, 2019. 25(55): p. 12659-12670.
- 30. Dupin, A. and F.C. Simmel, Signalling and differentiation in emulsion-based multi-compartmentalized in vitro gene circuits. Nature chemistry, 2019. 11(1): p. 32-39.
- 31. Schild, V.R., et al., Light-Patterned Current Generation in a Droplet Bilayer Array. Scientific Reports, 2017. 7.
- 32. Sarles, S.A. and D.J. Leo, Tailored Current--Voltage Relationships of Droplet-Interface Bilayers Using Biomolecules and External Feedback Control. Journal of Intelligent Material Systems and Structures, 2009. 20(10): p. 1233-1247.

- 33. Taylor, G., et al., Electrophysiological interrogation of asymmetric droplet interface bilayers reveals surface-bound alamethicin induces lipid flip-flop. Biochimia Biophysica Acta- Biomembranes, 2019. 1861(1): p. 335-343.
- 34. Najem, J.S., et al., Activation of bacterial channel MscL in mechanically stimulated droplet interface bilayers. Scientific Reports, 2015. 5(13726).
- 35. Freeman, E.C., et al., The mechanoelectrical response of droplet interface bilayer membranes. Soft Matter 2016. 12: p. 3021-3031.
- 36. Rosholm, K.R., et al., Activation of the mechanosensitive ion channel MscL by mechanical stimulation of supported Droplet-Hydrogel bilayers. Sci Rep, 2017. 7: p. 45180.
- 37. Makhoul-Mansour, M.M. and E.C. Freeman, Photo-Triggered Soft Materials With Differentiated Diffusive Pathways, in ASME 2019 Conference on Smart Materials, Adaptive Structures and Intelligent Systems. 2019, American Society of Mechanical Engineers Digital Collection: Louisville, Kentucky, USA. p. 1-9.
- 38. Punnamaraju, S., H. You, and A. Steckl, Triggered release of molecules across droplet interface bilayer lipid membranes using photopolymerizable lipids. Langmuir, 2012. 28(20): p. 7657-7664.
- 39. Syeda, R., et al., Screening blockers against a potassium channel with a droplet interface bilayer array. Journal of the American Chemical Society, 2008. 130(46): p. 15543-8.
- 40. Sarles, S.A. and D.J. Leo, Regulated attachment method for reconstituting lipid bilayers of prescribed size within flexible substrates. Analytical chemistry, 2010. 82(3): p. 959-966.

- 41. Najem, J.S., et al., Dynamical nonlinear memory capacitance in biomimetic membranes. Nature communications, 2019. 10(1): p. 1-11.
- 42. El-Beyrouthy, J., et al., A new approach for investigating the response of lipid membranes to electrocompression by coupling droplet mechanics and membrane biophysics. Journal of the Royal Society Interface, 2019. 16(161): p. 20190652.
- 43. Rofeh, J. and L. Theogarajan, Instantaneous tension measurements in droplet interface bilayers using an inexpensive, integrated pendant drop camera. Soft Matter, 2020.
- 44. Gross, L.C., et al., Determining membrane capacitance by dynamic control of droplet interface bilayer area. Langmuir, 2011. 27(23): p. 14335-42.
- 45. Downs, F.G., et al., Multi-responsive hydrogel structures from patterned droplet networks. Nature Chemistry, 2020. 12(4): p. 363-371.
- 46. Friddin, M.S., et al., Optically assembled droplet interface bilayer (OptiDIB) networks from cell-sized microdroplets. Royal society of Chemistry-Soft Matter, 2016. 12: p. 7731-7734.
- 47. Bolognesi, G., et al., Sculpting and fusing biomimetic vesicle networks using optical tweezers. Nature Communications, 2018. 9(1): p. 1882.
- 48. Makhoul-Mansour, M., et al., Ferrofluid-Based Droplet Interface Bilayer Networks. Langmuir, 2017. 33(45): p. 13000-13007.
- 49. Challita, E.J., M.M. Makhoul-Mansour, and E.C. Freeman, Reconfiguring droplet interface bilayer networks through sacrificial membranes. Biomicrofluidics, 2018. 12(3): p. 034112.
- 50. Strutt, R., et al., Activating mechanosensitive channels embedded in droplet interface bilayers using membrane asymmetry. Chemical Science, 2021.

- 51. Steinberg, M.S., Differential adhesion in morphogenesis: a modern view. Current opinion in genetics & development, 2007. 17(4): p. 281-286.
- 52. Rauzi, M. and P.-F. Lenne, Cortical forces in cell shape changes and tissue morphogenesis, in Current topics in developmental biology. 2011, Elsevier. p. 93-144.
- 53. Lecuit, T., P.-F. Lenne, and E. Munro, Force generation, transmission, and integration during cell and tissue morphogenesis. Annual review of cell and developmental biology, 2011. 27: p. 157-184.
- 54. Guillot, C. and T. Lecuit, Mechanics of epithelial tissue homeostasis and morphogenesis. Science, 2013. 340(6137): p. 1185-1189.
- 55. David, R., et al., Tissue cohesion and the mechanics of cell rearrangement. Development, 2014. 141(19): p. 3672-3682.
- 56. Oda, H. and S. Tsukita, Real-time imaging of cell-cell adherens junctions reveals that Drosophila mesoderm invagination begins with two phases of apical constriction of cells. Journal of cell science, 2001. 114(3): p. 493-501.
- 57. Manning, M.L., et al., Coaction of intercellular adhesion and cortical tension specifies tissue surface tension. Proceedings of the National Academy of Sciences, 2010. 107(28): p. 12517-12522.
- 58. Amack, J.D. and M.L. Manning, Knowing the boundaries: extending the differential adhesion hypothesis in embryonic cell sorting. Science, 2012. 338(6104): p. 212-215.
- 59. Mierke, C.T., Initiation of a neoplasm or tumor, in Physics of Cancer. 2015, IOP Publishing. p. 1-1-1-54.

- 60. Bayley, H., et al., Droplet Interface Bilayers Royal Society of Chemistry 2008. 4(12): p. 1191-1208.
- 61. Aghdaei, S., et al., Formation of artificial lipid bilayers using droplet dielectrophoresis. Lab on a Chip, 2008. 8(10): p. 1617-1620.
- 62. Berthier, J. and K.A. Brakke, The physics of microdroplets. 2012: John Wiley & Sons.
- 63. Zhu, T., et al., Analytical model of microfluidic transport of non-magnetic particles in ferrofluids under the influence of a permanent magnet. Microfluidics and Nanofluidics, 2011. 10(6): p. 1233-1245.
- 64. Kirby, B.J., Micro-and nanoscale fluid mechanics: transport in microfluidic devices. 2010: Cambridge University Press.
- 65. Rosensweig, R.E., Ferrohydrodynamics. 2013: Courier Corporation.
- 66. Bergeron, V., Forces and structure in thin liquid soap films. Journal of Physics-Condensed Matter, 1999. 11(19): p. R215-R238.
- 67. Dupin, A. and F.C. Simmel, Signalling and differentiation in emulsion-based multi-compartmentalized in vitro gene circuits. Nature Chemistry, 2018: p. 1.
- 68. Freeman, E.C., et al., Multiscale modeling of droplet interface bilayer membrane networks. Biomicrofluidics, 2015. 9(6): p. 064101.
- 69. Xu, J., F.J. Sigworth, and D.A. LaVan, Synthetic protocells to mimic and test cell function. Adv Mater, 2010. 22(1): p. 120-7.
- 70. Li, X., et al., Peptide-Mediated Membrane Transport of Macromolecular Cargo Driven by Membrane Asymmetry. Anal Chem, 2017.

- 71. Alcinesio, A., et al., Controlled packing and single-droplet resolution of 3D-printed functional synthetic tissues. Nature Communications, 2020. 11(1): p. 1-13.
- 72. Furst, E.M. and T.M. Squires, Microrheology. 2017: Oxford University Press.
- 73. Zhu, G.-P., et al., Nonlinear deformation of a ferrofluid droplet in a uniform magnetic field. Langmuir, 2011. 27(24): p. 14834-14841.
- 74. Nguyen, N.T., et al., Magnetowetting and sliding motion of a sessile ferrofluid droplet in the presence of a permanent magnet. Langmuir, 2010. 26(15): p. 12553-9.

CHAPTER 6

⁵ M. M. Makhoul-Mansour, J. B. El-Beyrouthy, H. L. Mumme, E. C. Freeman, Soft Matter 2019, 15, 8718. Reprinted here with permission of the publisher

6.1. Abstract

Controlled transport within a network of aqueous subcompartments provides a foundation for the construction of biologically inspired materials. These materials are commonly assembled using the droplet interface bilayer (DIB) technique, adhering droplets together into a network of lipid membranes. DIB structures may be functionalized to generate conductive pathways by enhancing the permeability of pre-selected membranes, a strategy inspired by nature. Traditionally these pathways are generated by dissolving pore-forming toxins (PFTs) in the aqueous phase. A downside of this approach when working with larger DIB networks is that transport is enabled in all membranes bordering the droplets containing the dissolved PFT, instead of occurring exclusively between stained droplets. To rectify this limitation, photopolymerizable phospholipids (23:2 DiynePC) are incorporated within the aqueous phase of the DIB platform, forming conductive pathways in the lipid membranes post-exposure to UV-C light. Notably these pathways are only formed in the membrane if both adhered droplets contain the photoresponsive lipids. Patterned DIB networks can then be generated by controlling the lipid composition within select droplets which creates conductive routes one droplet thick. We propose that the incorporation of photo-polymerizable phospholipids within the aqueous phase of DIB networks will improve the resolution of the patterned conductive pathways and reduce diffusive loss within the synthetic biological network.

6.2. Introduction

Living cells coordinate behaviors that are foundational to the natural world, aided by collections of membranous barriers providing an internal structure. These lipid membranes are fundamental cellular elements, delimiting the cells and restricting the undesired diffusion of polar molecules [1]. When transmembrane exchange is necessary for chemical signaling, biosynthesis, or other functions, the lipid bilayers' permeability is altered through membrane-embedded biomolecules acting as pores, channels, and transporters [1-3]. This allows for precise exchanges and spatiotemporal control over the internal composition of each individual cell.

Cellular organisms are able to facilitate complex schemes for communication and adaptation using these mechanisms. These remarkable capabilities have been the focus of bioinspired materials research attempting to reproduce cellular phenomena in engineered structures [4, 5]. While fully reproducing cellular phenomena within the laboratory is unrealistic, it is still possible to replicate select portions of the desired membranous phenomena through the creation of artificial lipid membranes exploiting self-assembly principles.

One approach for recreating lipid membranes is the droplet interface bilayer (DIB) technique (Figure 6.1), establishing biomimetic membranes between lipid-coated aqueous droplets [6-8]. Benefits of this technique include low material consumption, the ability to repeatedly assemble and disconnect multiple lipid bilayers [9, 10], the ability to create asymmetric membranes [11], and the relative ease of implementation. Droplets are deposited in an oil reservoir with lipids dissolved in either phase. After being provided sufficient time for the formation of lipid monolayers at the droplet surfaces, the droplets are brought into contact and lipid bilayers spontaneously form at their interfaces [7, 8, 12]. These membranes may be electrically approximated as a capacitor in parallel with a resistor [13-15] (Figure 6.1.a), and the interfacial membrane dimensions at equilibrium are a function of the monolayer and bilayer tensions [16] (Figure 6.1.b). The DIB technique has

been recently widely employed as a reliable platform for the reliable construction of membrane-based materials [17-22].

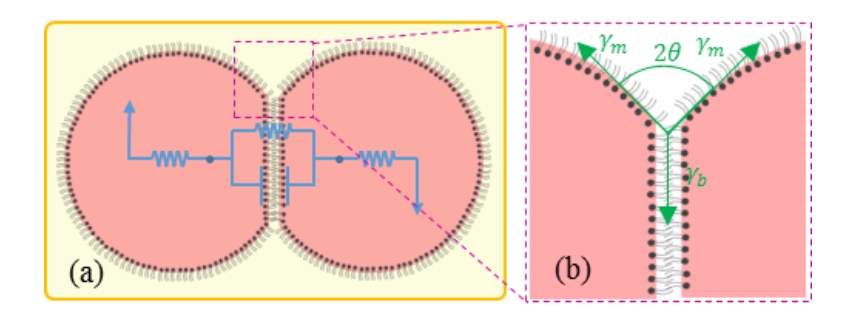


Figure 6.1- Schematic representation of the droplet interface bilayer (DIB) technique. After being introduced into an oil medium, aqueous droplets acquire a lipid coating referred to as lipid monolayer. As droplets are brought together, oil at their interface is gradually expelled and the lipid bilayer spontaneously forms. A lipid bilayer can be electrically modeled as a capacitor in parallel with a high amplitude resistor. The bilayer interfacial tension is balanced with the two opposing monolayer tensions separated by the angle of contact 2θ .

An additional advantage of the DIB technique is the ability to combine multiple membranes into larger networks. Each droplet is separated from neighboring droplets through either their semi-permeable lipid membranes or the insulating oil. Consequently, each droplet may be treated as a separate compartment or domain. Exchange between neighboring droplets is typically minimized unless the membranes between them are functionalized with transport-enabling biomolecules. This functionalization is typically accomplished through embedded proteins and peptides such as alpha-hemolysin (α HI) [18, 23, 24] producing stimuli-responsive soft structures that mimic the versatility of cellular organisms. The collective action of multiple droplets with varying designated functions

working in parallel provides the desired emergent properties of the bioinspired materials [25, 26].

PFT-enabled exchange of droplet contents between different compartments within DIB networks has been successfully implemented in various studies [5, 17, 18, 22, 27]. While αHL is one of the most reliable agents for creating nanopores in lipid membranes [28] and has been used to create diffusion pathways for membrane-based materials [5, 18], it typically establishes pores in all bilayers surrounding the carrier droplet as depicted in Figure 6.2.a. Unintentional diffusive exchange occurs as a result where multiple membranes are functionalized with the pore [10, 29, 30].

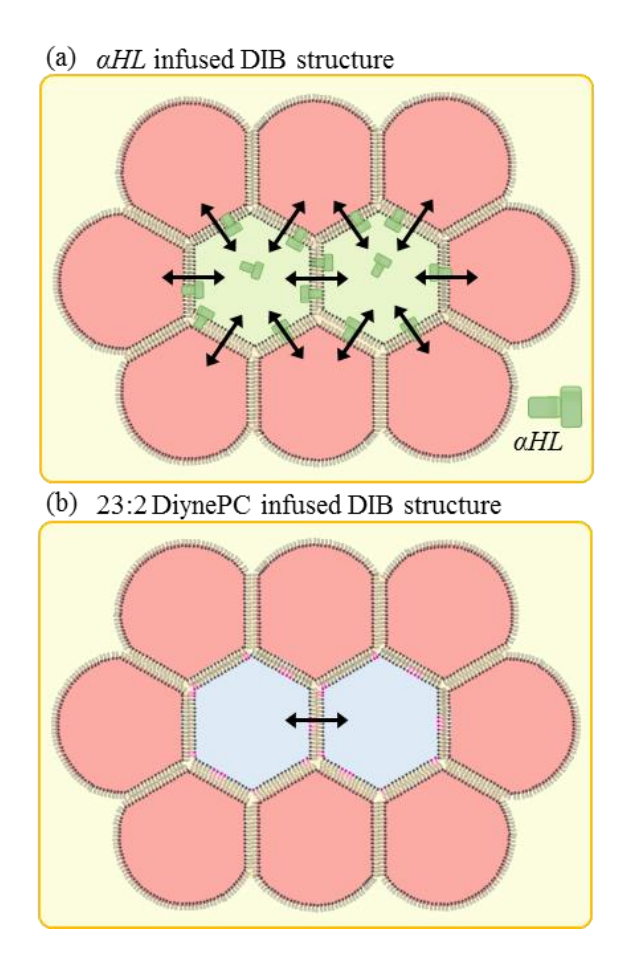


Figure 6.2- Schematic representation of two different scenarios for the generation of diffusive pathways within DIB structures as indicated by arrows across the interfacial

membranes. Red droplets contain DPhPC lipids, green droplets contain DPhPC as well as the pore forming toxin αHL, and the blue droplets contain a mixture of DPhPC and 23:2 DiynePC photopolymerizable phospholipids. In (a) when the two central droplets are infused with αHL, diffusive pathways are generated in all bordering bilayers. (b) In contrast, if the central droplets are infused with 23:2 DiynePC polymerizable lipids and exposed to UV-C light thus triggering lipid polymerization, diffusive pathways can only be generated between leaflets both containing the DiynePC microdomains.

Naturally occurring membrane-bound transporters such as αHl span the entire thickness of the membrane interior. This is unsurprising given their intended role but leads to this previously noted shortcoming in diffusive loss when reassembling these materials. An ideal replacement for these pores would only enable exchange between droplets that both share a common characteristic, eliminating the unintentional diffusive exchange by restricting how the channels are constructed such as in Figure 6.2.b. This replacement requires an alternative approach for modifying the membrane permeability.

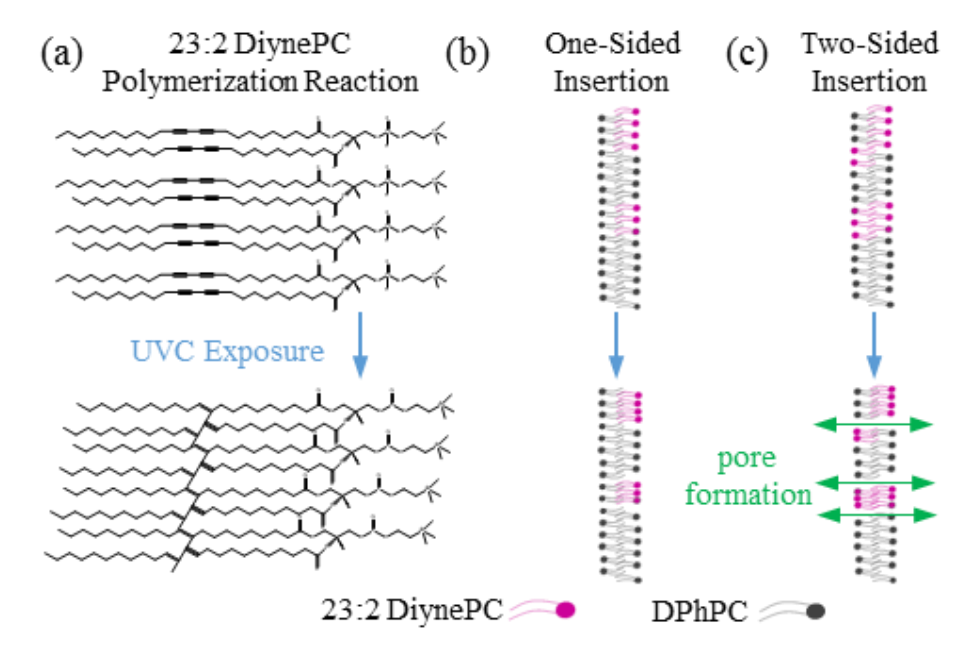


Figure 6.3- Schematic representations: (a) Cross-linking of 23:2 DiynePC phospholipids after the application of UV-C light for 5 minutes. (b) (c) Cross-linking of 23:2 DiynePC lipids within a lipid bilayer when it was introduced from (b) one side and (c) two sides of the bilayer. As DiynePC polymerized, the lipid chains tightly packed together resulting in the formation of structural pores within the lipid bilayer whenever polymerizable lipids were present on both sides as shown in (c). Pores in this case are a result of polymerizable lipids tightly packing together forming discontinuities in the molecular distribution at the monolayer and bilayer levels. Owing to the positioning of the diacetylene groups within each lipid molecule and to the ordered alignment polymerization condition, no cross-leaflet polymerization is anticipated. Polymerization is constricted to occur between molecules present on the same leaflet.

The permeability of a lipid membrane is also influenced by the membrane's lipid composition. When multiple types of lipids are incorporated within model bilayers, their suprastructure or lateral organization is not random [31] and is viewed in the context of the fluid mosaic model [32]. Bilayers containing a mixture of different lipids often exhibit an amphiphilic self-organization phenomenon [31-35] that helps minimize unfavorable interactions between dissimilar lipids [36, 37]. Furthermore, the presence of coexisting lipid microdomains or phases has been observed to enhance transmembrane diffusion [38, 39], and these microdomains may be created through photoresponsive lipids. 23:2 DiynePC [DC (8,9) PC], also known as 1,2-bis(10,12-tricosadiynoyl)-sn-glycero-3 phosphocholine, is a synthetic phospholipid containing two diacetylene groups. The diacetylene groups render this lipid polymerizable through UV-C exposure similar to various types of other synthetic polymerizable lipids (optimized at 254 nm irradiation wavelength [35, 40-44]).

When diacetylene-containing lipid compounds are arranged in a highly ordered arrays [35, 45], UV-C light causes the two conjugated triple bonds of the lipid monomers to be replaced in the final polymer by an alternating double-bonded and triple-bonded conjugated structure, linking the lipids together and forming stable microdomains within the membrane [46] as illustrated in Figure 6.3. This polymerization mechanism occurs when lipids are present at a condensed and highly ordered (corresponding to a correct alignment of the diacetylene groups) state [47].

The polymerization of UV-sensitive lipids within liposomes allowed for the release of their contents across the membrane, including calcein, HPPH (2-(1-Hexyloxyethyl)-2-devinyl pyropheophorbide-a) and even doxorubicin [48, 49], demonstrating enhanced membrane permeability through photopolymerization. The incorporation of photopolymerizable lipids in DIBs was first suggested by Punnamaraju et al. [48, 50] as a method for studying phototriggered drug delivery systems in vitro. The introduction of the photosensitive lipids into the oil phase of a DIB was shown to allow for successful calcein diffusion across the membrane after UV-C exposure and formation of transmembrane pores [50] in agreement with previously reported results.

The cause of the increased membrane permeability when 23:2 DiynePC lipids are incorporated is expected to require the presence of polymerized microdomains in both leaflets and is suggested to be the result of a transmembrane coordination of defects. Since the DIB approach allows for the creation of asymmetric membranes by varying the lipid composition within the droplets, it is possible to limit the formation of the transmembrane defects as a function of the droplet lipid compositions. The selective dissolution of DiynePC in the aqueous phase would only establish transmembrane defects between

droplets that both contain the DiynePC microdomains (Figure 6.3.b.) thus limiting droplet-droplet exchange to compatible droplets. This would allow for tailored membrane permeability through membrane structure and asymmetry.

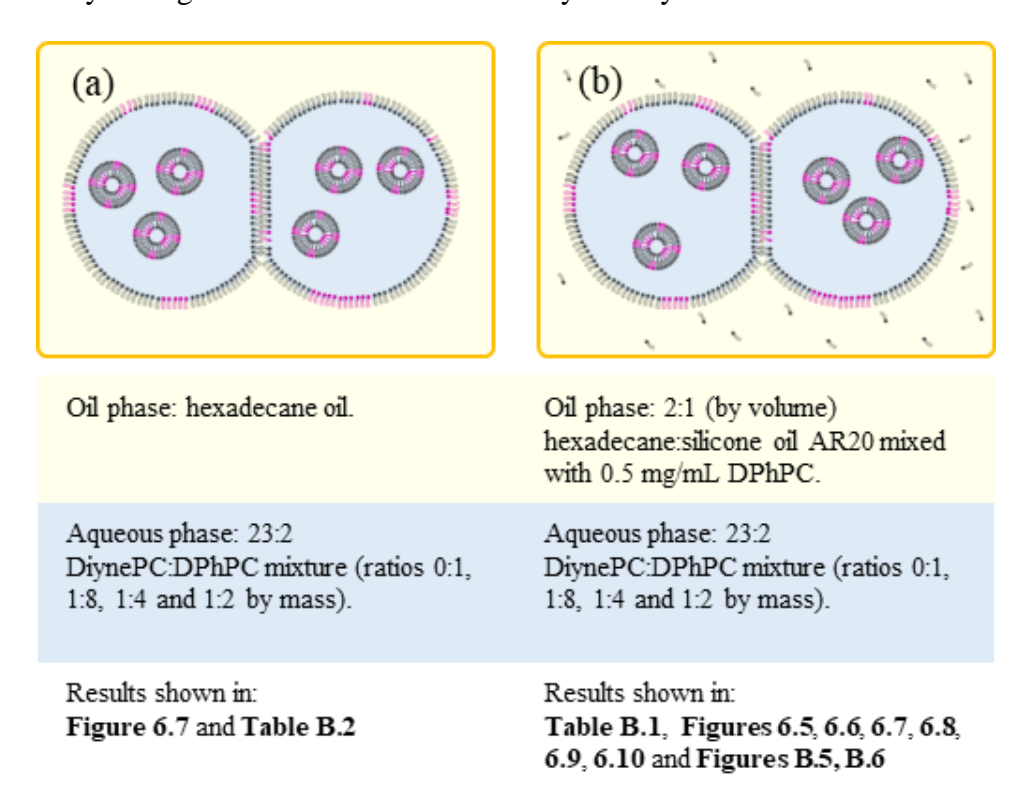


Figure 6.4- Summary of the oil/aqueous phases used in this work.

These phototriggered diffusive pathways may be established within larger DIB structures, only creating pores between droplets with similar compositions and avoiding the issues presented by αHl and similar PFTs. Light-sensitive DIB networks have been explored previously in the literature [4, 27, 51], altering the membrane characteristics either through bacteriorhodopsin or through the in vitro transcription/translation (IVTT) of αHl triggered through UV exposure. In this work, UV-C exposure is used to modify properties of the membranes by inducing an increased membrane permeability through the formation of photo-polymerized domains within the leaflets.

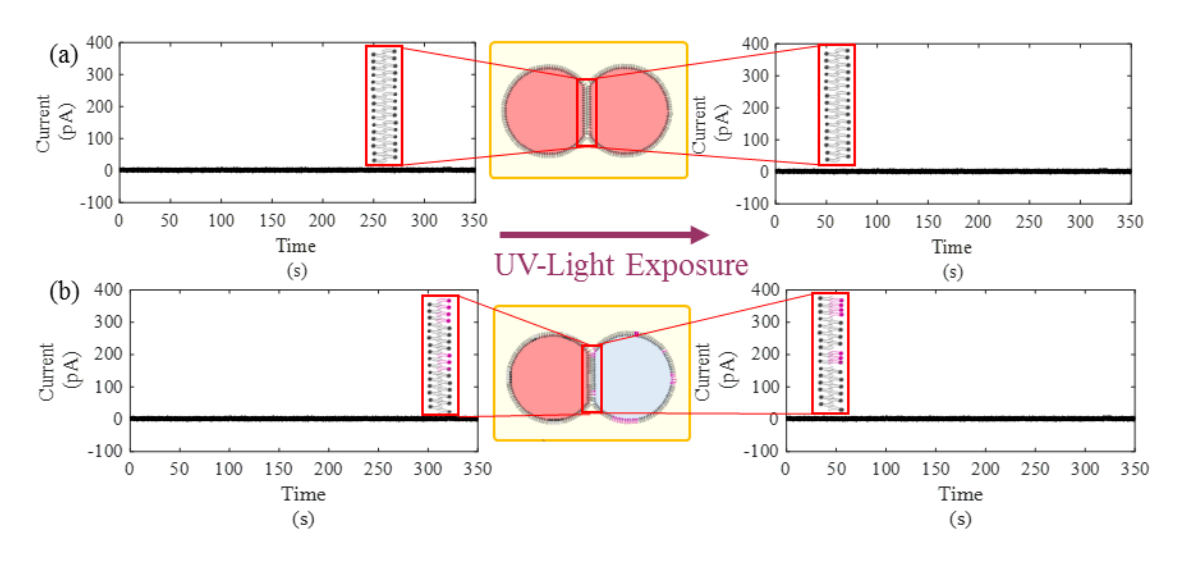


Figure 6.5- Current traces obtained for a constant applied voltage of +100 mV before and after application of UV-C light for 5 minutes. The red droplets contain DPhPC dissolved at 2.5 mg/mL and blue droplets contain 1:4 mixture of 23:2 DiynePC:DPhPC dissolved at 2.5 mg/mL. The solvent is 2:1 hexadecane:silicone oil AR20 0.5 mg/mL DPhPC oil-lipid mixture. In (a) the DIB is formed between two aqueous droplets only containing DPhPC. No pore formation is noted after the application of UV-C, and the membrane remains highly resistive. In (b) the DIB is formed between two aqueous droplets containing polymerizable and non-polymerizable phospholipids. No pore formation is noted after the application of UV-C. Similar traces were observed when the ratio of polymerizable to non-polymerizable lipids were 1:2 and 1:8 by mass respectively and when hexadecane alone was used as an external phase as well. All measurements were recorded in voltage clamp mode at a sampling frequency of 10 kHz and filtered at 1 kHz (using the embedded low-pass Bessel filter -80 dB/decade). Post-acquisition, data was filtered at 500 Hz using a fourth-order Butterworth low-pass filter in MATLAB.

In this manuscript we demonstrate that DiynePC-enabled diffusion only occurs in bilayers that incorporate polymerizable lipids within both leaflets as depicted in Figure 6.3. The qualities of DIBs formed with different ratios of added polymerizable lipids and different oils are assessed using tensiometry and their induced change in conductance are measured through electrophysiology. In light of these results, a suitable aqueous-lipid and oil-lipid mixtures combination is then determined and used to form larger 2D bilayer structures. The advantages of the phototriggered diffusive pathways are showcased by comparing the activity of αHL and polymerizable DiynePC in similar DIB structures. Finally, the diffusive capabilities of these bilayers is displayed through calcein diffusion.

6.3. Materials and Methods

Detailed protocols for solution preparation and experimental methodologies may be found in the Appendix B. A brief overview of these approaches is provided below.

Aqueous solutions containing varying ratios of DiynePC and 1,2-diphytanoyl-sn-glycero-3-phosphocholine (DPhPC) were prepared [52]. Droplets of these solutions were injected into oil reservoirs using microinjectors. This oil was either a 2:1 hexadecane:silicone oil AR20 mixture containing dissolved DPhPC at 0.5 mg/mL or hexadecane without lipids (Figure 6.4).

Monolayer surface tension measurements were taken using pendant drop tensiometry with a custom stage (illustrated in Figure B.1 in Appendix B) and the open-source software OpenDrop [53]. The kinetics of monolayer formation, monolayer tension at equilibrium, and influence of UV-C exposure were tracked as a function of the ratio of DiynePC:DPhPC within the aqueous phase. Changes in the equilibrium energy per area was tracked as evidence of successful photo-polymerization of the interface.

Membrane characterization was accomplished through electrophysiology. Droplets were directly deposited onto silver/silver-chloride (Ag/AgCl) electrodes coated in agarose within an appropriately grounded Faraday cage on a microscope stage and connected to electrophysiology equipment. Voltage was applied across the membrane using function generators with the patch-clamp amplifier in voltage-clamp mode, and the membrane response was recorded and exported for post-processing to extract the net membrane capacitance and conductance. Micrographs of the adhered droplet geometry were then combined with the electrical recordings to produce the membrane specific capacitance and conductance, or the capacitance and conductance per membrane area.

The solutions were cured either prior to droplet formation or in situ using a 254 nm UV-C mercury lamp for 5 minutes. UV-C enabled transmembrane exchange was characterized in single adhered droplet pairs and networks of adhered droplets for all cases. When droplet networks were desired, the droplets were deposited within an acrylic egg crate substrate to hold the droplets in place [14]. Diffusion of calcein was tracked using fluorescent microscopy and ImageJ.

6.4. Results and Discussion

Membrane Conductance with Asymmetric/Symmetric Distribution of 23:2 DiynePC Polymerizable Lipids

Photopolymerizable lipids were tested for enabling diffusive transport between adjacent droplets. Transmembrane diffusion is hypothesized to occur as a result of photopolymerized DiynePC microdomains [50] interactions (Figure 6.3) across opposing monolayers. The differences between asymmetric and symmetric distributions of the UV-sensitive lipid was not reported in the literature, but the transport should only be enabled

when DiynePC is present in both leaflets in contrast to the behavior of αHl shown in Figure B.3 (Appendix B). This requirement for symmetric distributions of the phospholipids to enable transport is similar the mechanics of gramicidin dimers shown in Figure B.4 (Appendix B). However, DiynePC is preferred over gramicidin since it is not cation selective and may be further controlled by UV-C exposure. As a baseline point of reference, DIBs containing only the non-polymerizable DPhPC phospholipids were first tested. Current traces with a constant voltage before and after UV-C light exposure are shown in Figure 6.5.a. where no conductive currents are reported demonstrating that the induced defects are not functions of UV-C exposure alone. Next the symmetric/asymmetric DiynePC: DPhPC studies were conducted as shown in Figure 5.b. for asymmetric bilayers and Figure 6.6 for symmetric bilayers with different ratios of the polymerizable lipids. As suggested by the previous hypothesis and confirmed in Figure 6.5 and Figure 6.6, the enhanced membrane permeability only occurs when both adhered droplets contain photopolymerized DiynePC microdomains.

Several trends are noted. First, when the photopolymerizable lipids are present only on one side of the bilayer, no changes in membrane conductance are observed (Figure 6.5.b). This was consistent for all concentrations of the photopolymerizable lipids and all oils. Second, the symmetric membranes exhibited negligible conductance prior to UV-C exposure, even with greater ratios of DiynePC:DPhPC. All cases with symmetric distributions of DiynePC shown in Figure 6.6 exhibit drifting changes in conductance as the rafts in both leaflets align and separate across the membrane. Similar changes in membrane conductance were observed whether the solutions were polymerized in situ after membrane formation or prior to droplet deposition. Electrical recordings during

photopolymerization cannot be provided because of the high noise levels generated by the UV-C source [50]. The photopolymerized DIBs exhibit stability comparable to unmodified DPhPC DIBs and typically lasted for the maximum duration of an experiment (>6 hours) with an applied 100 mV DC voltage. Finally, while the membrane conductance varies with respect to time dependent on domain alignment, the measured increases in conductance generated by DiynePC are considerably larger than the increases provided by α H1 (Figure B.3 Appendix B).

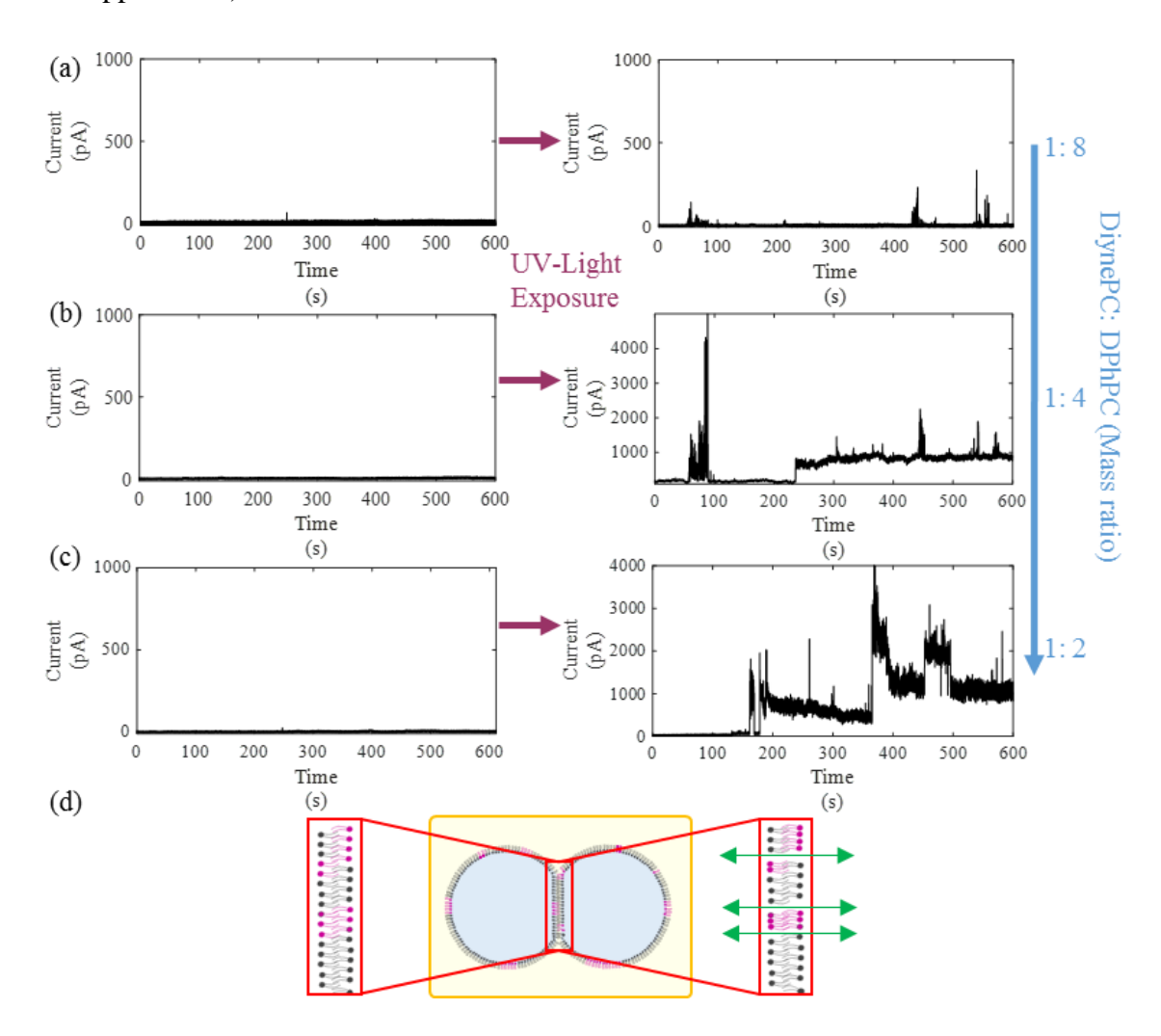


Figure 6.6- Current traces obtained for a constant applied voltage of +100 mV before and after application of UV-C light for 5 minutes. The DIBs are formed between two aqueous

droplets containing polymerizable and non-polymerizable phospholipids (23:2 DiynePC and DPhPC) dissolved at a concentration of 2.5 mg/ml in a 2:1 hexadecane:silicone oil AR 20 0.5 mg/mL DPhPC oil-lipid mixture. The ratio of polymerizable to non-polymerizable lipids by mass was (a) 1:8, (b) 1:4, and (c) 1:2. Polymerizable lipids were introduced form both sides of the bilayer. Similar trends can be observed when Hexadecane oil is used as an external phase. (d) Shows a schematic representation of the formed bilayer pre and post UV-C curing. All measurements were recorded in voltage clamp mode at a sampling frequency of 10 kHz and filtered at 1 kHz (using the embedded low-pass Bessel filter –80 dB/decade). Post-acquisition, data was filtered at 500 Hz using a fourth-order Butterworth low-pass filter in MATLAB.

Cyclic Voltammetry Results

Next cyclic voltammetry was used to further compare the conductive current induced by DiynePC with different lipid ratios. Lipid bilayers formed using traditional non-polymerizable phospholipids such as DPhPC are not expected to exhibit notable current-voltage dependent behavior relative to composite lipid membranes with incorporated peptides or more specifically pores [21, 24]. Figure 6.7 shows current vs. voltage traces obtained for bilayers containing the polymerized lipids. The bilayer containing polymerizable lipids exhibits an increase in conductance as the ratio of the DiynePC:DPhPC is augmented. This increase in conductance is likely caused by the increased probability of the polymerized lipid microdomains co-locating within the bilayer as the amount of DiynePC is increased, thus inducing localized lipid packing defects. This graph additionally shows that the 1:8 DiynePC:DPhPC mass ratio does not reliably

increase the membrane conductance compared to higher lipid ratios. Lipid mass ratios of 1:4 and 1:2 DiynePC:DPhPC respectively exhibit membrane conductance behaviors similar to those of pores and peptides [5].

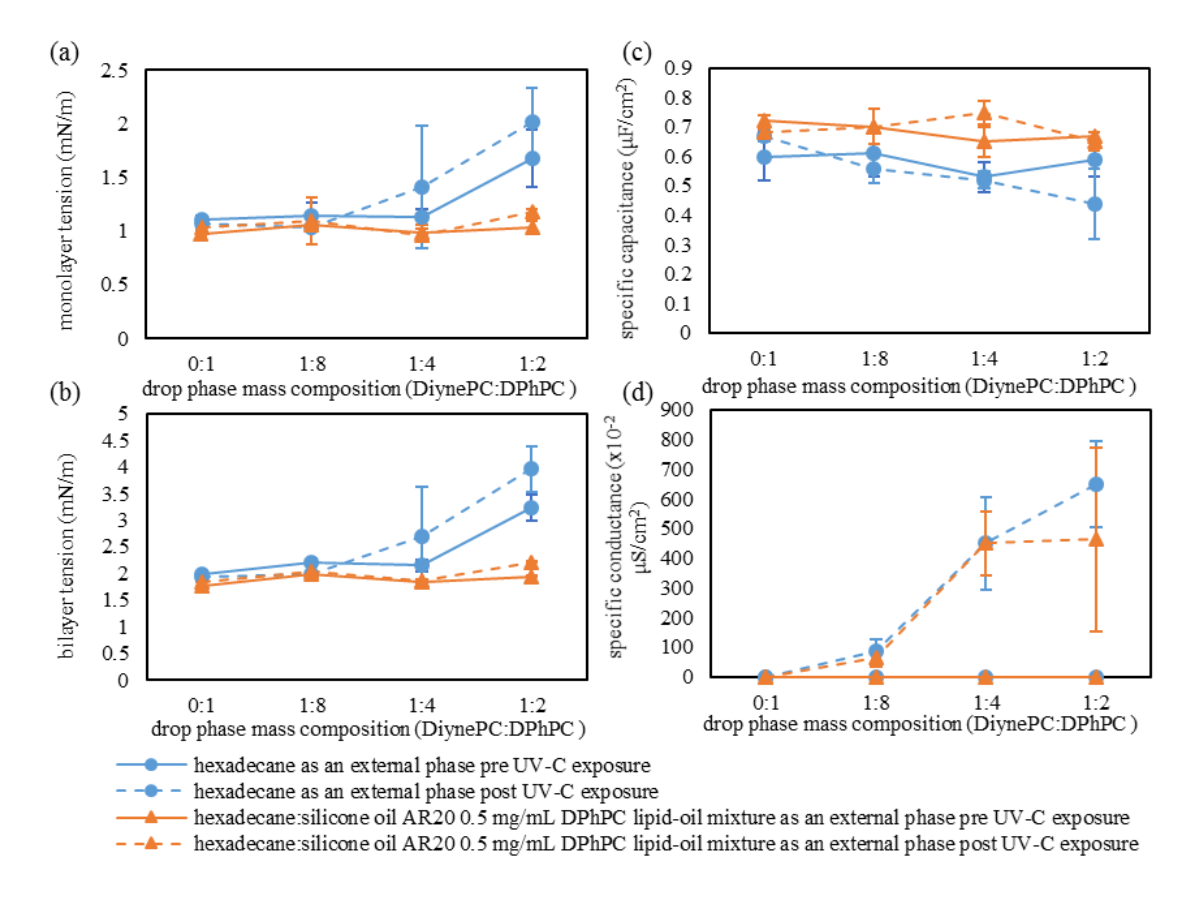


Figure 6.7- Measurement of the properties of lipid bilayers in hexadecane as well as 2:1 hexadecane:silicone oil AR20 DPhPC oil-lipid mixture for increasing concentrations of polymerizable lipids dissolved in the aqueous phase (2.5 mg/ml total) pre and post UVC exposure for 5 minutes. (a) shows the monolayer tension (mN/m), (b) shows the bilayer tension (mN/m), (c) shows the bilayer's specific capacitance (μ F/cm²) while (d) shows the bilayer's specific conductance (x10⁻² μ S/cm²).

DIB Properties

DIB properties including angle of contact, monolayer tension, bilayer tension, energy of adhesion, bilayer thickness, specific conductance, and specific capacitance were evaluated for bilayers formed in the hexadecane:silicone oil AR20 0.5 mg/mL DPhPC lipid-oil mixture (described in more details in the Materials section) where 23:2 DiynePC has been symmetrically introduced into the aqueous phase at different concentrations. This oil mixture has been selected as it enables greater droplet-droplet adhesion [54] as well as an ease in network creation by reducing gravitational influences [54]. DPhPC was dissolved in the oil mixture (lipids-out) and mixtures of DiynePC:DPhPC were selectively dissolved in the aqueous solutions to enable to formation of diffusive bridges. Dissolving DPhPC in both the aqueous and oil phases has been shown to enhance the DIB network stability [18], and the 2:1 hexadecane:silicone oil AR20 DPhPC is well-suited for lipid-out experiments. DiynePC was introduced only from the aqueous phase and was not dissolved in the oil phase, ensuring the ability to produce asymmetric membranes when necessary (Figure 6.4.b).

Table B.1 (Appendix B) includes measurements of the interfacial properties formed in a 2:1 hexadecane:silicone oil AR20 mixture with 0.5 mg/mL DPhPC in the continuous phase as used for the creation of droplet networks, and select trends are plotted in Figure 6.7. The DIBs specific capacitance as well as the monolayer tensions show no noticeable change pre and post polymerization for different introduced proportions of DiynePC. Meanwhile, as shown in the same table, the values for the contact angles show some change compared to a control case where no polymerizable lipids are present. However, there is not a clear relationship between the variation in the angle of contact and the proportion of

23:2 DiynePC introduced into the bilayer. These measurements are in a reasonable agreement with previously reported results for lipid bilayers formed through the DIB technique [54].

A clear change in membrane conductance pre and post UV-C exposure is demonstrated as measured by the specific conductance or conductance per area (Figure 7.d). Specific conductance is reported since the membrane dimensions vary with the amount of DiynePC. Bilayers that did not contain polymerizable lipids show no increase in their specific conductance. Small changes observed after UV irradiation in the case of DPhPC alone have been attributed in the literature with some disturbances caused by UV light or small motions among lipid molecules caused by formation of gauche defects[55]. Meanwhile, membranes containing DiynePC show a clear increase in their specific conductance post photo-polymerization. As expected from the cyclic voltammetry results, the specific conductance increases with the DiynePC:DPhPC ratio.

While dissolving DPhPC in the oil phase does not eliminate the influence of DiynePC on the membrane properties, it also does not isolate the influence of DiynePC on the interfacial properties as demonstrated in Figure 6.7.a and Figure 6.7.b (Table B.1 Appendix B). This was addressed by measuring these interfacial properties in hexadecane alone with no dissolved lipids in the oil (Figure 6.4.a). These experiments, summarized in Figure 6.7 and Table B.2 (Appendix B) show more decisive trends in the membrane parameters, highlighting the influence of DiynePC. A remarkable decrease in the angle of contact as reported by the bilayer and monolayer tensions (Figure 6.7.a-b) is noted prior to UV-C exposure as the ratio of DiynePC:DPhPC increases from 0:1 to 1:2. Post UV-C treatment, the angle of contact decreases further, suggesting the possible creation of

microdomains within the monolayer. Clear changes in the specific conductance of the membrane pre and post UV-C exposure are observed varying with the DiynePC:DPhPC ratio (Figure 6.7.d). It is worth noting that in Figure 6.7.c, Table B.1, and Table B.2 (Appendix B), the bilayers' specific capacitance do not exhibit definitive trends and fall within reported ranges for DPhPC membranes [54].

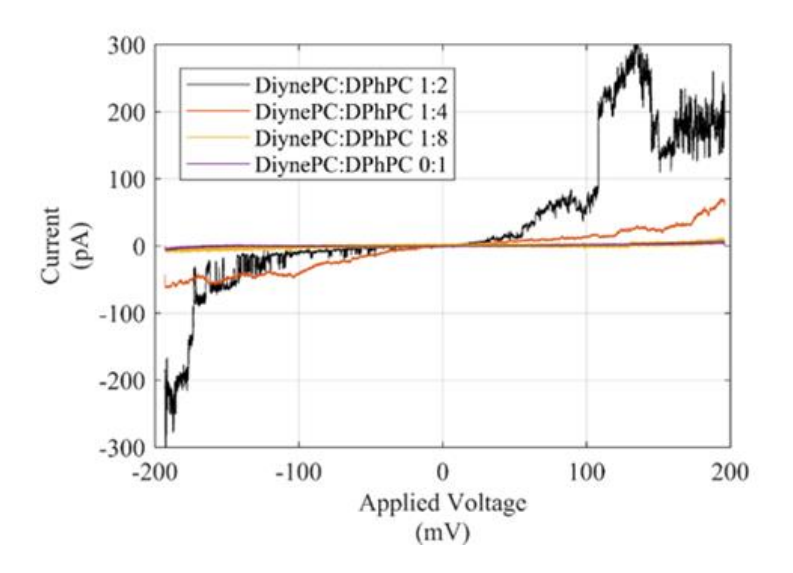


Figure 6.8- Current-voltage plots demonstrating pores formed post UV-C curing for different concentrations of polymerizable phospholipids (2.5 mg/ml in total in the aqueous phase) within the 2:1 hexadecane:silicone oil AR20 containing 0.5 mg/mL DPhPC lipid-oil mixture. A 4 mV/s voltage-sweep for these bilayers was performed and current responses recorded. All measurements were recorded in voltage clamp mode at a sampling frequency of 10 kHz and filtered at 1 kHz (using the embedded low-pass Bessel filter –80 dB/decade). Post-acquisition, data was filtered at 500 Hz using a fourth-order Butterworth low-pass filter in MATLAB.

While the 1:2 DiynePC:DPhPC droplet formulation allows for a highly permeable membrane (Figure 6.7.d) and shows properties that are in agreement with ranges for bilayer

properties previously reported in the literature (Figure 6.7.c) [54, 56], this mixture poses additional challenges for membrane formation. When using the 1:2 DiynePC:DPhPC lipid mass ratio an applied +150 mV DC voltage was necessary to induce bilayer formation through electrostatic compression even when using the 2:1 hexadecane:silicone oil AR20 DPhPC mixture. After formation, the membranes retained their integrity, and the droplets no longer required the external voltage to remain adhered together. Still, this renders the construction of a DIB network more challenging as voltage must be applied to each droplet

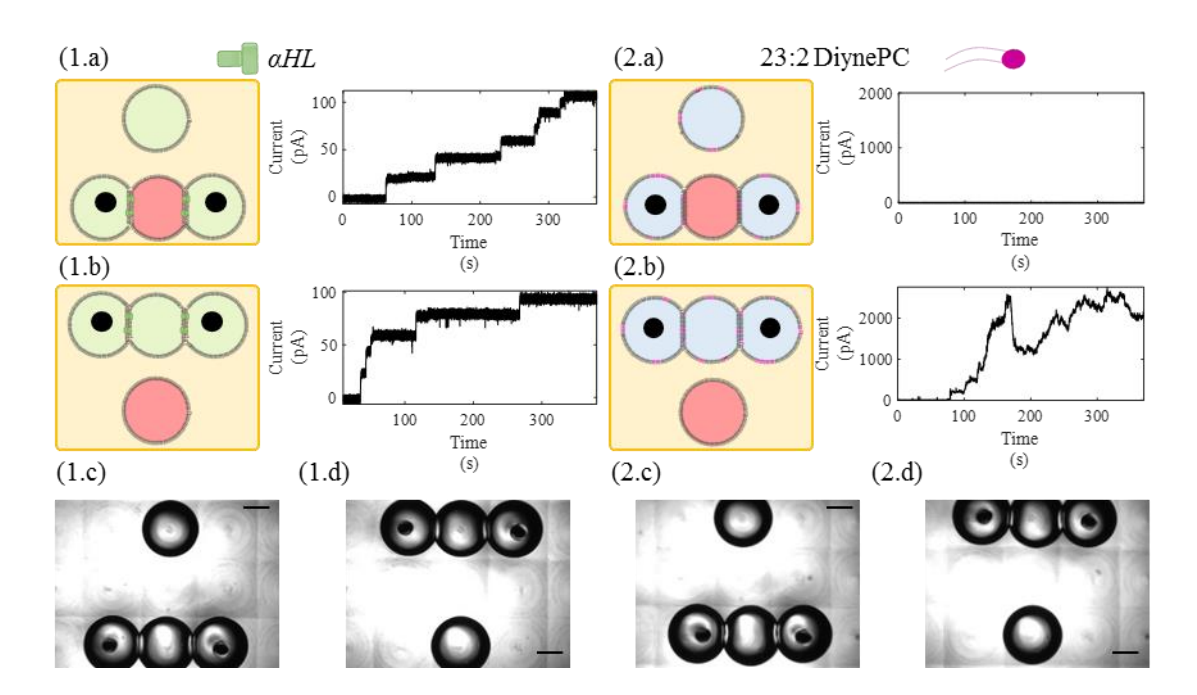


Figure 6.9- Current traces obtained for a constant applied voltage ($\pm 100 \text{ mV}$) and illustrating the properties of αHL and DiynePC. In both cases the red droplets contain only 2.5 mg/ml of DPhPC. Droplets are dispersed in a 2:1 hexadecane:silicone DPhPC lipid oil mixture to facilitate bilayer formation. A $\pm 200 \text{ mV}$ DC potential is applied between the electrodes, resulting in approximately $\pm 100 \text{ mV}$ per membrane. (1) The green droplets contain 1.25 $\mu g/mL$ of dissolved αHl . Both droplet configurations shown in (1.a) and (1.b)

result in the formation of a conductive pathway across the entire network since αHl is not required to insert from both sides of the membrane for pore formation. (2) Current traces obtained post application of a UV-C light for 5 minutes, illustrating the behavior of polymerized 23:2 DiynePC mixtures. The blue droplets contain a 1:4 mass ratio 23:2 DiynePC:DPhPC mixture dissolved at a total concentration of 2.5 mg/ml. In (2.a), the OFF configuration was switched by having a red droplet placed between two blue input droplets, stopping exchange across both membranes. In (2.b), the micro switch was turned to the ON configuration by moving the blue input droplets connected to the acquisition system so that all droplets containing polymerizable lipids were aligned in contrast with the case shown in (1.a) and (1.b). (1.c), (1.d), (2.c) and (2.d) show the images acquired for (1.a), (1.b), (2.a) and (2.b) respectively. All measurements were recorded in voltage clamp mode at a sampling frequency of 10 kHz and filtered at 1 kHz (using the embedded low-pass Bessel filter –80 dB/decade). Post-acquisition, data was filtered at 500 Hz using a fourth-order Butterworth low-pass filter in MATLAB. Scale bars represent 400 μm.

pair to induce bilayer formation. This drawback was not observed for the 1:8 and 1:4 DiynePC:DPhPC mixtures. The differences between the two solvents is summarized in Figure 6.4. The hexadecane solvent without dissolved lipids exhibits a slightly higher change in the specific conductance relative to the 2:1 hexadecane:silicone oil AR20 mixture with 0.5 mg/mL DPhPC (Figure 6.7.d). However, this value is a specific conductance or conductance per membrane area, and the reduction in contact angle and energy of adhesion with hexadecane alone (Table B.2 in Appendix B) will also diminish the net gain in membrane conductance. Furthermore the use of the 2:1 hexadecane:silicone oil AR20 solvent reduces gravitational influences on the droplets and is preferred for

network formation. From these experimental observations the best solution is to mix 23:2 DiynePC with DPhPC at a mass ratio of 1:4 and deposit these droplets into the 2:1 hexadecane:silicone oil AR20 DPhPC lipid-oil mixture to form stable DIB structures where the UV-sensitive lipids can induce droplet-droplet exchange after UV-C exposure. The remaining experimental results use this formulation.

Phototriggered Diffusive Pathways in DIB Networks

DiynePC may be used for phototriggered diffusive pathways through asymmetric distributions of the light-sensitive lipid. These diffusive pathways are only enabled when both droplets contain the UV-sensitive lipids, providing a greater degree of control over the diffusive transport and exploiting the ability to simply fabricate asymmetric membranes using the DIB technique. Transport is feasible across droplet chains after UV-C exposure only when all of the connected droplets contain DiynePC. Figure 6.9.2 shows a microswitch formed using four droplets. The droplet marked in red only contains nonpolymerizable phospholipids while the ones marked in blue contain the 1:4 DiynePC:DPhPC mixture. Figure 6.9.2.a shows the OFF configuration, with the anchor droplets (droplets connected to the electrodes) being connected to the red droplet. No pores can be formed through this configuration as polymerizable lipids are only present on one side in each of the two bilayers and the measured current remains negligible as expected. If αHl had been used instead of photopolymerized lipids as shown in Figure 6.9.1, the switch would have generated a conductive pathway in either configuration (Figure 6.9.1.a and Figure 6.9.1.b respectively). Figure 6.9.2.b shows the ON configuration that occurs when the anchor droplets are moved up to form two bilayers with the third photo-sensitive droplet sandwiched in between. As anticipated, pores were formed once 23:2 DiynePC was

present on both sides of each bilayer. Figure B.5 and Figure B.6 (Appendix B) show larger photo-sensitive DIB structures with conductive pathways generated between 4 then 6 polymerized membranes. Both figures show that the conductive pathway is not generated unless all droplets containing polymerized lipids align and form defects within the membranes separating the droplets.

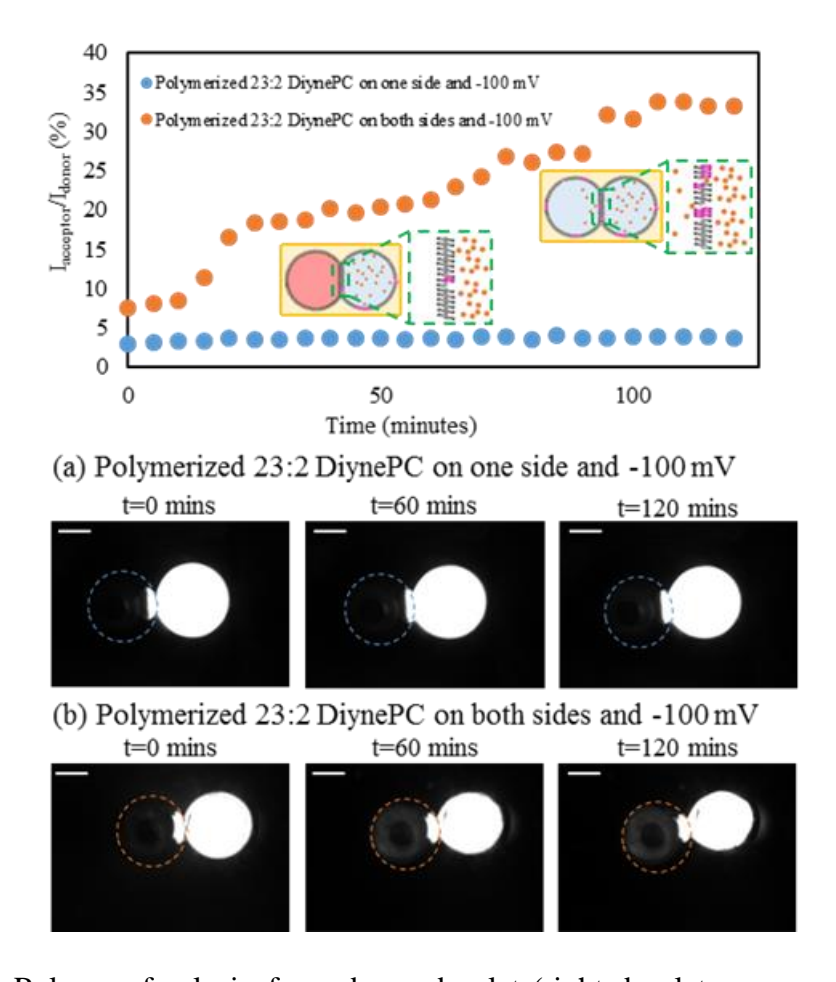


Figure 6.10- Release of calcein from donor droplet (right droplet corresponding to the reference side of the bilayer) to the acceptor droplet (left droplet). The plot shows the percentage of calcein fluorescence vs time in the acceptor droplet (I_{acceptor}) vs the donor (I_{donor}) droplet for the four experimental cases. (a), (b), (c) and (d) show the respective fluorescence images for the DIBs. Bright areas indicate the presence of calcein while dark areas do not contain calcein. In all experimental cases, a -100 mV was being applied and

the 2:1 hexadecane:silicone DPhPC oil-lipid mixture was used. (a) Images acquired for the control case where the donor droplet contained pre-polymerized 23:2 DiynePC (as well as DPhPC at a mass ratio of 1:4) and calcein (at a concentration of 0.25 mg/ml) while the acceptor droplet contained non-polymerizable lipids only (DPhPC). (b) Both droplets contain pre-polymerized 23:2 DiynePC (as well as DPhPC at a mass ratio of 1:4) but calcein is only present in the donor droplet at a concentration of 0.25 mg/ml. Scale bars represent 200 μ m.

Calcein Diffusion across a Single DIB

An advantage of DiynePC is its ability to facilitate the diffusion of larger molecules across the membrane. This is examined here by tracking the diffusion of calcein between two droplets using fluorescent microscopy. Figure 6.10 shows the diffusion of calcein across bilayers with incorporated polymerized lipids. Calcein is encapsulated in a donor droplet at a concentration of 0.25 mg/ml. When donor droplets containing polymerized 23:2 DiynePC along with DPhPC in a 1:4 mass ratio are coupled with an acceptor droplet containing DPhPC only, no significant release of calcein across the membrane is observed (Figure 6.10.a). This is because the distribution of DiynePC within the membrane is asymmetric, and transmembrane defects are not present as shown in Figure 6.5.a. When DiynePC was present in both the donor and receptor droplets as shown in Figure 6.10.b, calcein was capable of diffusing across the bilayer. The diffusive exchange is quantified as a function of the ratio of fluorescent intensities of the droplets. The ratio of the fluorescent intensity of the acceptor droplet vs. the donor droplet increased in this case whereas it remained constant in the control case (shown in Figure 6.10.a). The release of calcein in Figure 10.b, can be attributed to the enhanced permeability of the bilayer upon the symmetric introduction of C23 polymerizable lipids. This confirms previous results obtained in this work the selective introduction of DiynePC in the aqueous phase of DIBs. Conductive pores can only be created between droplets that share the same composition, and droplet-droplet exchange is limited to droplets with similar lipid compositions.

6.5. Conclusion

Herein we present a new application for UV-polymerizable lipids within the DIB platform. Our research shows that when diacetylene-enabled lipids are incorporated and polymerized on both leaflets of a lipid membrane, pores are produced within the membrane confirming previous hypotheses on the mechanics of DiynePC-aided transmembrane diffusion [48, 50, 57]. A key advantage of this approach is the requirement for DiynePC in both leaflets for enhanced membrane permeability. This approach exploits the capability to create asymmetric membranes using the DIB technique, producing patterned diffusive pathways within the droplet network. When compared to pores formed by αHL and gramicidin, defects induced by the UV-triggered lipid packing alteration are advantageous due to their symmetry requirements for conductance and their non-selectivity for transported molecules. Our approach reduces unwanted diffusion by patterning diffusive pathways in droplet networks through UV-C exposure and lipid microdomains.

6.6. References

1. Apellániz, B., et al., All-or-none versus graded: single-vesicle analysis reveals lipid composition effects on membrane permeabilization. Biophysical journal, 2010. 99(11): p. 3619-3628.

- 2. Cafiso, D.S., ALAMETHICIN: A Peptide Model for V oltage Gating and Protein-Membrane Interactions Annual Reviews-Biophysical Biolmolecular Structures 1994. 23: p. 141-165.
- 3. Andersen, O., Ion movement through gramicidin A channels. Single-channel measurements at very high potentials. Biophysical journal, 1983. 41(2): p. 119-133.
- 4. Booth, M.J., et al., Light-patterning of synthetic tissues with single droplet resolution. Scientific reports, 2017. 7(1): p. 9315.
- 5. Challita, E.J., et al., Encapsulating Networks of Droplet Interface Bilayers in a Thermoreversible Organogel. Scientific reports, 2018. 8(1): p. 6494-6505.
- 6. Bibette, J., F.L. Calderon, and P. Poulin, Emulsions: basic principles. Reports on Progress in Physics, 1999. 62(6): p. 969.
- 7. Funakoshi, K., H. Suzuki, and S. Takeuchi, Lipid bilayer formation by contacting monolayers in a microfluidic device for membrane protein analysis. Analytical chemistry, 2006. 78(24): p. 8169-8174.
- 8. Bayley, H., et al., Droplet interface bilayers. Molecular BioSystems, 2008. 4(12): p. 1191-208.
- 9. Syeda, R., et al., Screening blockers against a potassium channel with a droplet interface bilayer array. J Am Chem Soc, 2008. 130(46): p. 15543-8.
- 10. Challita, E.J. and E.C. Freeman, Hydrogel Microelectrodes for the Rapid, Reliable, and Repeatable Characterization of Lipid Membranes. Langmuir, 2018. 34(50): p. 15166-15173.

- 11. Taylor, G., et al., Electrophysiological interrogation of asymmetric droplet interface bilayers reveals surface-bound alamethic iniduces lipid flip-flop. Biochimica et Biophysica Acta (BBA) Biomembranes, 2018.
- 12. Venkatesan, G.A., et al., Adsorption Kinetics Dictate Monolayer Self-Assembly for Both Lipid-In and Lipid-Out Approaches to Droplet Interface Bilayer Formation. ACS-Langmuir, 2015. 31(47): p. 12883-12893.
- 13. Creasy, M.A., et al., Deterministic model of biomolecular networks with stimuliresponsive properties. Journal of Intelligent Material Systems and Structures, 2014. 26(8): p. 921-930.
- 14. Freeman, E.C., et al., Multiscale modeling of droplet interface bilayer membrane networks. Biomicrofluidics, 2015. 9(6): p. 064101.
- 15. Hwang, W.L., et al., Electrical Behavior of Droplet Interface Bilayer Networks: Experimental Analysis and Modeling. Journal of the American Chemical Society, 2007. 129(38): p. 11854-11864.
- 16. Dixit, S.S., et al., Droplet Shape Analysis and Permeability Studies in Droplet Lipid Bilayers. ACS-Langmuir, 2012. 28(19): p. 7442-7451.
- 17. Villar, G., A.D. Graham, and H. Bayley, A tissue-like printed material. Science, 2013. 340(6128): p. 48-52.
- 18. Wauer, T., et al., Construction and manipulation of functional three-dimensional droplet networks. ACS Nano, 2014. 8(1): p. 771-9.
- 19. Bayoumi, M., et al., Multi-compartment encapsulation of communicating droplets and droplet networks in hydrogel as a model for artificial cells. Sci Rep, 2017. 7: p. 45167.

- 20. Ma, S., et al., Gel Microrods for 3D Tissue Printing. Advanced Biosystems, 2017. 1(8): p. e1700075.
- 21. Sarles, S.A. and D.J. Leo, Physical encapsulation of droplet interface bilayers for durable, portable biomolecular networks. Lab on a Chip, 2010. 10(6): p. 710-7.
- 22. Elani, Y., et al., Engineering multi-compartment vesicle networks. Chemical Science, 2013. 4(8): p. 3332.
- 23. Holden, M.A. and H. Bayley, Direct introduction of single protein channels and pores into lipid bilayers. Journal of the American Chemical Society, 2005. 127(18): p. 6502-6503.
- 24. Punnamaraju, S. and A.J. Steckl, Voltage control of droplet interface bilayer lipid membrane dimensions. Langmuir, 2011. 27(2): p. 618-26.
- 25. Maglia, G., et al., Droplet networks with incorporated protein diodes show collective properties. Nature Nanotechnology, 2009. 4(7): p. 437-440.
- 26. Holden, M.A., D. Needham, and H. Bayley, Functional bionetworks from nanoliter water droplets. J Am Chem Soc, 2007. 129(27): p. 8650-5.
- 27. Booth, M.J., et al., Light-activated communication in synthetic tissues. Sci Adv, 2016. 2(4): p. e1600056.
- 28. Renner, S., A. Bessonov, and F.C. Simmel, Voltage-controlled insertion of single α-hemolysin and Mycobacterium smegmatis nanopores into lipid bilayer membranes. Applied Physics Letters, 2011. 98(8): p. 083701.
- 29. Gouaux, J.E., et al., Subunit stoichiometry of staphylococcal alpha-hemolysin in crystals and on membranes: a heptameric transmembrane pore. Proceedings of the National Academy of Sciences, 1994. 91(26): p. 12828-12831.

- 30. Song, L., et al., Structure of Staphylococcal alpha -Hemolysin, a Heptameric Transmembrane Pore. Science, 1996. 274(5294): p. 1859-1865.
- 31. Armitage, B.A., et al., Polymerization and domain formation in lipid assemblies, in Biopolymers Liquid Crystalline Polymers Phase Emulsion. 1996, Springer. p. 53-84.
- 32. Okazaki, T., Y. Tatsu, and K. Morigaki, Phase separation of lipid microdomains controlled by polymerized lipid bilayer matrices. Langmuir, 2009. 26(6): p. 4126-4129.
- 33. O'Brien, D.F., et al., Polymerization of preformed self-organized assemblies. Accounts of chemical research, 1998. 31(12): p. 861-868.
- 34. Collins, M.D., Interleaflet coupling mechanisms in bilayers of lipids and cholesterol. Biophysical journal, 2008. 94(5): p. L32-L34.
- 35. Leaver, J., et al., The physical properties and photopolymerization of diacetylene-containing phospholipid liposomes. Biochimica et biophysica acta (BBA)-biomembranes, 1983. 732(1): p. 210-218.
- 36. Lingwood, D. and K. Simons, Lipid Rafts As a Membrane-Organizing Principle. Science, 2010. 327(5961): p. 46-50.
- 37. Simons, K. and W.L. Vaz, Model systems, lipid rafts, and cell membranes. Annu. Rev. Biophys. Biomol. Struct., 2004. 33: p. 269-295.
- 38. Wu, S.H.-w. and H.M. McConnell, Lateral phase separations and perpendicular transport in membranes. Biochemical and biophysical research communications, 1973. 55(2): p. 484-491.
- 39. Cruzeiro-Hansson, L. and O.G. Mouritsen, Passive ion permeability of lipid membranes modelled via lipid-domain interfacial area. Biochimica et Biophysica Acta (BBA)-Biomembranes, 1988. 944(1): p. 63-72.

- 40. Johnston, D.S., et al., Phospholipid polymers—synthesis and spectral characteristics. Biochimica et Biophysica Acta (BBA)-Biomembranes, 1980. 602(1): p. 57-69.
- 41. Morigaki, K., et al., Patterning Solid-Supported Lipid Bilayer Membranes by Lithographic Polymerization of a Diacetylene Lipid. Angewandte Chemie International Edition, 2001. 40(1): p. 172-174.
- 42. Morigaki, K., et al., Photopolymerization of diacetylene lipid bilayers and its application to the construction of micropatterned biomimetic membranes. Langmuir, 2002. 18(10): p. 4082-4089.
- 43. Georger, J.H., et al., Helical and tubular microstructures formed by polymerizable phosphatidylcholines. Journal of the American Chemical Society, 1987. 109(20): p. 6169-6175.
- 44. Freeman, F.J., J.A. Hayard, and D. Chapman, Liposomes formed from polymerizable diacetylenic phospholipids and their potential as drug delivery systems. Biochemical Society Transactions, 1987. 15.
- 45. Wegner, G., Topochemical polymerization of monomers with conjugated triple bonds. Die Makromolekulare Chemie: Macromolecular Chemistry and Physics, 1972. 154(1): p. 35-48.
- 46. Hayward, J.A. and D. Chapman, Biomembrane surfaces as models for polymer design: the potential for haemocompatibility. Biomaterials, 1984. 5(3): p. 135-142.
- 47. Jonas, U., et al., Reversible color switching and unusual solution polymerization of hydrazide-modified diacetylene lipids. Journal of the American Chemical Society, 1999. 121(19): p. 4580-4588.

- 48. Yavlovich, A., et al., Design of liposomes containing photopolymerizable phospholipids for triggered release of contents. Journal of thermal analysis and calorimetry, 2009. 98(1): p. 97-104.
- 49. Sine, J., et al., Photo activation of HPPH encapsulated in "Pocket" liposomes triggers multiple drug release and tumor cell killing in mouse breast cancer xenografts. International journal of nanomedicine, 2015. 10: p. 125.
- 50. Punnamaraju, S., H. You, and A. Steckl, Triggered release of molecules across droplet interface bilayer lipid membranes using photopolymerizable lipids. Langmuir, 2012. 28(20): p. 7657-7664.
- 51. Schild, V.R., et al., Light-Patterned Current Generation in a Droplet Bilayer Array. Scientific Reports, 2017. 7.
- 52. Szoka Jr, F. and D. Papahadjopoulos, Comparative properties and methods of preparation of lipid vesicles (liposomes). Annual review of biophysics and bioengineering, 1980. 9(1): p. 467-508.
- 53. Berry, J.D., et al., Measurement of surface and interfacial tension using pendant drop tensiometry. Journal of Colloid and Interface Science, 2015. 454: p. 226-237.
- 54. Taylor, G.J., et al., Direct in situ measurement of specific capacitance, monolayer tension, and bilayer tension in a droplet interface bilayer. Soft Matter, 2015. 11(38): p. 7592-605.
- 55. Heitz, B.A., et al., Polymerized planar suspended lipid bilayers for single ion channel recordings: comparison of several dienoyl lipids. Langmuir, 2011. 27(5): p. 1882-1890.

- 56. Makhoul-Mansour, M., et al., Ferrofluid-Based Droplet Interface Bilayer Networks. Langmuir, 2017. 33(45): p. 13000-13007.
- 57. Yavlovich, A., et al., Light-sensitive lipid-based nanoparticles for drug delivery: design principles and future considerations for biological applications. Molecular membrane biology, 2010. 27(7): p. 364-381.

CHAPTER 7

ENABLING MEMBRANOUS SOFT MATERIALS WITH THE ABILITY TO MORPH $\mbox{THROUGH LIPID RAFTS}^{\,6}$

 $^{^6}$ M. M. Makhoul-Mansour, J. B. El-Beyrouthy, E. C. Freeman, 2021, To be Submitted to *Advanced Materials Interfaces*.

7.1. Abstract

Natural cellular membranes can spontaneously organize their lipid constituents into uniform yet separate domains of different sizes, lifetimes, and properties. This mechanism referred to as "raft hypothesis" is thought to be at the center of vital cellular functions such as apical sorting, protein trafficking, the clustering of proteins, and regulating local membrane physical properties (including cortical tension). Inspired by this natural mechanism, the functionalization of DIB-tissues (Droplet Interface Bilayer) using thermally driven lipid rafts is explored herein. The formation and dissipation of lipid rafts is then linked to changes in the interfacial membranes 'properties. Most notably membranes' monolayer and bilayer tension (as well as area reflected through the contact angle) have shown to increase as rafts dissipate, reform, and align as a results of heating and consequent cooling. Results from this work could be built upon to implement morphing capabilities inspired by natural tissues intercalation mechanisms (the Differential Adhesion Hypothesis-DAH) and carried through lipid rafts reorganization and scattering in DIB-structures.

7.2. Introduction

Plasma Membranes and the DAH

A comprehensive theoretical framework described life as fundamentally being an isolated self-sustaining chemical reaction capable of successfully undergoing evolution [1]. Hence during some point in the evolution of primary forms of life, compartmentalization is thought to have occurred to preserve self-sustaining information (transmitted to offspring's) by reducing the free diffusive loss and separating beneficial molecular components from parasites [2]. The earliest compartmentalization concept is thought to

have emerged during the prebiotic chemistry phase [3, 4]. Later, the encapsulation of crucial life-nurturing chemical reaction within amphiphilic lipid vesicles gave rise to protocells and at later stages more complex cellular organisms [2, 4]. In cellular organisms, compartmentalization is often accomplished through networks of plasma membranes [2]. Plasma membranes are semi-permeable and able to respond to multiple signals thus allowing individual cells and tissues to interact with each other and with their external environment through governed exchange [3, 4].

It has been long proposed that during developmental stages (pre-gastrulation, gastrulation and organogenesis to name), certain embryonic tissues may behave like liquid cell masses flowing from one configuration to another through tissue surface tension forces [5-7]. First proposed by Phillips *et al.* [5, 6], this behavior of cells that resembles droplet coalescence and adhesion mechanisms in emulsions, was later expanded to other types of embryonic and non-embryonic tissues (epithelial [8], bone, ovarian, cancerous [9]) and explained through the DAH (Differential Adhesion Hypothesis). Intended to provide an explanation for the spontaneous liquid-like tissue behavior, the DAH models tissues as emulsive systems: cells behave similarly to microdroplets whose varying degrees of surface adhesion causes them to spontaneously reorganize and minimize their interfacial free energy [9, 10].

Fully reproducing natural living systems within the laboratory is an unrealistic goal. Yet, what the DAH tells us is that stabilized adhesive emulsions can still be employed to replicate select portions of cellular phenomena exploiting self-assembly and interfacial chemistry principles. When strategically functionalized, emulsive systems can acquire some of the hallmarks of Ganti's chemoton model and thus can be used as an initial

promising approach for developing and approximating synthetic tissues. Here, we build on previous works [11, 12] and further develop the Droplet Interface Bilayer (DIB) platform. This technique combines advantages from stabilized adhesive emulsions and membrane modeling as it assembles model lipid membranes at the interfaces of lipid-coated aqueous microdroplets submerged in an oil environment [11, 13] (Figure 7.1). Tissue-inspired structures can be built using this platform and used in a variety of applications involving biocompatible sensors, micro actuators, chemical microrobots and chemical computing.

The ability to shape shift in response to triggers would allow for this new class of materials to be used in more complex applications. Inspired by nature where function follows form and the DAH where localized intercalation events are carried through an imbalance to tensions leading to variable adhesion, we propose to investigate the ability to functionalize DIB structures to respond to external triggers and shape shift through a tension imbalance or varying degrees of surface adhesion cause a spontaneous shape shift to minimize the total interfacial free energy. In previous works, we have explored this concept and functionalized DIB-tissues by either integrating ferrofluids into the platform or using electrowetting as means to control local tension (hence adhesion). The main mechanism of shape-shifting was controlled differential adhesion for growth and shape change. The first results were DIB-structures that show sensitivity to nearby magnetic force fields through a shape-shift response inspired by natural cellular intercalation events [12]. Meanwhile the second results were DIB structures that showed shape morphing capabilities with applied electrical field (albeit the need for integrated electrodes in this case)[14]. Here, we propose a similar approach, where DIB structures are sensitized to temperature and

respond by shapeshifting. We hypothesize that such functionalization can be executed by embedding lipid nanodomains into membranous structures.

Lipid Nanodomains in Model Membranes

When formed using one class of lipids (typically DPhPC- 1,2-diphytanoyl-sn-glycero-3-phosphocholine [11, 13, 15]) interfacial DIBs are considered homogenous in terms of chemical composition [3, 16]. In a behavior reminiscent of natural plasma membranes, model membranes exhibit the formation of molecular clusters of variable sizes/lifetime when two or more lipids are mixed. This behavior arises from the nonideal mixing of different membrane components and free energy minimization [3, 16-18].

This aspect of compartmentalization is referred to as "raft hypothesis" [16-21]. According to this hypothesis, preferential interactions between sterols (such as cholesterol) and certain phospholipids (such as DPhPC) can trigger the formation of tightly packed membrane nanodomains with distinct composition in comparison to surrounding membranes. This unique state of lipid arrangement is referred to as the liquid ordered (L0) phase [17, 18, 20] (Figure 7.2). The L0 phase is fluid, similar to the more common disordered lipid (Ld- Figure 7.2) phase, hence allowing molecular motion and flexibility and protein insertion. The more physiologically relevant interactions are between saturated lipids (such as DPhPC), sphingolipids (such as bSM), and sterols (such as cholesterol) as this mixture is commonly found in the plasma membranes of mammalian cells [22]. Here, the L0 and Ld phases are able to coexist throughout a broad space of compositional and physical parameters partially due to their distinct molecular arrangement and various physical properties (lipid packing, rigidity, and permeability) [3]. It is this coexistence of ordered and disordered lipid phases that is believed to be behind raft formation in living

cells. A third state of lipid order arises in the presence of some membrane-active sterols, most importantly cholesterol and its analogues in other organisms. This state referred to as the gel/solid phase [3] (S- Figure 7.2), is only observed in model membranes (and not their natural counterparts).

The dynamic formation and dissipation of lipid nanodomains are thought to play an important role in a wide range of essential cellular processes such as apical sorting, protein trafficking, the clustering of proteins, and regulating local membrane physical properties (including cortical tension) [16-21, 23]. Here, the effects of raft formation and dissipation on the structural and mechanical properties of DIBs (such as bilayer tension, area, angle of contact and energy of adhesion...) are explored and conclusions made to whether this method can be used in the functionalization of these membranous materials to exhibit dynamic structural adaptation events channeling cellular tension driven events explained by the DAH. Our goal is to test whether the temperature-driven nanodomain formation (and membrane homogenization) can be used to drive significant structural morphing at the single membrane level, a strategy commonly found in natural tissues [17, 18, 20, 21, 24]. We build on previous works where the formation of lipid nanodomains in DIBs assembled on a hydrogel layer, has been confirmed using a custom-made interferometric scattering microscopy (iSCAT) [16]. Several mixtures of saturated lipids, sphingolipids, and sterols are tested (in terms of monolayer tension, bilayer tension, angle of contact and energy of adhesion) with varying temperature cycling and compared to homogenous DIBs traditionally used in this platform. These results can then be used to refine temperature enabled morphing capabilities of DIB-tissues in future works.

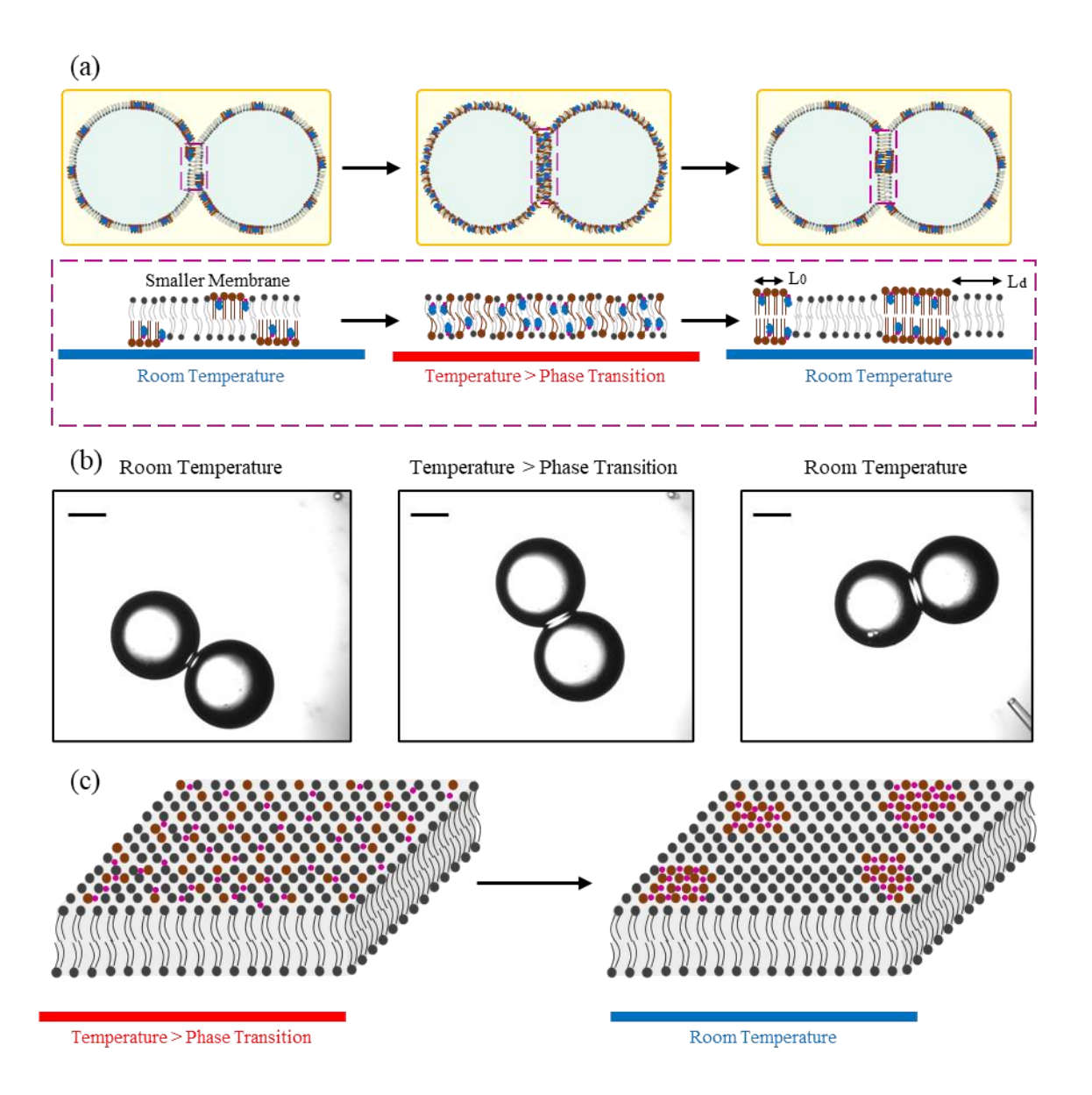


Figure 7.1- In the literature, graphical methods (such as iSCAT [16]) have been used to detect the formation of bSM nanodomains in model lipid membranes. Here, the effect of the formation of lipid nanodomains in membranes containing a mixture of DPhPC, cholesterol and bSM (in a 1:1:1 molar ratio) on interfacial tension and contact angle is examined. (a) Schematic representation and (b) experimental images of a DIB formed at room temperature then gradually brought to 46° C and consequently brought back to room temperature. Initially, when the membrane is formed at room temperature, L0 nanodomains

are postulated to exist albeit not in an optimal setup in both leaflets, meanwhile, at temperatures above phase transition, these domains are scattered. Upon cooling the membrane below the phase transition temperature, L0 nanodomains re-appear from a uniform Ld phase (as shown in (c)) and are though to align resulting in a larger membrane compared to the original one. Scale bars represent 250 μ m.

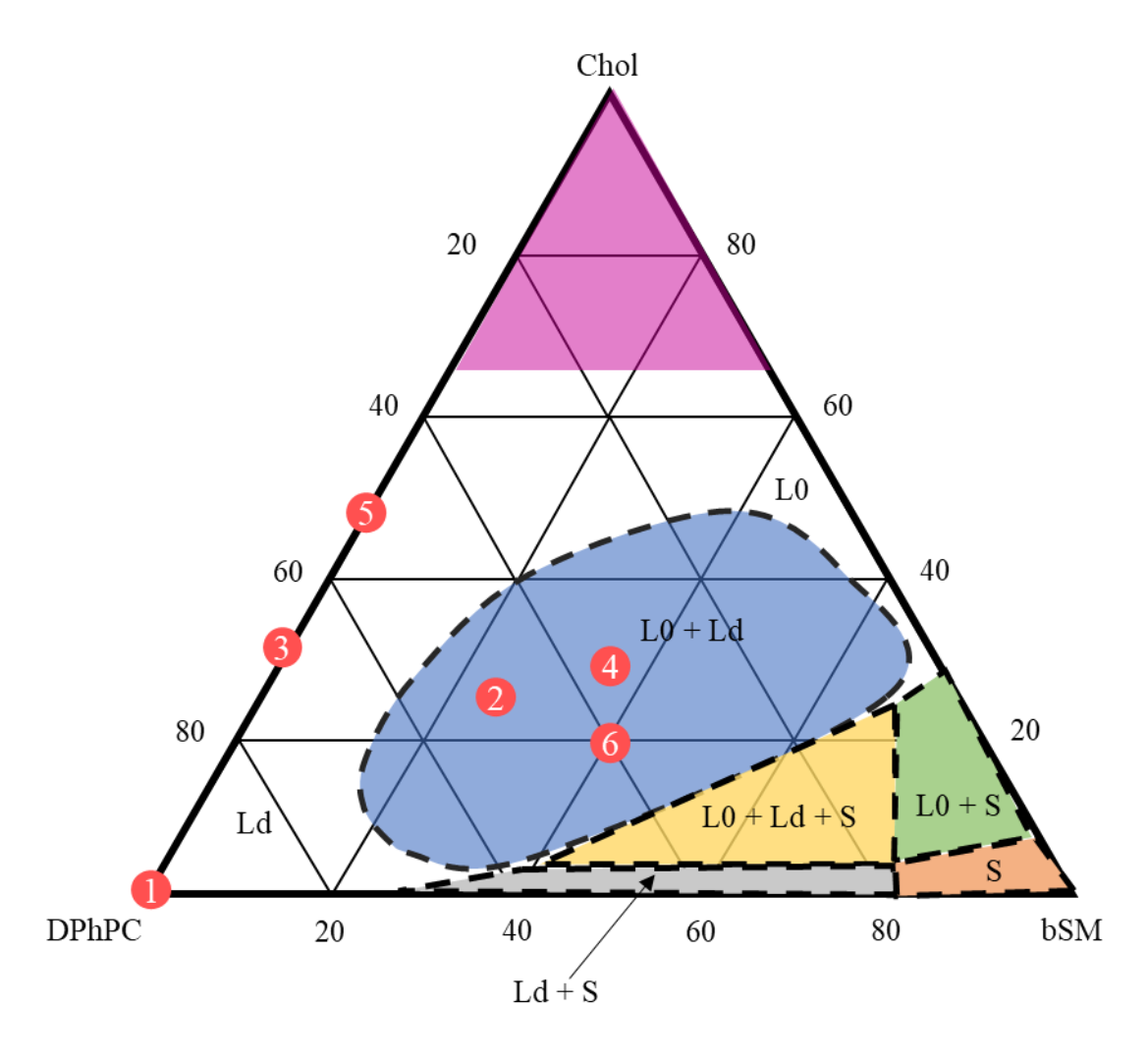


Figure 7.2- DIBs tested here were composed of DPhPC, bSM and Cholesterol at different molar compositions: (1) 1:0:0, (2) 2:1:1, (3) 2:0:1, (4) 1:1:1, (5) 1:0:1, and (6) 2:1:2. (2), (4) and (6) and lie in the L0+Ld phase coexistence region. While (1), (3) and (5) lie in the

Ld phase. L0: liquid ordered, Ld: liquid disordered and S: solid/gel phase. The purple shaded region at the very top of the triangle is a region where no membrane is formed (as per literature). Phase boundaries are reproduced from [Bezlyepkina, N., et al., Phase diagram and tie-line determination for the ternary mixture DOPC/eSM/cholesterol. Biophysical Journal, 2013. 104(7): p. 1456-64].

7.3. Materials

Background Buffer Solutions

The background aqueous buffer solution was used to hydrate all lipid mixtures and was prepared by adding 250 mM Potassium Chloride (KCl, Sigma-Aldrich, St. Louis, MO) and 10 mM 3-(N-morpholino) propanesulfonic acid (MOPS, Sigma-Aldrich, St. Louis, MO) yielding a pH of ~7.0 as measured.

Aqueous Lipid Solutions

Lipid mixtures were prepared according to previously established protocols [25, 26]. A mixture of zwitterionic phospholipids (DPhPC, 1,2-diphytanoyl-sn-glycero-3-phosphocholine, Avanti Polar Lipids, Alabaster, AL), Brain SM Sphingomyelin (Brain, Porcine- 18:0 SM Octadecanoyl Sphingomyelin, Avanti Polar Lipids, Alabaster, AL) lipids, and cholesterol (ovine wool, greater than 98%, Avanti Polar Lipids, Alabaster, AL) and at 1:0:0, 2:1:1, 2:0:1, 1:1:1, 1:0:1, and 2:1:2 molar ratios (Figure 7.2) respectively were first dissolved in chloroform (Sigma-Aldrich, St. Louis, MO) yielding homogenous and clear lipid mixtures in the organic solvent. Upon adequate mixing through stirring, chloroform was evaporated using a dry argon stream in a fume hood. Residual chloroform was further dried by placing the vial in a vacuum chamber for a minimum of 5 hours. The dried lipid films were rehydrated by adding the previously described background aqueous

buffer solution (250 mM KCl and 10 mM MOPS) to the vials followed by gentle agitation resulting in final lipid concentration of 2.0 mg/ml. Liposomes are then prepared by thawfreezing the solutions (a minimum of 5 cycles) and were then stored at 2 °C. Subsequently and prior to the first usage, the solutions were first sonicated using a bath sonicator with a surrounding water temperature of 45 °C for 25 minutes (Elmasonic S100h Ultrasonic sonicator, Elma Schmid Bauer GmbH, Gottlieb-Daimler-Straße Singen, Germany) and then using a probe tip sonicator (2 mm standard probe tip with a maximum oscillation amplitude of 200 μm, from QSONICA Q55 Probe Tip Ultrasonicator, QSONICA, Newtown, CT) until a clear consistency was achieved and no lipids aggregations were observed. Tip sonication was held in 30 W cycles of 3 minutes each with an average of 5 cycles. These solutions were afterwards stored at 2 °C and could be directly used.

Oil Solutions

Hexadecane oil (Sigma Aldrich, St. Louis, MO) was used as the surrounding continuous phase with no further modifications.

7.4. Methods

Electrophysiological Measurements

Formerly established protocols were used for electrical recordings [12, 25-27] unless specifically stated otherwise. In short, all electrical recordings are conducted in voltage clamp mode (Whole Cell β =1) using the AXOpatch 200B patch clamp amplifier and the Digidata 1550 data acquisition system (Molecular Devices, Sunnyvale, CA) at a sampling frequency of 10 kHz and then filtered at 1 kHz using the embedded low-pass Bessel filter (-80 dB.decade $^{-1}$). A 500 Hz fourth-order Butterworth low-pass filter was applied post-acquisition in MATLAB for visualization purposes.

Pendant Drop Tension Measurements

Monolayer tension measurements were obtained using the pendant drop technique with the open-source software OpenDrop used in former works [12, 14, 25, 26, 28]. In summary, the experimental apparatus previously described in details [25] includes of a glass calibrated needle holding the lipid solution and is suspended inside a 3 mL glass cuvette containing the surrounding oil. The cuvette is placed on a heating plate whereby the oil temperature is controlled and monitored through an attached thermocouple heat sensor probe. A droplet is slowly injected into the oil, and as the lipid monolayer forms at the oil-water interface the droplet will gradually adopt a pendant shape. Heat is adequately applied as desired, and the monolayer tension measured when equilibrium temperature is reached within the surrounding oil. Recordings are taken using a CCD camera attached to a zoom lens. Frames are extracted using MATLAB and used to estimate the monolayer tension as a function of time.

Measurements of DIB Angle of Contact, Bilayer Tension, and Adhesion Energy

A DIB has been traditionally electrically modeled as a capacitor in parallel with a high amplitude resistance [13, 29]. In cases where lipid packing is optimal, no transmembrane channels are being used and no porosity is expected, the resistive current is mostly negligible, so the overall current of a bilayer can be reduced to its capacitive component.

The DIBs bilayer tension, angle of contact (defined herein as being the total angle between the droplets and the membrane's central line at equilibrium), and energy of adhesion are evaluated for various lipid profiles using *in situ* graphical DIB characterization techniques [25, 26]. Droplets are injected, given enough time for

monolayer formation and then brough together using a finely pulled glass micropipette to allow the formation of an interfacial membrane. The temperature of the surrounding oil phase is controlled using an ITO (Indium tin oxide) coated heating slide (Cell Microsystems, Durham, NC). Once the desired equilibrium temperature is reached, the membrane is given a few minutes to stabilize and then images are acquired for further analysis. Images are acquired using a CCD camera (DCC1645C-HQ, Leica Microsystems, Wetzlar, Germany) mounted on an inverted fluorescent microscope (Leica DMI3000B manual inverted microscope, Leica Microsystems, Buffalo Grove, IL) and post-processed using a previously developed MATLAB code.

7.5. Results

Monolayer Tension Changes as an Indicator for Raft Formation/Dissipation

Table 7.1 shows the changes in monolayer tension values with different lipid mixtures and at different temperatures (22, 34 and 46°C respectively). Mixtures that do not contain bSM lipids (1:0:0, 1:0:1 and 2:0:1 DPhPC:bSM:Chol molar ratios) show no significant changes in their interfacial tensions as expected. Meanwhile, mixtures containing bSM lipids (shaded in pink in Table 7.1 below) show changes in monolayer tension as the surrounding oil temperature is increased. Model membranes with mixtures of glycerophospholipids, sphingomyelins and cholesterol exhibit heterogeneity in the form of lipid nanodomains, a behavior speculated to reminisce from natural cellular membranes [3] (Cholesterol, phosphatidylcholine, and sphingomyelin being the main constituents of most mammalian cells plasma membranes [22]). These nanodomains exist at room temperature but dissipate at temperatures higher than the phase transition temperature. From Figure 7.2, all mixtures containing bSM that are being tested here would exhibit

coexisting liquid ordered and liquid disordered phases indicating lipid raft existence at room temperature. Interestingly, not all mixtures show the same trends as the surrounding temperature is elevated to beyond the phase transition one. The 2:1:2 DPhPC:bSM:Chol mixture provides an opposing trend compared to the 2:1:1 and 1:1:1 mixtures as it shows an increase in tension compared to a decrease in tension observed in the other cases. In both cases, we can conclude that the formation/dissipation of lipid nanodomains within a lipid monolayer leads to changes in the interfacial tension whether it be a decrease or an increase (Figure 7.2). Several factors could be influencing this behavior, the authors theorize one of them to be the molar ratio of bSM to cholesterol. As this ratio changes from 1:1 to 1:2 so does the trend in monolayer tension shift from a decrease with an increasing temperature to an increase with increasing temperature. While these results don't fully explain the behavior of these lipid mixtures with varying temperature, it can still be inferred that as previously shown in the literature, lipid rafts disperse beyond phase transition temperature and form at room temperature for mixtures of bSM, Chol and a saturated phospholipid [16, 23, 30].

Table 7.1 – Results for monolayer tension with varying lipid mixtures at three selected temperatures. The mixture of DPhPC, sphingomyelin, and cholesterol is known to generate lipid rafts at room temperature which dissipate with elevated temperature. Notably, these compositions (highlighted in pink) are the only mixtures which exhibit trends in the monolayer temperature. The final case (2:1:2) provides an opposing trend compared to the 2:1:1 and 1:1:1 mixtures (tension increases with temperature rather than decreases).

	Interfacial Tension (mN/m)				
Temperature (°C)	22 (n=3)	34 (n=3)	46 (n=3)		
2mg/ml DPhPC:bSM:Chol (1:0:0)	1.15 (±0.04)	1.12 (±0.02)	1.17 (±0.01)		
2mg/ml DPhPC:bSM:Chol (2:1:1)	1.03 (±0.01)	0.92 (±0.03)	0.88 (±0.04)		
2mg/ml DPhPC:bSM:Chol (2:0:1)	1.38 (±0.06)	1.38 (±0.07)	1.39 (±0.01)		
2mg/ml DPhPC:bSM:Chol (1:1:1)	0.97 (±0.17)	0.78 (±0.09)	0.72 (±0.12)		
2mg/ml DPhPC:bSM:Chol (1:0:1)	2.01 (±0.04)	2.04 (±0.05)	2.02 (±0.15)		
2mg/ml DPhPC:bSM:Chol (2:1:2)	0.84 (±0.03)	0.93 (±0.08)	1.06 (±0.04)		
Molar Composition					

Effect of Temperature and Lipid Composition on the Angle of Contact, Bilayer Tension, and Adhesion Energy of DIBs

Lipid Nanodomains and Asymetry: Interfacing with Single-lipid Microdroplets

In Figure 7.1, we hypothesize that an enhanced alignment in lipid nanodomains is triggered by an increase in the temperature to above phase transition followed by gradual cooling to room temperature. This hypothesis is tested by examining the effect of this temperature cycling on DIBs when nanodomains are introduced from one side then from both sides of the membrane in comparison to single-lipid interfacial membranes.

Figure 7.3 showcases the effect of temperature cycling on lipid nanodomain alignment from the perspective of the angle of contact. Tables 7.2,7.3, 7.5 and 7.6 were used for the creation of this figure. Results in Table 7.2 were obtained for DIBs formed with a DPhPC:bSM:Chol 1:1:1 molar ratio at 22°C (with adequate time for monolayer formation that was conducted at 46°C). Results shown there can be used as a reference point to measure the effect of preheating the lipid mixtures prior to forming the membrane and to separate the effect of heating the lipid mixture from the effect of heating a formed membrane on lipid rafts organization. Meanwhile results in Tables 7.3, 7.4 and 7.5 were

obtained for membranes formed with a lipid molar composition of 1:1:1 (symmetric with rafts-Figure 7.3-a), 1:0:0 (symmetric no rafts-Figure 7.3-c) and 1:1:1/1:0:0 (asymmetric - Figure 7.3-b). Droplets are injected at 22°C, given enough time for monolayer formation, then brought together into interfacial membranes. Consequently, without separating any membrane, the temperature is cycled up to 46°C passing by 34°C and then back to 22°C- a cycle repeated twice. At each temperature level, membrane properties are recorded once equilibrium is achieved (equilibrium here referring to membrane size).

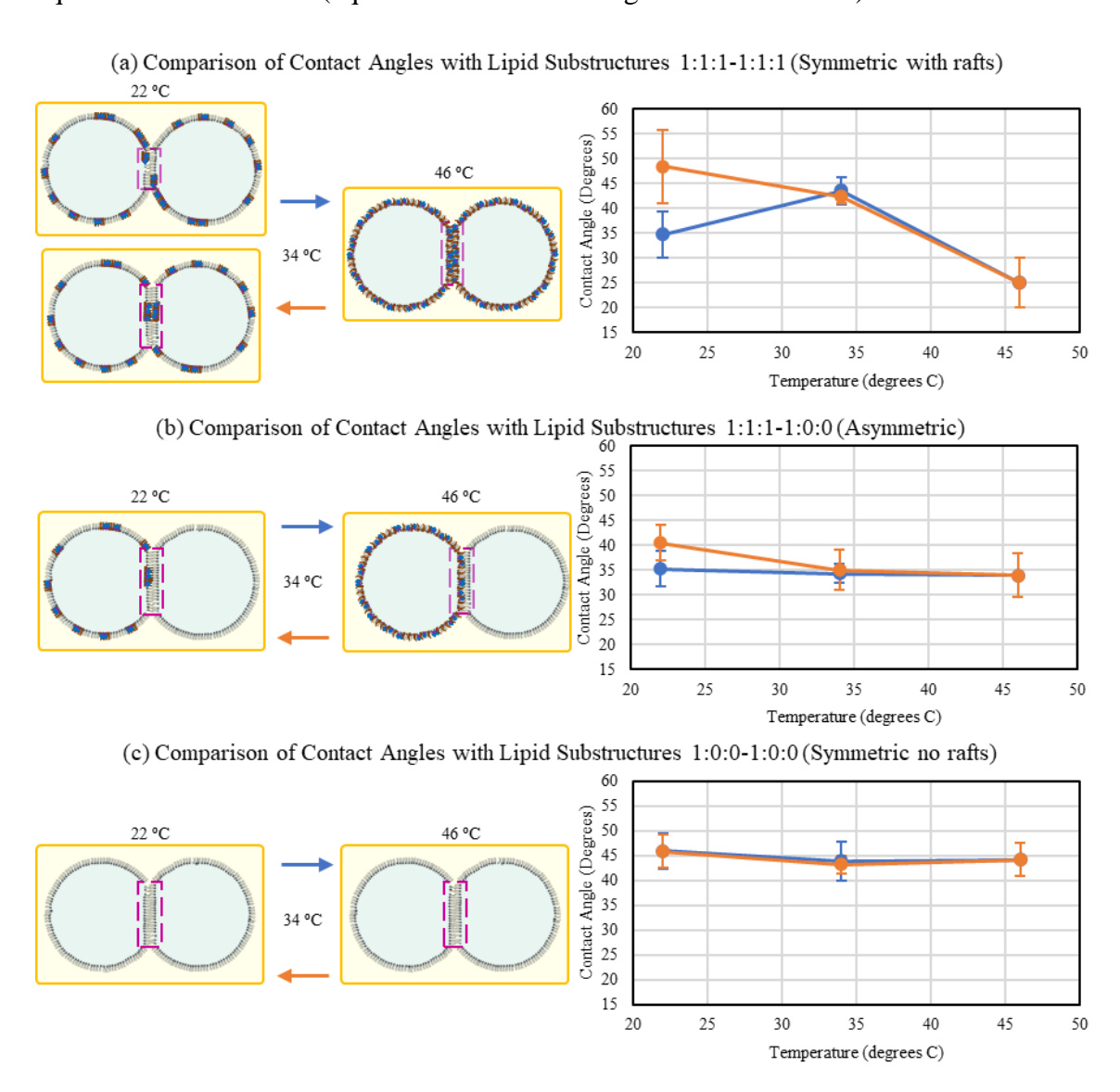


Figure 7.3 – Membranes formed various compositions were created using the DIB technique and the angle of contact was measured at the temperatures as shown in panel. Droplets are brought together at room temperature to form the interfacial membranes; after membrane formation, the droplets were heated to 46 °C to dissipate existing rafts in the leaflets then cooled again. Notably, cases with bSM on both membrane sides (shown in (a)) exhibit shifts in the angle of contact (directly linked to membrane favorability) that is not exhibited for asymmetric cases in (b) or DPhPC cases in (c) suggesting that the rafts reform in collocated spots within the membrane.

Table 7.2 – Droplets with a DPhPC:bSM:Chol molar composition of 1:1:1 were injected at 46 °C and given enough time for monolayer formation. The oil temperature was then reduced to 22 °C and then the droplets were brought together to usher membrane formation. The properties of these membranes were consequently recorded, and the average (n=3) and standard deviation reported.

22 °C				
monolayer tension angle of contact energy of adhesion bilayer tension				
DPhPC:bSM:Chol	(mN/m)	(deg)	(mN/m)	(mN/m)
1:1:1	$0.97 (\pm 0.04)$	34.73 (4.73)	0.089	1.85 (0.024)

Results in Table 7.3 show that upon initial heating membranes with a 1:1:1 lipid molar ratio exhibit a quick increase in size reflected through an increase in the area, angle of contact and adhesion energy. This initial increase (when reaching 34 °C) can be explained with an initial unfavourability in membrane formation at initial room temperature due to misalignment of lipid rafts, and a reduced unfavourability as rafts dissipate and lipid monolayers become more homogenous. As the temperature is further

increased to beyond the phase transition, lipid rafts further scatter, making the overall lipid mixture and hence monolayer more homogenized. Yet, a decrease in membrane size is observed and is most likely attributed to the effects of convection in both the oil and water phase. As temperature is reduced back to room temperature, membrane size increases showcasing a more favorable membrane (with a higher energy of adhesion). This increase in membrane size is hypothesized to stem from an alignment in lipid rafts resulting in more space for favorable interactions between similar lipid tails. As the temperature is cycled back up, a similar behavior to the one observed in the first cycle is observed most likely indicating that this membrane behavior is controlled via temperature shifts.

Another approach to check this conclusion can be carried by injecting droplets at 46 °C and waiting for monolayer formation before assembling interfacial membranes and registering their properties gradually as temperature is cooled down to room conditions then brought back up to 46 °C. Results of this approach are reported in Table 7.4. As previously observed, upon cooling, membranes show an increased favorability in terms of size and adhesion when compared to membranes that are formed at room temperature without previous heating (of the membrane itself). This favorability is reduced at 46 °C most likely due to previously described convection and heat transfer reasons.

Further tests involving symmetric membranes that do not contain cholesterol or bSM lipids and asymmetric membranes with cholesterol and bSM introduced from one side only, are performed to further confirm observations previously made. Table 7.5 shows results obtained for the same previously described test involving symmetric membranes formed with DPhPC lipids only. No rafts are expected to be produced in this case. Results show that membranes do not exhibit changes in their observed properties, with no

statistically significant change with 95% confidence interval and hence means for the angle of contact, energy of adhesion and bilayer tension cannot be concluded to be statistically different between each temperature step.

Table 7.3 – Droplets with a DPhPC:bSM:Chol molar composition of 1:1:1 were injected at 22 °C and given enough time for monolayer formation. The droplets were brought together to usher membrane formation. The oil temperature was then raised to 34 then 46 °C before cycling back to 22 °C and consequently 46 °C. The droplets were not separated at any given stage and the membrane remained formed. The properties of these membranes were recorded at each stage, and the average (n=3) and standard deviation reported.

		22 °C		
DPhPC:bSM:Chol	monolayer tension (mN/m)	angle of contact (deg)	energy of adhesion (mN/m)	bilayer tension (mN/m)
1:1:1	0.97 (±0.17)	26.17 (±12.55) 34 °C	0.058	1.8821 (±0.049)
DPhPC:bSM:Chol	monolayer tension (mN/m)	bilayer tension (mN/m)		
1:1:1	$0.78 \ (\pm 0.09)$	43.50 (±2.73)	0.11	1.45 (±0.014)
		46 °C		
DPhPC:bSM:Chol	monolayer tension (mN/m)	angle of contact (deg)	energy of adhesion (mN/m)	bilayer tension (mN/m)
1:1:1	0.72 (±0.12)	25.056 (±5.08)	0.036	1.41 (±0.015)
		34 °C		
DPhPC:bSM:Chol	monolayer tension (mN/m)	angle of contact (deg)	energy of adhesion (mN/m)	bilayer tension (mN/m)
1:1:1	0.78 (±0.09)	42.39 (±1.43)	0.11	1.45 (±0.0071)
		22 °C		
DPhPC:bSM:Chol	monolayer tension (mN/m)	angle of contact (deg)	energy of adhesion (mN/m)	bilayer tension (mN/m)
1:1:1	$0.97 (\pm 0.17)$	48.52 (±7.36)	0.17	1.77 (±0.053)
		34 °C		
DPhPC:bSM:Chol	monolayer tension (mN/m)	angle of contact (deg)	energy of adhesion (mN/m)	bilayer tension (mN/m)
1:1:1	$0.78 \ (\pm 0.09)$	42.22 (±1.83)	0.11	1.46 (±0.009)
		46 °C		
	monolayer tension	angle of contact	energy of adhesion	bilayer tension
DPhPC:bSM:Chol	(mN/m)	(deg)	(mN/m)	(mN/m)
1:1:1	$0.72 (\pm 0.12)$	25.16 (±6.97)	0.036	$1.40 (\pm 0.02)$

Table 7.4 – Droplets with a DPhPC:bSM:Chol molar composition of 1:1:1 were injected at 46 °C and given enough time for monolayer formation and then the droplets were brought together to usher membrane formation. The oil temperature was then reduced to 22 °C passing by 34 °C and cycling back to 46 °C. The properties of these membranes were consequently recorded at each stage, and the average (n=3) and standard deviation reported.

		46 °C					
DPhPC:bSM:Chol	monolayer tension (mN/m)	angle of contact (deg)	energy of adhesion (mN/m)	bilayer tension (mN/m)			
1:1:1	0.72 (±0.12)	28.00 (±1.33)	0.043	1.40 (±0.01)			
		34 °C					
DPhPC:bSM:Chol	monolayer tension angle of contact energy of adhesion bilayer tension DPhPC:bSM:Chol (mN/m) (deg) (mN/m) (mN/m)						
1:1:1	$0.78 \ (\pm 0.09)$	38.34 (±0.88)	0.087	1.47 (±0.01)			
		22 °C					
DDbDC.bSM.Chol	monolayer tension	angle of contact	energy of adhesion	bilayer tension			
DPhPC:bSM:Chol	(mN/m)	(deg)	(mN/m)	(mN/m)			
1:1:1	0.97 (±0.17)	48.12 (±24.37)	0.19	1.75 (±0.17)			
	(")						
	(")	48.12 (±24.37)					
1:1:1	0.97 (±0.17) monolayer tension	48.12 (±24.37) 34 °C angle of contact	0.19 energy of adhesion	1.75 (±0.17) bilayer tension			
1:1:1 DPhPC:bSM:Chol	0.97 (±0.17) monolayer tension (mN/m)	48.12 (±24.37) 34 °C angle of contact (deg)	0.19 energy of adhesion (mN/m)	1.75 (±0.17) bilayer tension (mN/m)			
1:1:1 DPhPC:bSM:Chol	0.97 (±0.17) monolayer tension (mN/m)	48.12 (±24.37) 34 °C angle of contact (deg) 47.51 (±25.84)	0.19 energy of adhesion (mN/m)	1.75 (±0.17) bilayer tension (mN/m)			

Meanwhile, asymmetric membranes formed by introducing bSM and cholesterol from one side only (in the 1:1:1 molar ratio with DPhPC as mentioned in Table 7.6) are examined and show a slightly more complex behavior. While the total angle of contact (defined here as being the angle formed between the two droplets) does not show significant change with temperature cycling, the bilayer tension and energy of adhesion have a slightly more complex performance due to the changes in monolayer tension observed in the previous section. As a result, the bilayer tension (as well as energy of

adhesion) shows a decrease with an increasing temperature. As membranes are cooled down back to room temperature, they restore their tension (bilayer) previously exhibited upon initial formation. More investigation where the monolayer tension is monitored with cycling temperatures to check for any hysteresis, could be performed to dynamically reflect tension changes. While we assume that monolayer tension does not exhibit significant hysteresis with temperature, results in Table 7.6 suggest that this assumption could be revisited in future works.

Table 7.5 – Droplets with a DPhPC:bSM:Chol molar composition of 1:0:0 were injected at 22 °C and given enough time for monolayer formation. The droplets were brought together to usher membrane formation. The oil temperature was then raised to 34 then 46 °C before cycling back to 22 °C and consequently 46 °C. The droplets were not separated at any given stage and the membrane remained formed. The properties of these membranes were recorded at each stage, and the average (n=3) and standard deviation reported.

		22 °C		
DPhPC:bSM:Chol	monolayer tension (mN/m)	angle of contact (deg)	energy of adhesion (mN/m)	bilayer tension (mN/m)
1:0:0	1.15 (±0.04)	45.90 (±3.6)	0.18	2.12 (±0.03)
		34 °C		
DPhPC:bSM:Chol	monolayer tension (mN/m)	angle of contact (deg)	energy of adhesion (mN/m)	bilayer tension (mN/m)
1:0:0	1.12 (±0.02)	44.93 (±3.95)	0.17	2.07 (±0.03)
		46 °C		
	monolayer tension	angle of contact	energy of adhesion	bilayer tension
DPhPC:bSM:Chol	(mN/m)	(deg)	(mN/m)	(mN/m)
DPhPC:bSM:Chol 1:0:0	(mN/m) 1.17 (±0.01)	(deg) 44.20 (±3.44)	(mN/m) 0.17	(mN/m) 2.16 (±0.02)
	,		,	
	,	44.20 (±3.44)	,	
1:0:0	1.17 (±0.01) monolayer tension	44.20 (±3.44) 34 °C angle of contact	0.17 energy of adhesion	2.16 (±0.02) bilayer tension
1:0:0 DPhPC:bSM:Chol	1.17 (±0.01) monolayer tension (mN/m)	44.20 (±3.44) 34 °C angle of contact (deg)	0.17 energy of adhesion (mN/m)	2.16 (±0.02) bilayer tension (mN/m)
1:0:0 DPhPC:bSM:Chol	1.17 (±0.01) monolayer tension (mN/m)	44.20 (±3.44) 34 °C angle of contact (deg) 43.19 (±1.82)	0.17 energy of adhesion (mN/m)	2.16 (±0.02) bilayer tension (mN/m)

		34 °C		
DPhPC:bSM:Chol	monolayer tension (mN/m)	angle of contact (deg)	energy of adhesion (mN/m)	bilayer tension (mN/m)
1:0:0	1.12 (±0.02)	46.54 (±1.07)	0.18	2.06 (±0.01)
		46 °C		
DPhPC:bSM:Chol	monolayer tension (mN/m)	angle of contact (deg)	energy of adhesion (mN/m)	bilayer tension (mN/m)
1:0:0	1.17 (±0.01)	41.27 (±0.51)	0.15	2.19 (±0.01)

Table 7.6– Droplets with a DPhPC:bSM:Chol molar composition of 1:1:1 and 1:0:0 (asymmetric membrane) were injected at 22 °C and given enough time for monolayer formation. The droplets were brought together to usher membrane formation. The oil temperature was then raised to 34 then 46 °C before cycling back to 22 °C and consequently 46 °C. The droplets were not separated at any given stage and the membrane remained formed. The properties of these membranes were recorded at each stage, and the average (n=3) and standard deviation reported.

		22 °C			
	monolayer tension	angle of contact	energy of adhesion	bilayer tension	
DPhPC:bSM:Chol	(mN/m)	(deg)	(mN/m)	(mN/m)	
1:0:0	0.97 (0.17)	17.20 (1.58)	0.05	2.02.(0.010)	
1:1:1	1.15 (0.04)	18.05 (1.97)	0.03	2.03 (0.019)	
		34 °C			
	monolayer tension	angle of contact	energy of adhesion	bilayer tension	
DPhPC:bSM:Chol	(mN/m)	(deg)	(mN/m)	(mN/m)	
1:0:0	1.12 (±0.02)	17.63 (±0.90)	0.04	1.94 (10.01)	
1:1:1	$0.78 (\pm 0.09)$	16.67 (±1.03)	0.04	1.84 (±0.01)	
		46 °C			
	monolayer tension	angle of contact	energy of adhesion	bilayer tension	
DPhPC:bSM:Chol	(mN/m)	(deg)	(mN/m)	(mN/m)	
1:0:0	1.17 (±0.01)	17.92 (±2.51)	0.04	1.95 (10.02)	
1:1:1	0.72 (±0.12)	15.97 (±1.91)	0.04	1.85 (±0.02)	
		34 °C			
monolayer tension angle of contact energy of adhesion bilayer tension					
DPhPC:bSM:Chol	(mN/m)	(deg)	(mN/m)	(mN/m)	
1:0:0	1.12 (±0.02)	18.02 (±2.01)	0.04	1.92 (10.02)	
1:1:1	$0.78 (\pm 0.09)$	17.01 (±2.08)	0.04	1.83 (±0.02)	
		22 °C			
	monolayer tension	angle of contact	energy of adhesion	bilayer tension	
DPhPC:bSM:Chol	(mN/m)	(deg)	(mN/m)	(mN/m)	
1:0:0	0.97 (±0.17)	20.43 (±2.35)	0.07	2 00 (±0 02)	
1:1:1	1.15 (±0.04)	20.05 (±1.26)	0.07	2.00 (±0.02)	
		34 °C			
		220			

DPhPC:bSM:Chol	monolayer tension (mN/m)	angle of contact (deg)	energy of adhesion (mN/m)	bilayer tension (mN/m)	
1:0:0	1.12 (±0.02)	18.17 (±1.48)	0.04	1.94 (+0.02)	
1:1:1	$0.78 (\pm 0.09)$	17.17 (±1.64)	0.04	$1.84 (\pm 0.02)$	
		46 °C			
	monolayer tension	angle of contact	energy of adhesion	bilayer tension	
DPhPC:bSM:Chol	(mN/m)	(deg)	(mN/m)	(mN/m)	
1:0:0	1.17 (±0.01)	15.50 (±1.33)	0.02	1.07 (+0.01)	
1:1:1	$0.72 (\pm 0.12)$	15.26 (±1.42)	0.03	$1.87 (\pm 0.01)$	

7.6. Discussion

Results from Tables 7.2-7.6 suggest that membranes containing DPhPC, bSM and Cholesterol at a molar ratio of 1:1:1, when initially formed at room are energetically unfavorable membranes. When temperature is raised to above phase transition, it is theorized that nanodomains become scattered. As membranes are brought back below the phase transition temperature, literature suggest that L0 nanodomains re-appear within a uniform Ld phase and are align resulting in a more energetically favorable membrane (as we observed). These membranes retain this favorability at room temperature regardless of whether the temperature is kept constant or brought back up (cycled to above phase transition and back to ambient temperature). More interestingly, membranes undergo a significant structural change reflected through an area increase similar to electrowetting effects [14, 26]. These interesting results are preliminary by nature and serve as basis for further studies where the formation of nanodomains would be confirmed via other techniques then isolated before examining its effect on membrane properties and tissue morphology.

7.7. Conclusion

In this chapter, the effect of raft formation and dissipation on the properties and geometry of interfacial lipid membranes formed using the DIB platform are explored.

Lipid mixtures with a molar ratio of 1:1:1 DPhPC:bSM:Chol initially form smaller membranes that are not energetically favorable due to a misalignment of lipid rafts. Temperature-driven nanodomain scattering and then re-organization has shown to affect a DIB's size, angle of contact, tension and energy of adhesion (increase) and results in more energetically favorable membranes as lipid nanodomains realigned. Large scale thermally driven morphing of DIB-based tissues is yet to be explored through this approach, however preliminary results from this chapter could be built upon to yield optimized and maybe even reversible morphing capabilities carried through lipid rafts reorganization and scattering. This strategy could be further enhanced and finetuned taking cues from nature and implementing elements identified by the DAH as the driving forces behind tissue structural adaptation.

7.8. References

- 1. Gánti, T., Introduction, in Chemoton theory: theoretical foundations of fluid machineries, P.G. Mezey, Editor. 2003, Kluwer Academic/Plenum Publishers. p. 1-8.
- Aufinger, L. and F.C. Simmel, *Establishing communication between artificial cells*.
 Chemistry–A European Journal, 2019. 25(55): p. 12659-12670.
- Cebecauer, M., et al., Membrane Lipid Nanodomains. Chemical Reviews, 2018.
 118(23): p. 11259-11297.
- Deamer, D., The Role of Lipid Membranes in Life's Origin. Life (Basel), 2017. 7(1):p. 5.

- 5. Phillips, H., M. Steinberg, and B. Lipton, *Embryonic tissues as elasticoviscous liquids: II. Direct evidence for cell slippage in centrifuged aggregates.*Developmental biology, 1977. **59**(2): p. 124-134.
- 6. PHILLIPS, H.M., Liquid-tissue mechanics in amphibian gastrulation: germ-layer assembly in Rana pipiens. American Zoologist, 1978. **18**(1): p. 81-93.
- 7. Davis, G.S., H.M. Phillips, and M.S. Steinberg, Germ-Layer Surface Tensions and "Tissue Affinities" inRana pipiensGastrulae: Quantitative Measurements.

 Developmental biology, 1997. 192(2): p. 630-644.
- 8. Guillot, C. and T. Lecuit, *Mechanics of epithelial tissue homeostasis and morphogenesis*. Science, 2013. **340**(6137): p. 1185-1189.
- 9. Mierke, C.T., *Initiation of a neoplasm or tumor*. 2015, IOP Publishing: Bristol, UK.
- 10. Manning, M.L., et al., Coaction of intercellular adhesion and cortical tension specifies tissue surface tension. Proceedings of the National Academy of Sciences, 2010. **107**(28): p. 12517-12522.
- 11. Makhoul-Mansour, M.M. and E.C. Freeman, *Droplet-Based Membranous Soft Materials*. Langmuir, 2021. **37**(11): p. 3231-3247.
- 12. Makhoul-Mansour, M.M., et al., *Imbuing Membranous Materials with Magnetically-Driven Reconfiguration Events*. 2021: Unpublished Work.
- 13. Bayley, H., et al., *Droplet interface bilayers*. Molecular BioSystems, 2008. **4**(12): p. 1191-208.
- 14. B.El-Beyrouthy, J., et al., Distributed Compaction of Synthetic Tissues through
 Asymmetric Electrowetting: Modeling and Experimental Observations. 2021.

- 15. Sarles, S.A. and D.J. Leo, *Physical encapsulation of droplet interface bilayers for durable, portable biomolecular networks.* Lab on a Chip, 2010. **10**(6): p. 710-7.
- de Wit, G., et al., *Dynamic label-free imaging of lipid nanodomains*. Proceedings of the National Academy of Science USA, 2015. **112**(40): p. 12299-303.
- 17. Levental, I., K.R. Levental, and F.A. Heberle, *Lipid Rafts: Controversies Resolved,*Mysteries Remain. Trends in Cell Biology, 2020. **30**(5): p. 341-353.
- 18. Hanzal-Bayer, M.F. and J.F. Hancock, *Lipid rafts and membrane traffic*. FEBS Letters, 2007. **581**(11): p. 2098-104.
- 19. Nicolson, G.L., The Fluid-Mosaic Model of Membrane Structure: still relevant to understanding the structure, function and dynamics of biological membranes after more than 40 years. Biochim Biophys Acta, 2014. **1838**(6): p. 1451-66.
- 20. Lingwood, D. and K. Simons, *Lipid Rafts As a Membrane-Organizing Principle*. Science, 2010. **327**(5961): p. 46-50.
- 21. Simons, K. and E. Ikonen, Functional rafts in cell membranes. Nature, 1997. **387**(6633): p. 569-72.
- 22. Filippov, A., G. Oradd, and G. Lindblom, *Influence of cholesterol and water content on phospholipid lateral diffusion in bilayers*. Langmuir, 2003. **19**(16): p. 6397-6400.
- 23. Danial, J.S., et al., On demand modulation of lipid composition in an individual bilayer. Soft Matter, 2017. **13**(9): p. 1788-1793.
- 24. Kossatz, S., et al., Efficient treatment of breast cancer xenografts with multifunctionalized iron oxide nanoparticles combining magnetic hyperthermia and anti-cancer drug delivery. Breast Cancer Research, 2015. 17(1): p. 66.

- 25. Makhoul-Mansour, M.M., et al., *Photopolymerized microdomains in both lipid leaflets establish diffusive transport pathways across biomimetic membranes*. Soft Matter, 2019. **15**(43): p. 8718-8727.
- 26. El-Beyrouthy, J., et al., A new approach for investigating the response of lipid membranes to electrocompression by coupling droplet mechanics and membrane biophysics. Journal of the Royal Society Interface, 2019. **16**(161): p. 20190652.
- 27. Makhoul-Mansour, M.M., et al., *A skin-inspired soft material with directional mechanosensation*. Bioinspiration & Biomimetics, 2021. **16**(4).
- 28. Berry, J.D., et al., Measurement of surface and interfacial tension using pendant drop tensiometry. J Colloid Interface Sci, 2015. **454**: p. 226-37.
- 29. Holden, M.A., D. Needham, and H. Bayley, *Functional bionetworks from nanoliter* water droplets. Journal of the American Chemical Society, 2007. **129**(27): p. 8650-8655.
- 30. Hansen, J.S., et al., *Lipid directed intrinsic membrane protein segregation*. Journal of the American Chemical Society, 2013. **135**(46): p. 17294-7.

CHAPTER 8

CONCLUSIONS AND SUMMARY

8.1. Summary- Overview of this Document

The main focus of the work presented in this document is functionalizing membranous soft materials to respond to new external stimuli and enabling them with morphing capabilities inspired by natural cellular adaptation mechanisms. These materials are assembled using the DIB (droplet interface bilayer) technique and build upon previous work in this platform. DIB-based tissues can be customized to include various protein/peptide channels, transmembrane channels and various active biomolecules yielding an assembly where the overall functionality is determined by the composition and arrangement of the individual lipid coated compartments, the chemical communication (transport in overall tissue) between subcompartments is dictated by their neighbors and internal composition (lipid/channel profile). Morphing capabilities inspired by natural cellular processes have been introduced into the DIB platform to change how the synthetic tissue internally communicates and adapts to the external environment by altering the relative element locations and chemical composition.

The introductory chapter (Chapter 1) presented the overall goals and approach behind enabling morphing and chemical adaptation capabilities in DIB-tissues inspired by cellular systems, lipid membranes and bottom-up synthetic biology.

Chapter 2 contains an extensive literature review on the recent advances in the construction, manipulation and functionalization of DIB structures as well as the platform itself.

Chapter 3 describes an initial study involving ferrofluid manipulation. The introduction of biocompatible ferrofluids into the DIB platform is examined there and their compatibility in terms of interfacial membrane properties and the ability to sustain transmembrane peptide/protein channel while keeping the magnetic droplets within the structure is established. The introduction of ferrofluid into the platform has given these structure magnetic actuation capabilities which are later used in more advanced applications.

Chapter 4 builds on results obtained in Chapter 3 and studies the effect of localized membrane failure on DIB-structures assembled using biocompatible ferrofluids. Once failure is electrically induced in localized spots, the remaining droplets rearrange into new configurations, hence rewiring the droplet-droplet chemical communication pathways. A coupled mechanical-electrical model is used both to validate experimental observation and to propose future and more advanced ones.

Ferrofluid research is completed in Chapter 5 where adaptive DIB architectures inspired by nature where function follows form, are explored and enabled with a sensitivity to magnetic force fields using ferrofluid droplets. Rearranging the droplets within a larger DIB structure alters the internal patterns of communication as the properties of each interfacial membranes is a function of the droplet pair rather than a single compartment. Upon exposing heterogenous DIB structures (with magnetic and non-magnetic aqueous compartments), transition rearrangement events in the membranes bordering magnetic

compartments are triggered. This concept is further explored and used to alter internal communication pathways in DIB structures by integrating pore forming channels within select compartments: communicative pathways are established by changing the internal configuration of the structure putting droplets of compatible composition into contact.

In Chapter 6, the focus is shifted from adaptation via structural morphing to adaptation via changing internal chemical composition. The end goal is to use both forms of adaptation in conjunction within larger and more complex DIB-systems. Establishing directional and remotely activated communicative pathways within DIB-systems is investigated in this chapter by examining the integration of photopolymerizable lipids into the platform. The incorporation of photopolymerizable lipids has shown their ability to establish conductive pathways in the lipid membranes post-exposure to UV-C light exclusively between compartments of compatible chemical composition. The end result is an improved resolution of the patterned conductive pathways in DIB-tissues and an overall reduced diffusive loss.

The final core chapter (Chapter 7) discusses ongoing research inspired by the DAH (differential adhesion hypothesis) where differences in tissue surface tension drive local changes in the droplet arrangements. This was postulated by investigating the possibility of using physiologically inspired lipid mixtures shown to form nanodomains at room temperature. The effect of applied heat (beyond phase transition temperature) and consequent cooling (with some temperature cycling) on the mechanical properties of the underlying membranes is examined and the results suggested for future studies. The effect of changes in temperature on the membranes is likely attributed to an induced alignment

in lipid nanodomains causing an increase in the adhesion between droplets (a mechanism seen in cellular intercalation events and explained through the DAH).

8.2. Contributions

This research was mainly concerned with implementing strategies for chemical and structural adaptation within droplet based synthetic-tissue taking cues from biological examples and using a bottom-up synthetic biology approach.

Magnetic Functionalization of DIB-based Materials

The compatibility of ferrofluids with the DIB platform in terms of mechanical properties of the resulting interfacial bilayers as well as the capability of sustaining healthy transmembrane channel activity was established.

Ferrofluids can be embedded within DIB structures yielding magnetically sensitive membranous systems with various types of building blocks capable of establishing chemical communication through peptide/protein channels.

This incorporation further facilitated the construction of 2D DIB systems and has allowed us to study the effect of localized membrane failure on their overall equilibrium architecture.

Tissue-inspired Structural Adaptation of DIB-based Materials

Structural adaptation within DIB systems in response to magnetic force fields was made possible through the permanent incorporation of ferrofluid compartments into these systems.

Structural morphing mechanisms inspired by cellular intercalation events and optimized through mechanics of gel emulsions (jamming), self-assembly principles, and

transport across synthetic model membranes showed that DIB tissues are dynamic and exhibit long term reconfiguration capabilities.

DIB-tissues when optimally functionalized, channeled their natural counterparts: function follows form and structure when influenced by external factors, dictates functionality.

Akin to the DAH, DIBs were functionalized to exhibit morphing capabilities driven by differential adhesion in response to thermal triggers, a mechanism linked back to lipid nanodomain reorganization and alignment.

Chemical Adaptation of DIB-based Materials in Response to UV-light: Directional Permeability

An adaptation through a shift in chemical composition was achieved by incorporating photopolymerizable lipids into the aqueous phase of DIBs. Communication pathways are established exclusively between compartments of compatible lipid composition. Hence diffusive loss of information was reduced, and communication was constrained to targeted regions.

8.3. Final Remarks

Inspired by the structure and functionality of natural cellular tissues, DIB-based synthetic tissues strategically combine the advantages of membrane modeling techniques, emulsion chemistry and self-assembly principles. Recent developments in the platform have shown their capabilities in various applications ranging from chemical computing to soft microrobots and areas where biocompatibility is required, and hence more traditional engineering components are no longer suitable for use.

This document details research concerning the adaptability of DIB-tissues: its' natural inspirations, mechanisms (chemical vs structural), efforts in optimization, and future prospects. The current climate in this area of research has moved towards DIB-tissues operating in harsher, non-controlled conditions and hence shown that more work can still be dedicated towards the stability, durability, portability and endurance of these synthetic tissues.

APPENDIX A

SUPPLEMENTARY INFORMATION: IMBUING MEMBRANOUS MATERIALS

WITH MAGNETICALLY-DRIVEN RECONFIGURATION EVENTS ⁴

 $^{^4}$ M. M. Makhoul-Mansour, J. B. El-Beyrouthy, L. Mao, E. C. Freeman, Submitted to Scientific Reports $27/09/2021.\,$

Supplementary information includes a detailed overview of the experimental methodology, materials used and additional details.

A.1. Experimental Methodology

Materials

Background Aqueous Buffer Solution

The main aqueous buffer solution was prepared by adding ((250 mM) Potassium Chloride (KCl, Sigma-Aldrich, St. Louis, MO)) and ((10 mM) 3-(N-morpholino) propanesulfonic acid (MOPS, Sigma-Aldrich, St. Louis, MO)) to deionized water yielding roughly a pH of 7.0 as measured and was subsequently used for liposomes hydration. A commercial food dye (Kroger assorted water-based food coloring kit, purchased from a local grocery store) was used at a weak concentration (≤ 1µl dye.ml⁻¹ of solution) to induce a blue color in droplets for illustrative purposes only.

Aqueous Lipid Solutions

Zwitterionic lipids (1,2-diphytanoyl-sn-glycero-3-phosphocholine (DPhPC, Avanti Polar Lipids, Alabaster, AL) were first dispersed at the desired concentration in chloroform (Sigma-Aldrich, St. Louis, MO) yielding clear solutions. The organic solvent was then evaporated through exposure to a dry argon stream under a fume hood for several minutes. The resulting lipid film was then further dried by placing the vial in a room-temperature vacuum chamber for a minimum of 6 hours. Dried lipid films were consequently rehydrated by adding the previously described aqueous buffer solution ((250 mM) KCl and (10 mM) MOPS) yielding a final lipid concentration of (2.5 mg.ml⁻¹). Afterwards, the lipid-mixtures were homogenized by gently stirring them using a vortex agitator. These solutions subsequently underwent several thaw-freeze cycles 6 cycles and were afterwards

stored at 2 °C. Upon usage, the lipid solutions were sonicated using a probe tip sonicator (2 mm standard probe tip with a maximum oscillation amplitude of 200 µm, from QSONICA Q55 Probe Tip Ultrasonicator, QSONICA, Newtown, CT) until a clear consistency was achieved and no lipids aggregations were observed (30 W cycles of 2 minutes for a minimum of 5 cycles). The tip of a sonicator was roughly positioned in the middle of the lipid dispersion ensuring a uniform energy dissipation within the vials. This preparation process delivers a high-energy input into lipid suspensions and ensures that the resulting vesicles are optimal for DIB membrane formation.

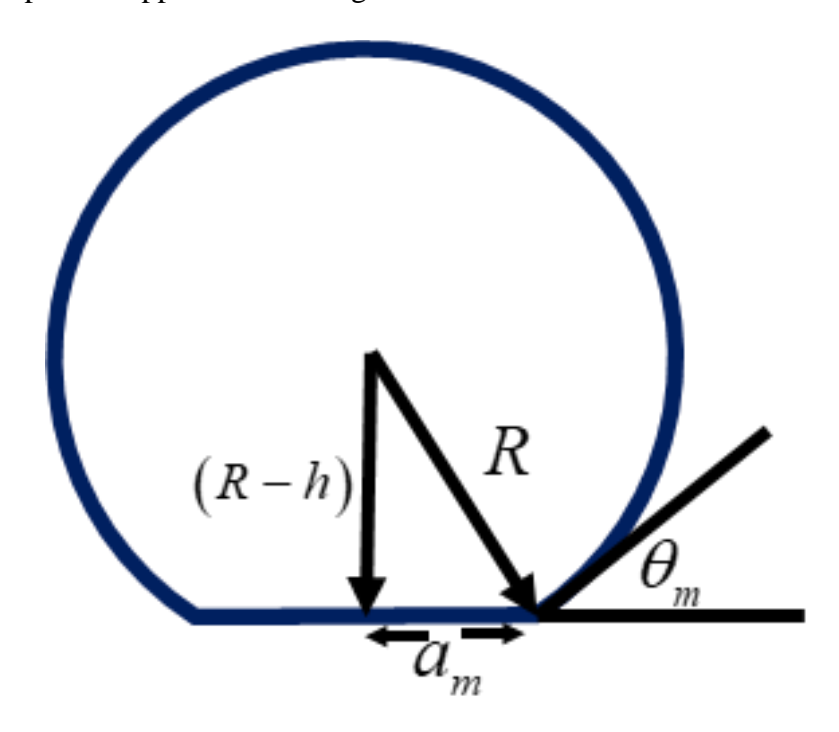
Alpha-Hemolysin Infused Solutions

A concentration of (2 μ g.mL⁻¹) of wild-type alpha hemolysin α Hl from Staphylococcus aureus (Sigma-Aldrich, St. Louis, MO) was added to the previously described buffer solution and stored at 2°C. This oligomerized PFT heptamers introduce themselves spontaneously into lipid bilayers to form mushroom-shaped pores that allow small molecules to pass through the membrane [1]. Each α Hl insertion event is usually marked by a stepwise increase in the measured transmembrane current (for a single lipid membrane, when multiple lipid membranes are monitored insertion events are seen as an increase in the measured current- not necessarily stepwise) [2, 3].

Aqueous Ferrofluid Solutions

EMG 507 and EMG 509 (EMG series water-based ferrofluid, Ferrotec, Santa Clara, CA), commercial water based ferrofluids with a magnetic particle concentration of 2% and 0.6% respectively (by volume) were used throughout this work. Parameters for each ferrofluid are provided in Table A2. 250 mM KCl and 10 mM MOPS salts were added to both ferrofluid solutions. EMG 507 has a distinctive black color reflecting its higher

concentration of magnetic nanoparticles while EMG 509 has lighter consistency (lower density) and a brown pigment reflecting its lower magnetic nanoparticles concentration. All ferrofluid solutions were systematically and periodically sonicated to ensure homogeneity using a probe tip sonicator (the same 2 mm standard probe tip with a maximum oscillation amplitude of 200 µm, from QSONICA Q55 Probe Tip Ultrasonicator, QSONICA, Newtown, CT). Sonication was held in 30 W cycles of 2 minutes each; on average, 4 cycles were required resulting in a more homogenous suspension of magnetic nanoparticles in the injected microdroplets. A uniform distribution of magnetic nanoparticles yields by extension a more uniform magnetic field force distribution upon the application of magnetic fields.



Supplementary Figure A.1- Spherical cap approximation for the droplet geometry and produced membrane radius am, apparent droplet radius R, spherical cap height h, and angle of contact θ_m .

Lipid-Oil Solution

When the lipid-out technique was used, Zwitterionic lipids (1,2-diphytanoyl-sn-glycero-3-phosphocholine (DPhPC), Avanti Polar Lipids, Alabaster, AL) were typically suspended in a 2:1 (volume ratio) mixture of hexadecane and silicone oil AR20 (both Sigma-Aldrich, St. Louis, MO) at a concentration of (0.5 mg.ml⁻¹). These solutions were bath-sonicated for 15 minutes (Elmasonic S100h Ultrasonic sonicator, Elma Schmid Bauer GmbH, Gottlieb-Daimler-Straße Singen, Germany) and afterwards stored at 2 °C. Prior to each use, the solutions were refreshed by sonicating them again for 15 minutes. This mixture was found to both increase the bilayers' stability while facilitating the magnetic manipulation of droplets, and separation/reformation of membranes [4, 5].

Supplementary Table A.1- Interfacial Tensions for Varying Solvents

Mixture	Monolayer Tension (γ_m) mN/m	Bilayer Tension (γ _b) mN/m	Energy of Adhesion (-△F) mN/m	Density kg/m ³
Hexadecane (DPhPC, Lipid-In, 2.5 mg/mL)	1.05 (±0.05)	1.83 (±0.11)	0.28	774
2:1 Hexadecane: Silicone Oil AR20 (DPhPC, Lipid-Out, 0.5 mg/mL)	1.10 (±0.03)	1.85 (±0.08)	0.36	853
1:1 Hexadecane: Silicone Oil AR20 (DPhPC, Lipid-Out, 0.5 mg/mL)	1.06 (±0.04)	1.59 (±0.07)	0.53	892

Methods

Experimental Setup (Solenoid-Based Magnetic Manipulation and Pneumatic Droplet Injections Systems)

An electromagnet-based manipulation system was designed to remotely control ferrofluid droplets. Four solenoids (originally purchased as air core solenoids, Ward's Science, VWR, Radnor, PA) with EFI Alloy 50 cores (2.5x7.5 inches cylindrical cores, Ed

Fagan, Franklin Lakes, NJ) are mounted in parallel pairs in the x and y directions offering a precise control over the planar position of the magnetic droplets (the distance between each solenoid pair is 12 cm while the distance from each solenoid to the center of the dish is 6 cm). These solenoids are powered through the 9111 BK Precision 60 V Multirange DC Power Supply (B&K PRECISION North America, Yorba Linda, CA). The magnitude of the magnetic energy provided by electromagnets can be controlled through the intensity of the current or voltage supplied to them. In order to move a droplet in 2D, using multiple solenoids at a time and precisely controlling the sequence in which a solenoid is magnetized are crucial. For this sake, power received by the electromagnets was interactively regulated through an ARDUINO MEGA 2560 microcontroller connected to an 8-channel relay module for ARDUINO, driven by a LABVIEW user interface. Such control scheme enabled us to actively control the direction of the applied magnetic field at a desired rate.

Larger DIB structures are constructed using the pneumatically driven 3D-droplet printer [6]. In short, a capillary tube (glass tubes, 1.1mm x 10 cm, World Precision Instruments Inc., Sarasota, FL pulled using the World Precision Instruments, P-1000, Sutter, Sarasota, FL) filled with the desired aqueous solution is connected to the printing needle and pressure clamp (HSPC-2-SB, ALA Scientific Instruments, Farmingdale, NY) using silicone tubes. Another ARDUINO computer-controlled microcontroller is used to send voltage pulses to the HSPC which translate into an applied pressure to the operating liquid into the tube. The position of the capillary tube (and consequently that of the printed aqueous droplets) is controlled using a three-axis motorized micro-step manipulator (MCL3). The size of the droplets is dictated by the amplitude of the applied pressure, the

duration of pressure application as well as the size of the glass tube opening. Adequate combination settings producing droplets with preset dimensions were calibrated for at the beginning of each experimental trial.

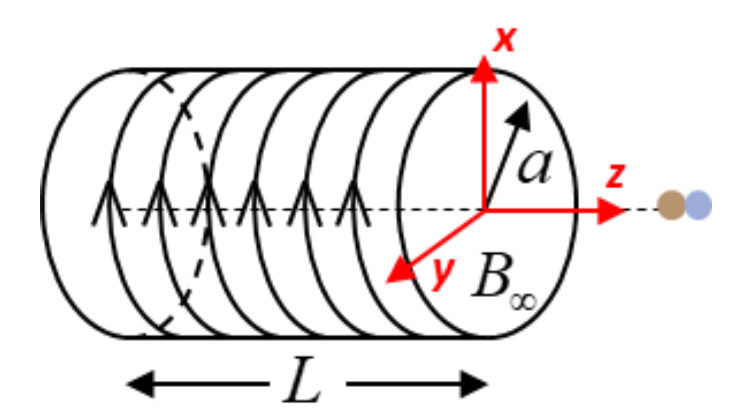
Pulled glass tubes (4 inches glass rods, 1.0mm x 10 cm, World Precision Instruments Inc., Sarasota, FL) were introduced into the dish to act as anchors for bilayer separation and reformation. The tips of these anchors were coated with agarose (3% by mass EZ Pack Agarose LE, Molecular Biology Grade, Benchmark Scientific, Sayresville, NJ) used to hold certain critical droplets in place. When electrical recordings are performed, droplets (~200-300 µm radius) were systematically injected on agarose (3% by mass) coated silver/silver chloride (Ag/AgCl) electrodes (125 µm in diameter, Good Fellow, Coraopolis, PA). Both electrodes as well as anchors' positions were controlled through a three-axis manual micromanipulator (Siskiyou, Grants Pass, OR). Images/videos of DIB networks were acquired using a CCD camera (high sensitivity DCC1645C-HQ, Thorlabs, Newton, NJ) mounted on an inverted microscope. Crosssectional images were also acquired using a CCD camera (high sensitivity DCC1240C, Thorlabs, Newton, NJ) to which zoom lenses (6.5X zoom lenses with a 0.7–4.5× magnification range, Thorlabs, Newton, NJ) were attached. Note that in all experiments, oil dishes were treated with sigmacote siliconizing reagent for glass and other surfaces (Sigma-Aldrich, St. Louis, MO) to prevent droplets from sticking to the surface.

Supplementary Table A.2- Provided Ferrofluid Magnetic Properties (as provided by FerroTec)

Parameter	EMG 507	EMG 509	
Initial Magnetic Susceptibility (<i>c_{ferro}</i>)	1.63	0.5	
Saturation Magnetization	110 Gauss	33 Gauss	
Density	1120 kg/m^3	1030 kg/m^3	
Magnetic Particle Concentration	2% vol	0.6% vol	

Application of a Variable Magnetic Field on a Single DIB-Experimental Approach

Using the magnetic manipulation stage described previously, a water microdroplet is deposited in the lipid-oil mixture and held in place using a fine-pulled glass tube (as described in the previous section). A lipid bilayer is formed by manually pushing an EMG 507 ferrofluid droplet into contact with the aqueous buffer droplet (using a second finely pulled glass rod). A magnetic field, perpendicular to the lipid membrane is then applied; top and side view images of the bilayer are acquired (once the DIB reaches an equilibrium size post magnetic field application). The intensity of the magnetic field is gradually amplified by augmenting the current supplied to the solenoid (in 0.5 A steps ranging from 0 A to 7.0 A) and the bilayer's response recorded once it reaches an equilibrium size. 3 samples were recorded and the data analyzed and averaged.



Supplementary Figure A.2- Definitions for the electromagnet configuration for manipulating a single DIB.

Electrophysiological Measurements

The obtained current traces were recorded in a Faraday cage (Thorlabs, Newton NJ) in voltage clamp mode (Whole Cell β =1) using the AXOpatch 200B patch clamp amplifier and the Digidata 1550 data acquisition system (Molecular Devices, Sunnyvale,

CA) at a sampling frequency of 10 kHz and then filtered at 1 kHz using the embedded low-pass Bessel filter (-80 dB.decade⁻¹). Post-acquisition, a 500 Hz fourth-order Butterworth low-pass filter was applied in MATLAB for visualization purposes. This approach has been thoroughly tested and used by us on previous occasions [7-9] and was employed as well for all electrical recordings here unless specifically stated otherwise.

Supplementary Table A.3- Experimental Parameters for Magnetic Separation of the Droplets

Variable	Value	Source
Solenoid Length (<i>L</i>)	18.4 cm	Measured
Solenoid Radius (a)	6.35 cm	Measured
Solenoid Turns (N)	~100	Measured
Ferrofluid Distance from Electromagnet	~5 cm	Variable
Monolayer Tension (γ_m)	1.10 mN/m	Measured
Bilayer Tension (γ_b)	1.85 mN/m	Measured
Droplet Radius (r_{ferro})	650 mm	Approximate
Electromagnet Maximum Relative	100,000	Manufacturer (EFI Alloy 50, Ed Fagan)
Permeability ($\mu_{r,core}$)		
Electromagnet Saturation Inductance	14,500 Gauss	Manufacturer (EFI Alloy 50, Ed Fagan)
Electromagnet Coercive Force	4.77 A/m	Manufacturer (EFI Alloy 50, Ed Fagan)

Pendant Drop Tension Measurements and Contact Angle Measurements

Monolayer tension measurements were obtained using the pendant drop technique with the open-source software OpenDrop [10]. The experimental apparatus consists of a calibrated needle containing the solution suspended within an oil reservoir inside a 3 mL glass cuvette. A droplet is suspended from the needle within the oil, and as the lipid monolayer forms at the oil-water interface the droplet will gradually adopt a pendant shape. Recordings are taken using a CCD camera attached to a zoom lens. Frames are extracted using MATLAB and used to estimate the monolayer tension as a function of time. The

equilibrium monolayer tension γ_m is obtained and provided for varying solvent in Table A.1.

The bilayer tension is obtained using the angle of contact between two adhered droplets. DIBs are formed for each solvent and images at exported again to MATLAB. The findcircles() algorithm is used to detect the outer edges of each droplet and their respective centers. These coordinates are used then to find the intersection points for the membrane and calculate the angle between the droplets. This angle is then used to estimate the bilayer tension using $\gamma_b = 2\gamma_m cos\theta_m$. The energy of adhesion $-\Delta F$ is defined as the difference between the two monolayer areas the new bilayer area, or $-\Delta F = 2\gamma_m - \gamma_b$. A.2. References

71.2. References

- 1. Song, L., et al., Structure of Staphylococcal alpha -Hemolysin, a Heptameric Transmembrane Pore. Science, 1996. 274(5294): p. 1859-1865.
- 2. Hwang, W.L., et al., Electrical Behavior of Droplet Interface Bilayer Networks: Experimental Analysis and Modeling. Journal of the American Chemical Society, 2007. 129(38): p. 11854-11864.
- 3. Makhoul-Mansour, M., E.J. Challita, and E.C. Freeman. Ferrofluid Droplet Based Micro-Magnetic Sensors and Actuators. in ASME 2017 Conference on Smart Materials, Adaptive Structures and Intelligent Systems. 2017. American Society of Mechanical Engineers.
- 4. Challita, E.J., M.M. Makhoul-Mansour, and E.C. Freeman, Reconfiguring droplet interface bilayer networks through sacrificial membranes. Biomicrofluidics, 2018. 12(3): p. 034112.

- 5. Taylor, G.J., et al., Direct in situ measurement of specific capacitance, monolayer tension, and bilayer tension in a droplet interface bilayer. Soft Matter, 2015. 11(38): p. 7592-605.
- 6. Challita, E.J., et al., Encapsulating Networks of Droplet Interface Bilayers in a Thermoreversible Organogel. Scientific reports, 2018. 8(1): p. 6494-6505.
- 7. El-Beyrouthy, J., et al., A new approach for investigating the response of lipid membranes to electrocompression by coupling droplet mechanics and membrane biophysics. Journal of the Royal Society Interface, 2019. 16(161): p. 20190652.
- 8. Makhoul-Mansour, M., et al., Ferrofluid-Based Droplet Interface Bilayer Networks. Langmuir, 2017. 33(45): p. 13000-13007.
- 9. Makhoul-Mansour, M.M., et al., Photopolymerized microdomains in both lipid leaflets establish diffusive transport pathways across biomimetic membranes. Soft Matter, 2019. 15(43): p. 8718-8727.
- 10. Berry, J.D., et al., Measurement of surface and interfacial tension using pendant drop tensiometry. J Colloid Interface Sci, 2015. 454: p. 226-37.

APPENDIX B

SUPPLEMENTARY INFORMATION: PHOTOPOLYMERIZED MICRODOMAINS IN BOTH LIPID LEAFLETS ESTABLISH DIFFUSIVE TRANSPORT PATHWAYS ACROSS BIOMIMETIC MEMBRANES⁵

⁵ M. M. Makhoul-Mansour, J. B. El-Beyrouthy, H. L. Mumme, E. C. Freeman, Soft Matter 2019, 15, 8718. Reprinted here with permission of the publisher

B.1. Materials

Background Buffer Solutions

An aqueous buffer solution was prepared by adding 250 mM Potassium Chloride (KCl, Sigma-Aldrich, St. Louis, MO) and 10 mM 3-(N-morpholino) propanesulfonic acid (MOPS, Sigma-Aldrich, St. Louis, MO) resulting in a pH of ~7.0 as measured. This solution was used when preparing liposomes.

Alpha-Hemolysin Solutions

A concentration of 1.25 μ g/mL of wild-type alpha hemolysin (α Hl) from Staphylococcus aureus (Sigma-Aldrich, St. Louis, MO) was added to the buffer solution and stored at 2°C.

Gramicidin Solutions

The lipid-in method for DIB formation is used in this case, where lipids are dissolved in the aqueous phase. Zwitterionic lipids (1,2-diphytanoyl-sn-glycero-3-phosphocholine (DPhPC), Avanti Polar Lipids, Alabaster, AL) were suspended in the aqueous buffer solution (250 mM KCl and 10 mM MOPS) at a concentration of 2.5 mg/ml. All lipid solutions were sonicated using a probe tip sonicator (QSONICA Q55 Probe Tip Ultrasonicator, QSONICA, Newtown, CT) and afterwards stored at 2 °C. Gramicidin from Bacillus aneurinolyticus (Bacillus brevis, Sigma-Aldrich, St. Louis, MO) a linear polypeptide antibiotic complex is tested in this work. A mixture of gramicidin A, B, C, and D was first dissolved at a concentration of 50 mg/ml in methanol (Sigma-Aldrich, St. Louis, MO). This solution was further diluted to a concentration of 5 mg/ml. Following an additional 2000-fold dilution, gramicidin was added to the above lipid-water solution at a

concentration of 25 ng/ml. All solutions containing gramicidin were kept in the dark and stored at 2 °C.

DiynePC Solutions

A mixture of 1,2-di- (10z,12z-tricosadiynoyl)-sn-glycero-3-phosphocholine (23:2 DiynePC, Avanti Polar Lipids, Alabaster, AL)) polymerizable lipids and zwitterionic lipids (DPhPC) at 1:8, 1:4, 1:2, and 0:1 (control case, contains only DPhPC) mass ratios respectively were first dissolved in chloroform (Sigma-Aldrich, St. Louis, MO) to assure a homogenous mixture yielding clear solutions in the organic solvent. Once lipid combinations were thoroughly mixed in the organic solvent, chloroform was then removed through evaporation using a dry argon stream in a fume hood. The resulting lipid film was then further dried to remove residual traces of chloroform by placing the vial in a vacuum chamber for a minimum of 6 hours. Lipid film hydration was accomplished by adding an aqueous buffer solution (250 mM KCl and 10 mM MOPS) to the vials followed by gentle agitation. The final lipid concentration in each solution was 2.5 mg/ml. These solutions subsequently underwent several thaw-freeze cycles (a minimum of 5 cycles) and were afterwards kept in the dark and stored at 2 °C. Upon usage, the solutions were sonicated using a probe tip sonicator (2 mm standard probe tip with a maximum oscillation amplitude of 200 µm, from QSONICA Q55 Probe Tip Ultrasonicator, QSONICA, Newtown, CT) until a clear consistency was achieved and no lipids aggregations were observed. Sonication was held in 30 W cycles of 3 minutes each at a temperature less than the transition temperature of these lipids ($\leq 40^{\circ}$ C [1]). On average, a minimum of 5 cycles was required before the solutions became clear.

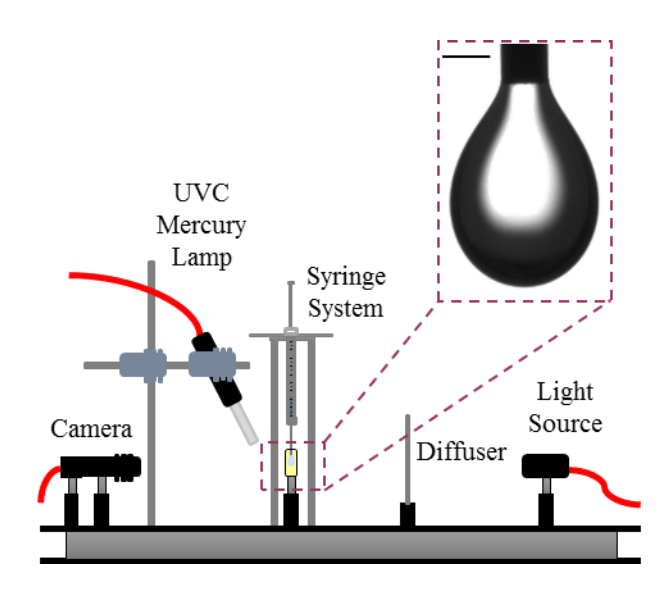


Figure B.1- Schematic representation of the pendant drop experimental setup for measuring the interfacial surface tension. The diffused light of a halogen lamp passes through a Quartz cuvette. Once the measurements have been executed, samples of the water-lipid mixtures were set aside and exposed for 5 minutes to UVC light using the UVC Mercury lamp shown in this schematic. Scale bar represents $300~\mu m$.

Oil Solutions

Typically, the lipid-in and out methods for DIB formation were simultaneously used [2]. Zwitterionic lipids (DPhPC) were suspended in a 2:1 (volume ratio) mixture of hexadecane and silicone oil AR20 (both Sigma-Aldrich, St. Louis, MO) at a concentration of 0.5 mg/ml. All oil-lipid solutions were sonicated for 20 minutes (Elmasonic S100h Ultrasonic sonicator, Elma Schmid Bauer GmbH, Gottlieb-Daimler-Straße Singen, Germany) and afterwards stored at 2 °C. Each lipid-oil solution was then refreshed by sonicating for 15 minutes prior to each use. This oil mixture was found to increase the bilayers' stability [3, 4]. When specifically stated, hexadecane (Sigma Aldrich, St. Louis, MO) was used as the surrounding continuous phase with no further modifications in order

to isolate the effect of photopolymerizable lipids. Please note that no polymerizable lipids were dissolved in the oil phase but only the zwitterionic non-polymerizable phospholipids (DPhPC), ensuring control over the DiynePC distribution within the membrane.

Calcein Solutions

Mixtures of 23:2 DiynePC polymerizable lipids (also referred to as C23 lipids) and Zwitterionic lipids (DPhPC) at 1:4 and 0:1 (control case, contains only DPhPC) mass ratios were suspended in an aqueous buffer solution (250 mM KCl and 10 mM MOPS) at a concentration of 0.25 mg/mL. Calcein (Cayman Chemical Company, Ann Arbor, MI) was added to the solutions at a 0.25 mg/mL concentration. Calcein has an excitation wavelength of 495 nm, an emission wavelength of 515 nm and a net charge of -3. These solutions were exposed to UV-C light (as described in this document) for 5 minutes prior to the addition of calcein.

B.2. Experimental Methods

UV-C Induced Polymerization

A UV-C mercury lamp (11.73 cm total length, 254 nm supplied wavelength, Analytik Jena, Jena, Germany) connected to an input power supply (PS-1 AC Power Supply, 115 V/60 Hz, Analytik Jena, Jena, Germany) was placed 5-7 cm away from the lipid solutions vials for 5 minutes (polymerization occurring rapidly for different diacetylene infused lipids at short irradiation times and decreasing in rate for periods longer than that [5]). After UV-C exposure, the previously transparent lipid solutions would assume their pre-sonication white-opaque color indicating that polymerization had occurred. Lipid polymerization was also performed after droplet deposition on site in a similar manner.

Protocol for Electrophysiological Measurements

The obtained current traces were recorded in voltage-clamp mode (Whole Cell β = 1) at a sampling frequency of 10 kHz and filtered at 1 kHz using the embedded low-pass Bessel filter (-80 dB/decade). Post-acquisition, a 500 Hz fourth-order Butterworth low-pass filter was applied in MATLAB before plotting the measured current traces. All measurements were carried in a dark room to minimize the possibility of spontaneous lipid crosslinking (although very minimal [6]) and reduce external noise. This approach was used for all electrical recordings unless specifically stated otherwise.

Alpha-Hemolysin/Gramicidin Functionality

The obtained current traces with a DC applied voltage of +50 mV were recorded using the previously described electrophysiological protocol. Changes in the current reflect changes in the membrane conductance, either through the insertion of pores or generation of defects in the membrane structure.

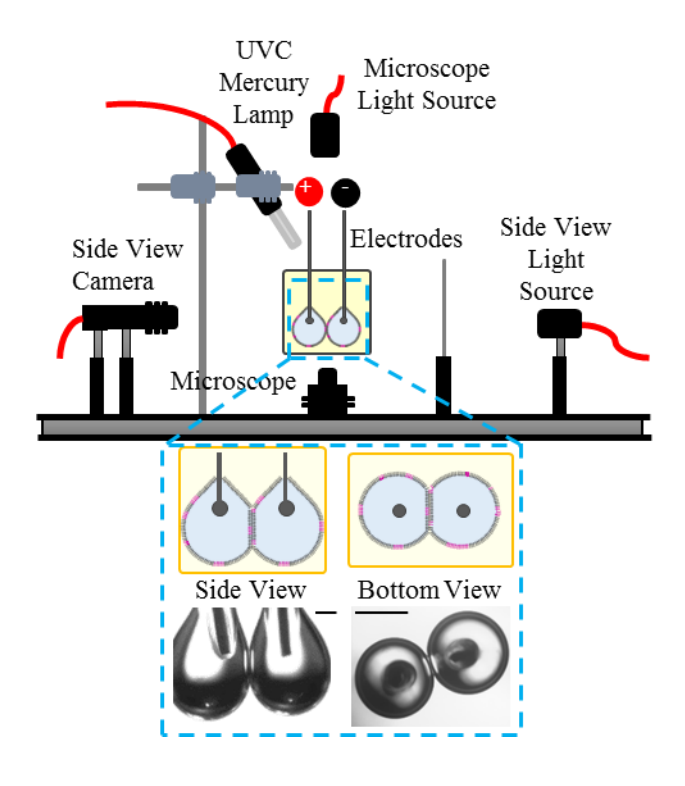


Figure B.2- Schematic representation of the bilayer characterization experimental setup. Side and bottom view images of the lipid bilayer are simultaneously acquired using two different cameras. These images are then used to determine the bilayer's dimensions and by extension its area. Properties of the bilayers are evaluated pre and post UV-C exposure and lipid polymerization. Droplets are suspended from Ag/AgCl electrodes Scale bars represent 250 µm each.

Single Bilayer Conductivity with DiynePC

Using the same experimental setup for assessing bilayer properties (described in detail in the following section), the change in bilayer electrical conductivity upon the gradual introduction of polymerizable lipids was analyzed for the hexadecane: silicone oil AR20 lipid-mixture as well as for bilayers formed in hexadecane oil. Four different subcases were analyzed: a classical control subcase with no polymerizable lipids and three additional subcases where the polymerizable lipids were introduced at ratios of 1:8, 1:4 and 1:2 DiynePC:DPhPC by mass. In all cases, the conductivity of every bilayer was examined prior to any UV-C exposure. The droplets were then separated and exposed for 5 minutes to UV-C-light as previously described. Following their exposure and the formation of cross-linked rafts in the lipid monolayers, the droplets were brought into contact to form the membrane and the conductivity of the bilayer was assessed again. Current traces obtained for various applied voltages ranging from +50 to +150 mV were recorded using the previously described electrophysiological protocol. It is possible to photopolymerize the DIB membrane directly when droplets are in contact and even separate droplets, expose them to UV-C light and the reform the lipid bilayer. However direct UV-C exposure produces significant noise in our measurements (also noted by previous works [7]) so all electrical equipment had to be disconnected during UV-C exposure. Cases where either bilayer were polymerized in situ while the droplets were still in contact, or cases where droplets were separated, exposed to UV-C light and the bilayers reformed were similarly conducted but current traces could not be recorded due to the high level of noise produced by the UV-C lamp.

Measurements of Interfacial Properties

Measurement of Monolayer Interfacial Tensions

Surface tensions of lipid monolayers were assessed using the pendant drop technique and open-source software OpenDrop [8] as described in previous works [9, 10] and depicted in Figure B.1. Interfacial tension was assessed for four different lipid mixtures with a 2:1 hexadecane:silicone oil AR20 mixture containing 0.5 mg/mL DPhPC as the continuous phase. The tested aqueous phases include a control case with no polymerizable lipids (only DPhPC was included), then cases with 1:8, 1:4, and 1:2 DiynePC:DPhPC (Table 6.1). The same measurements were repeated in hexadecane oil alone without dissolved lipids (Table 6.2).

Measurements of DIB Specific Capacitance, Angle of Contact, Bilayer Tension, Adhesion Energy and Thickness

A DIB may be electrically approximated as a capacitor in parallel with a high amplitude resistance [11, 12]. Since the membrane resistance is often in the order of $G\Omega$ - $T\Omega$ [11, 13], the resistive current is mostly negligible, and the overall current of a bilayer reduced to its capacitive component. However, in cases where a porous bilayer is anticipated, this resistive current is no longer negligible and constitutes a part of the current

response. An evaluation of photopolymerizable DIBs specific capacitance, thickness, bilayer tension, angle of contact (defined herein as being the total angle between the droplets at equilibrium), energy of adhesion and specific conductance (defined as the ratio of the average cross-bilayer current with a constant +100 mV measured for 10 minutes divided by the bilayer area) is conducted using in situ DIB characterization techniques frequently used and tested [3, 10, 14-16]. Since some resistive current is anticipated, a 10 mV, 50 Hz sine wave voltage was applied (33120A function generator, Hewlett-Packard, Palo Alto, CA) when evaluating the nominal capacitance of the bilayers. A MATLAB script is used to extract the capacitive and resistive components of the measured current through curve-fitting. Droplets (~500 µm radius) were systematically injected on agarose (2% by mass EZ Pack Agarose LE, Molecular Biology Grade, Benchmark Scientific, Sayresville, NJ) coated silver/silver chloride (Ag/AgCl) electrodes (125 µm in diameter, GoodFellow, Coroapolis, PA). Each electrode position was controlled through a three-axis manual micromanipulator (Siskiyou, Grants Pass, OR). All electrical measurements were acquired using previously described electrophysiological protocol and conducted using the AXOpatch 200B patch clamp amplifier and the Digidata 1440A data acquisition system (Molecular Devices, Sunnyvale, CA). Stray capacitance was accounted before beginning any measurement by using the patch-clamp amplifier built-in whole-cell compensation. When evaluating each case, bottom-view images of the pre-formed, stabilized DIB were acquired using a CCD camera (high sensitivity DCC1645C-HQ, Thorlabs, Newton, NJ) mounted on an inverted microscope. Cross-sectional images of the droplets were also acquired using a CCD camera (high sensitivity DCC1240C, Thorlabs, Newton, NJ) to which zoom lenses (6.5X zoom lenses with a 0.7–4.5× magnification range, Thorlabs,

Newton, NJ) were attached. Supplementary Figure 2 shows a schematic representation of this experimental setup. A more accurate determination of the lipid-bilayer area can be obtained by approximating the contact of the two droplets with an ellipse whose major and minor axes are those obtained from the cross-sectional images [16]. Bilayer properties in hexadecane as well as the 2:1 hexadecane: silicone oil AR20 DPhPC mixture were assessed for four different cases: a control case with no polymerizable lipids (only DPhPC was included), and cases with 1:8, 1:4, and 1:2 DiynePC: DPhPC mass ratios. For each case, 7 samples were evaluated and the corresponding data (average and standard deviation) reported. A linear 4 mV/s voltage-sweep for these bilayers was also performed and current responses recorded.

Bilayer Network Directional Conductivity upon DiynePC Introduction

Droplets (~400 µm radius, the size of these droplets was mainly restricted by the size of the in-house made crate substrate) were systematically injected first on agarose coated silver/silver chloride electrodes. These two droplets are referred to as input droplets. Additional droplets were deposited in the same fashion into the wells of a crate substrate from previous studies [17]. The droplets were placed in their initial positions using a glass rod (GR100-4 Glass Rod, World Precision Instruments, Inc., Sarasota, FL) pulled to fine points using a programmable pipet puller with pretested settings. All electrical measurements were acquired using the previously described electrophysiological protocol. The total voltage applied on the networks was varied so that each bilayer had an individual applied voltage of +100 mV and was estimated using a bilayer-equivalent circuit model [4]. Images were acquired using a CCD camera (DCC1645C-HQ, Leica Microsystems, Wetzlar, Germany) mounted on an inverted fluorescent microscope (Leica DMI3000B

manual inverted microscope, Leica Microsystems, Buffalo Grove, IL). The 2:1 hexadecane: silicone oil AR20 lipid-oil mixture mentioned in previous sections was used. Two types of lipid-aqueous solutions were used: a first polymerizable type (marked in blue in various figures) and a second non-polymerizable type (marked otherwise in red). The first type consists of the aqueous lipid suspension with a 1:4 DiynePC: DPhPC ratio of lipids mentioned in a previous section. This solution was treated with UV-C light for 5 minutes prior to each experiment. The second solution contained DPhPC alone.

Calcein Diffusion Across a Single Lipid Bilayer

Calcein was always introduced from the reference side of the bilayer only (donor droplet). Two cases were studied for 120 minutes each. In the first case (control case) the donor droplet contained pre-polymerized 23:2 DiynePC and DPhPC (at a mass ratio of 1:4). Meanwhile, the acceptor droplet contained only non-polymerizable DPhPC phospholipid. In the second case, both droplets contained pre-polymerized 23:2 DiynePC (at a 1:4 mass ratio with DPhPC). A -100 mV constant voltage was applied in all cases and the hexadecane silicone oil AR20 DPhPC oil-lipid mixture was used as an external phase. Fluorescent microscopy (Leica DMI3000B inverted microscope with a connected External light source for fluorescence excitation Leica EL6000, Leica Microsystems, Buffalo Grove, IL) was used to visualize calcein. Images were acquired every 5 minutes and used to determine the diffusion of calcein across lipid bilayers. ImageJ software (NIH) was used to quantify the fluorescent intensity of both donor and acceptor droplets with time. The fluorescent intensity was measured along the line passing by the center of the droplet and perpendicular to the line intersecting the DIB: intensity was then averaged from

the edge of the DIB to a distance of 125 μm across this line. The relative intensity is then the ratio of the average intensity in the acceptor droplet to that in the donor droplet.

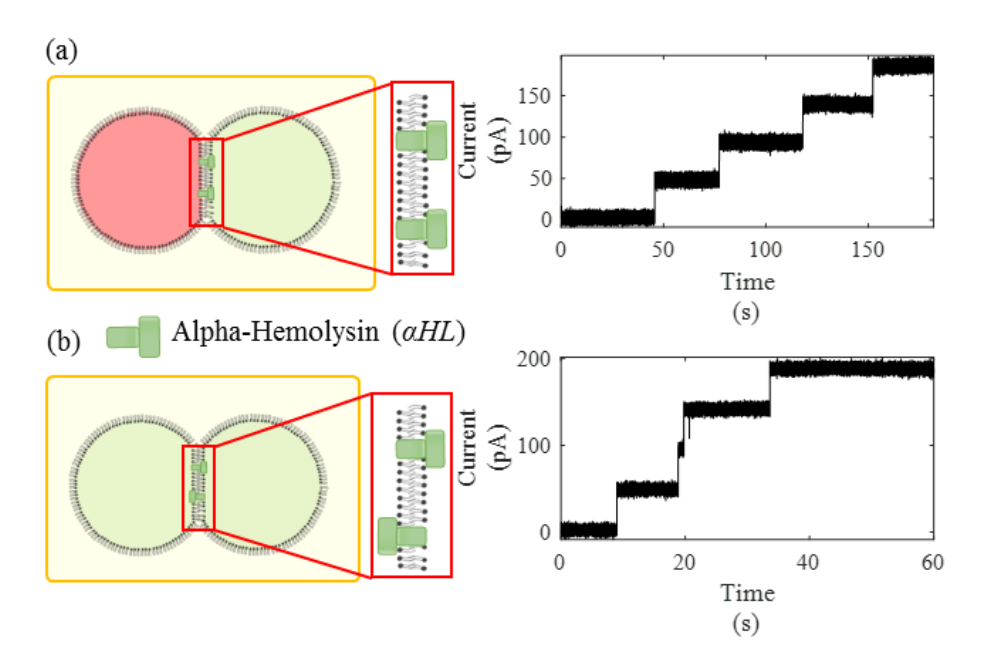


Figure B.3- α Hl insertion activity is showcased upon the application of a constant +50 mV voltage as a typical current response with stepwise increases. In all cases, α Hl was added at a concentration of 1.25 μ g/mL. (a) shows the current response whenever α Hl was added to the reference side of the bilayer. Meanwhile (b) shows the current response when α Hl was added to both sides of the bilayer. All measurements were recorded in voltage clamp mode at a sampling frequency of 10 kHz and filtered at 1 kHz (using the embedded low-pass Bessel filter -80 dB/decade). Post-acquisition, data was filtered at 500 Hz using a fourth order Butterworth low-pass filter in MATLAB.

B.2. Supplementary Results

αHl Insertion Activity in a Single Lipid Bilayer

The αHl insertion mechanism is spontaneous [18, 19]. This PFT inserts into a lipid bilayer by oligomerizing cooperatively into hexamers or heptamers on the membrane surface [18]. These heptamers then insert into lipid bilayers to form mushroom-shaped pores that allow passage of small molecules [20]. While showing different sensitivity depending on membrane composition, the full insertion mechanism of αHL happens whether the monomers are present on one or both sides of the bilayer [18, 20-22]. As shown from the current traces with a fixed +50 mV potential in Figure B.3, α Hl retained its activity whether it was added asymmetrically from one side of the bilayer (trans side as shown in Figure B.3.a.) or symmetrically from both sides of the bilayer (cis and trans sides as shown in Figure B.3.b.). Each additional αHI insertion event was marked by the stepwise increase in the measured current. The insertion of α Hl does not show any significant differences between having the initiating monomers present on one side or both sides of the bilayer as shown here and can by extension occur between a droplet containing the pore forming toxin (PFT) and any other droplet, generating additional channels which might cause undesired changes in the qualities of adjacent membranes.

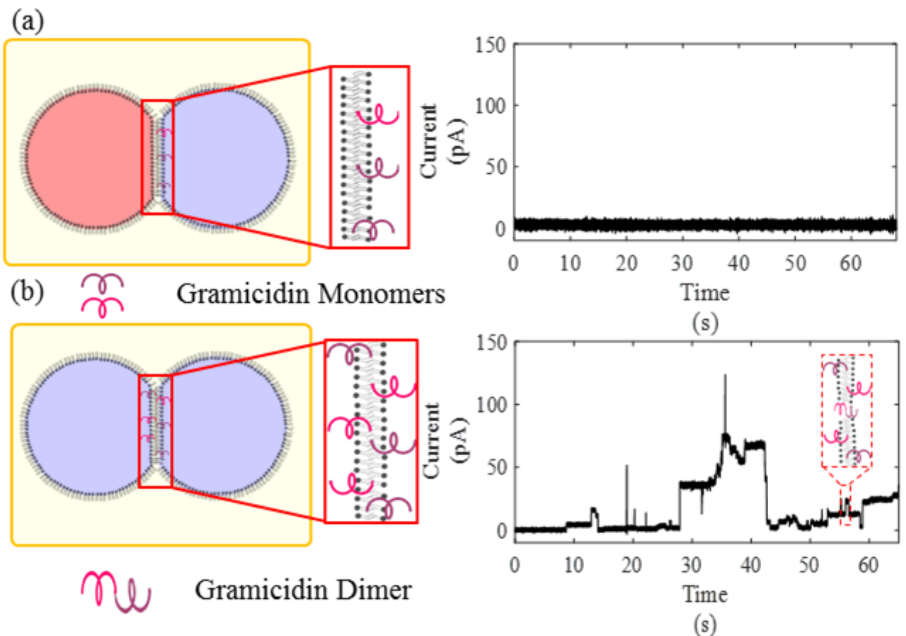


Figure B.4- The typical response of +50 mV constant voltage applied to bilayers for Gramicidin are brief current stepwise discrete increments, resulting from the transient dimerization of the peptide. A mixture of Gramicidin A, B, C and D were used at a concentration of 25 ng/ml resulting in response current steps with different amplitudes. Gramicidin was added from the reference side only in (a) compared to both sides in (b). All measurements were recorded in voltage clamp mode at a sampling frequency of 10 kHz and filtered at 1 kHz (using the embedded low-pass Bessel filter -80 dB/decade). Post-acquisition, data was filtered at 500 Hz using a fourth order Butterworth low-pass filter in MATLAB.

Gramicidin Insertion Activity in a Single Lipid Bilayer

Gramicidin channels are cross-membrane structures. When dissolved, gramicidin structures exist as mixtures of parallel and antiparallel dimers as well as disordered monomers [23-25]. Gramicidin channels across the membrane are formed from the dimerization of helical monomers that had been inserted into each monolayer leaflet. These

channels can be either (i) symmetrical dimers with a single conductance state, or (ii) homodimers with different conductance states or even (iii) heterodimers formed between dissimilar homologues with multiple conductance states [26]. In all cases, the monomers have to be present on both sides of the DIB for insertion to occur – changes in the conductivity are not exhibited with the asymmetric introduction of gramicidin. This property of the dimers was confirmed within the DIB platform in Figure B.4, as the current trace in panel a indicates no dimerization in the bilayer while that of panel b clearly shows different dimerization incidences with different conductance levels as expected from the employed gramicidin mixtures when the membrane potential is held constant at 50 mV. This limits the droplet-droplet exchange to droplet pairs that both contain gramicidin. Yet the concern with using gramicidin in DIB structures lies in its selectivity [26-28]. These gramicidin dimeric pores exhibit a selectivity for small monovalent cations [28-30] posing additional challenges for the transport of anionic or larger molecules.

Interfacial Properties of DIBs

The key results are summarized in the main text (Chapter 6), Figure 6.7. The measured parameters for the 2:1 hexadecane:silicone oil AR20 with 0.5 mg/mL DPhPC and hexadecane solvents are listed here in Table B.1 and Table B.2. The energy of adhesion reflects the favorability of membrane formation and is defined by the difference in energy per area replacing two monolayer surfaces with a single bilayer, or $2\gamma_m$ - γ_b . The bilayer thickness is calculated by approximating the membrane as a parallel plate capacitor, where $h=\epsilon_0\epsilon_r/C_s$. h is the bilayer dielectric thickness, ϵ_0 is vacuum permittivity, ϵ_r is the relative permittivity of the membrane interior (2.2 [3, 10]), and Cs is the specific capacitance of the membrane.

Table B.1- Measurement of the properties of DIBs in 2:1 hexadecane:silicone 0.5 mg/mL DPhPC lipid-oil mixture with different ratios of polymerizable lipids dissolved in the aqueous phase (2.5 mg/ml total) before and after 5 minutes UV-C exposure. Each experiment was repeated 7 times. The standard deviation is reported for directly measured values including the monolayer tension and angle of contact. Errors in the remaining secondary values are calculated using error propagation.

DiynePC	DPhPC	monolayer tension (mN/m)	angle of contact (deg)	specific capacitance (μF/cm ²)	energy of adhesion (mN/m)	bilayer tension (mN/m)	bilayer thickness (Å)	specific conductance (x 10 ⁻² µS/cm ²)
1	2	1.04 (±0.05)	39.60 (±0.38)	0.67 (±0.01)	0.12 (±0.10)	1.95 (±0.01)	29.14 (±0.34)	0.04 (±0.002)
1	4	0.98 (±0.08)	37.17 (±3.21)	0.65 (±0.05)	0.10 (±0.10)	1.85 (±0.05)	30.34 (±2.50)	0.24 (±0.15)
1	8	1.06 (±0.04)	42.77 (±2.56)	0.70 (±0.06)	0.16 (±0.08)	1.98 (±0.02)	28.04 (±2.21)	0.25 (±0.02)
0	1	0.97 (±0.02)	48.20 (±2.35)	0.72 (±0.02)	0.17 (±0.04)	1.76 (±0.01)	27.26 (±0.81)	0.06 (±0.01)
			UVC (254 nm v	vavelength) appli	ed to drop phase for	5 minutes		
1	2	1.18 (±0.02)	40.61 (±0.65)	0.65 (±0.03)	0.15 (±0.04)	2.22 (±0.01)	30.41 (±1.64)	463.79 (±309.06)
1	4	0.96 (±0.06)	33.16 (±2.36)	0.75 (±0.04)	0.08 (±0.07)	1.86 (±0.03)	26.01 (±1.34)	451.00 (±108.09)
1	8	1.10 (±0.22)	44.30 (±1.90)	0.70 (±0.06)	0.16 (±0.14)	2.03 (±0.16)	28.24 (±2.13)	65.07 (±30.67)
0	1	1.03 (±0.01)	51.95 (±1.74)	0.68 (±0.01)	0.21 (±0.02)	1.85 (±0.01)	28.54 (±0.49)	0.06 (±0.02)

Table B.2- Measurement of the properties of lipid bilayers in Hexadecane oil with different concentrations of polymerizable lipids dissolved in the aqueous phase (2.5 mg/ml total) pre and post UVC exposure for 5 minutes.

DiynePC	DPhPC	monolayer tension (mN/m)	angle of contact (deg)	specific capacitance (µF/cm²)	energy of adhesion (mN/m)	bilayer tension (mN/m)	bilayer thickness (Å)	specific conductance (x 10 ⁻² µS/cm ²)
1	2	1.68 (±0.27)	30.51 (±3.38)	0.59 (±0.06)	0.11 (±0.11)	3.24 (±0.24)	33.26 (±3.44)	$0.18~(\pm~0.01)$
1	4	1.13 (±0.07)	34.10 (±5.03)	0.53 (±0.05)	0.12 (±0.10)	2.16 (±0.11)	36.99 (±3.18)	0.19 (±0.02)
1	8	1.15 (±0.12)	38.49 (±3.11)	0.61 (±0.08)	0.13 (±0.12)	2.21 (±0.07)	32.23 (±3.63)	0.25 (±0.03)
0	1	1.11 (±0.04)	51.87 (±6.14)	0.60 (±0.08)	0.22 (±0.08)	1.99 (±0.06)	32.97 (±5.03)	0.22 (±0.03)
			UVC (254 nm	wavelength) app	olied to drop phase fo	or 5 minutes		
1	2	2.02 (±0.32)	20.46 (±3.54)	0.44 (±0.12)	0.07 (±0.06)	3.97 (±0.43)	46.49 (±10.33)	648.25 (±145.79)
1	4	1.41 (±0.57)	31.54 (±2.25)	0.52 (±0.03)	0.11 (±0.07)	2.71 (±0.91)	37.26 (±1.74)	449.92 (±156.22)
1	8	1.04 (±0.03)	35.85 (±3.62)	0.56 (±0.05)	0.10 (±0.06)	1.98 (±0.02)	35.04 (±3.06)	85.06 (±40.04)
0	1	1.07 (±0.06)	50.23 (±0.74)	0.67 (±0.02)	0.20 (±0.12)	1.94 (±0.01)	29.04 (±0.64)	0.25 (±0.01)

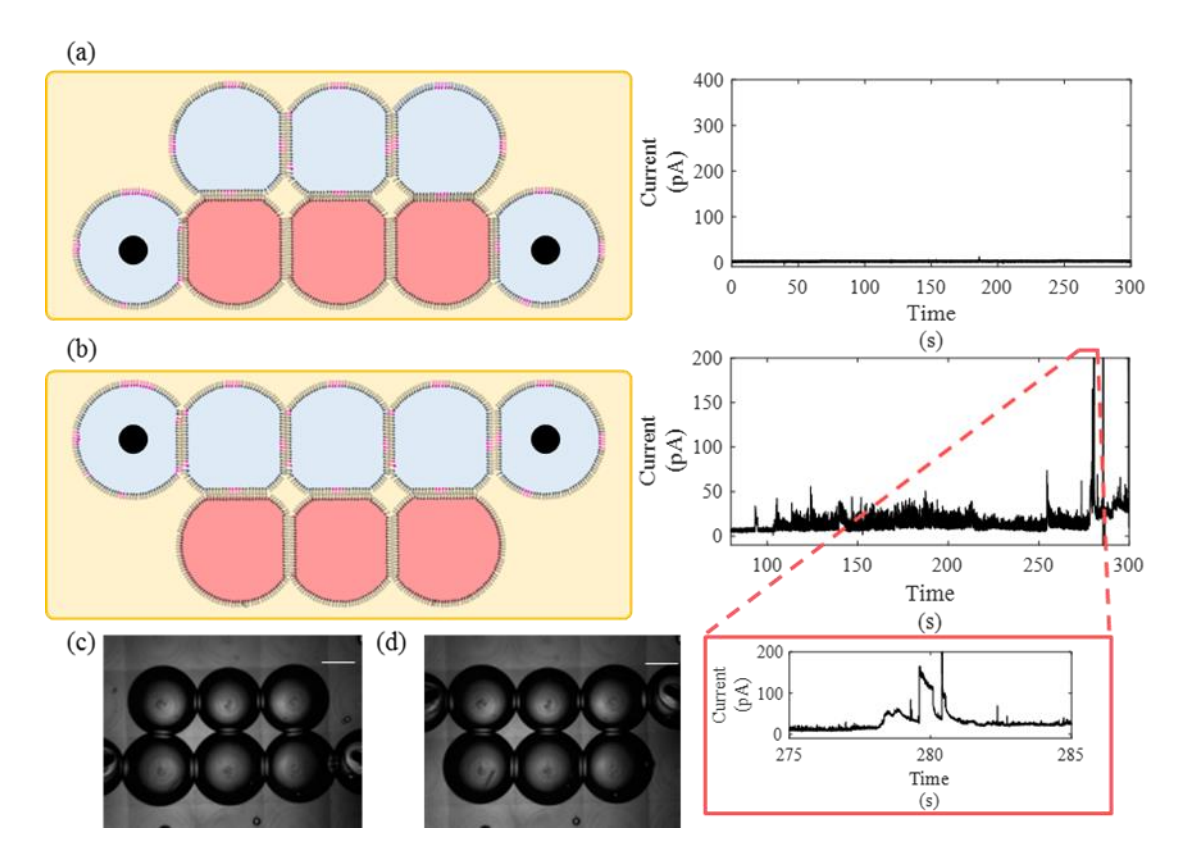


Figure B.5- Blue droplets contain both polymerizable and non-polymerizable phospholipids (23: 2 DiynePC and DPhPC) dissolved at a concentration of 2.5 mg/ml in a 2:1 hexadecane: silicone oil AR20 0.5 mg/mL DPhPC oil-lipid mixture. Meanwhile, red droplets only contain DPhPC. The ratio of polymerizable to non-polymerizable lipids was a 1:4 by mass. In (a), the micro switch was switched OFF by moving the input droplets so that red droplets are placed between the two. In (b), the micro switch was turned to the ON configuration by moving the input blue droplets connected to the acquisition system so that all droplets containing polymerizable lipids were aligned. Bilayers were then given time to form and the corresponding current recorded. (c) and (d) show the images acquired for (a) and (b) respectively. All measurements were recorded in voltage clamp mode at a sampling frequency of 10 kHz and filtered at 1 kHz (using the embedded low-pass Bessel filter –80

dB/decade). Post-acquisition, data was filtered at 500 Hz using a fourth order Butterworth low-pass filter in MATLAB. Scale bars represent 400 µm each.

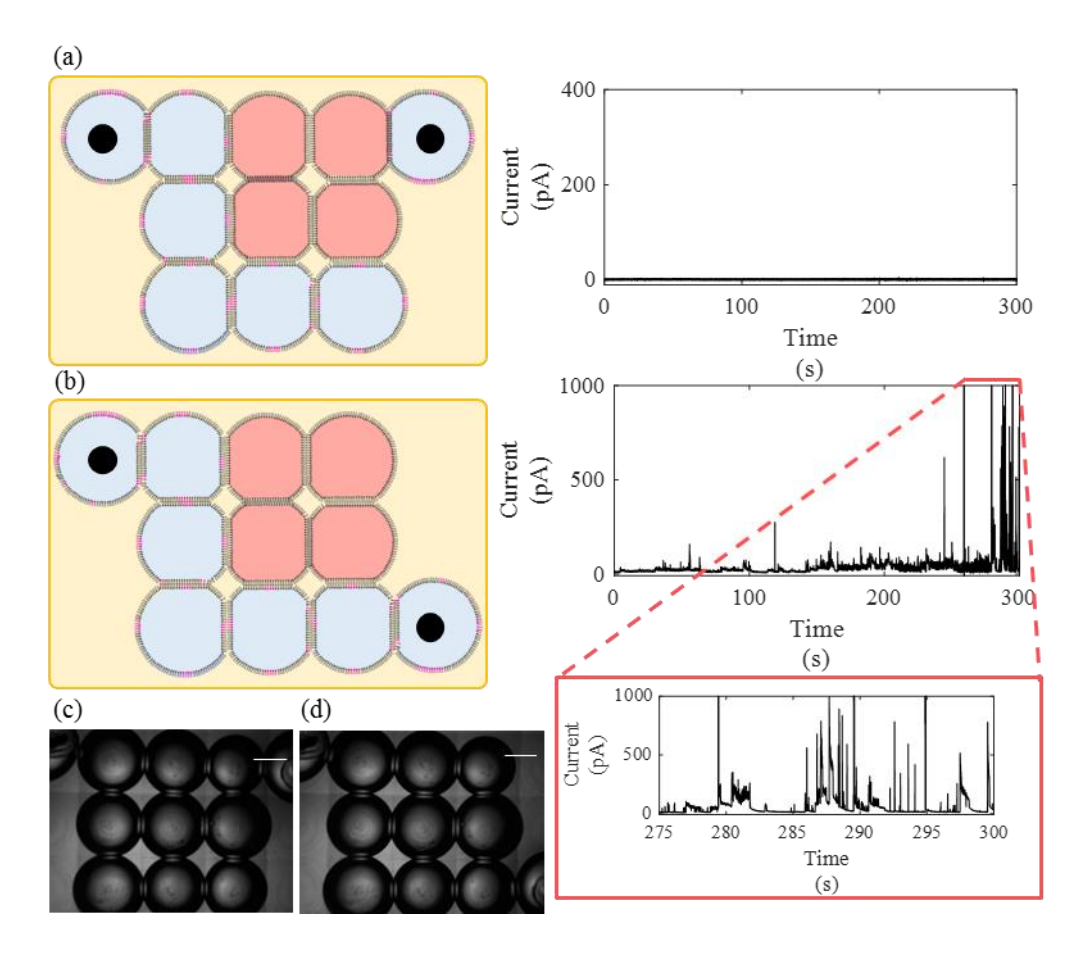


Figure B.6- Blue droplets contain both polymerizable and non-polymerizable phospholipids (23: 2 DiynePC and DPhPC) dissolved at a concentration of 2.5 mg/ml in a a 2:1 hexadecane: silicone oil AR20 0.5 mg/mL DPhPC oil-lipid mixture. Meanwhile, red droplets only contain DPhPC. The ratio of polymerizable to non-polymerizable lipids was a 1:4 by mass. In (a), the micro switch was switched OFF by moving the input droplets so that red droplets are placed between the two. In (b), the micro switch was turned to the ON configuration by moving the input blue droplets connected to the acquisition system so that all droplets containing polymerizable lipids were aligned. Bilayers were then given time to

form and the corresponding current recorded. (c) and (d) show the images acquired for (a) and (b) respectively. All measurements were recorded in voltage clamp mode at a sampling frequency of 10 kHz and filtered at 1 kHz (using the embedded low-pass Bessel filter -80 dB/decade). Post-acquisition, data was filtered at 500 Hz using a fourth order Butterworth low-pass filter in MATLAB. Scale bars represent 400 μ m each.

Figure B.5 and Figure B.6 provide additional examples of conductive pathways established by linking chains of droplets containing photopolymerized DiynePC. In each of these cases the conductivity is only increased when each droplet between the two electrodes contains the photoresponsive lipids. These plots are similar to Figure 6.9 in the primary text (Chapter 6) with larger networks of droplets.

Measurement of Monolayer Interfacial Tensions

Table B.3 contains the measure monolayer surface tension with increasing UV-C exposure with varying lipid ratios and surrounding solvents. The kinetics of monolayer formation are also presented in Figure B.7. All cases show a rapid initial decay in the monolayer tension as lipids assemble at the oil-water interface. The 1:4 DiynePC:DPhPC mixture in hexadecane without lipids in the surrounding solvent is the one exception, noting a greater period of time necessary for liposome unfolding and monolayer assembly. After the monolayers were established as indicated by a stable interfacial tension, image acquisition was paused for UV-C exposure for 150 seconds. After each exposure, the monolayer tension increased temporarily before decaying back to a value that was slightly above the previous equilibrium tension.

Table B.3- Equilibrium monolayer tension results for different aqueous lipid mixtures exposed directly on-site to UV-C light presented in Figure B.7.

Monolayer Tension average	2.5 mg/ml DPhPC in 2:1 hexadecane: silicone and 0.5 mg/ml DPhPC oil- lipid mixture	2.5 mg/ml DPhPC in hexadecane oil	2.5 mg/ml 1:4 23:2 DiynePC: DPhPC in hexadecane oil	2.5 mg/ml 1:4 23:2 DiynePC: DPhPC in 2:1 hexadecane:silicone and 0.5 mg/ml DPhPC oil- lipid mixture
pre-UV-C	1.02	1.15	1.11	1.07
+2:30 mins UV-C	1.06	1.14	1.72	1.04
+2:30 mins UV-C	1.08	1.16	1.45	1.08

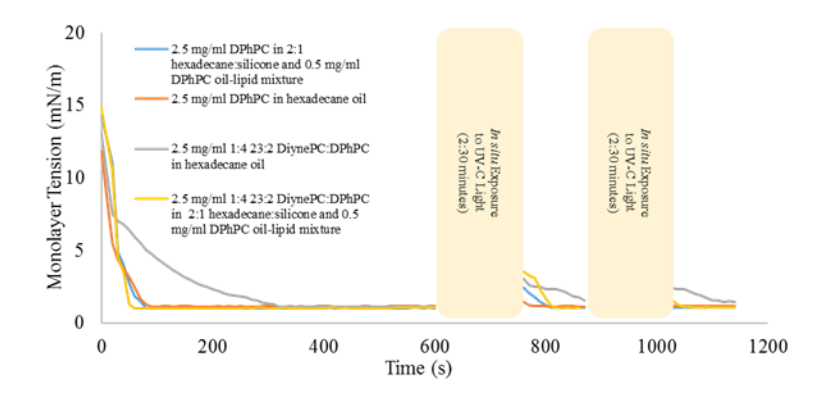


Figure B.7- Monolayer tension results for different aqueous lipid mixtures exposed directly on-site to UV-C light. Aqueous solutions are first introduced into the oil phase and the monolayer tension measured. The droplets are then exposed to UV-C light for 2:30 minutes and the subsequent monolayer tension measured for the following 2 minutes. This process is repeated again, and the tension measured. The monolayer tension could not be measured during exposure to UV-C light since the camera had to be covered to prevent any damage to the lenses. In the contrary, the results reported in Table 6.1 and Table 6.2 in the main text (Chapter 6) correspond to aqueous solutions that have been pre-exposed to UV-C light for 5 minutes.

B.3. References

- 1. Blume, A., Phase transitions of polymerizable phospholipids. Chemistry and physics of lipids, 1991. 57(2-3): p. 253-273.
- 2. Hwang, W.L., et al., Asymmetric droplet interface bilayers. Journal of the American Chemical Society, 2008. 130(18): p. 5878-5879.
- 3. Taylor, G.J., et al., Direct in situ measurement of specific capacitance, monolayer tension, and bilayer tension in a droplet interface bilayer. Soft Matter, 2015. 11(38): p. 7592-605.
- 4. Challita, E.J., M.M. Makhoul-Mansour, and E.C. Freeman, Reconfiguring droplet interface bilayer networks through sacrificial membranes. Biomicrofluidics, 2018. 12(3): p. 034112.
- 5. Leaver, J., et al., The physical properties and photopolymerization of diacetylene-containing phospholipid liposomes. Biochimica et biophysica acta (BBA)-biomembranes, 1983. 732(1): p. 210-218.
- 6. Johnston, D.S., et al., Phospholipid polymers—synthesis and spectral characteristics. Biochimica et Biophysica Acta (BBA)-Biomembranes, 1980. 602(1): p. 57-69.
- 7. Punnamaraju, S., H. You, and A. Steckl, Triggered release of molecules across droplet interface bilayer lipid membranes using photopolymerizable lipids. Langmuir, 2012. 28(20): p. 7657-7664.
- 8. Berry, J.D., et al., Measurement of surface and interfacial tension using pendant drop tensiometry. Journal of Colloid and Interface Science, 2015. 454: p. 226-237.

- 9. Venkatesan, G.A., et al., Adsorption Kinetics Dictate Monolayer Self-Assembly for Both Lipid-In and Lipid-Out Approaches to Droplet Interface Bilayer Formation. ACS-Langmuir, 2015. 31(47): p. 12883-12893.
- 10. Makhoul-Mansour, M., et al., Ferrofluid-Based Droplet Interface Bilayer Networks. Langmuir, 2017. 33(45): p. 13000-13007.
- 11. Bayley, H., et al., Droplet interface bilayers. Molecular BioSystems, 2008. 4(12): p. 1191-208.
- 12. Holden, M.A., D. Needham, and H. Bayley, Functional bionetworks from nanoliter water droplets. Journal of the American Chemical Society, 2007. 129(27): p. 8650-8655.
- 13. Danelon, C., et al., Cell membranes suspended across nanoaperture arrays. Langmuir, 2006. 22(1): p. 22-25.
- 14. Gross, L.C., et al., Determining membrane capacitance by dynamic control of droplet interface bilayer area. Langmuir, 2011. 27(23): p. 14335-42.
- 15. Gross, L.C.M., Applications of Droplet Interface Bilayers: Specific Capacitance Measurements and Membrane Protein Corralling, in St John's College. 2011, University of Oxford p. 255.
- Rofeh, J.D., Block Copolymer Membranes for Protein Nanopore-Based Biosensing. 2017, University of California Santa Barbara.
- 17. Freeman, E.C., et al., Multiscale modeling of droplet interface bilayer membrane networks. Biomicrofluidics, 2015. 9(6): p. 064101.
- 18. Parker, M.W. and S.C. Feil, Pore-forming protein toxins: from structure to function. Prog Biophys Mol Biol, 2005. 88(1): p. 91-142.

- 19. Iacovache, I., F.G. van der Goot, and L. Pernot, Pore formation: an ancient yet complex form of attack. Biochimica et Biophysica Acta (BBA)-Biomembranes, 2008. 1778(7-8): p. 1611-1623.
- 20. Song, L., et al., Structure of Staphylococcal alpha -Hemolysin, a Heptameric Transmembrane Pore. Science, 1996. 274(5294): p. 1859-1865.
- 21. Gouaux, J.E., et al., Subunit stoichiometry of staphylococcal alpha-hemolysin in crystals and on membranes: a heptameric transmembrane pore. Proceedings of the National Academy of Sciences, 1994. 91(26): p. 12828-12831.
- 22. Henrickson, S.E., et al., Driven DNA transport into an asymmetric nanometer-scale pore. Phys Rev Lett, 2000. 85(14): p. 3057-60.
- 23. Veatch, W.R., E.T. Fossel, and E.R. Blout, Conformation of gramicidin A. Biochemistry, 1974. 13(26): p. 5249-5256.
- 24. Langs, D.A., Three-dimensional structure at 0.86 A of the uncomplexed form of the transmembrane ion channel peptide gramicidin A. Science, 1988. 241(4862): p. 188-191.
- 25. Kelkar, D.A. and A. Chattopadhyay, The gramicidin ion channel: a model membrane protein. Biochimica et Biophysica Acta (BBA)-Biomembranes, 2007. 1768(9): p. 2011-2025.
- 26. O'Connell, A.M., R.E. Koeppe, and O.S. Andersen, Kinetics of gramicidin channel formation in lipid bilayers: transmembrane monomer association. Science, 1990. 250(4985): p. 1256-1259.
- 27. Bamberg, E., H. Apell, and H. Alpes, Structure of the gramicidin A channel: Discrimination between the πL , D and the β helix by electrical measurements with lipid

bilayer membranes. Proceedings of the National Academy of Sciences, 1977. 74(6): p. 2402-2406.

- 28. Andersen, O., Ion movement through gramicidin A channels. Single-channel measurements at very high potentials. Biophysical journal, 1983. 41(2): p. 119-13.
- 29. Myers, V.B. and D. Haydon, Ion transfer across lipid membranes in the presence of gramicidin A: II. The ion selectivity. Biochimica et Biophysica Acta (BBA)-Biomembranes, 1972. 274(2): p. 313-322.
- 30. Mueller, P. and D. Rudin, Action potential phenomena in experimental bimolecular lipid membranes. Nature, 1967. 213(5076): p. 603.

APPENDIX C

A SKIN-INSPIRED SOFT MATERIAL WITH DIRECTIONAL

MECHANOSENSATION⁶

⁶ M. M. Makhoul-Mansour, E. J. Challita, A. Chaurasia, D. J. Leo, S. Sukharev, E. C. Freeman, Bioinspiration & Biomimetics 2021, 16.

C.1. Abstract

Lessons about artificial sensor design may be taken from evolutionarily perfected physiological systems. Mechanosensory cells in human skin are exquisitely sensitive to gentle touch and enable us to distinguish objects of different stiffnesses and textures. These cells are embedded in soft epidermal layers of gel-like consistency. Reproducing these mechanosensing capabilities in new soft materials may lead to development of adaptive mechanosensors which will further enhance the abilities of engineered membrane-based structures with bioinspired sensing strategies. This strategy is explored here using droplet interface bilayers (DIBs) embedded within a thermoreversible organogel. The interface between two lipid-coated aqueous inclusions contained within a soft polymeric matrix forms a lipid bilayer resembling the lipid matrix of cell membranes. These interfaces are functionalized with bacterial mechanosensitive channels (V23T MscL) which convert membrane tension into changes in membrane conductance, mimicking mechanosensitive channel activation in mammalian mechanosensory cells. The distortion of encapsulated adhered droplets by cyclical external forces are first explored using a finite element composite model illustrating the directional propagation of mechanical disturbances imposed by a piston. The model predicts that the orientation of the droplet pair forming the membrane relative to the direction of the compression plays a role in the membrane response. The directional dependence of mechanosensitive channel activation in response to gel compression is confirmed experimentally and shows that purely compressive perturbations normal to the interface invoke different channel activities as compared to shearing displacement along a plane of the membrane. The developed system containing specially positioned pairs of droplets functionalized with bacterial mechanosensitive

channels and embedded in a gel creates a skin-inspired soft material with a directional response to mechanical perturbation.

C.2. Introduction

Development of adaptable and responsive materials is a rapidly advancing branch of material science and engineering. Overlapping with the research of soft matter, it increasingly crosses paths with biochemistry and bioengineering. Lessons taken from physiology and evolution of biological sensory systems must be heeded for the development of flexible and adaptable sensors. Here we take inspiration from the biological sensory systems present in the mammalian skin. Mechanosensory cells such as Merkel cells and Pacinian corpuscles embedded in human skin (Figure C.1.a) are exquisitely sensitive to gentle touch and typically generate transient electrical responses to steps of pressure, amplifying the response of afferent neurons [1, 2]. The layer of epidermis surrounding these touch receptor cells can be approximated as an elastic gel. Compressing the surrounding gel (touch) transmits this pressure to the underlying cells. The main functional elements in these cells are mechanosensitive Piezo2 channels converting the applied pressure or tension into depolarizing electrical signals (Figure C.1.b) [1]. These cells are typically abundant in sensitive areas of the body such as fingertips [3, 4].

Herein we explore imbuing a soft, skin-similar gel with pressure-sensing capabilities. This task involves first producing a membranous architecture imbued with mechanosensitive channels, embedding this architecture in a soft polymeric matrix, then quantifying the response to perturbation. The aim is to generate electrical signals in response to the compression of the encapsulated gel, mimicking the functionality of mechanosensory cells. The membranous architecture is produced using the droplet

interface bilayer (DIB) technique (Figure C.2.a). In DIBs [5-8] phospholipids are used as an organic surfactant in a water-in-oil emulsion. Aqueous microdroplets containing dispersed lipids gradually acquire an ordered lipid monolayer coating when introduced into an oil phase. Once the lipid monolayers are fully assembled at the oil-water interface, manipulating the lipid-coated droplets into contact allows lipid monolayers to adhere together, gradually expelling the trapped oil from the interface and forming a stable lipid bilayer membrane. DIBs typically serve as a scaffold for the reconstitution of biological machinery, enabling applications including light-sensing [9-11], chemical microrobots [12, 13], energy storage and conversion [14-16], and the creation of synthetic tissues [17-19] based on the regulated exchange of fluid, solutes and ions through a web of interconnected lipid membranes.

DIBs have a number of advantages as membrane models over traditional black lipid films [20, 21] in terms of stability and flexible control of composition [22, 23]. Printing technology was successfully applied to create 2D and 3D arrays of droplets interconnected with bilayer membranes [18, 24, 25]. After initial successful reconstitutions of poreforming peptides (such as alpha-hemolysin (αHI) from Staphylococcus aureus [14-18, 25-30]), antibiotic peptides such as Alamethicin [19, 31-33], Gramicidin [34, 35], and Pep-1 [36], bacterial toxins forming proteinaceous pores PA63[37], as well as light-sensitive bacteriorhodopsin [15, 38] into DIBs, it became clear that voltage [8, 25] and light [38, 39] can be used as stimuli for triggering channel gating or charge transfer through the pumps across the membrane. Response to mechanical stimuli in DIBs was recently accomplished using the bacterial mechanosensitive channel of large conductance (MscL). This channel is one of the best characterized tension-activated channels [40-43] and was selected for this

reason. A mild gain-of-function mutant (V23T [43]) which gates at a decreased tension value was used for the majority of DIB experiments. The increase in tension was accomplished by controlled cyclic displacement and compression of the droplets, generating tension in the monolayers and the interfacial bilayer containing the channels [44-46]. In an alternative arrangement, hydrostatic pressure was applied to one droplet to activate the mechanosensitive channels [47].

MscL gating in a DIB membrane formed in oil is achieved by temporarily elevating the bilayer tension γ_b . This tension may be estimated as a function of the monolayer tension γ_m and the external angle of contact θ_m using the equation $\gamma_b = 2\gamma_m cos\theta_m$ [23, 48]. Perturbing the droplets through inflation or compression produces temporary increases in the monolayer tension as predicted by $\Delta \gamma_m = K_m (\frac{\Delta A_m}{A_m})$, where A_m is the monolayer area, and K_m is the monolayer compressibility modulus (~120 mN/m for DPhPC monolayers [49]), assuming small changes in the monolayer area. This then produces a similar increase in the bilayer tension, enabling gating of the embedded MscL channels through droplet perturbation [45-47]. Discussed variables are shown in Figure C.2.a.

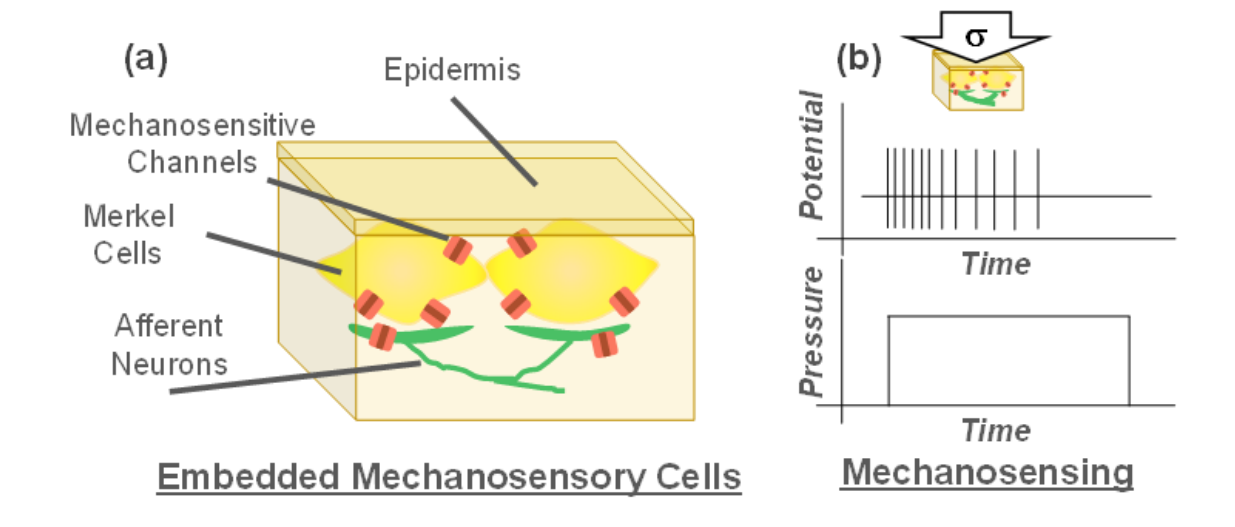


Figure C.1 - (a) Merkel cells and afferent neurons are embedded within the soft epidermis and contain mechanosensitive channels. (b) Disturbances of the soft surrounding gel are converted into electrical signals through the depolarization of the cells. The trace here is a representative sketch for illustrative purposes.

It is important to note that these increases in tension are transient, and cyclical distortion is crucial for gating MscL in DIBs [45]. In DIBs, the dispersed lipids in the surrounding liquids provide a reservoir of additional lipid material. Consequently, the lipid monolayers coating the droplets are able to gradually incorporate additional lipids in response to distortion [49, 50], restoring the original lipids-per-area even if the distortion of the droplet surface is maintained. Similarly, the excess tension applied to the membrane generates an increase in the bilayer area which similarly alleviates the bilayer tension through an increase in the external contact angle between the droplets [44, 46]. Research on the mechanics of MscL gating demonstrated that specific duty cycles for oscillation which permitted sufficient time for resetting the monolayer tension and contact angle to their resting values while increasing the velocity of droplet compression produced optimal gating [45]. These monolayer and bilayer interfaces do not have fixed numbers of lipids and consequently will exhibit a transient tension response to perturbation.

Here, we encapsulate DIBs containing MscL within an organogel (Figure C.2.b) [25, 51] serving as an artificial epidermis, and demonstrate that MscL may be activated through gel compression similar to pressure-sensitive mechanosensory cells. Organogels containing DIBs behave as a soft composite, where fluid inclusions are constrained within the gel and accommodate the deformation through localized softening [52]. Distorting the

gel produces distortions in the lipid layers surrounding the droplets, which may be used to activate embedded mechanosensitive channels by disrupting the tensions within the monolayer interface (Figure C.2.c) similar to DIBs in oil. This work provides the first account of mechanosensitive channel activation in a membrane system embedded in a soft viscoelastic gel. The findings shed new insights into the mechanisms of MscL gating in model membranes and demonstrate the potential of an artificial epidermis-like environment imbued with mechanosensory capabilities. This material concept will allow for governed exchange between encapsulated aqueous subcompartments through the application of mechanical forces.

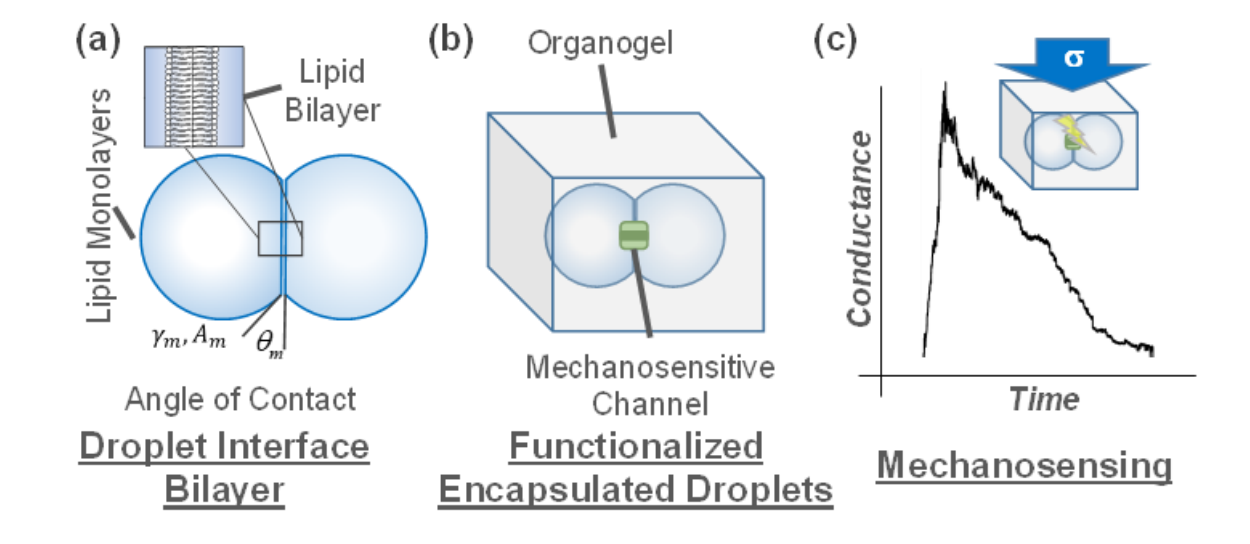


Figure C.2 - (a) Lipid membranes are formed between lipid-coated droplets using the droplet interface bilayer (DIB) technique. (b) DIBs functionalized with mechanosensitive channels may be encapsulated within a thermoreversible organogel, generating a fluid-insolid composite material. (c) Compression of the encapsulating gel may be used to activate the mechanosensitive channels through droplet distortion, mimicking mechanosensory cells. The trace shown here is an experimental conductance trace involving MscL activation.

C.3. Materials

C.3.1. Thermoreversible Organogel Preparation

Mixtures of hexadecane oil (Sigma-Aldrich, St. Louis, MO) and poly[styrene-b-(ethylene-co-butylene)-b-styrene (SEBS, G-1650E, Kraton) were prepared as previously described [25, 51]. This polymer contains polystyrene endblocks which are incompatible with hexadecane, causing the endblocks to gather together and provide a nanostructured polymer mesh within the organic solvent producing a viscoelastic material. The oilpolymer mixture was heated to 100 °C and stirred at 500 rpm until clear. Upon cooling, the gel solidifies and may be stored for future usage. SEBS was dissolved at 20 mg/mL within the oil, as this produced a gel that was solid enough to support mechanical perturbations (G' of approximately 20 Pa at room temperature as measured using a parallel plate rheometer [25]) while not requiring melt temperatures that would threaten the functionality of MscL (target gel transition temperature of 40 °C [25]). The resulting viscoelastic gel is highly viscous at room temperature with a weakly-elastic backbone formed by the polymeric matrix within the oil. This gel is softer than subcutaneous tissue (~ 1 kPa modulus of elasticity [53]) yet still sufficiently stiff to ensure droplet distortion and minimize elastocapillarity effects [54] given the low interfacial tensions of lipid-oil mixtures [23, 48] and expected droplet dimensions ($500 - 1000 \, \mu m$ diameter).

C.3.2. Preparation of MscL Proteoliposomes

Purified MscL was reconstituted in proteoliposomes and introduced into aqueous water droplets to render the membranes sensitive to mechanical perturbation as explored previously [44, 46]. The V23T gain-of-function mutant was used to enhance gating [43]. Proteoliposomes were prepared as originally described by Sukharev et al [41]. V23T MscL

was expressed in E. coli, (strain MJF465) grown at 37 °C to optical density 0.78 and induced with 0.5 mM isopropyl β-D-1-thiogalactopyranoside (IPTG) for 90 minutes. The retrieved cell pellet was then suspended in phenylmethylsulfonyl fluoride (PMSF, a protease inhibitor and FastDigest buffer/lysozyme solution) and broken with a French Press at 31,000 psi at 4 °C for homogenization. Cell debris was removed by centrifugation (8,000 RPM for 10 min at 4 °C) and then membranes were pelleted at 25,000 RPM for 45 minutes at 4 °C. Membrane pellets were solubilized in phosphate-buffered saline with 8 mM ndodecyl β -D-dodecylmaltoside (DDM) overnight at 4 °C. The solubilized extract was cleared with a 25000 RPM, 60 min ultracentrifugation and then incubated with nickelnitrilotriacetic acid (Ni-NTA) beads overnight, with slow tube rotation at 4°C. In the morning, the beads were washed with 10 mM imidazole solution and then the protein was eluted with a 10-to-500 mM steep imidazole gradient, also replacing DDM with 1% βoctylglucoside (OG). The content of eluted fractions was checked using standard SDS PAGE (12%) gels. The concentration of imidazole in MscL-containing fractions was decreased by dilution and the isolated protein was then reconstituted in 1,2-diphytanoylsn-glycero-3-phosphocholine (DPhPC, Avanti Polar Lipids) liposomes. The liposomes were dialyzed for 24 hours to remove excess octylglucoside, swapping the solution frequently. The resulting suspension was then centrifuged again at 14,000 rpm for 20 minutes and the proteoliposome pellets were stored at 4 oC. The presence of reconstituted MscL in proteoliposomes was verified again with a 12% sodium dodecyl sulfate polyacrylamide gel electrophoresis (SDS-PAGE).

C.3.3. Lipid Solutions

1,2-diphytanoyl-sn-glycero-3-phosphocholine phospholipids (DPhPC, Avanti Polar Lipids, Alabaster, AL) lipids are suspended in an electrolyte solution (10 mM MOPS, 500 mM KCl, Sigma-Aldrich, St. Louis, MO resulting in a pH=7 as measured) at a concentration of 2 mg/mL. This solution was then subjected to 5 freeze-thaw cycles. The MscL proteoliposome solution was then added for an approximate proteoliposome concentration of 10 ng/mL. The lipid solution was prepared for DIB formation by first extruding the solution through a filtering block (Avanti Mini Extruder, pore size 0.1 mm, Avanti Polar Lipids, Alabaster, AL) until clear, and then sonicated in a bath sonicator (Elmasonic S100h Ultrasonic sonicator, Elma Schmid Bauer GmbH, Gottlieb-Daimler-Straße Singen, Germany). Solutions were then stored at 4 °C and sonicated prior to each use.

C.4. Methods

C.4.1. Assessing MscL Functionality for DIBs Formed in Oil

Prior to assessing MscL functionality in the organogel, the MscL proteoliposomes were tested by replicating results from droplet compression in oil [44, 46] using hydrogel-filled holding pipettes [55]. Electrodes were prepared by shaping and smoothing the edges of capillary tubes (glass tubes, 1.0 mm OD, 0.58 mm ID, x 10 cm, World Precision Instruments Inc., Sarasota, FL) using a Bunsen burner which helped to hold the droplets submerged within the oil parallel to the focal plane. Following the shaping procedure, the capillary tubes were then filled with a hydrogel solution (40% w/v PEG-DMA 1000, Polyscience Inc, mixed with the buffer solution). Silver/silver-chloride (Ag/AgCl, 250 µm in diameter, Good Fellow, Coraopolis, PA) electrodes were threaded afterwards into the uncured hydrogel and subsequently cured into place with UV exposure (365 nm source

High Power UV Curing LED System, Thorlabs, Newton, NJ). The capillaries are attached to the patch-clamp amplifier (Axopatch 200B, Digidata 1550, Molecular Devices), with the ground electrode also attached to the piezoelectric actuator (P601, Physik Instrumente), controlled by a function generator (33120A function generator, Hewlett-Packard, Palo Alto, CA). Sharpened capillaries filled with the MscL-containing liposome suspension are attached to a manual microinjector (Sutter Instrument, Novato, CA) attached to a manual micromanipulator (Siskiyou Crossed roller 40TPI manual manipulator, 4-axis, Siskiyou, Grants Pass, OR) and droplets are deposited on the submerged ends of the capillaries containing the cured hydrogel. The hydrogel provides an anchor for droplet deposition as well as a conductive link between the droplet interiors and the Ag/AgCl electrodes. The droplets are oscillated in a sinusoidal fashion (200 mHz) and gating events associated with MscL are monitored by examining the transmembrane current. The obtained current traces were recorded in voltage clamp mode (Whole Cell, $\beta = 1$) using the patch clamp amplifier and Digidata acquisition system (Molecular Devices, Sunnyvale, CA) at a sampling frequency of 10 kHz and filtered at 1 kHz using the embedded low-pass Bessel filter (-80 dB/decade). Post-acquisition, a 1000 Hz fourth-order Butterworth low-pass filter was applied in MATLAB for visualization purposes. Images were acquired using a CCD camera (DFC365 FX, Leica Microsystems, Wetzlar, Germany) mounted on an inverted microscope (Leica DMI3000-B, Leica Microsystems, Wetzlar, Germany) in a Faraday cage minimizing external noise on an active vibration isolation stage (Thorlabs, Newton, NJ).

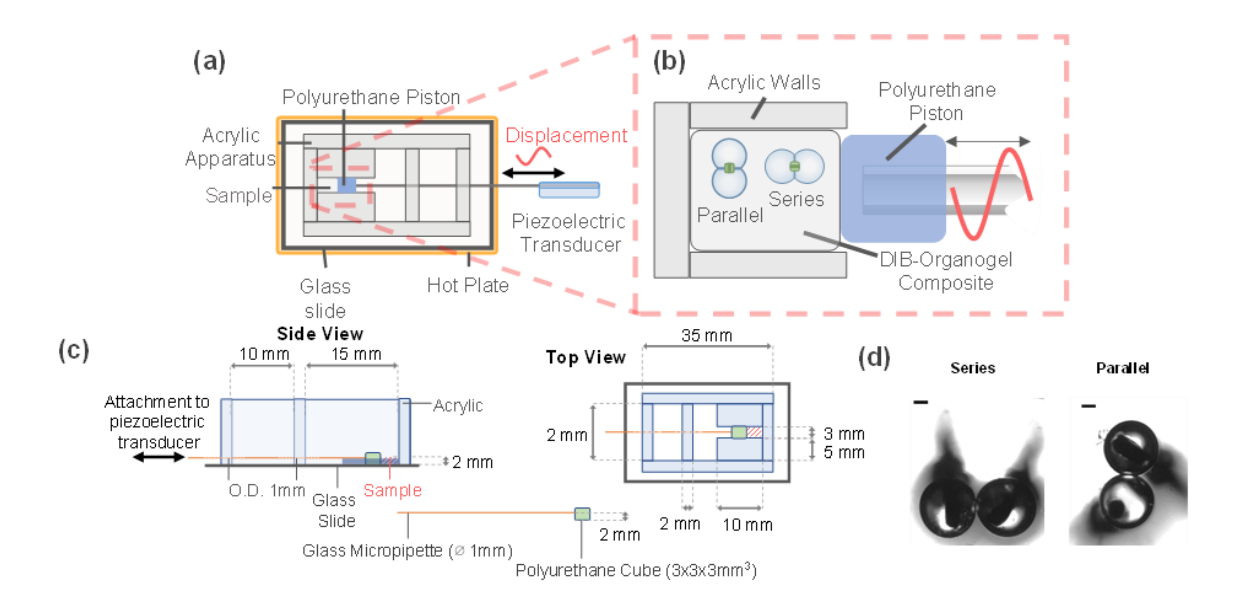


Figure C.3 - (a) The molten gel is poured into the mold within the acrylic apparatus, droplets are deposited, and the gel is cooled to room temperature. A piston connected to a piezoelectric transducer is used to cyclically compress the organogel containing DIBs. (b) The droplets are printed in the organogel either in parallel with the distortion direction, or in series with the distortion, offset from the center of the gel. The orientation of the printed droplets influences their response to compression. (c) This polyurethane dish was custom-made and designed in our lab according to the mentioned dimensions here. (d) Experimental images of the droplets with embedded electrodes in the two configurations. Scale bar is 250 μm.

C.3.2. Activating MscL in Organogel Composites

Figure C.3 summarizes the experimental approach for gating MscL within the organogel through external perturbations. An acrylic frame structure (additional details provided in Figure C.4) was used to hold the molten organogel. The acrylic structure is placed on an ITO (Indium tin oxide) coated heating slide (Cell Microsystems, Durham, NC). Molten organogel is poured around the electrodes and held just above the transition

temperature (40 °C). Two Ag/AgCl electrodes with agarose beads at their tips (2% by mass agarose solution EZ Pack Agarose LE, Molecular Biology Grade, Benchmark Scientific, Sayresville, NJ) are connected to the patch-clamp amplifier and data acquisition system (Axopatch 200B, Digidata 1550, Molecular Devices) and placed within the molten organogel. Glass micropipettes pulled to sharp points filled with the liposome suspension using microfils (World Precision Instruments, Sarasota, FL) are attached to manual micromanipulators and used to deposit droplets of the lipid solution within the molten gel onto the electrode ends. The membrane is formed at their interface, and the gel is allowed to cool to room temperature.

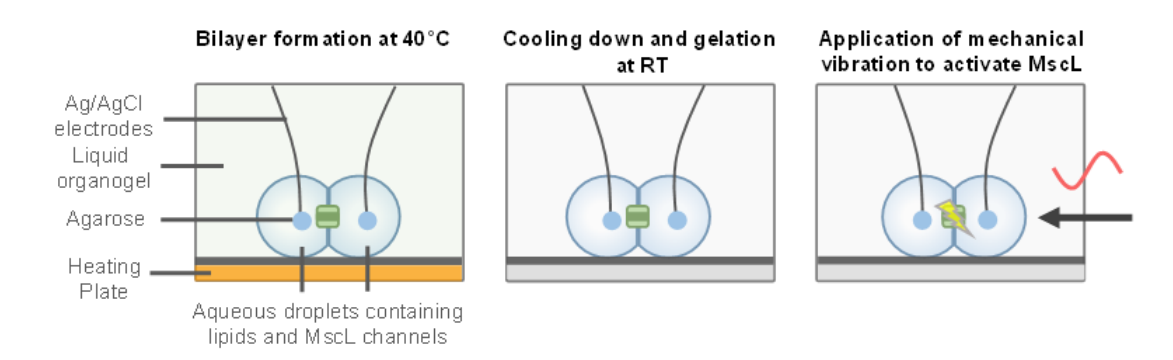


Figure C.4 - Droplets are deposited on the electrodes within the molten organogel at 40 °C. After membrane formation at the droplet intersection, the gel is allowed to cool to room temperature and solidify, encapsulating the droplets. Once the gel is solidified, a cyclical displacement is applied using a piston and piezoelectric actuator.

The droplets were printed in two configurations as shown in Figure C.4.b: in parallel and in series with respect to the direction of the compression from the piston. The droplets are typically printed off-center of the axis of the gel-compressing piston due to positioning constraints in the working surface. After formation of the membrane and

solidification of the surrounding gel, the gel is compressed with a piston fashioned from polyurethane (3x3x3 mm) anchored to the tip of a glass micropipette (O.D. 1 mm, glass tubes, 1.1 mm x 10 cm, World Precision Instruments Inc., Sarasota, FL). This micropipette is attached to a flexure-guided piezoelectric actuator (P601, Physik Instrumente), controlled by a function generator (33120A function generator, Hewlett-Packard, Palo Alto, CA) allowing for cyclical compression of the organogel cube within the mold. The gel may be assumed incompressible, and the boundaries are necessary for pouring and forming the molten organogel at 40 °C. The organogel cube containing the droplets was compressed with varying amplitudes (150, 200, and 250 µm) and frequencies in a sinusoidal fashion (100 mHz, 200 mHz, 500 mHz, and 1 Hz). The current produced during compression was recorded and converted to membrane conductance, where sudden jumps in this conductance represent MscL activity with multiple gating states dependent on the tension in the membrane [43]. If measuring changes in the membrane area is desired, an alternating triangle-wave voltage is supplied instead, and the capacitance is measured and converted into membrane area [44] (membranes' specific capacitance previously evaluated at $0.62 \,\mu\text{F/cm}^2[23]$).

C.4.3. Predicting Activation Mechanisms in Organogels through Finite Element Simulations

The droplets are fully encapsulated and constrained within the organogel. Consequently, their response to perturbation will be determined largely by the distortion of the surrounding polymeric matrix [54] given their low interfacial tensions [23, 48]. A global-local finite element model is constructed in order to understand the effect of deformation on droplet structure embedded inside an organogel matrix for computational

efficiency. The global model is a homogeneous block of organogel possessing voids for the droplets which is subjected to piston compression similar to the experimental setup in Figure C.4.b. Two local models are constructed with the droplet structure in-series and inparallel relatively to the applied piston deformation. A 5-parameter Mooney-Rivlin hyperelastic material model (c_{10} =-21.30Pa, c_{01} -28.28Pa, c_{20} =4.16Pa, c_{11} =-17.55Pa, $c_{02}=29.11$ Pa, $D_1=0$) is used for the organogel with a modulus of elasticity of approximately 20 Pa to mirror experimental conditions [25]. For the fluid within the voids, a second order Ogden hyperelastic model is used (μ_1 =0.54Pa, α_1 =4.98, μ_1 =53.4kPa, α_2 =2.51E-4, D₁=0, D₂=0). Ogden material parameters are chosen such that the initial shear modulus of the droplets is ten times smaller than the modulus for the organogel to approximate the compliance of the liquid inclusions relative to the gel. In both cases the material model has zero incompressibility parameter (D_i=0) i.e. both materials are fully incompressible. A hybrid *u-p* element formulation is used for the nonlinear finite element solution. Given the lack of available friction coefficient between the gel and the surrounding mold, a rough contact formulation for the interactions of the mold and the gel is used which does not allow sliding of the gel but does allow separation of the contact as the piston compresses the gel. This separation only occurs at the far edge where the deformation is applied. The acrylic surface on the sides of the mold is hydrophobic and cured gels demonstrated the ability to adhere to glass and plastic surfaces even during inversion [25] so some degree of bonding is anticipated.

The monolayer and bilayer interfaces are not explicitly modelled here given their transient nature [49, 50]. Furthermore, the equilibrium tensions of the monolayer and bilayer interfaces (~1-2 mN/m [23, 48]) are sufficiently low that their elastocapillary

contributions are negligible [52]. Consequently, the coupling between the droplets and the gel is a one-way coupling where the monolayer and bilayer areas are dictated by the shape of the distorted encapsulating gel. The deformed droplet geometries are exported and post-processed to calculate the area of the annulus between the droplets as well as the surrounding monolayer area. Predictions for the maximum changes in bilayer area and monolayer areas are assigned based on these values respectively.

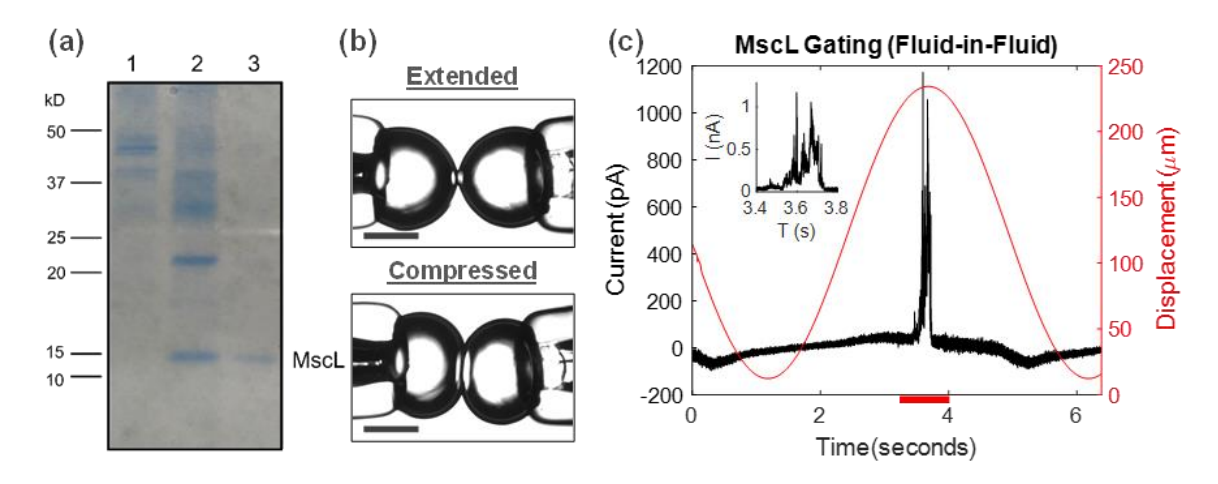


Figure C.5 - V23T MscL were tested in DIBs formed within oil to ensure functionality and provide comparisons to the organogel cases. Here, the droplets are suspended from hydrogel-filled capillary tubes and compressed in a sinusoidal fashion. (a) Results from gel electrophoresis of eluted fractions prior to reconstitution in proteoliposomes. The Ni-NTA-bound V23T MscL protein was eluted with a linear 10-500 mM gradient of imidazole. The gel shows the flow-through fraction collected at the beginning of the gradient (lane 1), the peak of protein elution still containing contaminating bands (lane 2) and a fraction collected in the second half of the gradient carrying a pure MscL band. Fraction 3 was used for reconstitutions. (b) The droplets are directly coupled to the oscillation and the membrane area is adjusted accordingly without constraints on expansion (53). Scale bars are 500 μm.

KCl recording buffer) combined with the oscillator compression shows that MscL gates at peak compression as observed in previous works (44). Current is reported rather than conductivity due to the presence of mechanoelectric current (42). Inset provides a closer look at the gating peak.

C.5. Results and Discussions

C.5.1. V23T MscL Activation within DIBs Formed in Oil

First, MscL functionality was tested without encapsulation. When MscL is included within a single DIB suspended in oil that is compressed periodically to vary the tension within the membrane, gating is observed at peak compression similarly to previous results [45, 46] as shown in Figure C.5 by plotting the actuator displacement and the measured current. The sudden jump in current represents the opening of several MscL channels within the membrane, showing that the produced MscL proteoliposomes are functional. Furthermore, the results from gel electrophoresis confirm the existence of V23T MscL within the proteoliposomes (Figure C.5.a).

In this setting, the droplets are perturbed from a spherical shape which transiently increases the monolayer tension at the droplet surface through an increase in the area per lipid [49]. Each monolayer contributes to an increase in the bilayer tension, gating the embedded MscL channels. However, the observed gating ceases as the system reestablishes equilibrium monolayer tensions and contact angles through increases in the membrane area and incorporation of additional lipids from the reservoir within the droplets. This illustrates the transient nature of the tensions within DIBs in oil while demonstrating the functionality of the V23T MscL proteoliposomes.

C.5.2. Finite Element Model Predictions and Experimental Results for Organogel Compression Mechanics

With V23T functionality demonstrated, the research moves to investigating activation mechanics within the encapsulating gel. The finite element model was established to explore MscL activation in organogels. The mechanisms for activation are assumed to rely on similar mechanisms as the traditional DIB case, where the change in monolayer tension is a function of droplet distortion and the contact angle is a function of the change in bilayer area. However, the droplet distortion will now be determined by the distortion of the encapsulating gel. FEM predictions were used to predict the changes in geometry for the encapsulated droplets as the gel is gradually compressed, tracking changes in both the bilayer and monolayer areas which are linked to MscL activation. The monolayers and bilayer are not explicitly modelled here but assumed to remain confined by the shape of the surrounding gel.

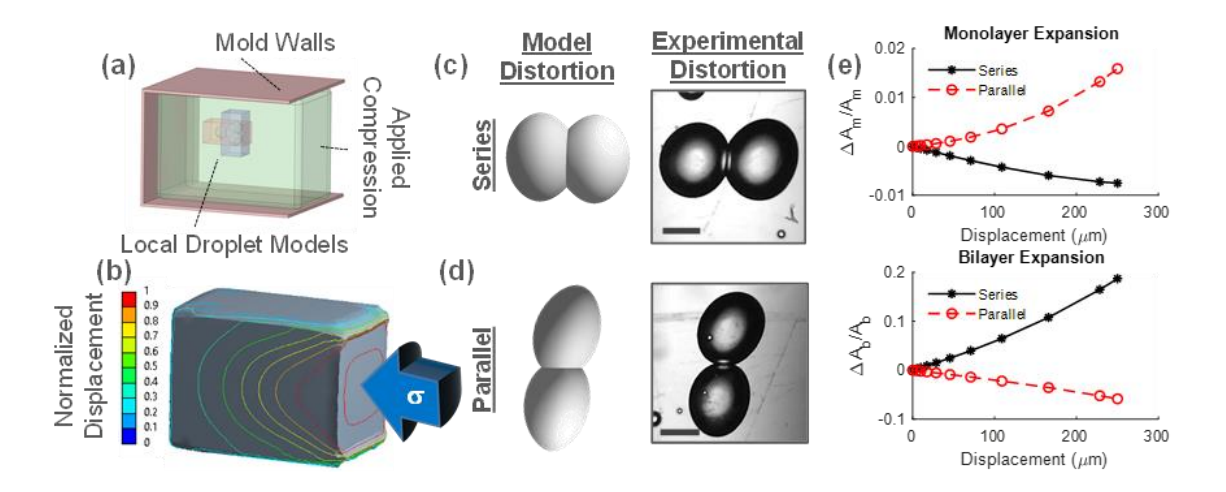


Figure C.6 - A finite element model is used to predict how droplet orientation relative to the compression influences their distortion. (a) The local droplet models are placed away from the organogel midline to mirror experiments and the gel is compressed into the mold,

simulating the piston. (b) As the organogel is compressed, the friction at the boundary of the gel and the mold produces a parabolic distortion in the gel. (c)–(d) This produces uneven compression of the droplets dependent on their distance from the boundaries that compares favorably with experimental observations (scale bar is 200 µm), confirming that the droplet shape is determined by the shape of the surrounding gel. (e) The changes in monolayer and bilayer area for the two configurations are plotted as a function of piston displacement, highlighting the influence of bilayer orientation relative to the compression.

Two orientations of the droplets are generated within the gel; in series and in parallel as shown in Figure C.6.a. As the gel is compressed into the mold (Figure C.6.a), the rough friction at the boundaries produces a parabolic distortion of the organogel as shown in Figure C.6.b. Experimental and simulated images of the droplets undergoing compression are provided in Figure C.6.c-d. The oil-infused gel exhibits a parabolic distortion maximized towards the center of the gel.

Comparison between the simulated droplet shapes and experimental images confirm the assumption that the droplet distortion conforms to the distortion of the surrounding gel. The changes in monolayer area and the change in bilayer area are both tracked as the area of the fluid-gel interface and area of the aperture between the inclusions respectively during compression as shown in Figure C.6.e. These plots assume that the membrane area expands to the maximum diameter allowed by the annulus between the droplets, and that the monolayer area is determined by the bounding surface between the droplets and the gel. Several trends are noted depending on the droplet orientation. In the parallel orientation, the monolayer area is predicted to increase approximately 1.5% at

maximum piston compression. This value aligns favorably with previous measurements of droplet distortion in oil necessary for MscL activation [46]. Furthermore, the bilayer area is observed to decrease with compression due to the deformation of the surrounding gel. These two phenomena are associated with increases in bilayer tension through increases in the monolayer area and reductions in the external angle of contact respectively. When the droplets are oriented in series, the opposite trends are observed. Here the bilayer is permitted to expand within the gel as the droplets are compressed, and as a result the surrounding monolayer area is diminished as the bilayer expands.

These predicted changes in the monolayer area A_m (relating back to droplets' elongation and flattening) as well as changes in the contact angle (θ_m in Figure C.2.a) are linked to changes in the interfacial tension of the bilayer responsible for MscL activation [48, 56, 57]. Consequently, we expect that droplets positioned in parallel will exhibit amplified MscL activations while droplets printed in series will exhibit reduced MscL activations.

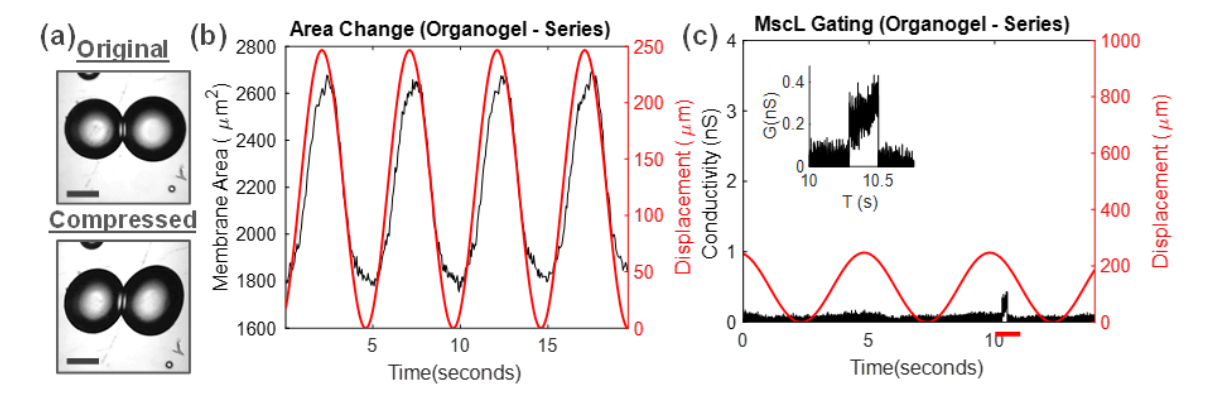


Figure C.7 - Results from V23T MscL-DIBs oriented in series within the gel. (a) The droplets within the gel are deformed with the surrounding gel (scale bar is 200 μ m). (b) Tracking the membrane capacitance and converting to membrane area assuming a fixed specific capacitance of 0.6 μ F/cm², showing that the membrane is able to freely expand

and contract in a synchronized fashion with the piston displacement. (c) Minimal changes in membrane conductivity were observed as the gel was compressed aside from occasional brief peaks as shown here. Inset provides a closer look at the gating peak.

C.5.3. Membrane Response and MscL V23T Activation in Organogel

Experiments involving MscL activation in the organogel were conducted for a varying range of compressions (150, 200, and 250 µm) and frequencies (100, 200, 500, and 1000 mHz) with the droplets printed in series and in parallel. For all cases with droplets printed in series, the membrane area shows cyclical expansion and contraction as shown in Figure C.7.b and observed in the literature [25]. However, MscL activation in the series orientation is infrequent and unreliable, with brief gating events observed approximately once every ten experiments (Figure C.7.c). The small amplitude suggests that the channel was not fully activated but was activated to a sub-conducting state [43]. This lack of activation is of interest since lateral compression of the droplets was used previously for DIBs in oil (Figure C.5). However, the mechanics of droplet distortion change considerably when the droplets are encapsulated within the gel as described in Figure C.6. Increase in the monolayer tension is limited to the brief period when the bilayer has not yet expanded (Figure C.7.b). These findings do not preclude the possibility of MscL activation within droplets adhered in series and compressed together inside the organogel; but activation is diminished.

When the droplets are printed in parallel to the direction of distortion, the bilayer membrane contracts in response to compression shown in Figure C.8.b and as predicted in Figure C.6.e. Gating is not observed at the 150 and 200 µm displacements of the actuator.

However, when the actuator is driven with a 250 µm amplitude, prolonged and repeated gating of MscL channels is observed as sudden variations in the membrane conductance. This full compression corresponds to a predicted increase in monolayer area of close to 2% (Figure C.6.e), which is the same reported threshold for activation within DIBs formed in oil [46].

The magnitude of the net membrane conductance produced by compression varies between 1 nS to 33 nS, implying activation ranging from sub states to multiple channels. The gating is transient (ranging from 0.2-20 seconds in duration with one notable outlier of several minutes), and a representative trace showcasing pronounced gating events is presented in Figure C.8.c. These behaviors are often amplified in comparison to gating events associated with DIB compression in oil as shown in Figure C.5. The observed prolonged activations are likely due to the inability of the membrane to alleviate the increase in monolayer tension through expansion as seen in the series configurations, given the constraints of the surrounding gel. Consequently, the primary mechanism for alleviating the tension is through monolayer equilibration with the lipid reservoir within the droplets which is slower [45] than membrane formation [44]. In addition, the displacement of the droplets due to uneven compression may be further responsible for developing shear forces in the membrane associated with inter-monolayer viscosity [58].

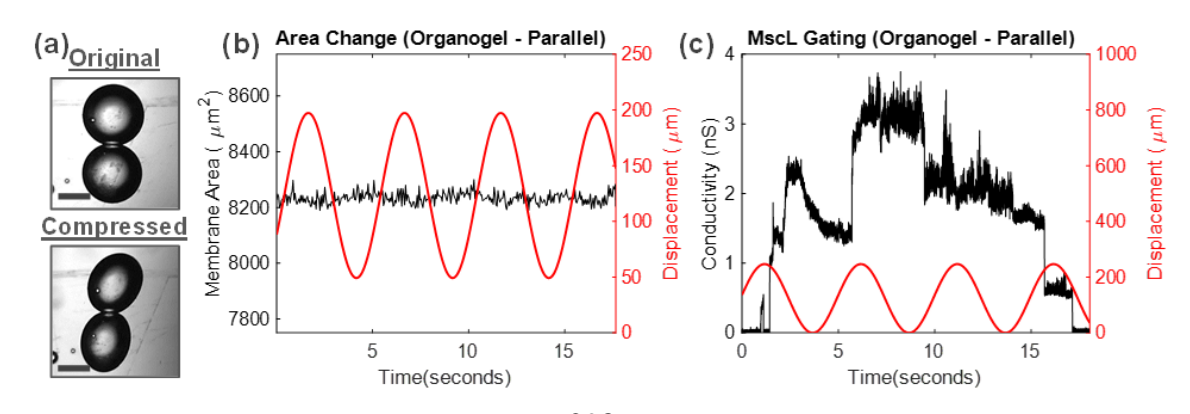


Figure C.8 - Results from V23T MscL-DIBs oriented in parallel within the gel. (a) The droplets deform with the surrounding gel as predicted by the FEM model (scale bar is 200 μm). (b) Tracking the membrane capacitance and converting to membrane area assuming a fixed specific capacitance of 0.6 $\mu F/cm^2$ shows minimal change in membrane area. The area appears to diminish slightly during compression, likely due to compression of the annulus compensating minimal bulging. The cyclical displacement applied here is 150 μm rather than 250 μm to avoid gating events which would complicate capacitance measurements. (c) Substantial changes in membrane conductance are observed during gel compression when the droplets were printed in parallel, indicating multiple gating events. From observation, the gating events are sustained across compression cycles and will occasionally combine with new channel activation events during peak compression.

These gating events occur at lower frequencies of compression (100 mHz, 200 mHz). When the gel is compressed cyclically at 500 mHz or 1 Hz, the observed gating phenomena shift from pronounced single peaks to a continuous stream of subconductive gating states that are indistinguishable from a leaky membrane, ranging between 0.3 and 1.0 nS conductivity. The authors caution the reader that these recordings may be associated with membrane disruption as opposed to true gating events associated with MscL activity, noting that there are transient effects related to the equilibration of monolayer tension with droplet distortion. There may be insufficient time for resetting the membrane tensions between compression steps as noted in previous studies on MscL gating in DIBs [45].

Pronounced MscL gating events are only observed for cases where the droplets are printed in parallel with the compression direction, and the gating was only observed for

cases where the displacement of the actuator was maximized at 250 µm combined with lower oscillation frequencies. This provides directional mechanosensation within the artificial system resembling the sensory epidermis. Results are summarized in Figure C.9. Examining the model predictions for droplets printed in parallel and in series at the prescribed compressions (Figure C.9.a), we note that the changes in monolayer and bilayer area enhance the gating probability for MscL in DIBs according to the equations in Figure C.9.b for droplets printed in parallel while diminishing the influence for droplets printed in series. Gating only occurs when these influences are maximized, and the frequency of compression-relaxation cycles must be sufficiently low to ensure that the monolayer tensions are able to partially reset in between compressions.

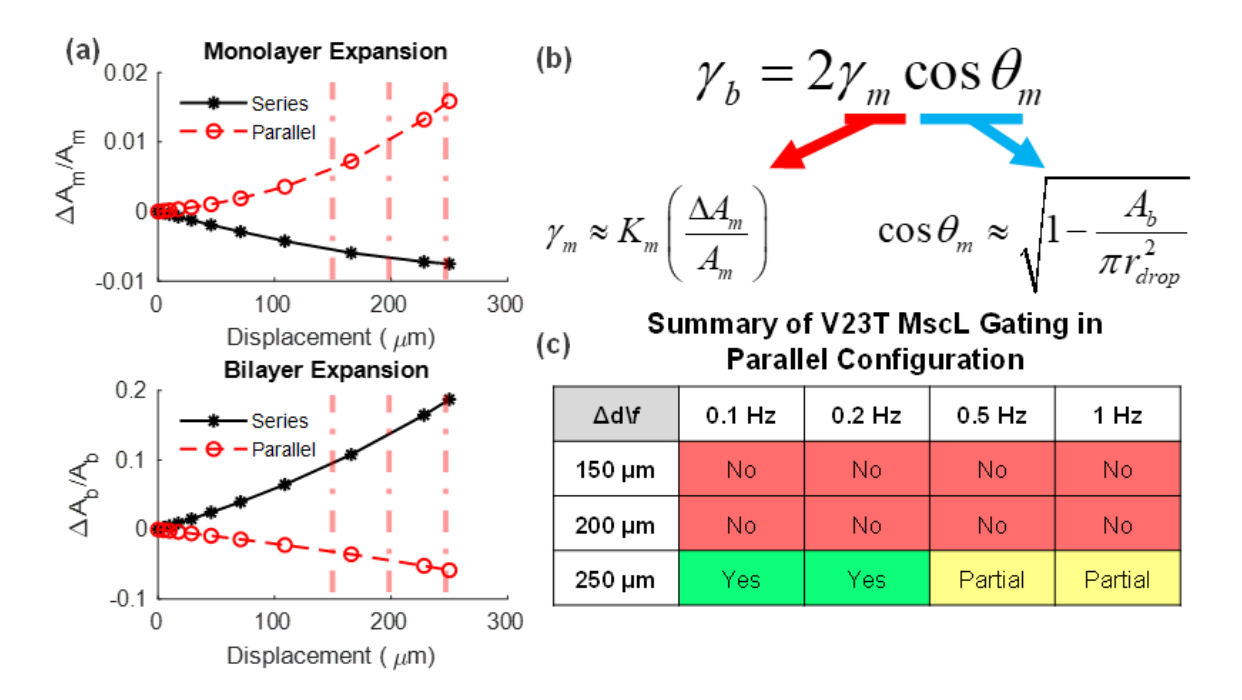


Figure C.9 - Summary of MscL activation results. (a) Droplets were deposited in parallel or in series with respect to the direction of compression. Results from the model for changes in bilayer and monolayer area are presented for these two cases, with bars indicating the three levels of compression. (b) MscL gating in DIBs is caused by elevated 300

bilayer tension, including increases in monolayer tension and reductions in the external angle of contact. Droplets printed in parallel to the direction of compression satisfy both criteria, while droplets printed in series exhibit the opposite trends. (c) Consequently, gating is only observed in cases with droplets printed in parallel. The amplitude and frequency of compression was varied, and results aligned with expectations from previous DIB MscL research.

C.5. Conclusions

In this manuscript biologically inspired mechanosensing in a composite material mimicking cutaneous mechanosensory cells within the epidermis is explored. Model membranes encapsulated within a soft thermoreversible gel were functionalized with a mechanosensitive channel isolated from Escherichia coli. This approach allows for a simple gating of MscL channels in a soft composite material, converting external mechanical forces applied to the soft gel into electrical activities and exchanges between encapsulated droplets. The mechanics of MscL stimulation within the soft gel is unique and different than previous work on MscL-DIB systems, and the surrounding gel provides means to distort the droplets through compression applied from the boundaries of the composite material as shown in the finite element method simulations.

The droplet distortion depends on the direction of the printed droplets relative to the compressed boundary (axis of compression), allowing for a directional sensitivity. If the droplets are printed in series with the compression, then the membrane is allowed to expand freely without generating sufficient tension; however, droplets printed in parallel constrain the membrane while amplifying droplet distortion as well as the monolayer area and tension increase. The gating events observed within the organogel exhibit higher conductance and prolonged durations of activation when compared to gating in fluid-influid DIB experiments.

This research demonstrates that it is possible to activate MscL within a composite organogel-DIB material, and furthermore this activation is dependent on the orientation of the droplets relative to the compression which provides an aspect of control over the channel gating. The phenomena is similar to mechanosensory cells converting distortion of the surrounding epidermis into electrical activity, and the platform approximates biological mechanosensation through deformation of the embedded droplets with functional interfaces.

C.7. References

- 1. Woo, S.-H., E.A. Lumpkin, and A. Patapoutian, Merkel cells and neurons keep in touch. Trends in cell biology, 2015. 25(2): p. 74-81.
- 2. Feng, J., et al., Piezo2 channel–Merkel cell signaling modulates the conversion of touch to itch. Science, 2018. 360(6388): p. 530-533.
- 3. Moll, I., et al., Human Merkel cells—aspects of cell biology, distribution and functions. European journal of cell biology, 2005. 84(2-3): p. 259-271.
- 4. Kim, D.-K. and K.A. Holbrook, The appearance, density, and distribution of Merkel cells in human embryonic and fetal skin: their relation to sweat gland and hair follicle development. Journal of investigative dermatology, 1995. 104(3): p. 411-416.
- 5. Bayley, H., et al., Droplet interface bilayers. Mol Biosyst, 2008. 4(12): p. 1191-208.

- 6. Stanley, C.E., et al., A microfluidic approach for high-throughput droplet interface bilayer (DIB) formation. Chem Commun (Camb), 2010. 46(10): p. 1620-2.
- 7. Holden, M.A., Building interconnected membrane networks. Methods Cell Biol, 2015. 128: p. 201-22.
- 8. Holden, M.A., D. Needham, and H. Bayley, Functional bionetworks from nanoliter water droplets. J Am Chem Soc, 2007. 129(27): p. 8650-5.
- 9. Punnamaraju, S., H. You, and A. Steckl, Triggered release of molecules across droplet interface bilayer lipid membranes using photopolymerizable lipids. Langmuir, 2012. 28(20): p. 7657-7664.
- 10. Makhoul-Mansour, M.M., et al., Photopolymerized microdomains in both lipid leaflets establish diffusive transport pathways across biomimetic membranes. Soft Matter, 2019. 15(43): p. 8718-8727.
- 11. Booth, M.J., et al., Light-activated communication in synthetic tissues. Sci Adv, 2016. 2(4): p. e1600056.
- 12. Urban, P.L., Compartmentalised chemistry: from studies on the origin of life to engineered biochemical systems. New Journal of Chemistry, 2014. 38(11): p. 5135-5141.
- 13. Jones, G., et al., Autonomous droplet architectures. Artificial life, 2015. 21(2): p. 195-204.
- 14. Bayley, H., et al., Droplet interface bilayers. Molecular BioSystems, 2008. 4(12): p. 1191-208.
- 15. Holden, M.A., D. Needham, and H. Bayley, Functional bionetworks from nanoliter water droplets. Journal of the American Chemical Society, 2007. 129(27): p. 8650-8655.

- 16. Maglia, G., et al., Droplet networks with incorporated protein diodes show collective properties. Nature Nanotechnology, 2009. 4: p. 437-440.
- 17. Booth, M.J., et al., Droplet Networks, from Lipid Bilayers to Synthetic Tissues, in Encyclopedia of Biophysics, G. Roberts and A. Watts, Editors. 2019, Springer Berlin Heidelberg: Berlin, Heidelberg. p. 1-13.
- 18. Villar, G., A.D. Graham, and H. Bayley, A tissue-like printed material. Science, 2013. 340(6128): p. 48-52.
- 19. Sarles, S.A. and D.J. Leo, Physical encapsulation of droplet interface bilayers for durable, portable biomolecular networks. Lab on a Chip, 2010. 10(6): p. 710-7.
- 20. Tien, H.T. and Dawidowi.Ea, Black Lipid Films in Aqueous Media a New Type of Interfacial Phenomenon Experimental Techniques and Thickness Measurements. Journal of Colloid and Interface Science, 1966. 22(5): p. 438-+.
- 21. Tien, H.T., Black lipid membranes in aqueous media: interfacial free energy measurements and effect of surfactants on film formation and stability. The Journal of physical chemistry, 1967. 71(11): p. 3395-3401.
- 22. Faugeras, V., et al., Membrane determinants for the passive translocation of analytes through droplet interface bilayers. Soft Matter, 2020.
- 23. El-Beyrouthy, J., et al., A new approach for investigating the response of lipid membranes to electrocompression by coupling droplet mechanics and membrane biophysics. Journal of the Royal Society Interface, 2019. 16(161): p. 20190652.
- 24. Alcinesio, A., et al., Controlled packing and single-droplet resolution of 3D-printed functional synthetic tissues. Nature Communications, 2020. 11(1): p. 1-13.

- 25. Challita, E.J., et al., Encapsulating Networks of Droplet Interface Bilayers in a Thermoreversible Organogel. Scientific Reports, 2018. 8(1): p. 6494.
- 26. Hwang, W.L., et al., Asymmetric droplet interface bilayers. Journal of the American Chemical Society, 2008. 130(18): p. 5878-5879.
- 27. Wauer, T., et al., Construction and manipulation of functional three-dimensional droplet networks. ACS Nano, 2014. 8(1): p. 771-9.
- 28. Hwang, W.L., et al., Electrical Behavior of Droplet Interface Bilayer Networks: Experimental Analysis and Modeling. Journal of the American Chemical Society, 2007. 129(38): p. 11854-11864.
- 29. Ma, S., et al., Gel Microrods for 3D Tissue Printing. Advanced Biosystems, 2017. 1(8): p. e1700075.
- 30. Dupin, A. and F.C. Simmel, Signalling and differentiation in emulsion-based multi-compartmentalized in vitro gene circuits. Nature chemistry, 2019. 11(1): p. 32-39.
- 31. Sarles, S.A. and D.J. Leo, Tailored Current--Voltage Relationships of Droplet-Interface Bilayers Using Biomolecules and External Feedback Control. Journal of Intelligent Material Systems and Structures, 2009. 20(10): p. 1233-1247.
- 32. Taylor, G.J. and S.A. Sarles, Heating-enabled formation of droplet interface bilayers using Escherichia coli total lipid extract. Langmuir, 2015. 31(1): p. 325-37.
- 33. Nguyen, M.-A., et al., Hydrodynamic trapping for rapid assembly and in situ electrical characterization of droplet interface bilayer arrays. Lab on a Chip, 2016. 16(18): p. 3576-3588.

- 34. Koner, S., et al., Memristive plasticity in artificial electrical synapses via geometrically reconfigurable, gramicidin-doped biomembranes. Nanoscale, 2019. 11(40): p. 18640-18652.
- 35. Aghdaei, S., et al., Formation of artificial lipid bilayers using droplet dielectrophoresis. Lab on a Chip, 2008. 8(10): p. 1617-1620.
- 36. Huang, J., et al., Direct quantitation of peptide-mediated protein transport across a droplet–interface bilayer. Journal of the American Chemical Society, 2011. 133(40): p. 15818-15821.
- 37. Fischer, A., et al., Ultrasensitive detection of protein translocated through toxin pores in droplet-interface bilayers. Proceedings of the National Academy of Sciences, 2011. 108(40): p. 16577-16581.
- 38. Schild, V.R., et al., Light-Patterned Current Generation in a Droplet Bilayer Array. Scientific Reports, 2017. 7.
- 39. Booth, M.J., et al., Light-patterning of synthetic tissues with single droplet resolution. Scientific reports, 2017. 7(1): p. 9315.
- 40. Sukharev, S.I., et al., A large-conductance mechanosensitive channel in E. coli encoded by mscL alone. Nature, 1994. 368(6468): p. 265.
- 41. Sukharev, S.I., et al., Energetic and spatial parameters for gating of the bacterial large conductance mechanosensitive channel, MscL. The Journal of general physiology, 1999. 113(4): p. 525-540.
- 42. Sukharev, S., et al., The gating mechanism of the large mechanosensitive channel MscL. Nature, 2001. 409(6821): p. 720.

- 43. Anishkin, A., C.-S. Chiang, and S. Sukharev, Gain-of-function mutations reveal expanded intermediate states and a sequential action of two gates in MscL. The Journal of general physiology, 2005. 125(2): p. 155-170.
- 44. Freeman, E.C., et al., The mechanoelectrical response of droplet interface bilayer membranes. Soft Matter, 2016. 12(12): p. 3021-31.
- 45. Najem, J.S., et al., Mechanics of Droplet Interface Bilayer "Unzipping" Defines the Bandwidth for the Mechanotransduction Response of Reconstituted MscL. Advanced Materials Interfaces, 2016.
- 46. Najem, J.S., et al., Activation of bacterial channel MscL in mechanically stimulated droplet interface bilayers. Sci Rep, 2015. 5: p. 13726.
- 47. Rosholm, K.R., et al., Activation of the mechanosensitive ion channel MscL by mechanical stimulation of supported Droplet-Hydrogel bilayers. Sci Rep, 2017. 7: p. 45180.
- 48. Taylor, G.J., et al., Direct in situ measurement of specific capacitance, monolayer tension, and bilayer tension in a droplet interface bilayer. Soft Matter, 2015. 11(38): p. 7592-605.
- 49. Yasmann, A. and S. Sukharev, Properties of diphytanoyl phospholipids at the airwater interface. Langmuir, 2014.
- 50. Venkatesan, G.A., et al., Adsorption kinetics dictate monolayer self-assembly for both lipid-in and lipid-out approaches to droplet interface bilayer formation. Langmuir, 2015. 31(47): p. 12883-12893.

- 51. Venkatesan, G.A. and S.A. Sarles, Droplet immobilization within a polymeric organogel improves lipid bilayer durability and portability. Lab on a Chip, 2016. 16(11): p. 2116-2125.
- 52. Style, R.W., J.S. Wettlaufer, and E.R. Dufresne, Surface tension and the mechanics of liquid inclusions in compliant solids. Soft Matter, 2015. 11(4): p. 672-679.
- 53. Iatridis, J.C., et al., Subcutaneous tissue mechanical behavior is linear and viscoelastic under uniaxial tension. Connective tissue research, 2003. 44(5): p. 208-217.
- 54. Style, R.W., et al., Elastocapillarity: Surface tension and the mechanics of soft solids. Annual Review of Condensed Matter Physics, 2017. 8: p. 99-118.
- 55. Challita, E.J. and E.C. Freeman, Hydrogel Microelectrodes for the Rapid, Reliable, and Repeatable Characterization of Lipid Membranes. Langmuir, 2018.
- 56. Thiam, A.R., N. Bremond, and J. Bibette, From stability to permeability of adhesive emulsion bilayers. Langmuir, 2012. 28(15): p. 6291-8.
- 57. Gross, L.C., et al., Determining membrane capacitance by dynamic control of droplet interface bilayer area. Langmuir, 2011. 27(23): p. 14335-42.
- 58. den Otter, W.K. and S. Shkulipa, Intermonolayer friction and surface shear viscosity of lipid bilayer membranes. Biophysical journal, 2007. 93(2): p. 423-433.